

A high optical access cryogenic optical tweezer array

by

Ting-Wei Hsu

B.S., Purdue University, 2016

M.S., University of Colorado Boulder, 2022

A thesis submitted to the
Faculty of the Graduate School of the
University of Colorado in partial fulfillment
of the requirements for the degree of
Doctor of Philosophy
Department of Physics

2024

Committee Members:

Cindy Regal, Chair

Adam Kaufman

Daniel Slichter

Ana Maria Rey

Longji Cui

Hsu, Ting-Wei (Ph.D., Physics)

A high optical access cryogenic optical tweezer array

Thesis directed by Prof. Cindy Regal

Arrays of single trapped neutral atoms are an emerging platform for quantum metrology, simulation, and information processing. They have seen the fastest qubit number scaling in the past few years. In this thesis, I present a set of new technologies, a cryogenic optical tweezer array and trapped single atoms using a metasurface focusing lens, that we developed for the next generation of optical tweezer platforms.

In the first part of the thesis, I describe a new apparatus that combines a cryogenic environment with high-NA optical access. We demonstrate a trapped array of single atoms with a vacuum-limited lifetime of up to 3000 seconds, which is difficult to achieve in room temperature tweezer experiments. Additionally, we characterize the heating of atoms in our apparatus and find no adverse effects from residual vibration introduced by the cryocooler. Interferometric measurements reveal residual vibration to be 2 nm RMS. With the long vacuum-limited lifetime, we measure imaging and cooling losses of trapped single atoms that can often be overwhelmed by vacuum loss in typical apparatus. We demonstrate an imaging loss rate of $3.8(4) \times 10^{-4}$ per 14 ms image, with an imaging assignment infidelity of 10^{-6} and a cooling loss rate of $5(4) \times 10^{-5}$ per 25 ms cooling pulse, among the lowest reported in alkali atoms. We also demonstrate preliminary single qubit rotations with a microwave antenna within the cryogenic housing and characterize magnetic field fluctuations to 0.5 mG over a period of half an hour, comparable to other tweezer experiments.

In the second part of my thesis, I describe a new approach to manipulate and control trapped single atoms in optical tweezers through the use of optical metasurfaces. Optical metasurfaces are planar photonic elements composed of a periodic array of subwavelength dielectric nanostructures. These nanostructures couple, either resonantly or off-resonantly, and re-radiate the incoming light with a transformed phase, polarization, and amplitude determined by the nanostructure's shape,

size, and material composition. In this thesis, we create a 0.55 NA metasurface lens with a focusing efficiency of up to 58% to trap single atoms to sub-micron positional confinement, and detect single ^{87}Rb atoms through the same lens. We also perform field-of-view measurements and find a diffraction-limited field-of-view of $\pm 10 \mu\text{m}$, which is in good agreement with numerical simulation. Finally, I present potential future metalens designs with qualities beneficial for creating large neutral atom tweezer arrays, including a doublet lens with a large field-of-view of up to 2 mm, a lens without chromatic aberration, and polarization multiplexed lenses for dynamically changing the trapping potential or for achromatic imaging of the trapped atoms.

Dedication

This work is dedicated to my family and to the friends who have made an impact on my life.

Acknowledgements

First and foremost, I would like to thank my advisor, Cindy Regal. The guidance and mentorship she provided during my PhD journey were exceptional. Working and learning in the Regal lab has been an amazing experience that I could not have imagined getting elsewhere. I am grateful for the freedom she gave me to pursue topics that interested me during the design and construction of the experiments.

Furthermore, I would like to thank the collaborators on the cryogenic experiments, Adam Kaufman and Daniel Slichter, as well as collaborators on the metalens project, Wenqi Zhu, Amit Agrawal, and Scott Papp. They offered invaluable scientific insight and technical expertise across different disciplines within AMO physics. I highly value the guidance they provided, and it was always refreshing to hear perspectives from other areas of the AMO community.

Next, I want to thank my lab mates for always being amazing through thick and thin and for putting up with my occasional minor (or often major) OCD tendencies when it comes to building the experiment (I often say, 'If it doesn't work, at least it looks nice and shiny.' If it looks nice, the chances of it working are probably pretty high.). It has been a pleasure to work with such a fantastic team in B240 (Zhenpu, Ting You, and Matteo). Each of you has expertise crucial to the success of the experiment, and I have learned a great deal from all of you.

Zhenpu, with whom I have had the pleasure of working with for the past 4 years, has extensive knowledge in science and experimental techniques. I can't imagine how much longer this experiment would take without him. We've learned a great deal from each other through the countless discussions we have had together. I have greatly enjoyed working with Ting You as well, and

I appreciate the many contributions he has made to the experiment. Matteo, with his background in trapped ions, brings technical expertise and experience that complement our skill set as neutral atom trappers. His insights from an ion trapper's perspective have proven very useful on several occasions. Additionally, I want to thank the undergraduate student Max, who has done excellent work building electronics and optics that we still use today.

I would also like to acknowledge the support from the JILA staff shop, including both the electronics and instrument shops. I have learned a great deal about electronics and machining from the experts who make JILA's research possible. I am particularly grateful to James Uhrich, Calvin Schwadron, and Adam Ellzey for their support, not only in the construction of the experiment but also as friends.

Finally, I would like to thank Amie for her friendship and support during my thesis writing and throughout the final year of my PhD. She taught me a great deal about maintaining a balanced life and emotional stability. I am very grateful for her companionship during this time.

One thing I will definitely miss are the late nights with Zhenpu, whether in the machine shop or in the lab. Neither of us can sleep if there's an unsolved problem, and we both enjoy turning chunks of metal into chips. I will also miss going to the gym with Zhenpu at night and then returning to work until midnight. I couldn't ask for better lab mates than Zhenpu, Ting You, and Matteo. Now that the experiment is in Zhenpu's and Ting You's hands, I'm excited to see what new developments will emerge in the future.

Contents

Chapter	
1	Introduction 1
1.1	Quantum information processing and simulation 2
1.1.1	Neutral atom QIP 3
1.2	Cryogenic optical tweezer array 4
1.3	Survey of cryogenic used in other quantum system 8
1.3.1	Horizon of impact on neutral atoms and molecules 9
1.4	Metasurface lens optical tweezer 10
1.5	Thesis outline 13
1.6	List of publications 15
2	Cryogenic tweezer array apparatus 16
2.1	Overview 16
2.2	Design of the cryogenic tweezer array apparatus 18
2.2.1	Major parts of the experimental apparatus 18
2.2.2	Science MOT 21
2.2.3	DC electric field control 23
2.2.4	Vacuum 29
2.2.5	Coldbox and cryopumping finger design concept 35
2.2.6	2D MOT assembly and 2D to 3D MOT transfer 37

2.2.7	Magnetic field in 3D MOT (science) chamber	41
2.2.8	BBR microwave	42
2.2.9	Thermal design and analysis	46
2.2.10	Optical access	50
2.3	Microscope	54
2.3.1	High NA objective	54
2.3.2	Tweezer light source and optical rail	55
2.3.3	Pinhole testing of the objective	58
2.4	Cryostat testing	60
2.4.1	AR coating testing	60
2.4.2	Vibration measurement	63
2.4.3	Heat load measurement	66
2.4.4	Tweezer cold window alignment measurement	69
2.4.5	Cold filter testing	72
3	Cryogenic tweezer atom characterization	75
3.1	Overview	75
3.2	MOT lifetime	76
3.2.1	Residual flux of 2D MOT	78
3.2.2	Dipole-push beam	80
3.3	Single atom lifetime	82
3.3.1	Heating in optical tweezer	83
3.3.2	Cooling loss	90
3.3.3	Imaging loss	92
3.3.4	Pulsed cooling	97
3.3.5	Vacuum-limited single atom lifetime	98
3.4	Tweezer FoV atom characterization	101

3.4.1	NA measurement	101
3.4.2	LGM loading	103
3.5	Impact of vacuum, loading rate and imaging loss on achieving large atom array . . .	107
3.5.1	Imaging loss vs detuning and intensity	107
3.5.2	Effect of imaging loss on defect-free array	109
3.5.3	Effect of vacuum loss on defect-free array	111
4	Cryogenic tweezer qubit manipulation	113
4.1	Overview	113
4.2	Microwave	115
4.2.1	B-field calibration and noise	117
4.2.2	Rabi	118
4.2.3	Ramsey	120
4.3	Eddy current measurement	122
4.4	Outlook	124
4.4.1	Atom Array, SLM and optical lattice	125
4.4.2	Cryogenic enhancement: cryopmping	126
4.4.3	ITO coating	127
5	Metasurface lens experiment	128
5.1	Overview	128
5.2	UHV system	129
5.2.1	ColdQuanta source cell	131
5.2.2	Science glass cell AR coating	133
5.2.3	Science glass cell	135
5.2.4	Metalens sample mounting	137
5.3	Metasurface Overview	138
5.3.1	Optical metasurface	139

5.3.2	Anisotropic plasmonic nano-antennas	141
5.3.3	Dielectric metasurface	142
5.4	Design principle of metasurface and metalens	147
5.5	Metalens sample	150
5.5.1	Non-polarization multiplexed lens	150
5.5.2	Metasurface fabrication	152
5.5.3	Optical testing	153
5.5.4	Metalens PSF with subwavelength pinhole	155
5.5.5	Atom image system test	158
5.6	Testing with atom	161
5.6.1	Single atom loading and detection	161
5.6.2	Trap depth	164
5.6.3	Trap frequency	165
5.6.4	Tweezer array setup and FoV	166
5.6.5	Focusing efficiency and FoV simulation	168
5.6.6	Discussion and challenges	170
5.7	Future sample	172
5.7.1	Polarization multiplexed lens	173
5.7.2	Doublet design	176
5.7.3	dual wavelength lens	180
5.8	Outlook	182
5.8.1	Polarization multiplex	182
5.8.2	Large FoV doublet metalens	184

Bibliography **186**

Appendix

A	Montana cold window test	202
	A.1 Double window thermal test	202
	A.2 Indium seal dimensional stability	203
B	SAES Rb Dispenser Activation	205
	B.1 The Alkali Metal Dispenser	205
	B.2 Dispenser Activation	206
C	Anodic Bonding	208
	C.1 Anodic Bonding	208
	C.2 Bonding Principle	209
	C.3 Metalens Cell Bonding Parameter	210
D	Basic Principle of cryopumping	212
	D.1 Cryopumping Principle	212
	D.1.1 Cryocondensation	213
	D.1.2 Cryosorption	214
	D.1.3 Cryotrapping	216
	D.2 Outgassing at low temperature	217
E	Stinger Cryostat	218
	E.1 Stinger cryocooler operating principle	218
	E.2 The UHV cryostat	220
	E.3 Compressor helium contamination issue	222

F	Laser phase noise from cryostat vibration	225
	F.1 Converting a vibration spectrum to phase noise	225
G	Release-recapture Gaussian vs harmonic trap	228
	G.1 Harmonic trap	228
	G.2 Gaussian and Airy	229
	G.3 Comparison	229

Tables

Table

2.1	List of window substrate used in cryogenic Rydberg tweezer experiment	52
3.1	Single atom cooling and detection parameters	100
5.1	Metalens Focusing Efficiency	157
5.2	Metalens Doublet Coefficients, NA 0.7, FoV= ± 1.1 mm, WD= 7 mm	177
B.1	Typical activation behavior of SAES alkali metal dispenser	207

Figures

Figure

1.1	Rydberg atom quantum computing	5
1.2	Cryogenic tweezer arrays	10
1.3	Metalens single atom trapping	12
2.1	Cryo overall view	20
2.2	MOT Coils	22
2.3	^{87}Rb Rydberg DC Stark polarizability	23
2.4	Example electrode configurations for DC electric field control	26
2.5	Cryogenic tweezer array DC electrode	27
2.6	Cryogenic tweezer array active E-field control simulation	28
2.7	Cryogenic tweezer array vacuum design schematic	31
2.8	Cryogenic tweezer array vacuum system	32
2.9	Cryogenic tweezer 2D MOT vacuum assembly	38
2.10	Cryogenic tweezer 2D MOT Optics package	40
2.11	Cryogenic tweezer bias coil assembly	42
2.12	Microwave spectrum inside of coldbox	44
2.13	BBR photoionization and Rydberg state decay	45
2.14	Compact double pane cold window design	47
2.15	Coldbox titanium thermal break	48

2.16	Indium seals and cutter	51
2.17	Coldbox optical access	53
2.18	Tweezer light source and optical rail	57
2.19	Special Optics objective pinhole test	59
2.20	AR coating liquid nitrogen stress test	62
2.21	Coldbox vibration measurement setup	64
2.22	Coldbox vibration measurement	65
2.23	Temperature vs. heat load (bare cryostat)	67
2.24	Copper braid and shield	68
2.25	Temperature vs. added heat load on the coldbox	68
2.26	Coldbox tweezer window alignment	69
2.27	Special Optics objective angular tolerance ZEMAX	71
2.28	DC electrode lowpass filter characterization	72
2.29	Microwave bandpass filter characterization	74
3.1	Cryogenic tweezer MOT	78
3.2	Cryogenic tweezer MOT background loading	80
3.3	Single atom lifetime timing sequence	82
3.4	Dark lifetime without cooling	84
3.5	Release and recapture temperature measurement method	86
3.6	Single atom heating rate of various configurations	87
3.7	Tweezer RIN and heating rate	89
3.8	Cooling loss measurement	91
3.9	Pulse cooling temperature measurement	92
3.10	Single atom imaging histogram	94
3.11	Single atom imaging loss	96
3.12	Single atom pulse cooling	97

3.13	Single atom vacuum-limited lifetime	99
3.14	Cryogenic tweezer trap depth and trap frequency	102
3.15	Cryogenic tweezer NA over FoV	103
3.16	LGM Illustration	104
3.17	Cryogenic tweezer LGM B-field vs time	105
3.18	Cryogenic tweezer LGM vs FoV	106
3.19	Single atom imaging loss detuning dependence	108
3.20	Sequence used for the rearrangement Monte-Carlo simulation	110
3.21	Effect of imaging and cooling loss on defect-free array probability	111
3.22	Effect of vacuum loss on defect-free array probability	112
4.1	Cryogenic tweezer qubit level diagram	115
4.2	Cryogenic tweezer qubit optical pumping	116
4.3	Cryogenic tweezer bias magnetic field calibration and noise	118
4.4	Cryogenic tweezer array microwave Rabi	120
4.5	Cryogenic tweezer array microwave Ramsey	121
4.6	Cryogenic tweezer array eddy current characterization	123
5.1	Metalens UHV Chamber	130
5.2	ColdQuanta Source	132
5.3	Metalens source MOT atom	133
5.4	Metalens science cell AR Coating	135
5.5	Metalens science cell	136
5.6	Metalens sample mounting	138
5.7	Microwave Metamaterial	139
5.8	Metasurface Overview	140
5.9	Plasmonic metasurface	142
5.10	Dielectric Pancharatnam-Berry phase metasurface	144

5.11 Dielectric HCA metasurface	146
5.12 Metasurface design principle	149
5.13 Non-polarization multiplexed metalens	152
5.14 0.55NA metalens zemax phase	153
5.15 Metalens Fabrication Steps	154
5.16 Metalens Focus Efficiency	156
5.17 Metalens Pinhole Test	159
5.18 Metalens Pinhole Test	160
5.19 Metalens MOT Image	162
5.20 Metalens Atom Trapping Histogram	163
5.21 Metalens Trap Depth Measurement	164
5.22 Metalens Trap Frequency Measurement	166
5.23 Metalens FoV Schematic	167
5.24 Atom array and metalens field of view	169
5.25 Metalens efficiency and FoV simulation	170
5.26 Polarization Multiplexed Metalens Principle	174
5.27 Polarization Multiplexed Metalens Phase	175
5.28 Polarization Multiplexed Metalens PSF	176
5.29 Metalens Doublet Schmidt Corrector	177
5.30 Metalens Doublet Zemax Simulation	178
5.31 Metalens Doublet Surface Phase	179
5.32 Hybrid Metalens	181
5.33 Polarization dependent trapping	184
5.34 Metalens doublet compare to state-of-the-art objective	185
A.1 Cryostat double window test	203
C.1 Anodic bonding	210

D.1	Different cryopumping regime	213
D.2	Cryopumping saturation curve of common gases	214
D.3	Xenon isotherm of some technical surface at 77 K	216
E.1	ColdEdge technologies Stinger Cryocooler block diagram	220
E.2	ColdEdge technologies Stinger Cryocooler block diagram	221
E.3	Helium flow of typical clogging event and slow degradation over long operating time	224
F.1	Vibration induced laser phase noise and vibration comparison to Jonathan Home group	227
G.1	Airy, Gaussian and harmonic trap shape	229
G.2	Airy, Gaussian and harmonic trap Release and Recapture	231

Chapter 1

Introduction

Scientists have been studying quantum mechanical phenomena for over a century, but it's only recently that we have begun to have the ability to create and manipulate quantum systems. Over the past few decades, the field of atomic physics has undergone numerous advances. The invention of lasers and improvements in optics and electronics provide new ways of creating quantum atomic systems with very low entropy. With laser cooling of atomic vapors, the first degenerate quantum gas with bosonic atoms was created and their quantum mechanical properties studied [1, 2].

While degenerate quantum gases are thriving, progress is also being made in cooling and controlling the quantum state of single neutral particles at a microscopic level, for example, optical trapping of single neutral atoms [3-5]. In this bottom-up approach, similar to the trapped ions [6,7], individual neutral quantum particles can be assembled into large systems, and their quantum mechanical properties can be harnessed. However, there are still challenges in fully controlling these neutral particles as a quantum resource, and extending control in bottom-up systems remains a major research interest.

Quantum systems are inherently fragile, as they are sensitive to perturbations from the environment, but also making them excellent candidates for sensing and metrology applications. For example, with Rydberg atoms, due to their large dipole moments, it is possible to detect electric fields down to $5 \mu\text{Vcm}^{-1}/\sqrt{\text{Hz}}$ [8]. Correspondingly, there are strong interactions between nearby Rydberg atoms, which provides a way to achieve controlled interactions for quantum simulation and quantum information processing.

On the other hand, due to the quantum mechanical nature of atoms, properties that satisfy certain quantum selection rules are very robust against environmental perturbations, leading to long quantum coherence. For example, the $^1S_0 \rightarrow ^3P_0$ transition of strontium atoms can be utilized to create the most accurate atomic clocks, with a uncertainty of 2×10^{-18} [9]. These long-coherence quantum states can be used for information storage.

These properties open new avenues, including the simulation of quantum systems in solid-state physics, chemistry, and materials science [10, 11]. Additionally, large quantum systems with single-particle control can be used to realize quantum computers, devices capable of solving problems such as factorization of large integers [12], solving linear systems of equations [13], and searching unsorted databases [14].

1.1 Quantum information processing and simulation

Consider a system with N quantum particles that has states $|0\rangle$ and $|1\rangle$. One would need 2^N complex amplitudes to describe the collective quantum state. This number grows exponentially with the size of the system. With a moderate-sized quantum system of $N = 100$, the computational resources needed to describe it already exceed the capacity of all classical computing hardware currently available in the world. In 1982, Feynman suggested [15] that in order to study a quantum mechanical system, it might be more feasible to simulate it in a more controlled analogous quantum system. This allows us to study the behavior of larger quantum systems by exploring sub-portions of the system in a more controlled manner. Some examples of quantum simulation include phase transitions in the Hubbard model [16, 17], dynamics of interacting spin chains [18, 19], and the antiferromagnetic ordering in optical lattices [20, 21].

In a universal quantum computer, qubits are used to store and carry out computational tasks. These qubits are quantum two-level systems, well isolated from the environment and with good coherence. Contrary to classical computers, a universal quantum computer will only need N qubits to represent the N -particle quantum state completely. Through a combination of one and two-qubit operations, any unitary transformation between many qubits can be realized [22]. This allows the

universal quantum computer to simulate the time evolution of any quantum systems with only a set of fundamental quantum logic operations. Apart from simulating quantum mechanical dynamics, the universal quantum computer can also be programmed such that the time evolution gives answers to computational problems that are resource-intensive to solve on a classical computer. Some notable examples include finding the prime factors of large integers through Shor’s algorithm [12] and speeding up unsorted database searches with Grover’s algorithm [14].

1.1.1 Neutral atom QIP

The concept of using neutral atoms as a quantum computing platform emerged relatively recently, about 15 years after ion traps and superconducting circuits. It was proposed in the early 2000s [23–25] that the long-range dipole-dipole interaction of Rydberg atoms could be tailored for entanglement and quantum computation. Rydberg atoms are atoms with electrons excited to a large principal quantum numbers ($n = 50 - 100$), resulting in a large induced dipole moment and long-range interaction spanning distances up to several micrometers, with natural decay times on the order of tens to hundreds of microseconds. Typically, Rydberg transitions can be excited with a single high-energy UV photon or one blue and one NIR photon via an intermediate state. The qubit states require long coherence; thus, they are normally encoded using weakly interacting ground states. However, depending on the application, qubits encoded in the Rydberg state are also common in quantum simulation, where resonant dipole-dipole interaction is used to implement spin-exchange interaction [26].

Reaching a regime where Rydberg interactions can be harnessed for quantum computing requires tools for trapping single atoms. One of the tools that provides single-particle-level trapping and control of neutral atoms is optical tweezers. Optical tweezers are microscopic optical dipole traps capable of confining single atoms at the sub-micron spatial scale. They achieve this by first trapping many atoms, and through the process of light-assisted collisions, only single atoms remain in each trap [3]. Many traps can be generated using diffraction with acousto-optic modulators (AOMs) or spatial light modulators (SLMs), providing a highly scalable and configurable platform

without the need for hardware changes [27, 28].

With this bottom-up approach, the first Rydberg atom two-qubit gate was demonstrated in 2010 [29, 30]. Since then, optical tweezers single-atom arrays have become one of the fastest-growing quantum computing platforms in terms of fidelity and scalability [31, 32].

1.2 Cryogenic optical tweezer array

Currently, in neutral atom quantum systems, qubit fidelity is reaching the point where quantum error correction is possible [31, 33]. To realize a useful fault-tolerant universal quantum computer, a large number of qubits is required. For example, with the currently achievable error rate, 2-qubit gate fidelity, and error-correcting scheme, factoring a 2048-bit RSA integer requires approximately 10^7 qubits [34]. Several approaches are possible to achieve qubit number scaling and error correction. For instance, coherent transport of atoms between different functional zones [35], mixed-species operation with spectator qubits [36, 37], and a network of small modular quantum processors connected via coherent optical links [38, 39]. As the size of the quantum system scales to hundreds or even thousands of qubits for quantum error correction, extremely weak or infrequent single-particle effects become increasingly relevant and problematic.

One challenge is to achieve better isolation of the atoms from the vacuum environment. With the shallow trap depth of optical tweezers compared to the trapped ions, the probability of losing an trapped atom after collision with residual background gas is almost unity. Considering a vacuum-limited lifetime τ_{vac} for a trapped single atom, the probability of losing an atom over certain time t is $e^{-t/\tau_{vac}}$. For typical state-of-the-art experiments at room temperature, τ_{vac} typically ranges from a few minutes to minutes [40–42] to recent advancements extending up to around 20 minutes with multi-round bake-out, chamber inside coated with fresh titanium, and no extra components enabling attainment of XHV pressure [43]. This time is enhanced as the number of qubits increases. Given N qubits, the probability of losing one atom after some time t now becomes $e^{-Nt/\tau_{vac}}$ [Fig. 1.1(a)]. Furthermore, as computation protocols become more complex and approaches rely on coherent transport and rearranging of the atoms, atom arrangement and quantum error correction sequences

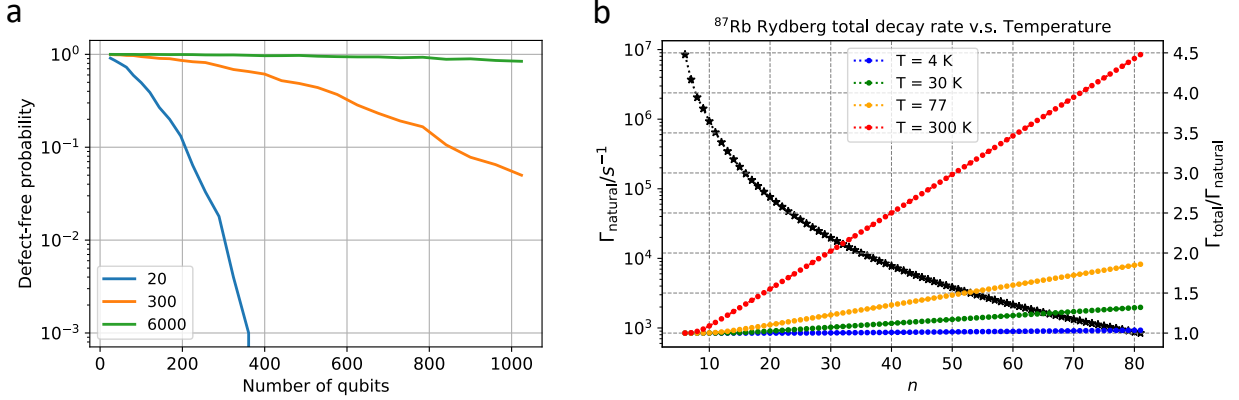


Figure 1.1: Examples of impact of a cryogenic environment in our apparatus (a) Probability of defect-free array versus qubit number in optical tweezer array under different vacuum lifetimes. Assuming no imperfection, and the array assembly time to be $t_{\text{assembly}} = 50 + 0.85N$ (ms) based on Ref. [27]. Orange is vacuum-limited lifetime of typical room temperature experiment, green is cryogenic experiment. Showing an order of magnitude improvement in defect-free probability for an array size of 1000 atoms. (b) ^{87}Rb Rydberg atom total decay lifetime ($\Gamma_{\text{total}} = \Gamma_{\text{natural}} + \Gamma_{\text{BBR}}$) versus BBR environment temperature. A factor of 3 increase in lifetime is possible by reducing the environment temperature from 300 K to 30 K for the $70S$ state. Black symbol is natural lifetime (Γ_{natural}) of the Rydberg state versus principle quantum number (left axis). The color symbols are ratio of BBR induced total Rydberg lifetime (Γ_{total}) to the Rydberg state natural lifetime (Γ_{natural}) (right axis). The Rydberg state natural lifetime (Γ_{natural}) is the intrinsic lifetime of the state in the absence of any external decay mechanisms.

can take up to several hundred milliseconds to seconds, which is many orders of magnitude longer than the simple two-qubit operation [29]. For quantum error correction and quantum simulation, the entangled system can scale to hundreds of atoms [35, 44, 45]. The loss of trapped atoms due to background gas collision during the sequence time is no longer negligible. Therefore, achieving a long single-atom lifetime is of paramount importance to achieve large-scale quantum computation with tweezer-trapped atoms.

Another challenge is the reduction of Rydberg state lifetime due to room temperature black-body radiation (BBR). There are two types of transitions that can be driven by the BBR, one is microwave transition to the adjacent Rydberg state and another one is infrared transitions to the states near ground state. In general the decay out of the particular Rydberg state is mainly through the microwave transition to the nearby Rydberg state. We will discuss this in more de-

tail in Sec. 2.2.8, showing the Rydberg decay contributions from different states at various BBR temperatures.

This effect is particularly significant in circular Rydberg states where the natural lifetime, in the absence of BBR, can reach seconds but is reduced by orders of magnitude at room temperature [46–48]. This is because each photon only carries one angular momentum, therefore, decay to the ground state is prohibited and the only decay channel out of these high angular momentum state is to other circular states of nearby Rydberg levels that is driven by the microwave BBR [49]. In fact, there are experiments that successfully trapped circular Rydberg state atoms in a cryostat and observe the effect of BBR on the circular state lifetime [50]. To fully leverage the lifetime of these circular states, a cryogenic environment with extensive microwave background control is typically required. This is beyond the design capability of the cryogenic tweezer array platform we described in this thesis.

Even in states typically used in current high-fidelity Rydberg gates, which we utilize in this thesis, thermal photons from BBR shorten the Rydberg state lifetime by a few factors. For example a factor of 2-3 (from 400 to 150 μs) in the 60S-80S states of ^{87}Rb [51], impairing Rydberg gate fidelity during qubit operation [52]. We see that around 2/3 of the decay is induced by the room temperature BBR and the rest from natural decay to the ground state [Fig. 1.1(b)].

Furthermore, for quantum simulation with large Rydberg ensembles, dephasing caused by decay to nearby Rydberg states is detrimental [53, 54]. These unwanted Rydberg states introduce erroneous dipole-dipole interaction, causing avalanching decoherence triggered by the microwave BBR [55, 56]. In quantum computation, decay to nearby Rydberg states is also problematic because it is generally difficult to detect these errors as these states remain dark during detection similar to the target Rydberg state, but with incorrect interaction [57]. For these cases, trapping at a 30 K environment is sufficient to suppress these decay to a negligible level (5 times shorter than the natural lifetime of the state).

Combining optical tweezers and a cryogenic environment can solve these aforementioned problems. Cryogenic shielding limits the BBR background and low outgassing. In addition, cryop-

umping at 4 K can freeze out almost all residual gas other than helium. However, until recently, there were no cryogenic adaptations of optical tweezers and quantum gas microscope-type experiments due to the stringent optical alignment and flatness required. A notable example from CNRS leverages cryogenic temperatures to achieve a 6,000-second lifetime in optical tweezers [58, 59], albeit with limited optical access and optical lens performance.

In this thesis, we introduce a new apparatus capable of high-NA optical access in a low vibration cryogenic environment. Our cryogenic Rb optical tweezer array apparatus incorporates an extensive set of components for quantum state manipulation in a configuration with high optical access for many atomic addressing and trapping beams.

For ground state hyperfine qubit manipulation, we integrate a microwave antenna inside the cryogenic shield to drive microwave qubit transitions at rates up to tens of kHz. Additionally, our apparatus includes a Raman laser to drive qubit transitions at rates of several hundreds of kHz for faster operation and to minimize decoherence.

Moreover, in terms of high optical access, this apparatus distinguishes itself from the setup in Ref. [58, 59] by employing an in-vacuum objective mounted at room temperature, focusing through the cold window on the custom cryogenic shields. This configuration creates a diffraction-limited field of view (FoV) of $\pm 225 \mu\text{m}$ at 0.55 NA, allowing for the creation of large arrays with uniform loading and detection.

The cryogenic shield, maintained at temperatures below 45, K, provides some BBR shielding and an environment with low outgassing. This temperature is primarily chosen for non-circular state Rydberg atoms, where the natural lifetime is short and does not require such a low BBR environment for decay suppression. For circular Rydberg states, a lower temperature BBR environment is needed to fully leverage the long natural lifetime of such states [50]. In addition to a cold temperature, to fully attenuate microwave radiation relevant to Rydberg transitions, ITO coating is also required. Although this is not utilized in the presented first iteration of our experiment, our design is fully compatible with having ITO coating on the windows.

With simply a 4 K cryopumping coldfinger, we have been able to measure a vacuum lifetime

of 3000 seconds, one of the longest observed in optical tweezer systems [40–42]. Furthermore, the large optical access of our apparatus makes it compatible with a 3D cross-beam bi-chromatic optical lattices that can simultaneously trap both ground and Rydberg state atoms. Looking ahead, this is a viable option for generating several thousand tightly confined trapping potentials in a laser-power-efficient manner.

1.3 Survey of cryogenic used in other quantum system

Cryogenic apparatus have a long standing history in atomic, molecular and optical (AMO) community and in superconducting circuits. Here I survey a few systems for comparative information.

Superconducting qubits are nonlinear quantum oscillators that use circuit elements made of superconducting materials to minimize dissipation. To introduce nonlinearity and address individual energy levels, Josephson junctions are used. The inductance of the Josephson junction is proportional to the current in the resonator [60]. The energy levels of these oscillators typically lie in the GHz range. To access the ground state, they must be cooled to temperatures of tens of millikelvin. Therefore, it is necessary to place them in a dilution refrigerator to suppress any thermal photons that could easily excite the energy levels of these resonators and destroy their coherence. For comparison, thermal photons from a 4 K environment peak at 400 GHz, which is sufficient to break Cooper pairs, whereas thermal photons at 50 mK, although peaking at 5 GHz which is close to the qubit operation frequency, are 10^{10} times smaller in intensity. Placing these qubits at the lowest available cryogenic temperature has enabled long qubit coherence of up to 1 ms [61] and high-fidelity two-qubit gate operations with errors as low as 6×10^{-3} [62].

Ion trap use individually trapped ions as qubits. Ions possess many favorable qualities, including optical and microwave transitions with long coherence times. They can be laser cooled, trapped in large quantities, and individually addressed and configured. They were among the earliest systems to demonstrate quantum state control and entanglement [6]. Recently, ion traps have been designed in chip form as a means to shuttle individual ions around and scale up the number of

qubits. However, problems arise when ions are close to the chip surface (tens to hundreds of μm). Impurities on the surface of the trap, thermal voltage and current noise (Johnson-Nyquist noise), and patch charges can generate electric field noise that modifies the trapping potential and causes motional state heating. Because ion trap quantum computing often uses these motional states for entanglement or requires the ions to be near the motional ground state during gate operations [63], heating reduces fidelity. It has been shown that placing the ion traps in a cryogenic environment can decrease motional heating by several orders of magnitude [63–65]. In fact, some of the best single qubit and Bell state fidelity has been achieved in cryogenic ion traps [66, 67]. Cryogenic environments enable a longer period of time before ions are hit by a background gas molecule, reduce thermally activated surface electric field noise that causes motional state heating [68], and also allow for rapid trap sample exchange.

1.3.1 Horizon of impact on neutral atoms and molecules

The technique developed in this thesis opens up a pathway to achieve high-quality optical access and robust optical alignment of beams required to trap and cool neutral particles while cycling from 400 K down to cryogenic temperatures. Moreover, the closed-cycle flow cryostat, vibration decoupling, novel thermal isolation design, and interferometric testing conducted on our system demonstrate its compatibility with optical lattice and cavity-type experiments, such as those in quantum gas microscopes and cavity optical lattice clocks. This sets our technique apart from the apparatus demonstrated in Ref. [58]. Adapting the technique we developed in this thesis will enable the construction of a new generation of systems capable of leveraging BBR suppression, reduced surface electric field noise (thermally induced) [63], and enhancing vacuum lifetime offered by a cryogenic environment without significant compromises in optical performance (Fig. 1.2).

This new generation of cryogenic systems can find applications in many neutral atom experiments, such as quantum metrology and trapped molecules. In quantum metrology, BBR-induced frequency shifts have long been recognized as a substantial hurdle to overcome in the pursuit of high-accuracy atomic clocks [69]. A few minutes of room temperature vacuum lifetime can result in

substantial atom loss during the interrogation of typical optical clock transition lifetimes exceeding 100 seconds (e.g., 160 seconds for ^{87}Sr) [41], leading to a reduced signal-to-noise ratio and requiring more cycles to achieve the required precision. Further, in recent molecular quantum computing proposals [70], room temperature BBR is relevant for driving transitions among ro-vibrational qubit subspaces.

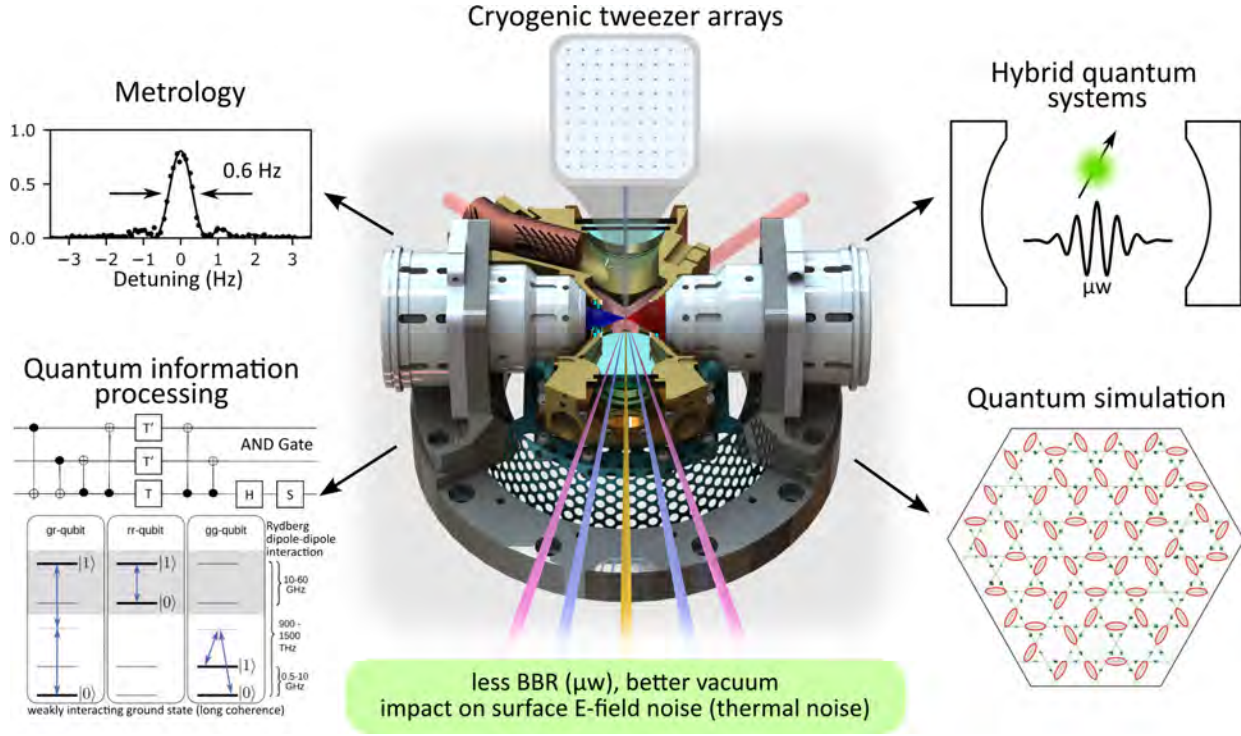


Figure 1.2: Cryogenic tweezer arrays provide a way to reduce noise and loss associated with the surrounding environment. The benefits of a high optical access system may find applications in metrology (image from Ref. [41]), hybrid quantum systems, quantum information processing (image from Ref. [71]) and quantum simulations (image from Ref. [45]).

1.4 Metasurface lens optical tweezer

In the second part of the thesis, I describe a new approach to manipulate and control trapped single atoms in optical tweezers through the use of optical metasurfaces. In the previous section, we introduced the importance of scaling the quantum system for quantum information processing applications. As more quantum systems are implemented with cryogenic technologies, maintaining

high-resolution optical control through conventional multi-element objective lenses may become problematic if these lenses need to be placed at cryogenic temperatures. One upcoming challenge in the neutral atom array community is developing scalable and multi-functional optical components that enable site-selective manipulation of hyperfine states and Rydberg excitations while operating in constrained environments with low scattering and cross-talk.

In ion trap experiments, limited optical access in cryogenic chip-scale ion traps has propelled a long-standing efforts in developing integrated optical components. In these cryogenic chip ion traps, fidelity is limited by optical alignment and vibration due to the presence of multi-layer radiation shields. It has been demonstrated that scalable planar photonics integrated with the ion trap chip can efficiently deliver light in a cryogenic environment. Eliminating the need to align beams into the cryostat has enabled improved robustness, parallelism, and addressing capabilities [72–74]. Neutral atoms can take on a similar trajectory and have many unique requirements. For example, control of single neutral atoms relies heavily on optical potentials for trapping, either in lattices or arrays of optical tweezers. Development of active components, from acousto-optic devices to spatial light modulators, are important for moving and addressing individual atoms [75, 76]. Static components that reduce reliance on large conventional optics for trapping and focusing will also alleviate constraints in increasingly complex vacuum chambers, such as the cryogenic system mentioned above, and improve scalability.. Advancing these specialized optical systems will benefit from connection to the forefront of integrated photonics development.

Metasurfaces are planar photonic elements composed of a periodic array of subwavelength dielectric or metallic nanostructures that have made significant impact on photonic systems in recent years. Contrary to traditional optical elements that rely on refraction for phase shift, the nanostructures constituting a metasurface couple, resonantly or off-resonantly, and re-radiate the incoming light with a transformed phase, polarization, and amplitude determined by the nanostructure shape, size, and material composition [77]. Figure 1.3(a) shows incident wavefront modified by the metasurface and focus to a point. Electromagnetic modeling, device optimization and fabrication of nanostructures with unprecedented complexity and resolution have enabled multi-functional



Figure 1.3: Main: Illustration of optical tweezer potential (orange) focused by the metasurface lens (blue). The concentric pattern is created by the nanopillars arranged in a phase pattern similar to a Fresnel lens. (a) A planar wavefront incident onto the metasurface lens. The light re-emitted by the individual nanopillar, with different phase, interfere at a distance and create a focused point. The nanopillars are made of silicon less than a micrometer tall, on top of a fused silica substrate. (c) Single Rb^{87} trapped by the optical tweezer potential created by the metasurface lens at its focus. Credit: Sean Kelley/NIST

control of the optical wavefront [77, 78]. By spatially varying the constituent nanopillar width in a pattern similar to a Fresnel lens the re-radiated light can converge at the far field to form a focal point, i. e. create a metasurface lens, shown in Fig. 1.3.

One major distinction between metasurface and conventional computer controlled holograms, for example, liquid-crystal spatial light modulator (LC-SLM) or digital micromirror devices (DMDs) is the gradient of wavefront control. LC-SLMs and DMDs have been used in combination with conventional high-numerical-aperture (high-NA) lenses in atom-array experiments to create arbitrary reconfigurable potentials through spatial modification of the optical wavefront using pixels larger than the optical wavelength. Metasurfaces in contrast consist of deep-subwavelength pillars and operate based upon a waveguide effect that provides large bend angles that can be used for high-NA optics and aggressive wavefront shaping. To tailor the wavefront, the pillars have a controlled size, spacing and shape, which further enables capabilities such as polarization [79], wavelength multiplexing [80] and large FoV focusing [81].

In atomic physics, metasurface optics are intriguing to explore given their combination of high

performance, multifunctional response, and low form-factor. Initial explorations in metasurfaces for atomic experiments have been used to create beamshaping and splitting elements in magneto-optical traps [82, 83].

In this thesis, we open up the use of metasurfaces to optical dipole traps, in the form of tightly-focused optical tweezers. We successfully trap single atoms with sub-wavelength confinement and simultaneously image the atoms using a single high-NA (0.55) metasurface lens. The FoV of the lens is also investigated, and the measurements are compared to numerical simulations with good agreement. To achieve the sub-wavelength trapping, a much more stringent focusing efficiencies and optical phase control is required. The demonstration of successful trapping an array of single atoms is an indication that potential deleterious effects of metasurface optics, for example, scattered light, the presence of undeflected zero-order light, or deformations due to absorption and heating of the lens makes negligible contributions to the trapping performance of large-spacing tweezers. This exemplary demonstration in this thesis, the first in single neutral atom array community, opens up new avenues of control and creating large mm-scale array of trapped single atoms.

1.5 Thesis outline

Chapter 2 we discuss the design details and considerations for constructing the high optical access radiation shield, which serves as the core of the cryogenic optical tweezer apparatus. We then present the mechanical and thermal testing of the cryostat and the high optical access cryogenic shield, including vibration measurements, optical alignment over temperature, and thermal load characterization.

In Chapter 3, we present atomic measurements of single atoms within the apparatus, demonstrating the capabilities of creating long-lived atom arrays. We also test the optical performance by measuring the FoV and NA of the tweezer with atoms. Furthermore, we show that with the long vacuum lifetime, one can measure and characterize cooling and imaging loss of single atoms to a level that was previously inaccessible due to vacuum loss. We demonstrate an imaging loss rate of $3.8(4) \times 10^{-4}$ per 14 ms image with an imaging infidelity of 10^{-6} . Additionally, we report a

cooling loss of $5(4) \times 10^{-5}$ per 25 ms cooling pulse, among one of the lowest ever reported in alkali atoms [43]. Finally, we show that our apparatus is compatible with the LGM enhanced loading technique previously developed in our group [84], achieving array loading efficiency over 80% across the FoV of the objective.

Chapter 4 presents single qubit rotation using the microwave antenna and an understanding of the Rabi frequency from the measurement based upon microwave field simulation. We also measure magnetic field stability and eddy current decay using microwave spectroscopy.

In Chapter 5, we describe the trapping of single atom array by combining a high-NA metasurface lens with tunable acousto-optic deflectors and characterize the tweezer foci with the trapped atoms. We measure the trap size (NA) of the tweezer generated by the metalens and compare it to the theoretical value. Additionally, we optically characterize the metalens with the pinhole and compare the results to the atom measurements, finding good agreement. Finally, I present some potential future metalens designs with qualities beneficial for creating large neutral atom tweezer arrays, including a large FoV of up to 2 mm, a lens without chromatic aberration, and polarization multiplexed lenses for dynamically changing the trapping potential or achromatic imaging of the trapped atoms.

1.6 List of publications

For reference, I am including the list of publications which I have contributed to.

- (1) M.O. Brown, T. Thiele, C. Kiehl, T-W. Hsu, and C. A. Regal. “Gray-molasses optical-tweezer loading: controlling collisions for scaling atom-array assembly.” *Physical Review X* 9(1), 011057 (2019).
- (2) T-W. Hsu, W. Zhu, T. Thiele, M. O. Brown, S. B. Papp, A. Agrawal, and C. A. Regal. “Single-atom trapping in a metasurface-lens optical tweezer.” *PRX Quantum* 3(3), 030316 (2022).
- (3) C. Kiehl, D. Wagner, T-W. Hsu, S. Knappe, C. A. Regal, and T. Thiele. “Coherence of Rabi oscillations with spin exchange.” *Physical Review Research* 5(1), L012002 (2023).
- (4) A high optical access cryogenic tweezer array with a 3000 second lifetime (in preparation)

Chapter 2

Cryogenic tweezer array apparatus

2.1 Overview

In recent years, techniques developed have allowed us to trap atoms with light for long periods of time, and the ability to drive coherent excitation to the Rydberg state has enabled on-demand interactions. The rapid progression of our ability to control and manipulate individual atoms has reached a point where the environmental isolation achievable at room temperature may become a limiting factor. Looking ahead, several challenges in neutral atom quantum systems could benefit from placing atoms in a cryogenic environment. The main challenges include achieving better vacuum isolation and shielding from room temperature BBR.

To achieve a large-scale quantum computer with hundreds or even thousands of atomic qubits, a long-lived array is required. Typically, state-of-the-art room temperature optical tweezers experiments have vacuum lifetimes on the order of 100-300 seconds [41, 42]. This is insufficient when considering that rearranging a large atom array can take hundreds of milliseconds. For instance, to maintain an array of 1000 atoms for 300 ms with 90% survival, a vacuum lifetime of 3000 seconds is necessary.

To achieve sufficient isolation, a vacuum environment in the extremely high vacuum (XHV) regime around 10^{-12} torr is necessary (we will discuss this in more detail in Sec. 2.2.4). Recently, an array with a vacuum lifetime of approximately 1200 seconds has been demonstrated using a room temperature setup [43]. However, the materials allowed in the vacuum chamber are very restricted. While achieving XHV at room temperature is challenging, it is routinely accomplished in cryo-

genic experiments, such as those in high-energy physics [85] and ion trapping [86]. Consequently, placing the atom array into a cryogenic environment is beneficial to further increase isolation from background gas collisions.

Another important challenge for neutral atom array experiments is shielding from the room temperature BBR environment. In quantum metrology, it is well-known that BBR background from room temperature can affect optical clock transitions, thereby introducing systematic errors in measurements [69]. In applications of quantum simulation and information utilizing Rydberg atoms, controlling the BBR environment is crucial. The typical transition energy between one Rydberg state to another falls within the range of 10-100 GHz, and room temperature BBR contains significant energies in this spectral range. This can cause decoherence by driving atoms to other Rydberg states and creating unwanted interactions. In quantum information, such decoherence introduces errors in gate operations [57]. In quantum simulation, for example, studying many-body dynamics with Rydberg dressed ensembles [53,54] and with resonantly driven Rydberg systems [87], researchers have observed that room temperature BBR microwaves can induce dephasing of individual Rydberg atoms and spontaneous avalanche dephasing of the entire ensemble, triggered by microwave BBR [55, 56].

Therefore, the natural progression to achieve better environment isolation is to place the atoms in a cryogenic environment. In this chapter, I describe the design and testing of a new cryogenic optical tweezer array apparatus. First, I discuss the design considerations of various aspects of the apparatus that are essential for the Rydberg atom quantum computing platform, including magnetic field control, vacuum environment considerations, and atom delivery. Then, I will show the design and simulations for the DC electric field and microwave environment essential for Rydberg and ground-state qubit control. Next, I will present the testing of the microscope objective and the design of the optical tweezer system. Finally, I will present performance tests of various parts of the apparatus, including cryostat vibrations, thermal loads and cooling power, tweezer optical alignments, and cryogenic filters for the DC electric field and microwave control.

2.2 Design of the cryogenic tweezer array apparatus

The use of cryogenics has a long-standing history in the atomic, molecular, and optical (AMO) experimental community. Some early demonstrations in neutral atoms [88] and ion trapping [86] have shown improvements in vacuum lifetime in a cryogenic environment compared to room temperature. In more recent years, there have been various efforts to implement cryogenic apparatus in ion trapping [68], circular Rydberg atoms [50, 89], and Bose-Einstein condensation [90] to reduce two-level noise, couple atoms to superconducting cavities/resonators, and achieve better vacuum. However, due to the stringent optical alignment and flatness required, there were no cryogenic adaptations of optical tweezers and quantum gas microscope-type experiments until recently. The most notable example of combining high-NA optical tweezers with cryogenics is an experiment at CNRS leveraging 4 K cryogenic shielding to achieve a 6000-second lifetime in an array of single trapped atoms [58], albeit with limited optical access due to layered radiation shields similar to a conventional cryostat design.

In this work, we present a cryogenic solution that takes a different approach compared to the traditional layered radiation shield design. Here, we construct a custom radiation shield that maintains the required optical alignment and flatness while still being able to attach to a standard cryostat interface. This approach is fully compatible with many technologies already developed for room temperature AMO experiments, such as in-vacuum objectives, and can be adapted to different types of AMO experiments that require a large amount of high-quality optical access with only slight modifications, such as quantum gas microscopes, optical tweezers, optical lattices, and high-finesse cavities.

2.2.1 Major parts of the experimental apparatus

The cryogenic tweezer apparatus can be separated into four major sections: atom source, science chamber, vacuum pumps, and the cryostat interface. The overall schematic CAD model of the experimental apparatus is shown in Fig. 2.1. The major components and a brief description

are listed as follows.

Source MOT chamber: The source MOT chamber, discussed in Sec. 2.2.6, contains the Rb atom source from an alkali metal dispenser in a glass cell [yellow part in Fig. 2.1], pre-cooled in the transverse direction to form a collimated beam. The glass cell is connected to an intermediate pumping stage through a pinhole to limit the vacuum conductance. The entire assembly is connected to the main chamber with a gate valve so that it can be isolated when the main chamber is vented. The source MOT assembly includes an optics package to provide all the necessary cooling lasers and can be moved to align the atom beam with the 3D MOT region inside the coldbox. The details of 3D MOT is in Sec. 2.2.2.

Science chamber: The main science chamber [depicted in gray in Fig. 2.1] CAD model, is a standard Kimball Physics chamber (MCF800-SphSq-G2E4C4A16) with viewports located in appropriate locations for the MOT beams, enabling high-NA optical access for the optical tweezer. The design for the window mounting for high-NA optical access is in Sec. 2.2.10. The main chamber contains the custom high optical access radiation shield (the coldbox), in-vacuum objectives (details in Sec. 2.3.1), and various electrical connections for thermometry, microwave (discussed in Sec. 2.2.8), and DC electric field electrodes (discussed in Sec. 2.2.3).

Ion pumps and NEG: The science chamber is pumped by three pumps: a 25 l/s ion pump, a SAES NexTorr Z200 200 l/s NEG + 5 l/s ion pump, and a SAES CapaciTorr Z200 200 l/s NEG. The pumps are green in Fig. 2.1 CAD model. The NEG's efficiently pump reactive gases, such as water and hydrogen, which are dominant in an unbaked UHV system. The non-reactive gases, such as CO and noble gases (e.g., helium, argon, etc.), are pumped by the ion pump. The details of the vacuum design is discussed in Sec. 2.2.4

Cryostat interface: The UHV cryostat comes with a 4.5" CF flange, which provides the mechanical mounting, stinger helium flow interface, and electrical connection for the heater and sensor in the cryostat. The cryostat connects to the science chamber through a flexible

vacuum bellow for small alignment adjustments and a reducer to interface with the 2.75" CF port on the science chamber. The orange-colored part in Fig. 2.1 is the Stinger UHV cryostat assembly. The details for the Stinger cryostat is described in Appendix E.

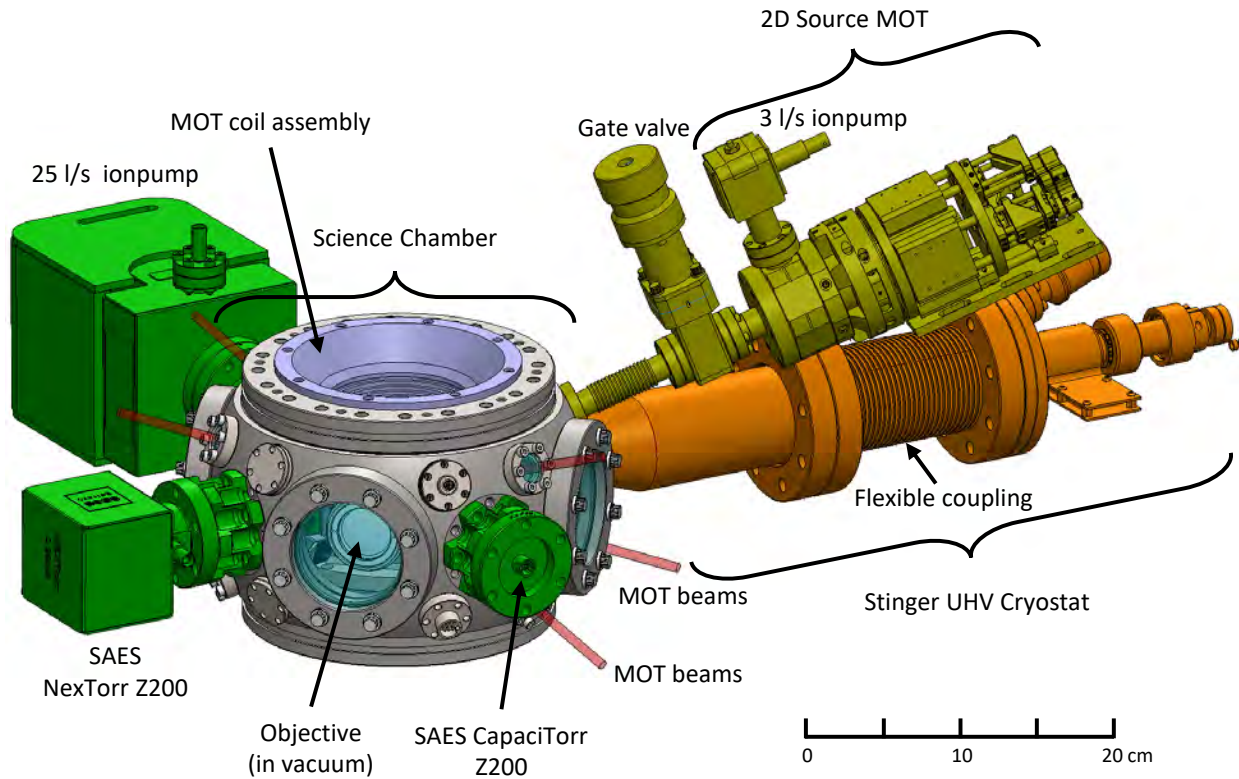


Figure 2.1: Overall view of the cryogenic Rydberg tweezer array apparatus. Yellow: 2D source MOT providing a pre-cooled source of Rb atoms. This part connects to the main chamber with a gate valve (MDC part number: 302000). Orange: Part of the chamber that contains the cryostat and interface with the Stinger cryocooler. Green: pumps for the main chamber, include the 25 l/s ion pump, SAES NexTorr Z200 combo pump and SAES CapaciTorr Z200. Gray: Main science chamber housing the custom high optical access cryogenic shield called "the coldbox" and the in-vacuum objectives.

2.2.2 Science MOT

For optical tweezer experiments, optical and magnetic field access for creating a MOT is essential. A MOT is the starting stage for all neutral atom trapping experiments, as it pre-cools and traps the atomic vapor from room temperature to a more manageable temperature around 100-200 μK . A MOT requires a quadrupole magnetic field with a gradient on the order of 10 G/cm. One of the most common approaches to obtaining such a gradient in a cryogenic environment is to use superconducting coils, as described in Ref. [50,58,90]. This is because the layered radiation shields commonly used in cryostats prevent the coil from being placed close to the atoms outside of vacuum. With the finite cooling power of the cryostat, joule heating from placing regular conductors to generate such a magnetic field gradient inside the cryostat is not permitted. However, with our custom large optical access radiation shield, the distance between the radiation shield and the atmosphere can be as short as 35 mm. This allows us to place coils in an anti-Helmholtz configuration, 75 mm apart, which enables us to generate a 10 G/cm gradient with a modest 2.5 A current through the coils. Another important aspect is the location of the MOT beams. Generally, three pairs are required, and they need to have projections onto three orthogonal axes, which puts constraints on the numerical aperture (NA) of the optical tweezer, as shown in [Fig. 2.2(b)]. The location of the MOT beams is largely determined by the small viewports on the science vacuum chamber.

The cross-section of the science chamber reveals the cold box and the MOT coils positioned from the bottom of the recessed viewport within the groove surrounding the glass window, placed as close to the cold box as possible [Fig. 2.2(a)]. The MOT coil is affixed to aluminum heatsinks, which also serve as support structures for mounting the coil onto the viewport. The magnetic field calculation generated from the MOT coils in the anti-Helmholtz configuration, with a total of 92 turns per coil, yields a fairly uniform 4 G/cm/A gradient [Fig. 2.2(c)]. In situations requiring a strong bias field in the vertical direction, the polarity of one of the coils can be reversed to operate in Helmholtz configuration, working alongside the external Z-bias coils (along the gravity direction)

to generate an additional magnetic field of around 10 G/A, as calculated in Fig. 2.2(d).

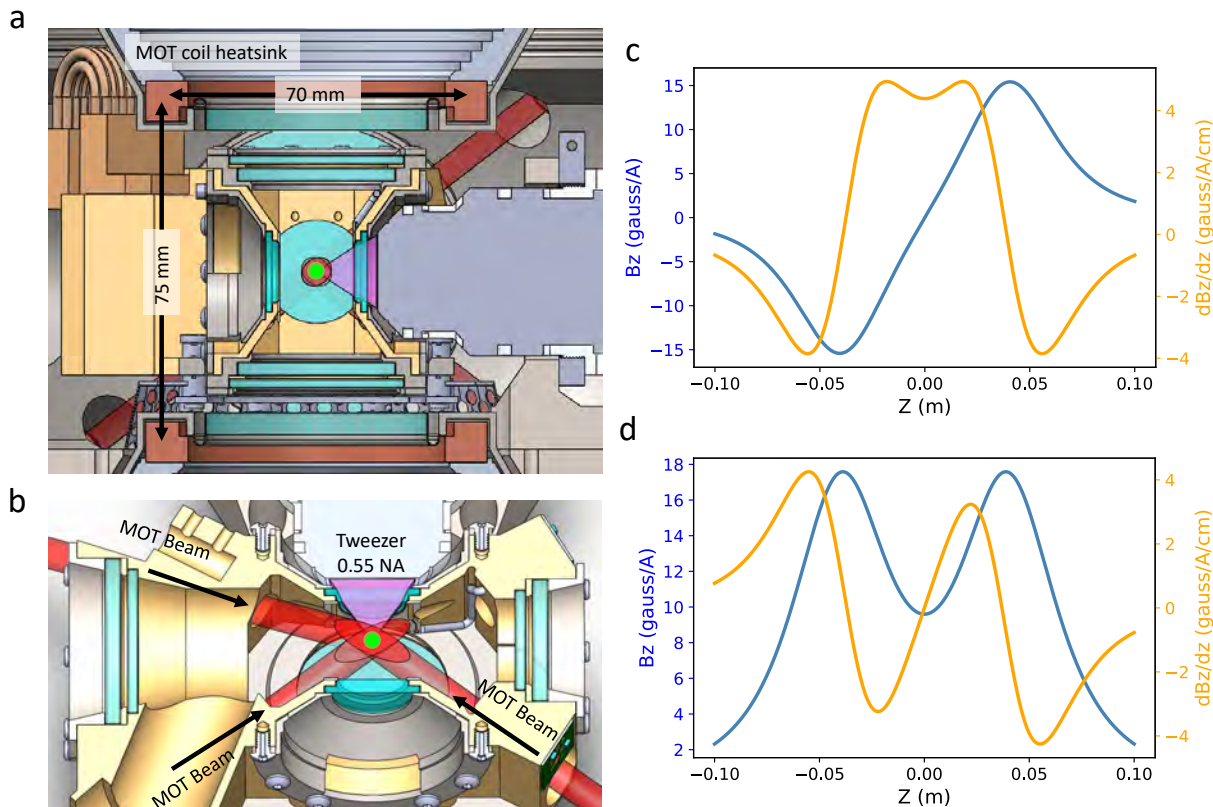


Figure 2.2: (a) Cross section showing the location of MOT coils with respect to the cold box. (b) Horizontal cut through the center of the tweezer and coldbox showing MOT beam positions with respect to the optical tweezer. (c) The calculated magnetic field gradient generated from the MOT coils in anti-Helmholtz configuration, giving a 4 G/cm/A gradient. (d) Magnetic field created by the MOT coil in Helmholtz configuration showing a 10 G/A bias field in vertical direction. This can be use in conjunction with the bias coil to create a larger field.

2.2.3 DC electric field control

Rydberg-mediated two-qubit gates and quantum simulations utilize long-range dipole-dipole interactions between adjacent Rydberg atoms. Depending on the principal quantum number of the Rydberg state, the interaction between Rydberg atoms can extend up to tens of micrometers. However, the large electric-dipole moments of the Rydberg states also make these atomic states susceptible to external perturbations. Depending on the exact state prepared and the angular momentum of such states, they can be sensitive to DC electric or magnetic fields. For example, in the case of rubidium $70S_{1/2}$ state, the polarizability is $0.6 \text{ GHz}/(\text{V}/\text{cm})^2$, while $70P_{3/2}$ and $70D_{5/2}$ have polarizabilities more than 4 times larger than the $70S_{1/2}$ state. The polarizability also strongly depends on the principal quantum number; the larger the principal quantum number, the greater the DC Stark polarizability. Plotting the DC Stark polarizability as a function of principal quantum number (n) reveals that it approximately follows an n^7 power law, as shown in Fig. 2.3. This means that controlling the local electric field at the atom location is necessary as we go to higher n for larger interaction.

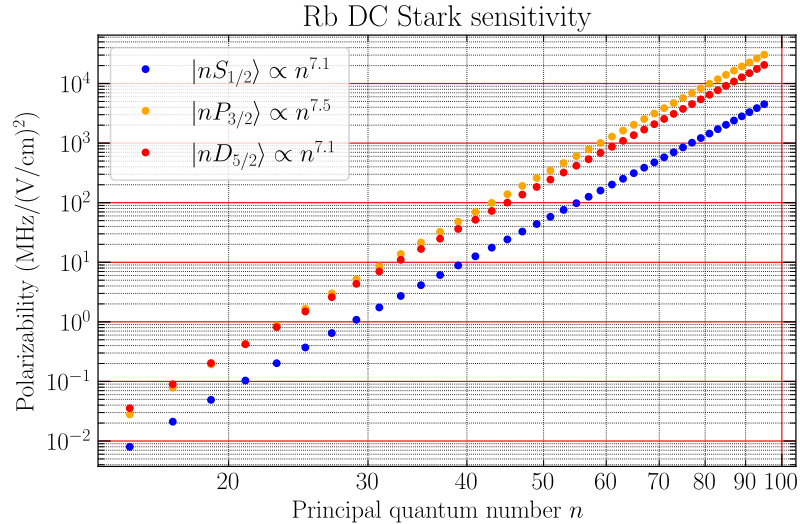


Figure 2.3: ^{87}Rb Rydberg DC Stark polarizability vs. principle quantum number showing the polarizability approximately follows a n^7 power law with respect to the principle quantum number. This polarizability allows us to estimate the required electric field stability in our setup.

Because the DC Stark polarizability in Rydberg atoms is induced by the external electric field, it is proportional to the strength of the external field. Thus, the energy shift is second-order proportional to the electric field, as can be seen in the unit of the y-axis in Fig. 2.3. To determine the level of electric field control required for our experiment, we can perform a simple estimation based on the Rabi frequency of the Rydberg transition that we wish to drive. Considering a Rabi oscillation with a period of 1 μ s, the Rabi frequency would be $\Omega = 2\pi \times 1$ MHz. While the intrinsic lifetime-limited linewidth of the Rydberg transition can be on the kHz scale, typical Rabi frequencies in the MHz range result in power-broadened spectral widths. We can compare the induced energy shift by the external electric field (E) and the Rabi frequency using the polarizability $\alpha = 0.6$ GHz/(V/cm)² for the 70S_{1/2} state with the following equation:

$$\Omega \approx \frac{\Delta U_{Stark}}{\hbar} = \frac{1}{2}\alpha E^2 \implies E \approx \sqrt{\frac{2\Omega}{\alpha}} = \sqrt{\frac{2\pi}{600}} \approx 0.1 \text{ V/cm} \quad (2.1)$$

From the equation above, we can observe that an external electric field drift on the order of 0.1 V/cm will shift the resonance by 1 MHz, which is sufficient to prevent excitation to the Rydberg level.

There have also been observations where the stray electric field from patch charges accumulated on dielectric surfaces near the Rydberg atom causes drifts in the transition frequency [91,92]. This effects the fidelity of ground-to-Rydberg excitation because over the course of few minutes the laser becomes detuned and require frequent calibration. In Refs. [91,92], the closest dielectric surface is on the order of 4 mm from the atoms, and the effect of patch charges became a problem without external compensation. In our design, we choose to keep the closest surface, typically for the tweezer optical access, 8 mm away from the atoms. The longer distance is intended to minimize the effect of patch charges, especially because these patch charges may be more difficult to eliminate in a cryogenic environment. With active electric field control in our platform, one of the goal is to compare the slow drift of the electric field at the atom location using the Rydberg transition when the coldbox is at room temperature versus at 45 K. With this comparison, we will be able

to answer some open questions regarding the impact of charge accumulation on low-temperature dielectric surfaces.

We can estimate how much patch charge (q_p) will create an electric field (E_p) with the same magnitude from Eq. 2.1 using simple Coulomb's Law with $r = 8$ mm.

$$E_p = \frac{q_p}{4\pi\epsilon_0 r^2} = 0.1 \text{ V/cm} \implies q_p \approx 10^6 e \quad (2.2)$$

Furthermore, due to the second-order sensitivity, the fluctuation of ΔU_{Stark} causing by the E-field fluctuations (dE) approaches zero when the DC E-field (E_{dc}) is zero. We can see this by taking the derivative of Ω .

$$\frac{d\Omega}{dE} = \alpha E_{dc} \quad (2.3)$$

Thus, by minimizing E_{dc} , the effect of dE (fast fluctuating E-field noise from the environment) in Rabi frequency is minimized, and the coherence is improved given the same rms E-field fluctuation. To compensate for the slowly drifting E-field from patch charges, as well as fields created from stray voltage sources, to near zero requires active DC electric field control near the trapped atoms.

There have been several approaches tested by other groups [92–95] that incorporate in-vacuum electrodes in Rydberg atom experiments to compensate residual electric fields. These approaches, using octopole designs aimed at achieving individual electric field control in the x, y, and z axes with sub-percent inter-axis coupling [92], enable compensation of residual fields to be less than 1 mV/cm [94]. However, they require bulky metal ring structures that are situated further away from the atoms [Fig. 2.4(a,b)].

To achieve active E-field control in our apparatus, we have chosen an approach with metal traces on alumina PCBs. Alumina is a well-characterized substrate that is UHV compatible. We get the PCBs from CERcuits, a Belgian company specialized in ceramic PCBs. The metal traces are directly deposited onto the alumina substrate with virtually no outgassing. This method allows us to produce different electrode designs relatively easily, with excellent dimensional accuracy, without altering the way they are mounted on the apparatus.

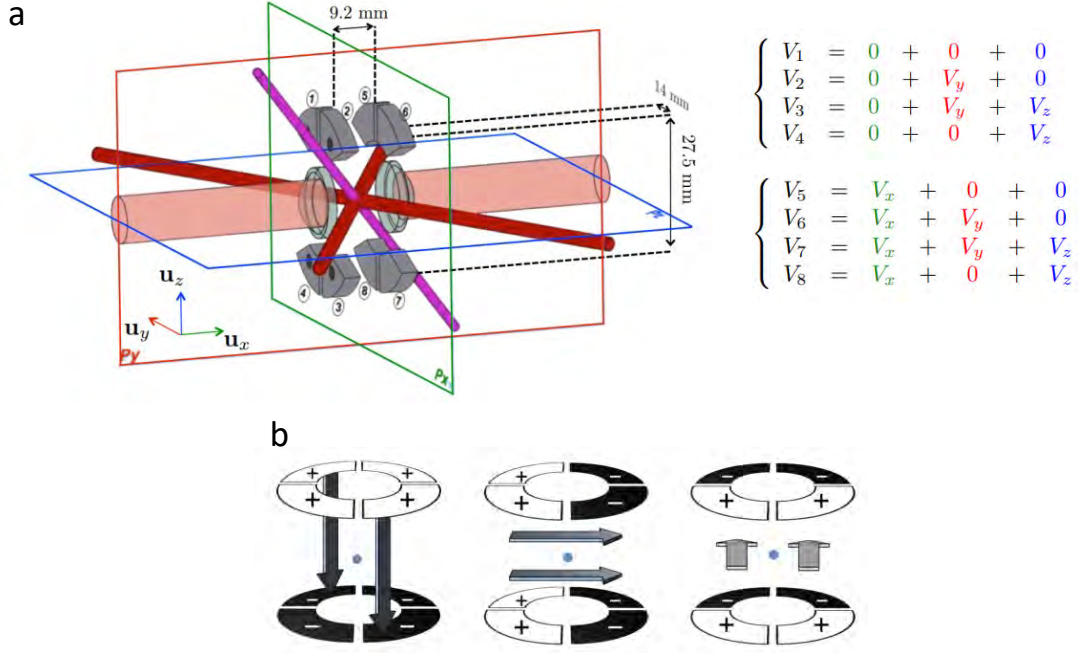


Figure 2.4: (a) Electrode example from Ref. [92,93] using small sections of concentric metal structure to achieve active electric field control with % level inter-axis coupling. The different voltage configuration at the bottom shows how an electric field in a particular direction can be generated by combining voltages in different segments. (b) Electrode examples from Ref. [94], to compensate the electric field with good homogeneity and very low residual level to less than 1 mV/cm for precision measurement of the Rydberg excitation spectrum.

Initially, the pattern took on a design similar to Fig. 2.4(b), with sectioned rings centered on the tweezer cold windows to create an octopole design. Although this design gives good crosstalk performance between axes, we found that it is hard for us to achieve a homogeneous E-field over the whole field of view (FoV) of the tweezer, most likely due to the large FoV (approximately ± 0.25 mm) compared to the size and separation of the ring sections (approximately 8 mm). After some iteration, we found that it is better to have straight electrodes forming the same octopole geometry rather than curved electrodes, the design shown in Fig. 2.5(a). The electrodes are silver conductive traces on 0.5 mm thick alumina substrate, the length of the electrode pattern is 13 mm, and they are separated 15 mm apart arranged as a square. The substrate has a 9 mm hole cut at the center for the tweezer light to pass through. The relative position of the two alumina substrates and electrodes with respect to the atoms and tweezers is shown in Fig. 2.5(b). The substrates are 19

mm apart from each other, with the trapped atoms located in between (8.5 mm from the atoms). This geometry ensures that the alumina substrate, which is dielectric, is located further away than the tweezer windows, thus not introducing stray charges closer to the atoms.

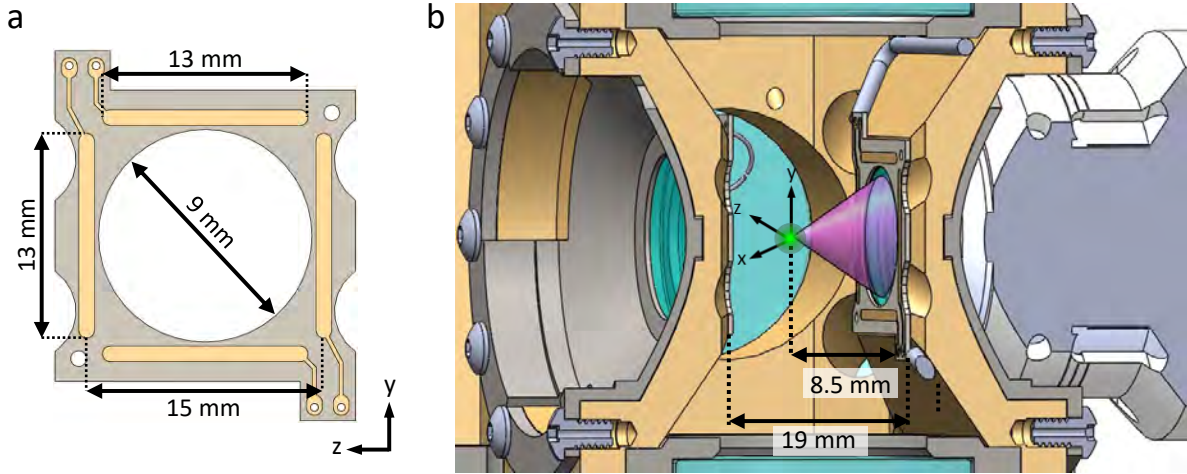


Figure 2.5: (a) DC electric field electrode design based on bar electrode octo-pole to independently control the electric field in x,y and z direction based on providing voltages on different pairs of electrodes. (b) Cross sectional cut of the coldbox, showing the relative positions of the two electrodes substrates surrounding the atoms. The electrode substrates are 8.5 mm from the atoms, 19 mm apart from each other, attached to the side of the coldbox with metal springs (not showing).

To verify the design of the bar-octopole electrode, we set up an simulation with the 3D model of the coldbox and electrodes into COMSOL and applied up to ± 100 volts on the electrodes with configuration shown in Fig. 2.6(a). Then, a series of cuts on the tweezer plane was made, and the homogeneity as well as the cross-coupling between the x, y, and z axes were analyzed. The resulting electric field vector on the tweezer plane (y-z plane) shows a large region with good uniformity [Fig. 2.6(b)]. To more precisely determine the uniformity and cross coupling of the fields a series of vertical ($x=0, y, z=0$) and horizontal ($x=0, y=0, z$) cuts on the $x=0$ plane [Fig. 2.6(b)] are made, shown in Fig. 2.6(c). Zoom in on portions of Fig. 2.6(c) shows that the bar electrode design can achieve cross-coupling between axes of less than 0.2% [Fig.2.6(d)], and electric field uniformity of better than 0.5% [Fig.2.6(e)].

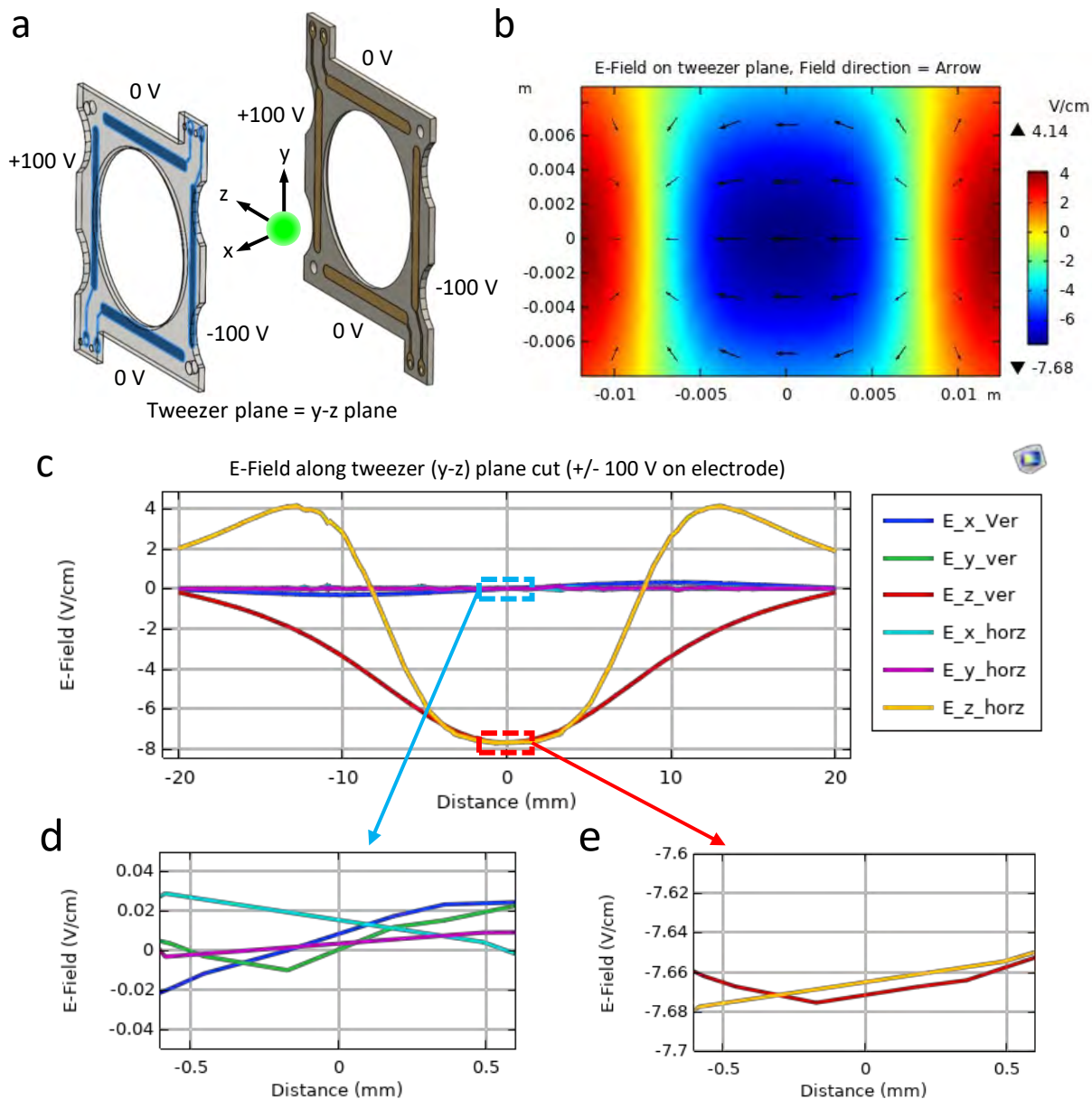


Figure 2.6: (a) Electrode positions relative to the atoms. The voltages set up for the simulation is marked next to the individual electrode. A voltage of $\pm 100\text{ V}$ is applied to the two opposing electrodes to create an electric field in the z-direction. (b) Plotting the generated electric field in z-direction across the tweezer plane (y-z plane), using the voltages applied in (a). (c) Line cut across tweezer plane (y-z plane) along y and z axis, showing the cross section profile of the electric fields in vertical and horizontal direction. (d,e) zoom in portion of (c) showing the E-field uniformity (e) and cross coupling to other axis (d).

2.2.4 Vacuum

Vacuum is one of the most important aspects of this apparatus, as one of the goals is to achieve very low atom loss due to background gas collisions. In this apparatus, the vacuum level across different parts of the system spans ranges from high-vacuum ($< 10^{-6}$ torr) to extreme-ultra-high vacuum (XHV) ($< 10^{-12}$ torr). It is not a trivial task to maintain vacuum levels across a range of 10^6 . To further complicate matters, the outgassing sources at different stages of vacuum also need to be considered. Having a good understanding of the material properties and characteristics under different temperatures is crucial to achieving this level of vacuum at the location of the atoms.

In order to determine the required vacuum environment for tweezers with lifetime of thousands of seconds, we need some estimations based on previously published results on atom losses due to background gas collisions. A typical rule of thumb from MOT measurements at room temperature is a lifetime of 1 second corresponds 10^{-8} torr, and it's inversely proportional to the pressure. A pressure to MOT loss rate coefficient of $P = 2 \times 10^{-8}$ Torr s/ τ is measured with a Rb MOT at a trap depth of 1 K [96]. With this conversion, we estimate a pressure of 5×10^{-12} Torr for a loss rate of 1 hour^{-1} , which was observed in a cryogenic MOT with a 4 K environment [88]. However, there are two caveats: typical MOTs exhibit lower loss rates than tweezers due to larger trapping volume, capture velocity, and Doppler cooling from the MOT beams. Also, due to the large portion of residual gas being hydrogen, the ion pump current reading is not an accurate indication of the real pressure in the chamber and can vary by a factor of 2 to 5 [97]. This inaccuracy arises from the different mass-to-charge ratio of hydrogen compared to nitrogen, which is typically what is used for ion pump pressure conversion.

To illustrate the effect of residual gas colliding with the Rb atoms we consider the hydrogen molecules, which are the dominant residual gas in typical UHV systems, colliding with Rb atoms [58, 98, 99], the equipartition theorem gives the following velocity:

$$\frac{1}{2}m_{H_2}V_{H_2}^2 = \frac{3}{2}k_B T \implies V_{H_2} = \sqrt{\frac{3k_B T}{m_{H_2}}} \simeq 1900 \text{ m/s @ } T = 300 \text{ K} \quad (2.4)$$

Now if the Rb atoms are initially trapped in a MOT, effectively at rest, the resulting velocity of head-on collision is

$$V_{s7\text{Rb}} = \frac{2m_{H_2}V_{H_2}}{m_{H_2} + m_{s7\text{Rb}}} \simeq 80 \text{ m/s @ } T = 300 \text{ K} \quad (2.5)$$

This is only a factor of 3 larger than the typical MOT capturing velocity, taking into consideration that most collisions occur at grazing angles and MOT trap depths are generally deeper (~ 1 K) compared to the tweezer (~ 1 mK) by a factor of 10^3 . In addition, the local pressure at the atoms is strongly dependent on the geometry of the vacuum chamber compared to the pressure measured at the pump.

Therefore, it is common to observe tweezer lifetimes that are shorter than MOT lifetimes, and both can be shorter than the lifetime corresponding to the pressure measured at the pumps [92, 100, 101]. To achieve a vacuum lifetime similar to that in Ref. [88], our goal is to create a vacuum environment with a pressure below 5×10^{-12} Torr. This pressure is also consistent with the inferred pressure from another cryogenic tweezer apparatus in Ref. [58] and $P = 6.2 \times 10^{-9}$ Torr s/τ determined with Li MOT cold-atom vacuum standard described in Refs. [102, 103] with hydrogen as the predominant background pressure at room temperature.

Now that we have established the pressure on the source side of the chamber and the tweezer side of the chamber, we can design the vacuum system accordingly. First we establish the schematic design of the vacuum system including various vacuum conductance C_i , pressures of different regions P_i , outgassing rates Q_i , pumping speeds S_i , and temperatures (Fig. 2.7). This allows us to better determine the required pressure in the intermediate vacuum chambers.

Once we have identified the intermediate vacuum chamber pressure and expected outgassing rate, illustrated in Fig. 2.7, we can start to determine the conductances C_1 , C_2 , and C_3 . To maximize differential pumping between the stages, we design these conductances to be as small as possible. Using equations for conductance in the molecular flow regime, where the mean free path

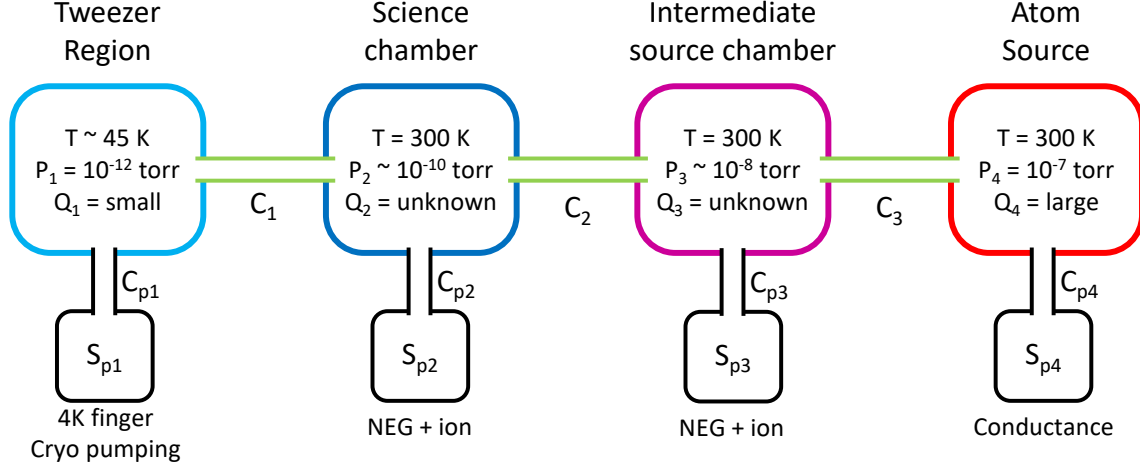


Figure 2.7: Schematic of cryogenic tweezer array vacuum systems including various outgassing rates Q_i , pumping speeds S_i and expected pressure P_i of different region of the vacuum systems as well as the conductance C_i between them. This provides a good guide for how different stages of system should be designed and the parameters required.

is much larger than the dimensions of the vacuum chamber, we arrive at the following numbers. The equations for different geometries can be found in Refs. [98,99]. The units for lengths in Eq. 2.6 is in centimeters.

$$\begin{aligned}
 C_1 &= 12.1 \frac{d^3}{l} = 12.1 \frac{0.2^3}{5} = 0.02 \text{ ls}^{-1} @ T = 300\text{K} \longrightarrow 0.006 \text{ ls}^{-1} @ T = 30\text{K} \\
 C_2 &= 12.1 \frac{0.15^3}{1.5} = 0.024 \text{ ls}^{-1} @ T = 300\text{K} \\
 C_3 &= 11.6 A = 11.6 \pi 0.03^2 = 0.05 \text{ ls}^{-1} @ T = 300\text{K}
 \end{aligned} \tag{2.6}$$

Now we can determine the required pumping speed (S_{pi}) and the pump conductance (C_{pi}) in conjunction with the expected outgassing rate (Q_i) within the given region in the system using methods from Ref. [98,104,105].

We will now discuss the requirements and pumping design at different regions of the system, starting from parts with the worst vacuum to the best vacuum. The atom source chamber is the part that has the worst vacuum. Due to the continuous operation of the rubidium dispenser from heating, there is significant outgassing from the decomposition of the chromate salts that generate the rubidium vapor. The source glass cell acts as a rubidium vapor cell, with the typical rubidium

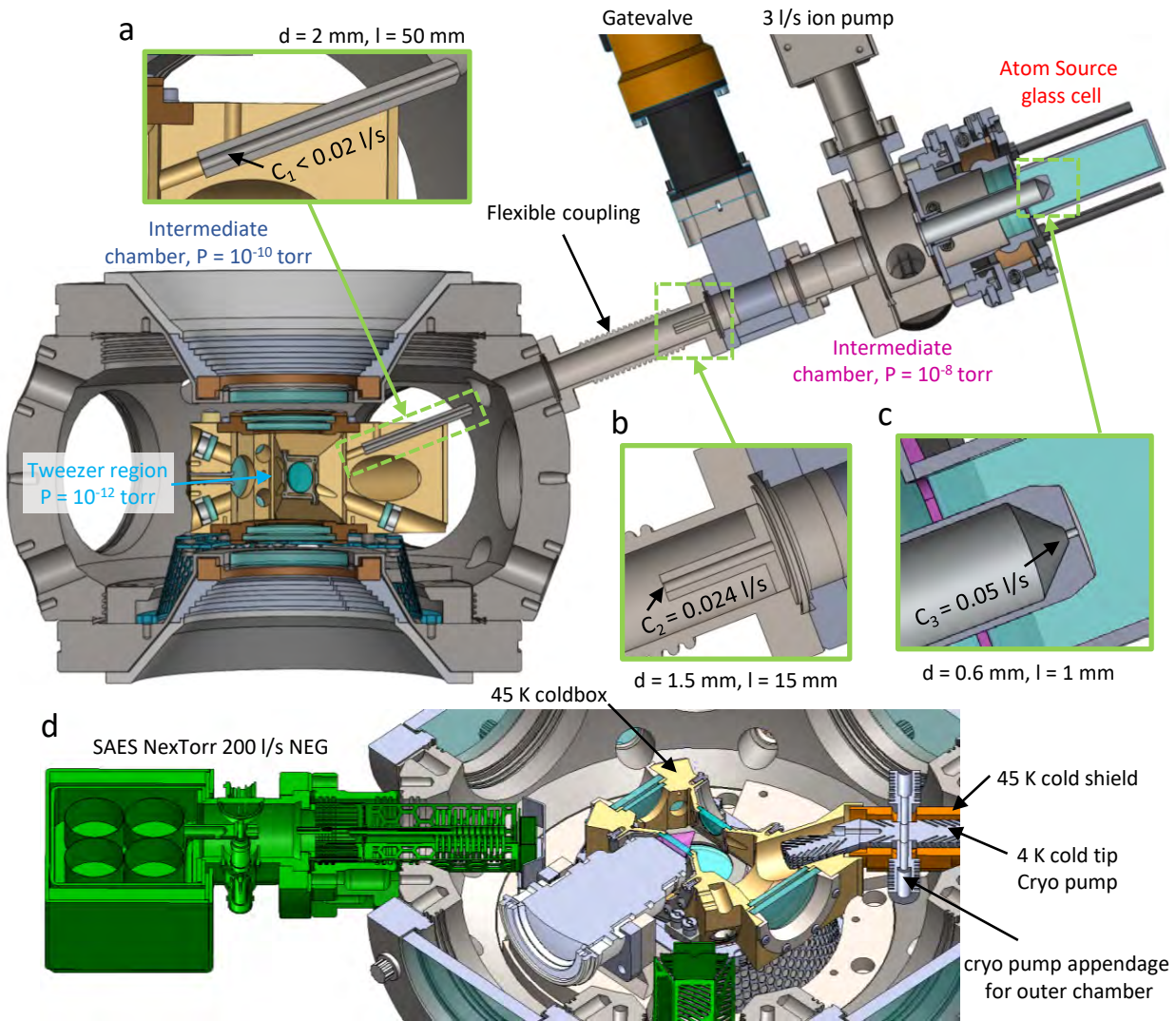


Figure 2.8: Cryogenic tweezer apparatus vacuum system showing the source chamber, intermediate vacuum chambers (science and differential pumping chamber after the source cell) and the coldbox. (a) The zoom in portion of 45 K differential pumping tube on the coldbox with the conductance $C_1 < 0.02 \text{ l/s}$. (b) The differential pumping tube between two intermediate chamber with the conductance $C_2 = 0.024 \text{ l/s}$. (c) The differential pumping pinhole separating the rubidium 2D MOT source vapor cell from the rest of the chamber with conductance $C_3 = 0.05 \text{ l/s}$. (d) The cross section of the science chamber showing the 4 K cryopumping cold finger and appendages. As well as the NEG pumps (in green) partially protrude into the chamber to maximize pumping capacity. In vacuum objective and the coldbox are also visible.

vapor pressure near room temperature being on the order of 10^{-7} torr [106]. There are no active pumps inside the source glass cell other than the pinhole with conductance C_3 ; since the majority

of the partial pressure is from rubidium, it does not affect the operation of the source cell. The dimensions for C_3 are 0.6 mm in diameter and 1 mm in length [Fig. 2.8(c)].

The next stage is the intermediate pumping chamber, which is pumped by a 3 l/s ion pump and a 25 l/s NEG. In order to maintain a pressure in the order of 10^{-8} to 10^{-9} torr, a differential pumping ratio of 100 is needed. With the value of C_3 being 0.05 l/s and outgassing Q_3 in the intermediate chamber being minimal, the total pumping speed $S_{p3} = 28$ l/s easily satisfies the ratio of 100.

The differential pumping in the final chamber just before the tweezer region is more complicated due to the large number of items inside this volume. This chamber contains several plastic parts, including PEEK thermal stand-offs, Kapton-coated wires, stainless rigid coaxial cables, microwave connectors, and Rogers PCB (Teflon). Fully characterizing the outgassing properties of this chamber is very difficult; only estimations can be made. Since most of the components contributing to outgassing are UHV plastics (data from Refs. [107–109]) we can estimate the types of residual gases to be expected from unbaked plastics in an UHV system, which are mostly H_2 , H_2O , CH_4 , CO , and CO_2 .

NEG pumps offer several advantages over other types of pumps, the most important ones being high pumping speed in a small form factor and no magnets, so stray magnetic fields are eliminated. Therefore, we choose to use multiple NEGs that partially protrude inside the chamber to achieve high conductance and pump reactive gases efficiently. However, ion pumps are still needed for pumping non-reactive gases such as helium, argon, and CH_4 . Three main pumps (green in Fig. 2.1) connecting to the main chamber through the 2.75" CF ports. A small tube with conductance C_2 [Fig.2.8(b)] separates the two intermediate chambers. The dimensions for C_2 are 1.5 mm in diameter and 15 mm long, with a conductance of 0.024 l/s. The NEGs are mounted in such that the pumping elements partially protrude into the main chamber to maximize pumping capacity [Fig. 2.8(d)]. The total pumping speed $S_{p2} = 200 \times 2 + 25 = 425$ l/s. With this pump configuration, we measure a pressure in the low 10^{-10} torr at room temperature and low 10^{-11} torr when the apparatus is cold.

Finally, we determine the requirements for the tweezer region. We opt for an aggressive differential pumping tube on the cold box, as shown in Fig. 2.8(a). The dimensions for C_1 are 2 mm in diameter and 50 mm long, with a conductance of 0.02 l/s at 300 K. However, since the tube is at 45 K, the conductance scales as \sqrt{T} , reducing to 0.006 l/s at 45 K.

Next, we estimate the effective cryopumping from the cold surfaces inside the cold box. While the precise pumping speed is challenging to calculate, we estimate the conductance from the trapped atoms to the 4 K cold finger to be in the order of 25 l/s. Typical cryopumping capacity on metal surfaces is in the order of 50 l/s/cm² [110–113]. Since we want the conductance to be the limiting factor, we design our cold finger with slits so the surface area is in the order of 50 cm², resulting in an effective pumping speed of hundreds of l/s, as depicted by the gray appendages surrounded by the 45 K shield in Fig. 2.8(d). For a more detailed discussion about the effect of temperature on pressure of different gasses, temperature vs gasses desorb from surfaces and cryopumping see Appendix D.

2.2.5 Coldbox and cryopumping finger design concept

The logic of design of the coldbox and the cryopumping coldfinger is the following. Since we know the outgassing rate of a surface is significantly reduced at low temperature, we aim to create a low temperature vacuum shield (coldbox) that has limited ability to cryopump but does not create additional adverse effect and is very clean in terms of outgassing properties. For this cold vacuum shield to be effective, the conductance from inside to the outside of the shield is limited. Then we place a 4 K cryopumping cold finger inside the coldbox with optimized surface area and conductance to cryopump on residual gasses. The primary gas load in a system that is already UHV at room temperature is mainly hydrogen which we rely mostly on cryosorption at 4 K to pump out. We choose metal for the cryopumping cold finger for several reasons, one is the volume that this cryopump act on is very small so we do not expect large gas load to saturate the surface quickly, assuming nightly regeneration of the cryopumping surface by warming up to 20 K. Additionally, the limited conductance between the coldfinger to the auxiliary ion pumps makes regeneration longer. Having porous materials such as activated charcoal will generate significant gas load and long regeneration time. With this configuration, we estimate a factor of 200 differential pumping ratio and ultimate pressure on the order of 10^{-12} torr. This estimation is based on the conductance (0.05 l/s) to the outside of the coldbox, cryopumping pressure curve from (Fig. D.2) and the surface sorption ability given by (Fig. D.3) from Appendix D.

One observation we have made is that despite the coldbox being held at 45 K, which should be sufficient to freeze out most of the gases other than hydrogen, helium, and neon, the outgassing behavior seems to be different after the coldbox is baked (using the build in heater) at 100 °C for a few days. We see almost an order of magnitude increase of single atom lifetime from ~ 400 s to ~ 3000 s. One hypothesis is that, the gases absorbed on the surface of the coldbox has an activation energy required for their release. Below this energy threshold, the surface act as a reservoir, continuously releasing background gas even at low temperatures. After baking, these reservoirs are depleted and the outgassing is further reduced. However, the effect of this

outgassing is not evident on the ionpump pressure reading on the outer vacuum chamber due to small conductance between inside of the coldbox and outer vacuum. After baking the coldbox we have virtually no outgassing from the cryogenic shield at 45 K, with the differential pumping ratio to be on the order of a few hundreds we expect the pressure in the tweezer region to be at least in the range of 10^{-12} torr. This will provide a lifetime in the order of thousands of seconds for atoms trapped in the tweezers.

One major difference between our experiment and many ion-trap experiments where the ions are enclosed in a 4 K radiation shield is that our experiment has a simpler design and larger optical access, but sacrificing the advantage of having large amount of 4 K cryopumping surface in line of sight from the atoms. Due to the low temperature of 4 K surfaces, residual gas molecules that collides with the wall are order of magnitude more probable of being trapped by the surface comparing to the 45 K coldbox due to Van-der-Waal's force and surface molecular potentials [110, 113]. Even for the gases not being absorbed on the first collision, the temperature of gas molecules that bounces off are significantly reduced and have lower probability of ejecting the atoms/ions from the trap. Therefore the experiments where the ions are trapped inside 4 K enclosures/boxes typically have better vacuum 10^{-13} to 10^{-15} torr (inferred by using the ion in the trap), comparing to the few 10^{-12} torr we achieve [68, 114].

2.2.6 2D MOT assembly and 2D to 3D MOT transfer

From Refs. [58, 59], we know that the oven + Zeeman slower approach as the atom source is problematic due to line-of-sight collisions from hot rubidium vapor. To exacerbate matters, the length of the Zeeman slower creates a rather collimated atom beam from the thermal source. Without a gate valve, collisions will result in an effective lifetime on the order of 300 seconds even when the vacuum environment is ideal [59].

To circumvent this issue, we decided to use a 2D MOT as our atom source to better control the atom flux entering the science chamber. The advantage of using a 2D MOT with an alkali metal dispenser instead of an oven is that there will be no line-of-sight between the rubidium source and the tweezer array. In this section, we describe the construction of the 2D MOT, including the vacuum package, atom source, and optics assembly. This approach allows us to create a compact, pre-cooled source of rubidium that can be easily integrated into the main experiment and aligned to the small differential pumping stages on the coldbox.

The vacuum package consists of a custom glass cell from ColdQuanta, with electrical feedthroughs on the side to supply current for the AMD (see Appendix B for dispenser details). On the glass cell, there is a pinhole, as shown in Fig. 2.8(c), with a conductance of 0.05 l/s to limit the rubidium vapor exiting the glass cell. After the pinhole, there is a 1" thick 2.75" CF adapter with side ports, creating a small pumping volume for the NEG's and ion pump to be attached, as shown in Fig. 2.9(a). The custom NEG assembly contains two 12 l/s NEG pumping elements welded onto the 1.33" CF electrical feedthrough [Fig. 2.9(b)]. The atomic beam passes through the space between the two NEG pallets.

A set of 4 permanent magnet bar assemblies creates a 25 G/cm quadrupole magnetic field in the transverse direction for the transverse cooling of the atomic vapor. The center of the field can be translated by changing the position of the magnet assembly through a translation stage. This aligns the 2D MOT with the first differential pumping pinhole on the 2D MOT cell [Fig. 2.10(a)].

Another critical component of the 2D MOT assembly is the optics package. Unlike con-

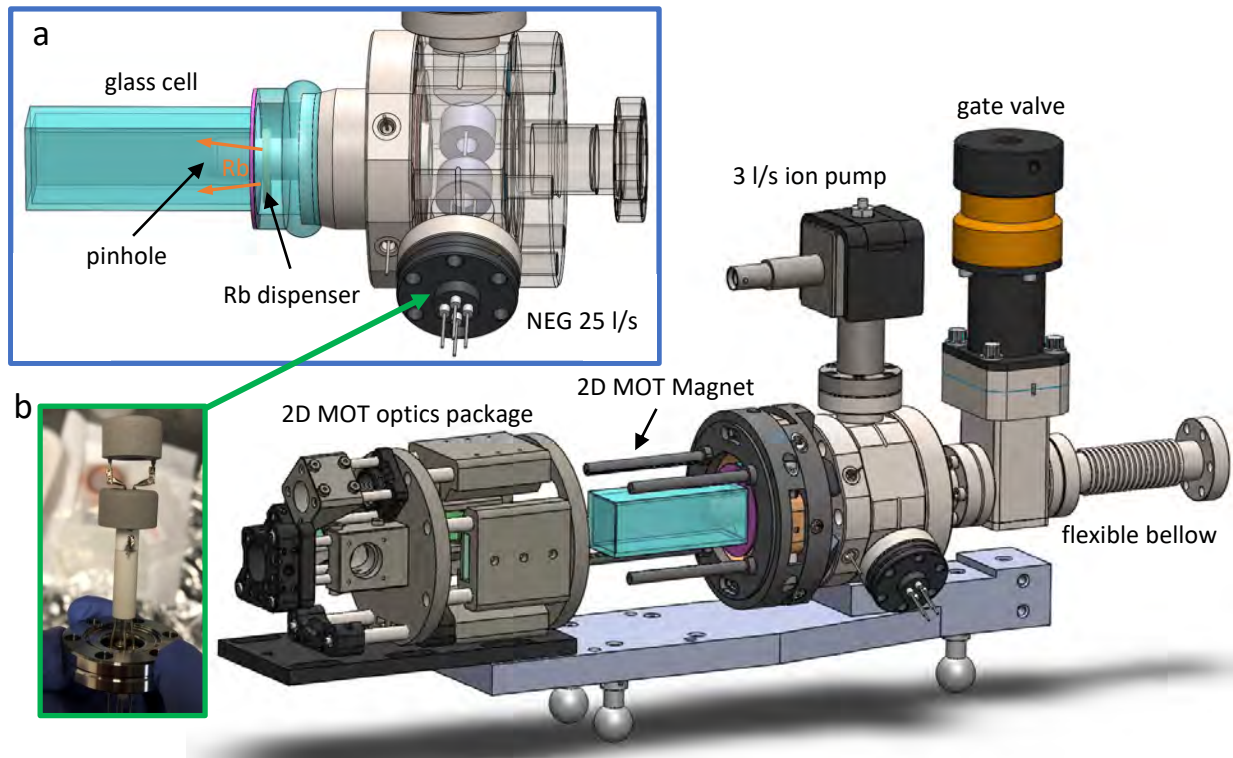


Figure 2.9: Cryogenic tweezer apparatus 2D source MOT vacuum assembly. The 2D MOT optics package is offset from the vacuum chamber for clarity. The Assembly includes a set of 4 permanent magnet rods generating a 25 G/cm 2D magnetic field gradient. A translation stage allows the position of the zero field to be aligned to the differential pumping pinhole. A 3 l/s ion pump is connected to the intermediate pumping chamber and a gate valve is used to isolate the assembly when the science chamber vents to air. (a) Shows the zoom in portion of glass cell and intermediate chamber for differential pumping. Including the ion pump and custom NEG assembly with 25 l/s pumping speed. (b) The picture of the custom NEG assembly consists of two 12 l/s NEG elements welded on a 1.33" CF UHV electrical feedthrough.

ventional approaches that utilize a large or elliptical laser beam [95, 115], which necessitate bulky lenses for beam generation, we opted to split a small beam into several paths to create an elongated trapping region, as depicted in Fig. 2.10(b). This multistage method has been studied in Refs. [116, 117], showing similar atom flux compared to the use of single large beam. Since the beams are wide and the alignment requirements are relatively relaxed, we chose to 3D print some of the optomechanics for beam distribution. The grey parts in Fig. 2.10(b) are 3D printed using HP Multi Jet Fusion in Nylon PA 12, and the beam splitting optics are glued to the 3D printed

parts. The completed optics package is shown in Fig. 2.10(d). The only requirement for operation is two fiber-coupled light sources for the MOT beams and push beam. After cooling the Rb atoms from the background vapor in the transverse direction (bright dot in the center of Fig. 2.10(a)), the atoms are propelled by a push beam with a velocity of 15-20 m/s into the science chamber through all the differential pumping tubes.

To characterize the performance of the 2D MOT, we measure the atom number loaded in the 3D MOT versus time, showing approximately 10^7 trapped atoms during typical operation, as depicted in Fig. 2.10(c) orange trace. The atom flux is extracted through fitting the slope of the atom number versus time at $t = 0$. The dashed line represents the fitted atom flux inside the coldbox at the tweezer region. With the push beam, we observe 4×10^6 atoms/s, and 3×10^5 atoms/s without the push beam but with the transverse cooling 2D MOT beams, which is more than 10 times smaller. Essentially no atoms are observed if both beams are switched off.

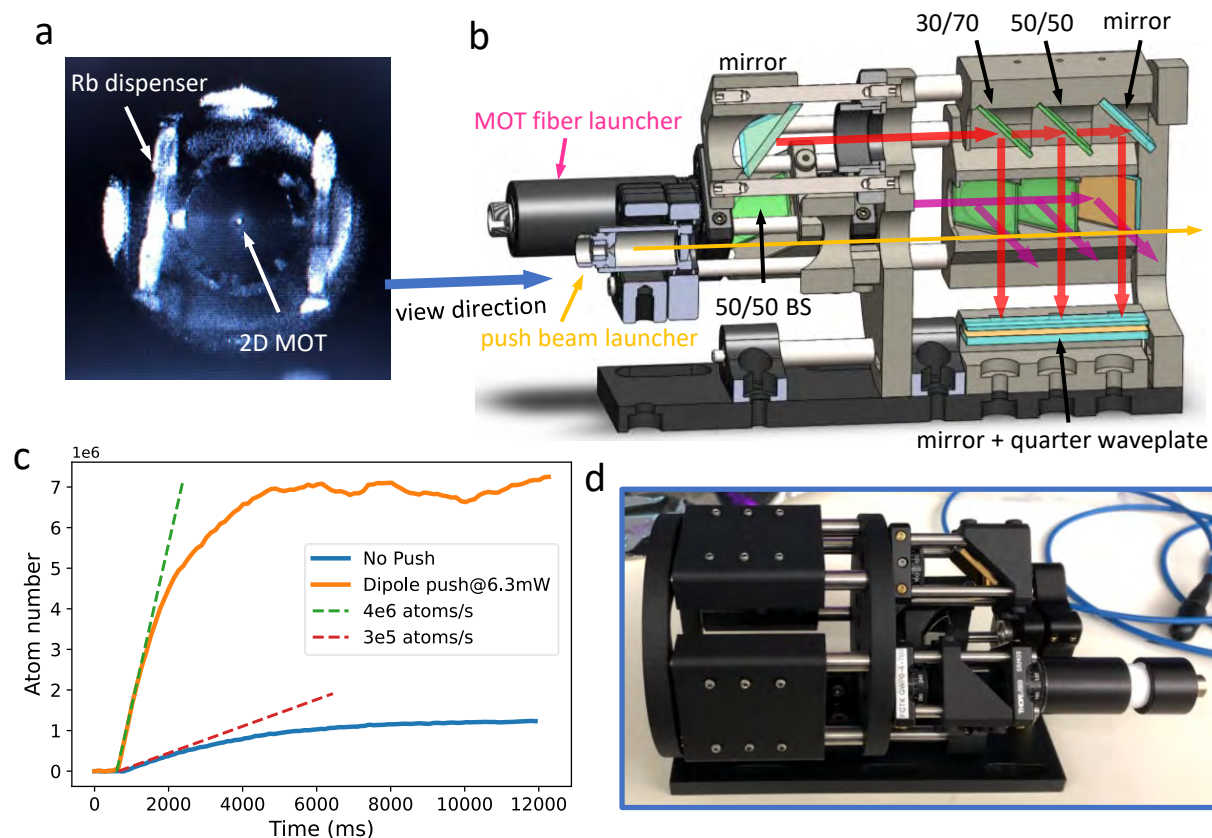


Figure 2.10: (a) Viewing from the push beam direction of the 2D MOT showing the pinhole and the Rb dispensers. The 2D MOT, aligned to the pinhole, is the bright dot at the center of the image. (b) Cryogenic tweezer apparatus 2D source MOT optics package. Grey parts are 3D printed with HP Multi Jet Fusion in Nylon PA 12. The MOT beams (red and purple) are split into 3 equal intensity paths and retro-reflected. Push beam (yellow) launched from the back pushes the transversely cooled atom out of the pinhole. (c) 3D MOT loading as a function of time showing 10^7 trapped atoms. Dashed line are the loading rate with and without the push beam showing $10\times$ difference in flux. (d) Photo of the completed 2D MOT optics package.

2.2.7 Magnetic field in 3D MOT (science) chamber

The DC magnetic field coils are necessary to cancel stray magnetic fields such as the Earth's magnetic field and fields created by magnetic objects nearby the vacuum chamber, such as optical breadboards and screws. The location of the coil is rather constrained, so there is really only one configuration to place three pairs of coils for magnetic field control in all three dimensions [highlighted in blue in Fig. 2.11(a)]. However, the coil is still designed with the possibility of generating up to a 100 Gauss bias field in mind. This is for a potential plan to prepare circular Rydberg states in the cryostat, which require an electric to magnetic field crossover. Due to the space constraint, the bias coils are not in a Helmholtz configuration, but the size of the coils is large enough, therefore within the Field of View (FoV) of the objective, a reasonable magnetic field homogeneity is maintained.

Due to the complicated mounting geometry of the nested coils, the coil mounts are 3D printed with HP Multi Jet Fusion in glass-reinforced nylon for high-temperature resistance in case the coils warm up during experimental operation. Because of the odd shape of the coil, we used COMSOL to see if the coil produces a uniform field and also to obtain the coil current to field conversion. The result shows that within a ± 1 cm region near the center, the magnetic field uniformity is around 0.02%. Figure 2.11(b) is the simulated field of the y-axis for illustration, but the simulation was done in all axes and showed similar uniformity. For both the x and y axes, we have 5.5 G/A. The z-axis is designed to be used as a circular state bias coil in the future, so it has 13 G/A.

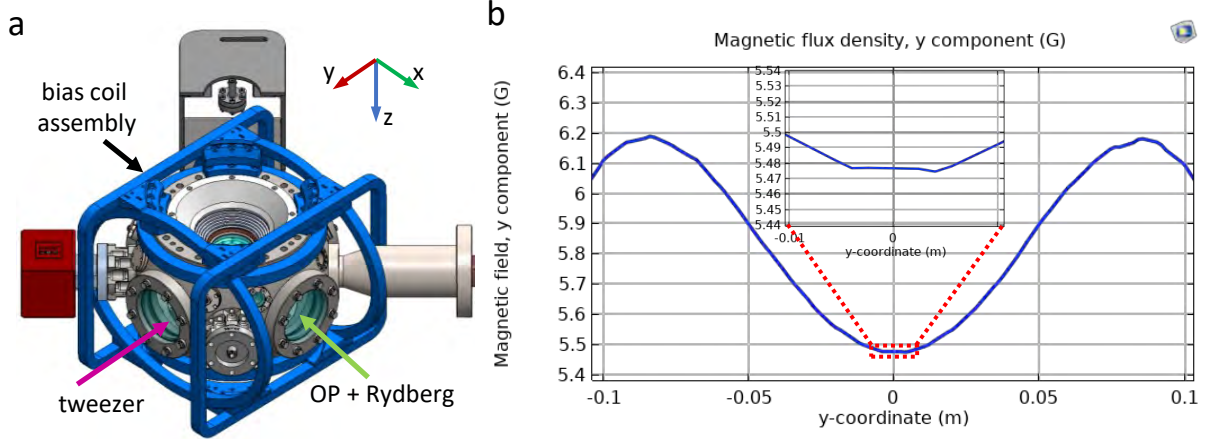


Figure 2.11: (a) Blue highlight is the bias coil assembly. Containing rectangular coil with round corners for x-axis, elliptical shape coil for y-axis and circular coils for z-axis. (b) is the COMSOL simulation for y axis bias coil at 1A current. Inset is zoom in of ± 1 cm region near the center of the coil showing 0.02% B-field uniformity. Simulations are also done on the x and z direction showing similar results in terms of uniformity.

2.2.8 BBR microwave

One of the requirements for the qubit state is a long coherence time. In neutral atom quantum computing platforms, it is common to use the $mf = 0$ ground hyperfine state (first-order not sensitive to B-fields) as qubit states [35, 118]. These states typically exhibit very long T1 (relaxation) times on the order of a few seconds or more, so the coherence is typically limited by environmental stability such as magnetic fields and AC-Stark shifts created by other light. With clever dynamical decoupling and magnetic field noise compensation, T2 coherence times of several seconds are achievable, but typically the bare coherence (T2*) is on the order of a few milliseconds [32, 35].

The hyperfine level typically has energy splittings on the order of a few gigahertz. In the case of ^{87}Rb , the clock transition between F=1 and F=2 is 6.835 GHz. It is difficult to efficiently couple microwaves into the metal chamber and metal coldbox from outside of the vacuum; therefore, we decided to put a resonant loop antenna inside the coldbox to drive this transition as a diagnostic tool. Alternatively, a pair of Raman lasers can be used to drive this transition at a higher Rabi

frequency. Having an antenna inside the coldbox allows us to place it only 15 mm away from the atom; however, this also creates a potential path for noisy room temperature BBR microwaves to enter the chamber.

Typically, a microwave source has broadband noise that is significantly higher than the room temperature BBR. So connecting it directly to the antenna inside the coldbox can introduce photons in the range of several tens of GHz. At $n = 70$, the adjacent Rydberg level spacing is 20 GHz; the room temperature BBR can easily couple these levels and create decay channels to unwanted quantum states.

To prevent unwanted room temperature BBR microwaves from entering the coldbox, a PCB with a microwave bandpass filter is attached to the coldbox and thermalized to the coldbox temperature of 45 K. This rejects the room temperature BBR outside of the passband and replaces the spectrum with 45 K microwave BBR.

To estimate the difference between room temperature and 45 K microwave spectra up to 100 GHz, which is within the transmission range of the coaxial cable, we calculate the BBR spectra of perfect blackbody at these two temperatures [orange and blue in Fig. 2.12(a)]. Within this range, we see a ratio of around 7 in power density [black trace in Fig. 2.12(a)]. To calculate the effect of microwave bandpass filter we multiply the room temperature BBR spectrum with the filter transfer function and add the 45 K BBR spectrum on top of it [black dash in Fig. 2.12(b)] is the resulting spectrum. Comparing the residual transmitted BBR through the filter with 45 K BBR spectrum [orange trace in Fig. 2.12(b)] we can see that beyond the passband of 6-8 GHz of the filter, the room temperature microwave BBR is attenuated to less than the BBR from the 45 K environment. This ensures that the microwave the atoms see is limited by the 45 K BBR instead of the 300 K microwave BBR coupled in from the coaxial cable.

BBR microwave impact on Rydberg atom lifetime

The reason the microwave environment needs careful consideration in our coldbox is that the coupling of the Rydberg level to the adjacent $n \pm 1$ principal quantum numbers is highly sensitive to stray microwaves from BBR. In quantum computing and simulation applications, three main types

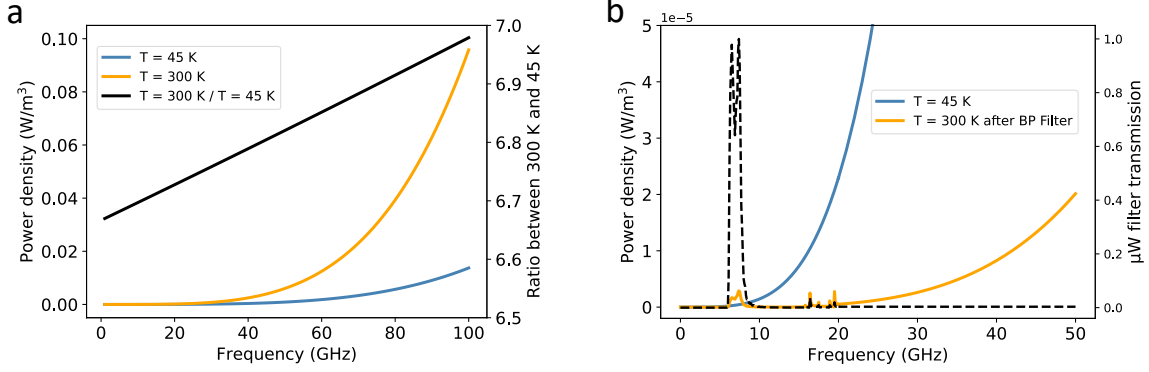


Figure 2.12: (a) Room temperature microwave spectrum (orange) and 45 K microwave spectrum (blue) in the range up to 100 GHz which is within the frequency range of Rydberg energy spacing between adjacent principle quantum number. The ratio between the BBR from 300 K and 45 K, roughly constant in this frequency range, is found to be around 6. (b) Bandpass filter transmission characteristics (plotted in black dashed line) and the filtered 300 K BBR spectrum (orange) comparing to the 45 K BBR spectrum showing a lower power density outside of the filter pass band.

of decoherence channels affect the Rydberg level: natural (vacuum-induced) decay to the ground state, BBR-induced photoionization of Rydberg atoms, and BBR microwave-induced transitions out of the Rydberg state. Natural decay represents the fundamental limit of the Rydberg state lifetime, which ideally we aim to achieve.

The effect of BBR photoionization due to environmental photons can be estimated using calculations from Ref. [119]. The plot in Fig. 2.13(a) shows that even at room temperature, the photoionization rate is much smaller than the natural decay rate of Rydberg states (typically in the range of hundreds of microseconds for $n > 40$). However, for circular Rydberg states with significantly longer natural lifetimes (10-100 milliseconds for $n > 40$), the BBR photoionization rate, even at 30 K ($\sim 10 \text{ s}^{-1}$), becomes a dominant decay source [47, 119].

Next, we consider the impact of BBR microwave-induced transitions out of Rydberg states. Plotting the decay rates for both natural and BBR microwave-induced processes for $n = 70S_{1/2}$, we observe in Fig. 2.13(b) that at room temperature (300 K), the decay induced by BBR microwaves is several times larger than natural decay (red data vs. blue data). At 30 K (green data), the decay

is primarily dominated by the natural decay rate [blue in Fig. 2.13(b)]. As previously discussed, for circular Rydberg states with much longer natural lifetimes, decay out of the Rydberg state is predominantly caused by BBR-induced transitions to adjacent Rydberg states, even at a microwave BBR temperature of 11 K [47].

In our current coldbox design operating at 45 K, the effective microwave BBR shielding for decay out of normal Rydberg states is estimated to be approximately 1/3 (in terms of BBR-induced decay rate) of an ideal 45 K BBR environment. This is due to the large optical access we put on the coldbox. The estimation is done by finding the total solid angle that is not covered by metal in the design. In reality, this fraction may be larger due to the size of the openings is similar to the microwave transition wavelength, potentially reducing the fraction of microwaves able to penetrate. In the future, in order to increase room temperature microwave BBR shielding, the windows on the coldbox can be replaced with ITO coated windows to form an Faraday cage.

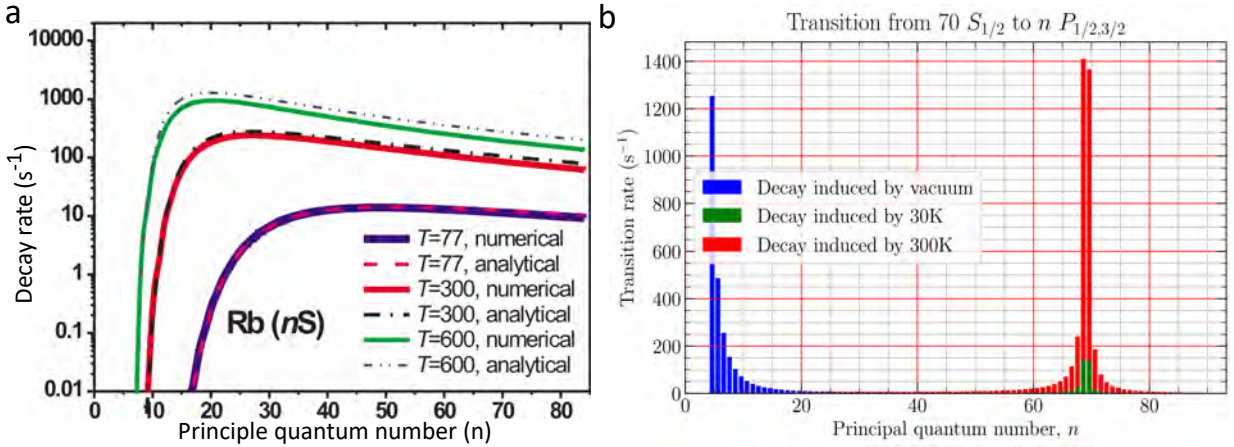


Figure 2.13: (a) BBR photoionization rate (s⁻¹) of rubidium nS Rydberg state as a function of principle quantum number n (plot from Ref. [119]). For $n > 20$ at least an order of magnitude reduction in ionization rate of the Rydberg state in 77 K microwave environment vs. in 300 K microwave environment is observed. (b) Decay rate out of $n = 70S_{1/2}$ Rydberg state to $nP_{1/2,3/2}$ Rydberg states. Three different configurations are simulated: (blue) is natural Rydberg state (vacuum induced) lifetime, (red) is decay induced by BBR microwave photon at 300 K, and (green) is the decay rate induced by BBR microwave photon at 30 K. At room temperature the BBR induced decay is several times higher than the natural decay rate, and at 30 K this rate is reduced to a level that is several times shorter comparing to the natural Rydberg lifetime.

2.2.9 Thermal design and analysis

Several important aspects need to be considered when designing the thermal isolation and thermal link of the apparatus. One consideration is how the tweezer is implemented in the cryogenic environment. Some approaches have been tried with success; in particular, in Refs. [58], they placed high-NA aspheric lenses in a cryogenic environment. With this approach, they could successfully generate an array of optical tweezers. However, it is hard to obtain a large uniform array due to the limitation of the field of view (FoV) inherent to the aspheric lens design. With the single lens approach, compromises need to be made on the optical performance between 780 nm and 850 nm, FoV, and size of the lens.

From early on, we set the design criteria of the apparatus to be as versatile as possible. We wanted to develop a set of technologies that could be easily adapted to other AMO experiments requiring large optical access with precise alignment requirements. To maximize the optical access, large windows are needed; however, the thermal conductivity of glass is low and the emissivity is near unity. This means that at the center of the large window, due to absorption of room temperature BBR, the temperature rises drastically compared to the edge. From COMSOL simulations, we found that with our window size of > 40 mm, a single-layer window needs to be on the order of 1 cm thick to achieve a temperature gradient of 10 K between the edges and the center. To circumvent this, we designed a double-pane window structure [an example shown in Fig. 2.14(b)], where we integrate a thermal break with a spacer between two relatively thin glasses. This allows the majority of the room temperature BBR to be shielded by the outer window, while the inner window stays cold. This allows a low thermal gradient on the inner window while keeping the total thickness of the structure less than that of a thick glass window. Simulating the thin double-pane window with radiative coupling to room temperature, we found that the design can tolerate the window to be as thin as 2 mm and still provide a very low thermal gradient on the inner window [Fig. 2.14(a)].

Conventional cryostats use thin-wall (< 0.5 mm) stainless steel tubes forming a truss structure

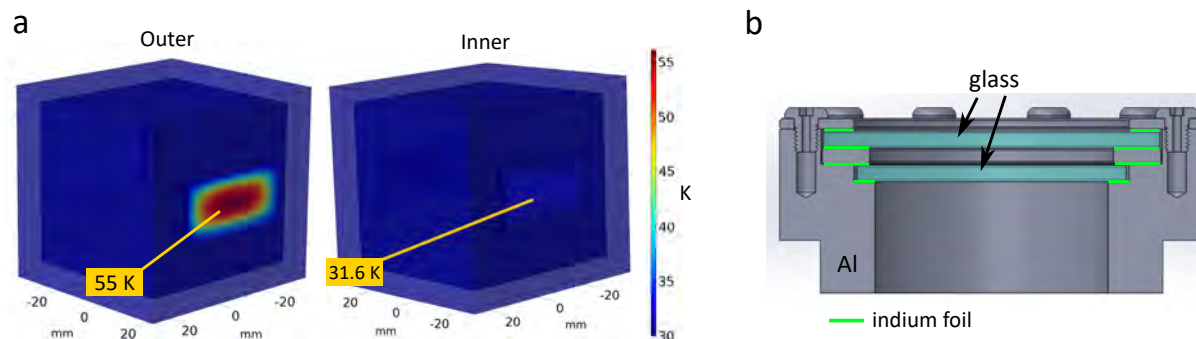


Figure 2.14: (a) COMSOL double pane window simulation with window thickness of 2 mm. Left is temperature of the outer window showing a 25 K temperature gradient. Right is the temperature of the inner window, which is the surface that the atom sees, only 1.6 K difference from the metal heatsink. (b) Example design of the double pane window that is used in the Montana cryostat test in Sec. 2.4.4. The indium gaskets shown in green act as thermal interface material between the glass and metal heatsink.

to connect between stages of different temperatures. This approach, while very effective in tension (load hanging from the top), is not very stable in compression, which is how our coldbox will be supported. Furthermore, due to space constraints in the room temperature vacuum chamber, we cannot use enough tubes to form a structure that provides sufficient rigidity. To overcome this challenge, we decided to use a thin-wall cone with a platform attached to the top for supporting the coldbox. The advantage of this method is twofold: first, the cone shape naturally nests well with the shape of the recessed viewport, and second, the cone provides a more symmetric support that creates less stress and torsional movement when cooled to cryogenic temperatures. The material is grade 5 Ti6Al4V alloy, which has one of the lowest thermal conductivities in metals [120] and has enough rigidity for structural applications. The cone consists of three parts laser welded together [a color-coded 3D render of the assembly is shown in Fig. 2.15(a)]. The bottom flange is 2 mm thick, the middle section is a 0.45 mm thin-wall cone with circular perforations to reduce thermal conductivity further, and the top flange is 1.5 mm thick. The top platform, also 1.5 mm thick, is attached to the flange with titanium screws and PEEK spacers to further reduce thermal conductivity. Finally, the coldbox is attached to the platform with PEEK spacers and titanium screws. The PEEK spacers

serve two purposes: they act as thermal breaks and provide some compliance to accommodate slight thermal expansion coefficient mismatches, ensuring that stresses are manageable and screws do not loosen after the assembly is cooled to cryogenic temperatures.

To verify that the thermal conductivity of the entire structure is sufficiently low, the entire structure is simulated with the thermal conductivities of the materials set to their room temperature values, which are normally larger compared to at cryogenic temperatures. The temperature at the coldbox attachment point and the chamber anchor point is set to 30 K and 300 K, respectively. This yields a heat conduction of 0.67 W flowing out through the support, which is an overestimate.

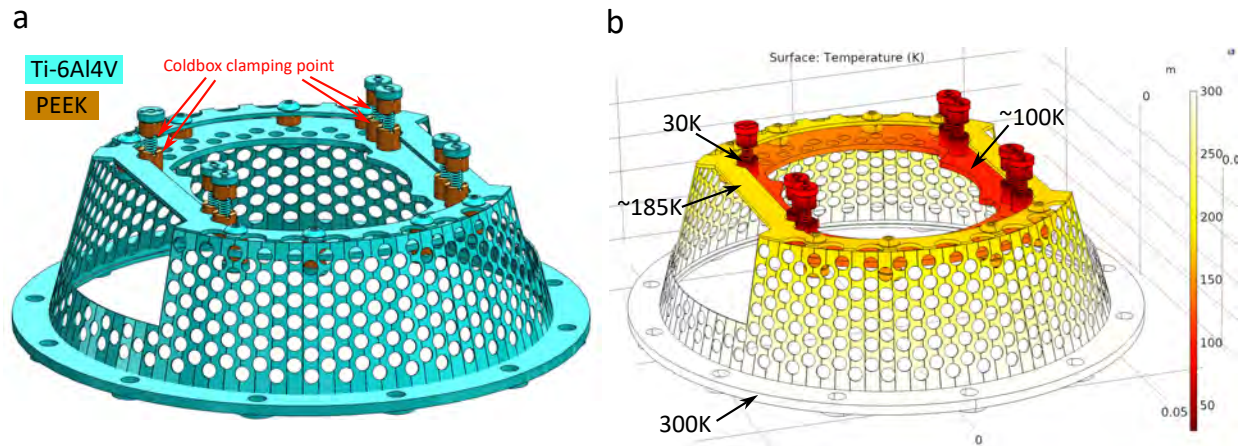


Figure 2.15: (a) The titanium thermal standoff. Blue colored parts are grade 5 titanium 6AL4V, which has thermal conductivity of $7 \text{ W/m} \cdot \text{K}$ lowest in structural metals. The cone portion of the titanium is 0.45 mm thick. The coldbox is clamped in between two PEEK standoff on 4 corners (pointed by red arrows). (b) Thermal analysis of the titanium standoff with COMSOL. The base is set to be 300 K and the coldbox clapping point is set to 30 K. The temperature of various location is marked with arrows. The total heat conduct through the titanium structure is around 0.67 W. Not taking into account the temperature dependence of thermal conductivity as well as assuming perfect thermal contact between parts.

To find the required cooling power and thermal conductivity for the copper braid that connects the cryostat's 30 K stage to the coldbox, we need to first estimate the amount of thermal load on the coldbox. The major heat sources and thermal load budget on the coldbox are listed as follows (see Zhenpu Zheng's thesis for detailed calculations).

Conduction from titanium support: Setting the boundary condition to be 30 K on the cold side and 300 K on the hot side, and not considering temperature-dependent thermal conductivity, the estimated upper bound for the heat load is **0.67 W**.

Radiative coupling of metal on the coldbox: The total surface area of the gold-plated metal part is 250 cm². The emissivity of matte gold is taken to be 0.47, and for polished stainless steel is 0.075. This gives a radiative heat load of **0.8 W**.

Radiative load on BK7 glass: The total surface area of the glass window is 52 cm². The emissivity of glass is near unity in infrared wavelength longer than 4 μm . The room temperature BBR spectrum peaks at 10 μm . Since the glass on the coldbox mostly faces the glass viewport on the room temperature chamber, we assume both emissivities to be 1. This gives a load of **2.5 W**.

Conductive heatload from stainless coaxial cable: The length of coax is 10 cm. The outer conductor is 304SS, inner conductor is BeCu. Using 30 K and 300 K as boundary condition, we find the load to be **0.2 W**.

Conductive heatload from DC wires: The DC electrode, coldbox heater, and temperature sensor are all connected with kapton-insulated phosphor bronze wire. There are a total of 15 wires, each with a diameter of 0.2 mm and a length of 20 cm. The total heat load is **0.045 W**.

The total estimated heat load is 4.2 W. This is below the specified cooling capacity of the radiation shield region of the cryostat which is 5 W @ 50 K. Now we have the number, we can estimate the temperature gradient across the copper braid. The copper braid is a standard P6-506 style from Technology Applications Inc. with braid length of 25 mm. This gives an estimated thermal conductance of 1.1 W/K @ 40 K. This is the largest copper braid we can fit in the space available. This gives a temperature difference of 4 K across the braid, which is a reasonable number.

2.2.10 Optical access

Since the window is now part of a high-NA optical system, the glass needs to maintain good flatness and mechanical alignment with respect to the vacuum chamber. Therefore, we need to carefully control the stresses on the glass when the coldbox is cooled to cryogenic temperatures. The difference in thermal expansion coefficient between copper and glass is quite significant; copper has a CTE of 16 ppm/K, while BK-7 glass has a CTE of 7 ppm/K. This amount of CTE mismatch can create stresses in the glass or, worse, cause mechanical failure. Typically, cryostats use compliant mounting such as springs to press the glass against the cold shield. This results in poor thermal contact between the glass and the metal surface, which is typically not an issue if there are multiple layers of radiation shield and only a small portion of the opening is glass. However, in our coldbox, about 30% of the surface area is glass, so a more efficient thermal link between the glass and metal is needed. This requires a mounting method that provides better thermal contact and better mechanical stability. Here, we choose to use indium foil as a thermal interface material due to its ductility at cryogenic temperature, however this limits the baking temperature of the coldbox to 120 °C. To process these foils into rings, we use specially made 'cookie cutters' and IPA as a lubricant to prevent the foil from sticking [as shown in Fig. 2.16(a)]. Indium remains soft even at cryogenic temperatures, which can absorb the difference in CTE between glass and metal. The glass essentially 'floats' between two pieces of indium foil. Through testing, we found that with relatively thin foils (0.2 - 0.3 mm) and a large number of screws to create even pressure, indium can maintain good mechanical stability and thermal contact while absorbing the difference in CTE. A completed double-pane window assembly is shown in [Fig. 2.16(b)].

With the efficient thermal contact between glass and metal part of the coldbox as well as the double pane window design, we put a large amount of optical ports on the cold box [shown in Fig. 2.17] is the available optical access on the coldbox. In total we have

Top/bottom: Two 0.57 NA (37 °) symmetric on z-axis

Side: Two 0.25 NA (15 °) symmetric on y-axis

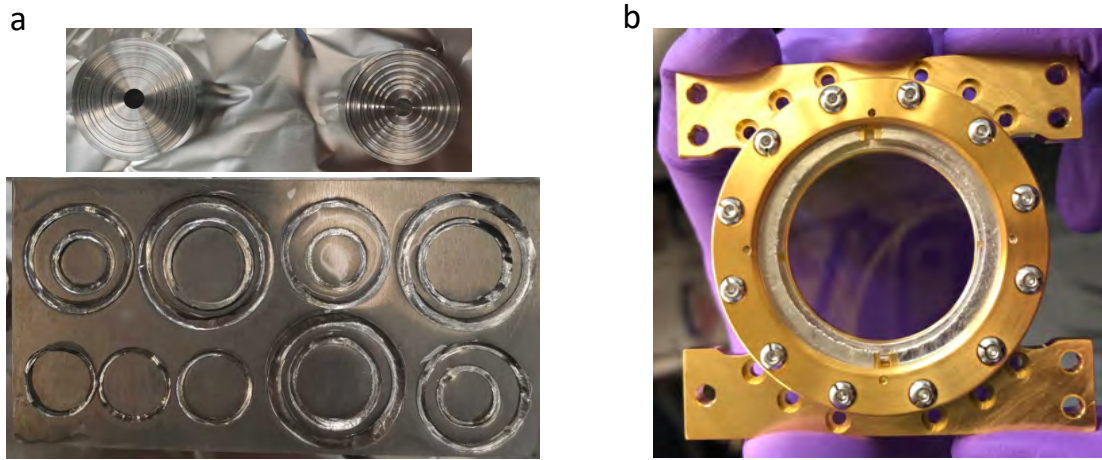


Figure 2.16: (a) Top: The cookie cutter used to cut the indium seal rings from 0.2 mm thick indium foils. Bottom: the cutted indium foil rings, methanol or IPA are used as a lubricat to prevent the indium from sticking to the cutter. (b) Photo of one of the completed double pane window structure, showing good thermal contact (flattening) between the indium seals and glass. The two layers of glass are visible in the photo.

Side tweezer: Two 0.55 NA, <0.1 mrad relative parallelism alignment error and $\lambda/5$ flatness.

MOT ports: 7 dedicated ports at 20° angle for MOT beams and probe beams.

Window substrate used in cryogenic Rydberg tweezer apparatus.					
Manufacture	Part #	Material	Coating	Size	Flatness
Edmund Optics	49634	BK-7	VIS-NIR (400-1000 nm)	35x35x3 mm	$\lambda/10$
Edmund Optics	37018	BK-7	VIS-NIR (400-1000 nm)	50 ϕ x3 mm	$\lambda/10$
Edmund Optics	83468	BK-7	NIR I (600-1050 nm)	12.5 ϕ x3 mm	$\lambda/4$
Edmund Optics	83471	BK-7	NIR I (600-1050 nm)	20 ϕ x3 mm	$\lambda/10$
Edmund Optics	37014	BK-7	VIS-NIR (400-1000 nm)	50 ϕ x2 mm	$\lambda/4$
Edmund Optics	37018	BK-7	VIS-NIR (400-1000 nm)	50 ϕ x3 mm	$\lambda/4$
Edmund Optics	15436	BK-7	VIS-NIR (400-1000 nm)	25.4 ϕ x2 mm	$\lambda/10$
Window thickness tolerance are listed to be ± 0.2 mm, but they are typically within ± 0.05 mm and very consistent between windows ($< 10 \mu\text{m}$ difference) from batch production					

Table 2.1: List of window substrate used in cryogenic Rydberg tweezer experiment

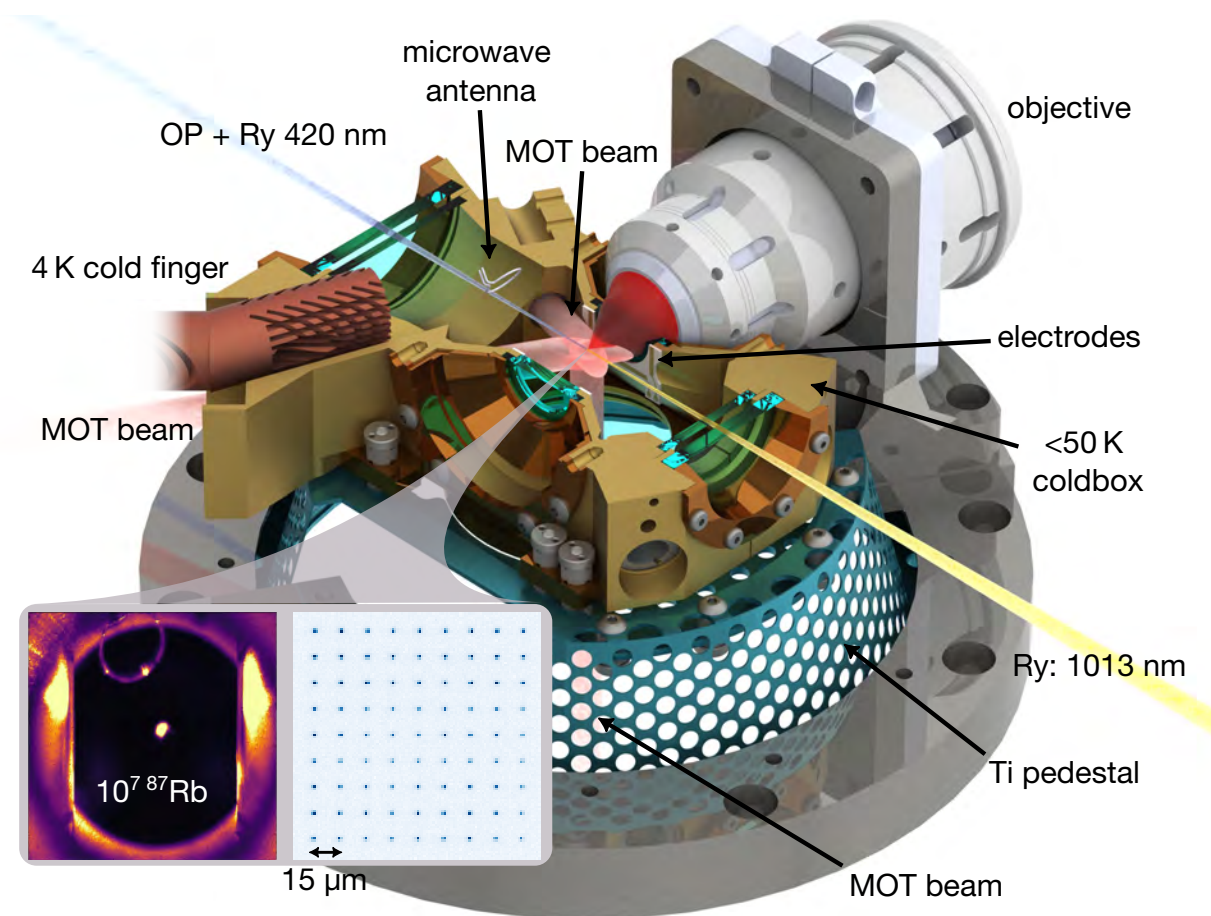


Figure 2.17: (a) Cross sectional cut of the CAD render of the core of the cryogenic tweezer experiment, showing the large optical access and high-NA tweezer access from the side of the coldbox.

2.3 Microscope

The most important part of achieving single atom trapping and manipulation is the high numerical aperture objective. These objectives, when performing optimally, can generate optical dipole traps that provide sub-wavelength confinement of atoms. We refer to these microscopic dipole traps as optical tweezers. The optical dipole trap uses far-detuned light from both the ^{87}Rb D1 and D2 transitions (795 nm and 780 nm, respectively). When the light is red-detuned, a dipole moment that is in-phase with the electric field of the light is induced, thus lowering the ground-state energy (AC-Stark shift). This creates a trapping potential that is proportional to the light intensity. When the trap is sufficiently tight (typically when the trap Gaussian waist is smaller than $2\ \mu\text{m}$), the trapped atoms become close enough to interact and form bound states. In the presence of near-resonant cooling light (MOT/PGC light), the atoms acquire energy from the light and can either both escape or remain in the dipole trap [121]. The result is either one or none of the atoms left in the trap, depending on the even or odd parity of the initially loaded trap. We call this process light-assisted collisions.

In our system, we use 830 nm light to create the optical tweezers and detection on the ^{87}Rb D2 transition at 780 nm. Both the tweezers and atom fluorescence pass through the high-NA objective. Ideally, the objective should be diffraction-limited at both wavelengths at the same focal plane. This sets many of the requirements for our optical systems.

2.3.1 High NA objective

There are generally two categories of high-NA objectives: infinite and finite conjugate. In a finite conjugate design, the objective takes the point source on the front focal plane and re-focuses it on the back focal plane. This is common in many microscope designs because only one lens is required to project the image to the eye or camera. In an infinite conjugate system, the objective takes the point source at the front focal plane and generates a collimated beam out the back, and vice versa. In our application, we use an infinite conjugate objective design because of our need

to place many optical elements before the light enters the objective. It is generally bad practice to focus light through plano-optical elements (waveplates, filters, PBS, etc.) since this creates additional aberration.

Our objective is custom-designed and made by Special Optics. It has an effective focal length (EFL) of 30 mm and is achromatic from 700 to 1100 nm. It has a designed numerical aperture (NA) of 0.55 and a working distance of 3 mm for BK-7 + 11 mm in vacuum. The objective is compensated to focus through the 3 mm window. The FoV of the objective is $\pm 200 \mu\text{m}$ around its optical axis. The objective is designed to be UHV compatible; therefore, the housing is made of titanium with vent slots, and it is non-magnetic due to its proximity to the atoms. Additionally, the objective is designed to withstand temperatures up to 150 °C if we wish to bake the chamber.

2.3.2 Tweezer light source and optical rail

The light source we use to trap single atoms comes from a MOGLabs MOAL 830 nm tapered amplifier. The TA is seeded by an IPS Photonics VBG external cavity diode laser. The light is coupled to the tweezer optical rail through a Coastal Connections angled-flat end-capped fiber for high power handling and to reduce unwanted interference inside the fiber. The flat termination is required to launch light at the tweezer rail to avoid aberration. In this configuration, we have 1.2 W of optical power available at the tweezer rail [Fig. 2.18(a)].

The AOD tweezer array is generated by a 2-axis AOD with a 6 mm active aperture from AA Optoelectronics (DTSXY-400-850.930). After the deflected array exits the AOD, it passes through a 1:1 relay lens and folding mirrors. Then it enters the final telescope with a magnification of 7. This creates a beam with a 16 mm Gaussian waist to fill the input aperture of the objective [Fig. 2.18(b)]. The relay and telescope lenses in the rail are carefully chosen and simulated in ZEMAX to ensure diffraction limited performance of the optical tweezer. The 1:1 relay is important since it creates extra space between the AOD and the final telescope for PBS and waveplates, which are used for cleaning the polarization and sampling the tweezer power for active intensity noise cancellation. The intensity noise is crucial for maintaining a long trap lifetime. We will discuss the heating effect

of the intensity noise in Sec. 3.3.1.

To create a static potential with SLM working along side the AOD movable tweezers for rearranging. A system of optical relays, similar to the AOD tweezers, is constructed [Fig. 2.18(c)]. The two trapping lights are combined with a PBS before entering the objective. The SLM system is constructed but not yet implemented in the experiment, so all the atom experiments in this thesis are done using AOD tweezers. In the longer term, a static potential generated with optical lattices will be implemented to create large amount of traps in a laser power efficient way.

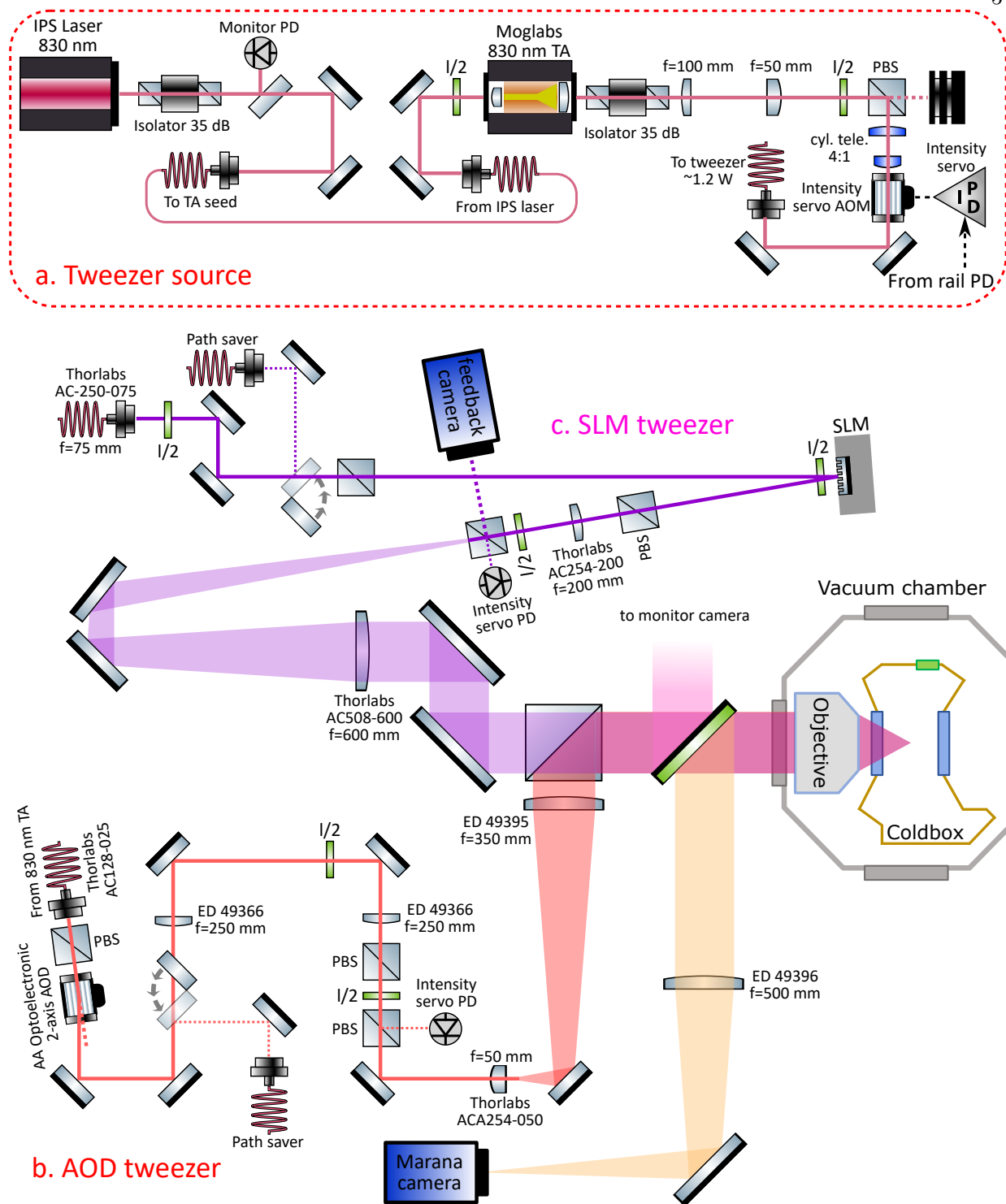


Figure 2.18: (a) The schematic of the tweezer light source including the 830 nm IPS seed laser and MOGLabs tapered amplifier. (b) Tweezer optical rail setup of the AOD tweezer path including relay lenses and part number. The optical performance of the whole rail system is verified with ZEMAX to guarantee operation at diffraction limit. (c) The rail schematic for SLM tweezer, also verified with ZEMAX to guarantee to be at diffraction limit. The two sets of tweezers are combined with a large PBS before entering the objective.

2.3.3 Pinhole testing of the objective

The objective is the most important optical element of the cryogenic tweezer apparatus. Once the objective is inside the vacuum chamber, any aberration would be hard to measure and correct. Therefore, careful testing needs to be performed before mounting it inside the vacuum chamber. Historically, there are two different types of measurements to assess the performance of the lens. One is the same type of pinhole measurement described in Sec. 5.5.4; the other is an interferometric measurement using a reference sphere at the focus of the objective, as described in [122]. If the lens passes the PSF measurement test, the interferometric test is not necessary, as it is only required if the optical phase of the aberration needs to be measured. We measure the PSF created by the objective with wavelengths of 780 nm, 826 nm, and 1013 nm to verify the objective's performance over the specified wavelength range. In the test setup, we align the objective precisely to within $10 \mu\text{rad}$ with respect to the test tweezer window, with the setup shown in [Fig. 2.19(a)], and obtain the pinhole image. The PSF image [an example shown in Fig. 2.19(b)] is fitted with Eq. 5.6, and the magnification is calibrated using the same method described in Sec. 5.5.4. The extracted on-axis NA is between 0.52 and 0.53, which is sufficiently close to the specified value of 0.55 from the manufacturer. We also measure the PSF over the FoV range of $\pm 200 \mu\text{m}$ by translating the pinhole [as shown in Fig. 2.19(c)]. We observe a slight degradation of NA to 0.5 beyond $150 \mu\text{m}$, which might be due to the FoV limit of the imaging lens that collimates the light onto the camera. Similar to Sec. 5.5.4, we also test the focal length dependence of the imaging lens, which is identical to the one used in the experiment. This allows us to know how much the imaging lens needs to be translated with respect to different wavelengths.

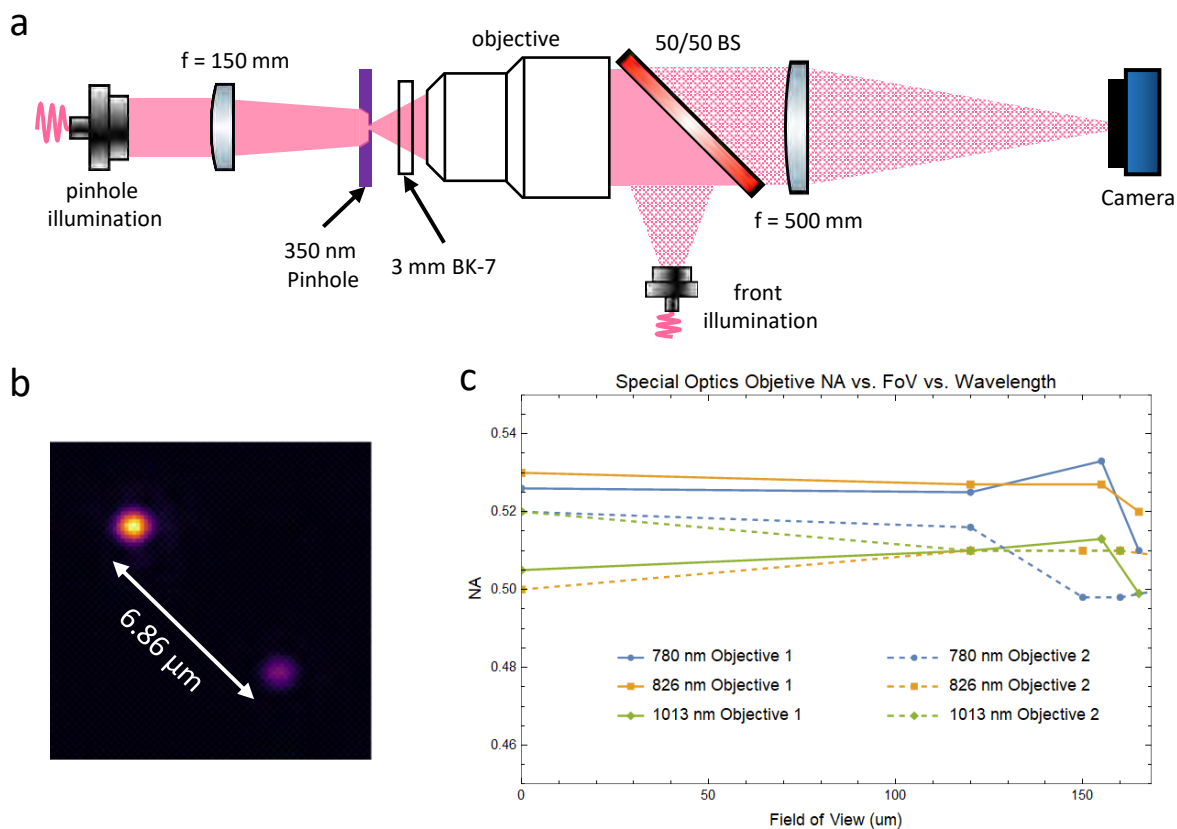


Figure 2.19: (a) Schematic diagram of Special Optics objective pinhole test setup, the pinhole is illuminated with a laser on the back, the front illumination is for initial search of the pinhole substrate. (b) Example pinhole image taken with the Special Optics objective @ 826 nm illumination. The imaging lens is the same as the one we used in the experiment for atom imaging. (c) The extracted NA from images similar to (b) over the FoV up to $\pm 175 \mu\text{m}$ and wavelengths of 780 nm, 826 nm and 1013 nm. Showing NA ranging from 0.51 to 0.53. This is close to the specified NA of 0.55 from the manufacturer.

2.4 Cryostat testing

In this section, we describe various tests on the mechanical aspect of the cryogenic tweezer apparatus. This includes vibration testing, heat load on the cryostat, alignment of the coldbox window versus temperature, stability of the anti-reflection (AR) coating under cryogenic temperatures, and characteristics of various DC electrodes and microwave filters when cooled to cryogenic temperatures.

2.4.1 AR coating testing

The glass windows on the coldbox are all AR coated to minimize unwanted reflections and maximize the power balance on the retro-reflected beams. Due to the extreme temperature range to which we subject our AR coating, choosing the correct types of AR coating is important. Typical AR coating types include electron-beam/thermal evaporation, ion-assisted deposition, magnetron sputtering, and ion-beam sputtering. We choose windows with a coating that is ion-beam sputtered. Ion-beam sputtering creates a coating that is fully dense, with no water absorption and good adhesion to the substrate. To prevent the need to have custom coatings made, we choose to use commercially available windows from Edmund Optics, Thorlabs, and Newport for windows on the coldbox. These large commercial optics vendors generally have their coating process well controlled compared to small batch custom jobs, so their coating generally is more consistent with better adhesion. We found that Edmund Optics provides a large selection of substrate sizes and coating types that are robust against thermal cycling with very minimal shift in spectral properties. The thickness tolerance and flatness from Edmund Optics are generally very good [Fig. 2.20(a)] as well despite having much looser tolerance specified on their website. The thickness tolerance is within $50\ \mu\text{m}$, and the wedge tolerance is within $0.1\ \text{mrad}$ from specification most of the time.

To test these windows before cutting them into the required shape, we thermally stress them in liquid nitrogen at $77\ \text{K}$. The window transmission is measured first. Then the windows are dipped in liquid nitrogen for a few minutes to thermalize, after removing from liquid nitrogen let

it warm up to room temperature in air. This process is repeated three times, and the substrate is wiped clean with solvents, and the coating is visually inspected for cracks and using the Scotch tape method [123] to check for adhesion. Finally, the reflection spectrum is measured again and they are compared [Fig. 2.20(b)]. We see very minimal change in the spectral bandwidth and reflectivity after thermal cycling.

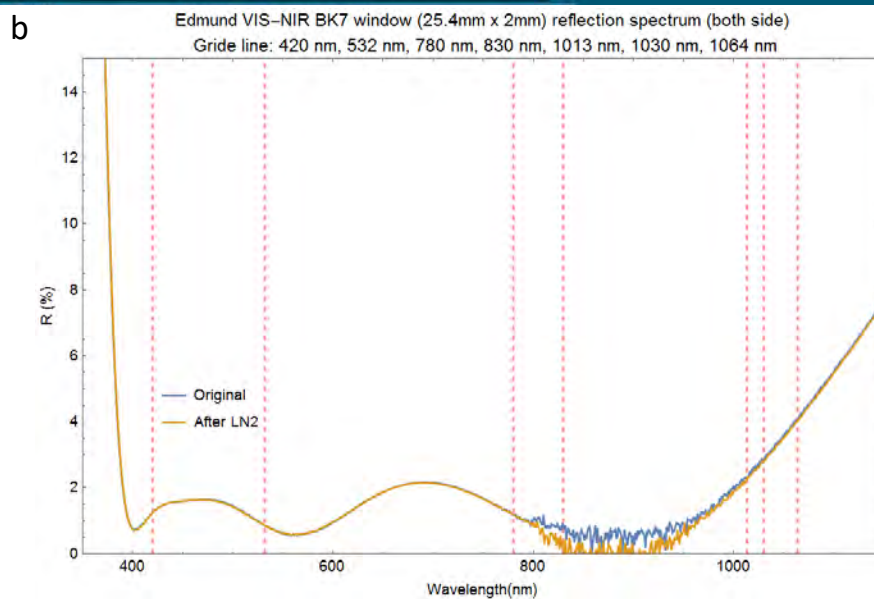
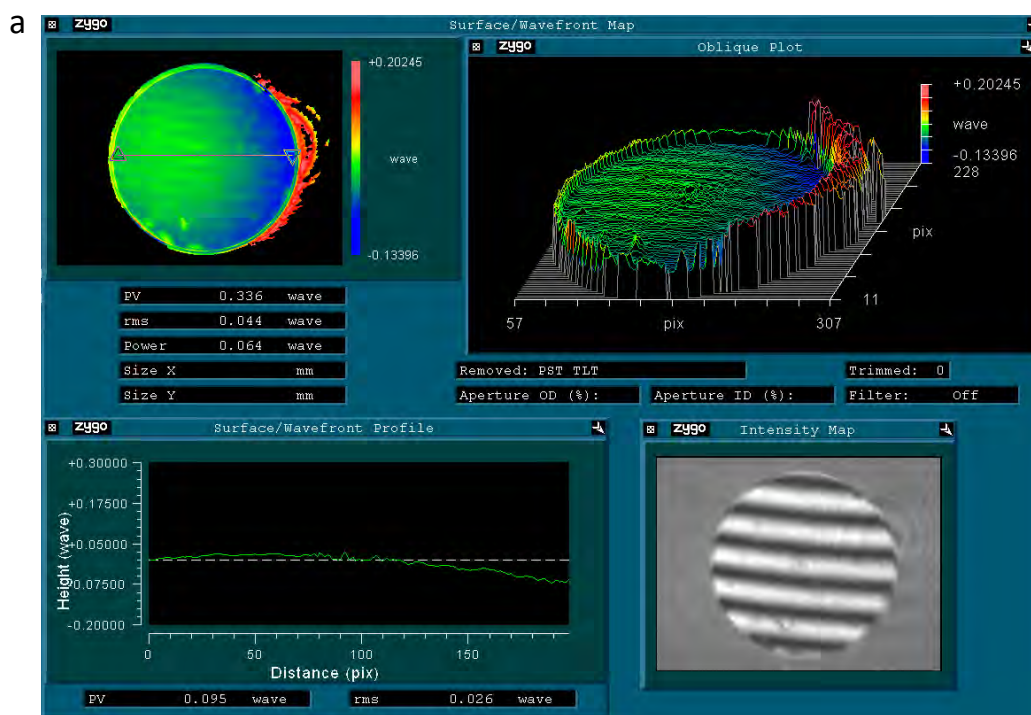


Figure 2.20: (a) The flatness and wedge measurement of the cold window substrate with the ZYGO fizeau interferometer. Showing better than $\lambda/10$ flatness @ 633 nm and wedge less than 0.05 mrad. (b) Reflection spectrum of the cold window substrates before and after thermal stressing in 77 K liquid nitrogen environment. The reflection spectrum remains the same and there is no visible damage of the coating. The dashed lines are wavelength of interest for our apparatus including Rydberg excitation (420 and 1013 nm), trapping (532, 830, 1030 and 1064 nm) and imaging (780 nm).

2.4.2 Vibration measurement

The Stinger cryostat provides a way of transferring the cooling power of the cryocooler without coupling vibration to the tweezer experiment. In AMO experiments, low vibration is particularly important due to the precise alignment of atoms and light required in most experiments. The main effect of vibration is that it changes the optical phase between the laser and the atoms. In many AMO experiments, lasers are used to prepare and excite the quantum states. In our particular example, a pair of blue (420 nm) and NIR (1013 nm) lasers are used to excite the atoms to the Rydberg state. If the relative position between the atom and the surrounding optics changes even by a fraction of a wavelength, the optical phase seen by the atom will be drastically different. For a detailed discussion of how vibration introduce excess phase noise and comparison to other cryogenic ion trap experiments [124,125], see Appendix F.

Another effect, which is much less of a concern, is excess vibration can create excitation in the motion of the atom inside the trap due to the jitter of the trap with respect to gravity, similar to shaking a ball sitting in a bowl. This heating effect is more prominent in optical tweezer and optical lattice experiments due to the trapping potential typically being very shallow, ~ 1 mK or less. This makes them sensitive to vibration at lower frequencies and smaller amplitudes. Although, in our design we are second-order sensitive to these vibrations because the objective is mechanically referenced to the same CF flange as the coldbox.

To measure displacement well below one optical wavelength between the coldbox and the optical table, it is impossible to measure it through mechanical means. Therefore, we add a small reflector on the coldbox [Fig. 2.21(a)] and construct an interferometer between the coldbox and a reference mirror on the optical table. Figure 2.21(b) shows how the interferometer is set up with respect to the vacuum chamber and the coldbox. The green dashed box represents the interferometer breadboard fixed on the optical table.

The PZT mirror in [Fig. 2.21(b)] is used to calibrate and adjust the interferometer so that the output at the photodiode sits at zero crossing. This is done to maintain the maximum sensitivity

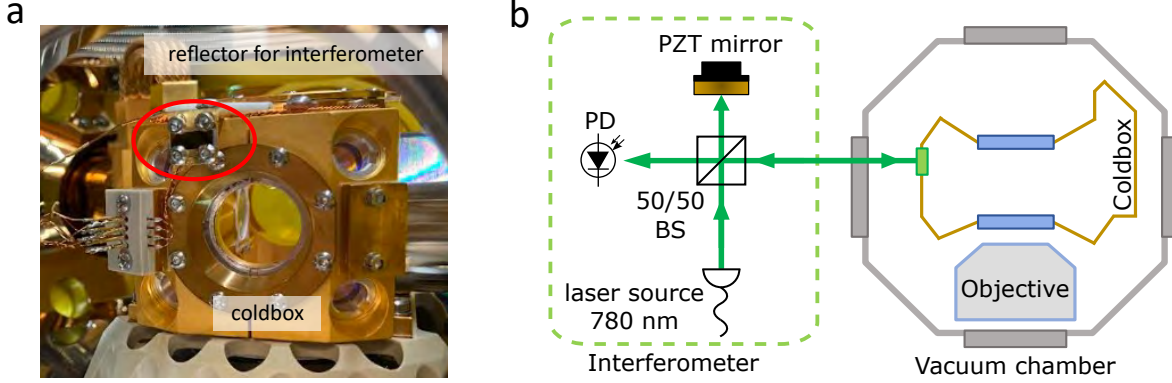


Figure 2.21: (a) Photo of the small reflector attached to the side of the coldbox as part of the interferometer for vibration measurement. (b) Schematic diagram of the interferometer setup between the coldbox reflector and the optical table. The interferometer assembly (green dashed box) is on an optical breadboard attached to the optical table and launches light onto the reflector pictured in (a).

of the interferometer, as the slope of the intensity (I) changes as a function of displacement (l) as follows:

$$I(l) = I_0(1 + \cos(2\frac{\pi}{\lambda}l)) \quad \longrightarrow \quad \frac{dI}{dl} \left(\frac{\pi}{2} \right) = I_0 \frac{4\pi}{\lambda} \quad , \quad \text{units : } \frac{\text{V}}{\text{nm}} \quad (2.7)$$

This gives us the calibration between the recorded photodiode voltage and displacement. Since our vibration is well within $\lambda/4$, we do not need to consider the phase wrapping of the interferometer signal. Scanning the PZT voltage [orange trace in Fig. 2.22(a)], a sinusoidal oscillation in photodiode voltage is observed [blue trace in Fig. 2.22(a)]. Fitting the photodiode amplitude (I_0), we can obtain a conversion factor of 50.2 nm/V. With the calibration, a time trace of vibration amplitude can be extracted [Fig. 2.22(b)]. Without damping of the stinger flex line with lead shots, the GM vibration excites mechanical resonances on the optical table every time the GM cycles [blue trace in Fig. 2.22(b)] with excursions roughly every second. With damping of the flex line, those excursions disappear [orange trace in Fig. 2.22(b)]. Taking the displacement time trace, a power spectral density of the vibration can be calculated [Fig. 2.22(c)]. The three regions in [Fig. 2.22(c)] correspond to different mechanical responses of the apparatus, including the optical table. Region (i), between 1 - 10 Hz, is the excitation due to GM cycle, mostly concentrated around a few Hz

range. Region (ii), between 10 - 200 Hz, comprises the mechanical resonances of the optical breadboards and optics mounts. The blue trace shows peaks where the resonances are excited by the GM when there is no lead shot damping. Region (iii), larger than 200 Hz, is where there is no more mechanical vibration, and we are measuring the noise floor where the blue (no damping) and orange (damped) traces become identical.

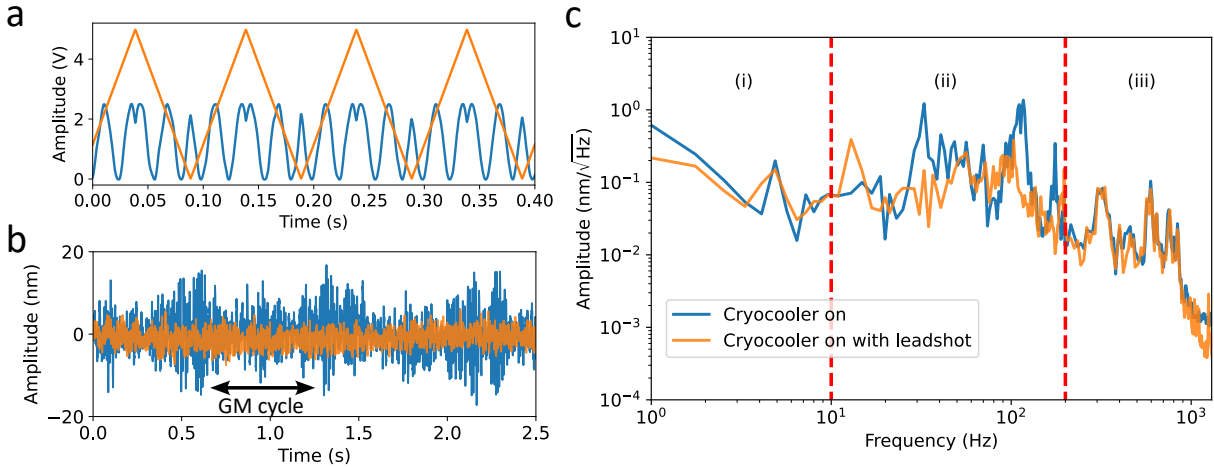


Figure 2.22: (a) Photodiode voltage (orange) vs. piezo voltage (blue). Linearly scanning the piezo voltage, result in a sinusoidal oscillation in the interferometer signal. This curve is used to obtain the calibration factor for converting volts on the PD to nm. (b) The time trace of the photodiode voltage. Blue is with GM on, we can see the mechanical excitation around every second caused by 1 Hz GM operating frequency. The orange trace is with damping on the stinger line with lead shots. Showing the vibration being largely eliminated. (c) The PSD of the time trace in (b). Region (i) is low frequency vibration from the operation of the cryostat. (ii) is the mechanical vibration of the structures on the optical table excited by the GM. (iii) is the residual vibration from the building and the optical table.

Without damping of the flexline, the peak-to-peak displacement of the coldbox relative to the optical table is in the order of 30 nm, which is in good agreement with interferometric measurements done in Ref. [126]. With damping, the peak-to-peak displacement decreases to around 10 nm, similar to the residual vibration from the background environment when the GM is off. From the time traces in [Fig. 2.22(b)] we can calculate the RMS displacement. For the blue trace, it is 4.8 nm, and for the orange trace, it is 2.1 nm. The undamped RMS vibration agrees very well with Ref. [126] and shows that with rigid mounting Stinger offers pretty low vibration in general.

These vibration values are significantly smaller than the atom wavefunction distribution, typically in the order of ~ 80 nm. We deem this level of vibration sufficient to maintain the coherence of the incident laser light and mostly limited by residual vibration from the building and optical table.

2.4.3 Heat load measurement

In Sec. 2.2.9, we discuss the expected heat load on the cryostat. However, precise measurements are still needed to confirm that we are not overloading the cryostat and that the copper thermal braid is sufficiently sized and the cryopumping cold finger is at a sufficiently low temperature to provide efficient cryopumping. To provide accurate monitoring of the temperature, we place temperature sensors in a few critical places, including the 4 K stage of the cryostat, the radiation shield stage of the cryostat before the copper thermal braid, and the far side of the coldbox to measure the upper bound of the coldbox temperature.

There are two heat load measurements we conducted with the cryostat. In the first measurement, we attach a heater directly to the radiation shield of the cryostat with the cryostat disconnected from the rest of the system. This allows us to measure the exact cooling power on both the radiation shield and the 4 K stage. The heater and temperature sensor can be seen on the radiation shield [Fig. 2.23(a)]. The end of the cryostat is capped with aluminum foil to eliminate any BBR load on the 4 K stage. With heat load applied on the 4 K stage, temperatures are recorded [Fig. 2.23(b)]. Between applied loads of 0-0.5 W, the temperature of the 4 K stage remains fairly constant, showing a cooling capacity of >600 mW is available. Beyond that, we see a temperature rise of 2.5 K/W on the 4 K stage. The shield temperature rises with 1.75 K/W, which is expected since the returned helium gas from the 4 K stage cools the radiation shield. The same measurement is done on the radiation shield [Fig. 2.23(c)]. We observe an 8.5 K/W capacity on the radiation shield with a base temperature of 12 K. The thermal link between the 4 K stage and the shield is 2 mK/K, which is negligible for our application.

The second measurement is conducted with the coldbox attached. We measure the temperature dependence versus additional heat load applied with the heater on the coldbox. With

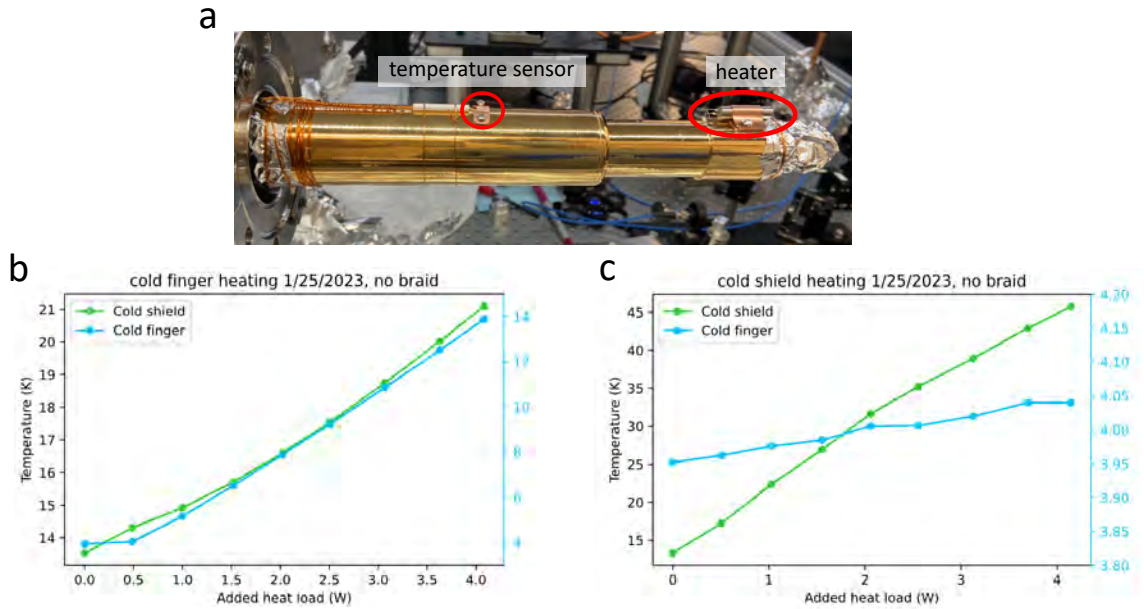


Figure 2.23: (a) Locations of the temperature sensors and heater for heatload testing of the bare cryostat (b) Temperature of the 4 K stage and the radiation shield vs. load applied on the on the 4K stage. Beyond the rated 600 mW cooling power it shows a 2.5 K/W cooling capacity on the 4 K stage. (c) Temperature of the 4 K stage and the radiation shield vs. load applied on the on the radiation shield. The radiation shield shows a cooling capacity of 8.5 K/W.

temperature sensors attached to different parts of the system (Fig. 2.24), we can record the temperature difference between the radiation shield and the coldbox (gradient across the copper braid).

Then, we can extrapolate the total BBR load on the coldbox as well as the thermal conductivity of the copper thermal braid by plotting temperature as a function of applied load (Fig. 2.25). The green data is from the radiation shield, and the orange data represent the cold box. The dashed line is a linear fit to the data, and the crossing point is where the thermal gradient across the copper braid is zero (equal to BBR load on the coldbox). We extract the thermal conductivity of the copper braid to be 2.2 W/K and the BBR load to be 2 W. However, if we use the load versus temperature curve in Fig. 2.23(c), we get a load of 3 W. So, it is safe to assume the BBR load is between 2-3 W, which is fairly close to our estimation in sec. 2.2.9. The discrepancy between the two methods might arise from the nonlinearity of the copper braid thermal conductivity with temperature or the unknown load on the 4 K cold tip raising the base temperature of the radiation

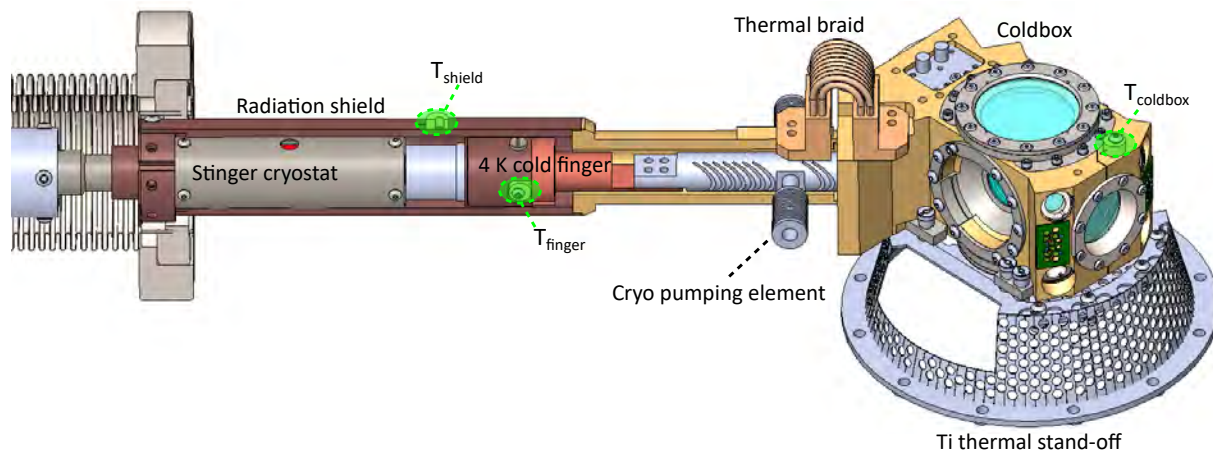


Figure 2.24: (a) Schematic showing the titanium thermal standoff and temperature sensor locations on the coldbox. There are three temperature sensors, one on the coldbox, one on the radiation shield and one on the 4 K stage of the cryostat. Two heaters, one located on the 4 K stage of the cryostat and another one located on the coldbox.

shield.

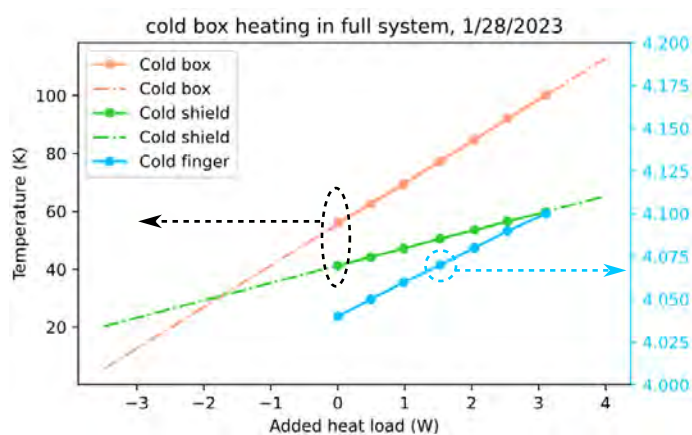


Figure 2.25: Temperature from three temperature sensors (described in Fig.2.24) vs. the applied heat load on the coldbox. This allows us to extract the thermal load on the coldbox and the thermal conductivity of the copper thermal braid. The crossing between the green and orange dash line is where the temperature gradient across the copper braid vanishes. This allows us to extract the thermal load on the coldbox and the thermal conductivity of the copper thermal braid.

2.4.4 Tweezer cold window alignment measurement

Once the coldbox is installed, we set up a system to monitor the angular change of the two coldbox windows and the objective with respect to each other. Since there is currently only one objective installed, a reference beam is set up on the side adjacent to the objective for monitoring the alignment. This beam defines the optical axis of the coldbox windows as well as the AOD tweezer system. This beam is also used as the reference for aligning the objective and the tweezer rail.

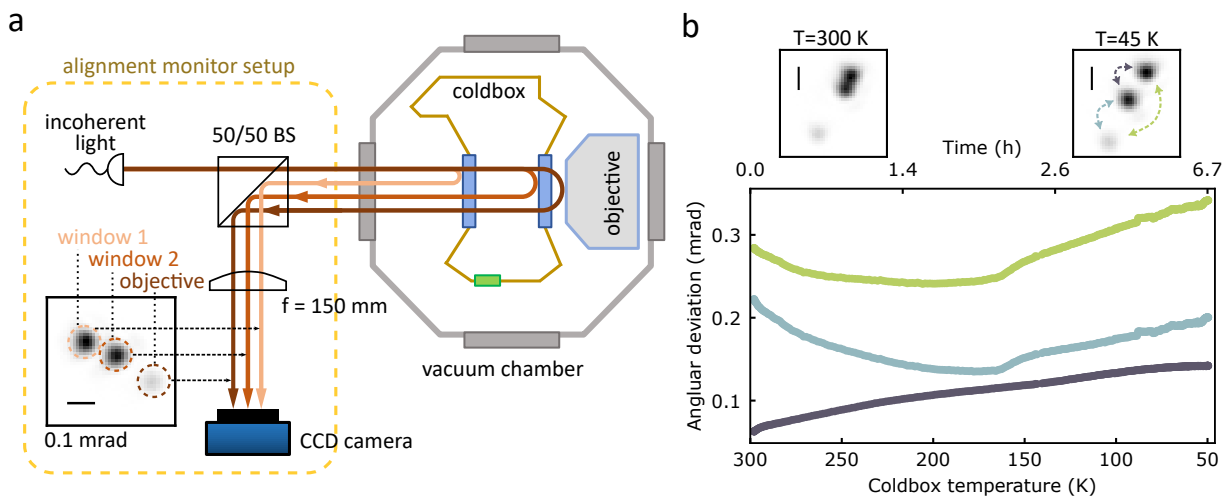


Figure 2.26: (a) Schematic of alignment monitoring setup for coldbox tweezer window alignment. An incoherent light is launched and reflect off both cold windows and the objective front face creating the total of three reflections (inset). With a lens focus onto the CCD, the reflections are converted to angular change. (b) The relative alignment of tweezer windows vs temperature recorded during the cryostat cooldown. Inset shows the image on the CCD camera showing the reflection from all three surfaces. This gives an alignment error of ~ 0.3 mrad between the coldbox and the objctive.

The monitoring setup [Fig. 2.26(a)] uses a collimated incoherent light source with a 10 nm bandwidth centering at 840 nm to eliminate interference from different sides of the windows. The 10 nm bandwidth is sufficiently small to minimize chromatic focal shift of the focusing lens. The reflected light from the windows and the objective is picked off by a 50/50 beam splitter and send to a focusing lens with an EFL=150 mm. This focusing lens focuses the colimmed beam into tight

spots while converting the input angular change into position change on the CCD camera.

The focused spots have $25\ \mu\text{m}$ Gaussian waist and the pixel size of the CCD camera is $3.45\ \mu\text{m}$. With typical fit uncertainty to the centroid of the Gaussian beam around 1 pixel, we can achieve $< 20\ \mu\text{rad}$ angular resolution on this monitoring system.

This system is also used to align the objective to the cold window. The mount of the objective consists of three parts, the base plate, the vertical flange mount and the threaded flange where the objective is mounted on [Fig. 2.17]. These three pieces separates translation degree of freedom from the angular degrees of freedom of the objective. The bolted connection between the base plate and the vertical flange mount is first shimmed with copper shims to the correct angle using the monitoring system to within $0.2\ \text{mrad}$. Then the objective together with the threaded flange plate can be slid to center the objective to the reference beam using the transmitted light. Finally, the bolts that connects the threaded flange plate to the vertical mount is tightened.

During cooldown, we record the angular change of the cold tweezer window [Fig. 2.26(b)]. The results show that after the initial relaxation from the first few cooldowns, the angular alignment stays relatively stable in subsequent cooldowns. We can see that the most alignment error between the window and the objective is $0.3\ \text{mrad}$.

To verify the angular tolerance between the window and the objective, we simulate the optical system in ZEMAX. We set up the simulation with collimated light input to the objective and plot the Strehl ratio over FoV of the light focused through the tweezer window. Changing the tilt of the tweezer window up to $2\ \text{mrad}$ we can see how the Strehl ratio changes as the window tilt angle increases [Fig. 2.27]. From this we can conservatively obtain within $1.5\ \text{mrad}$ tweezer window tilt, the objective can remain diffraction limited over the design FoV. Which is much larger than the angular alignment error of $0.3\ \text{mrad}$ between the tweezer window and the objective.

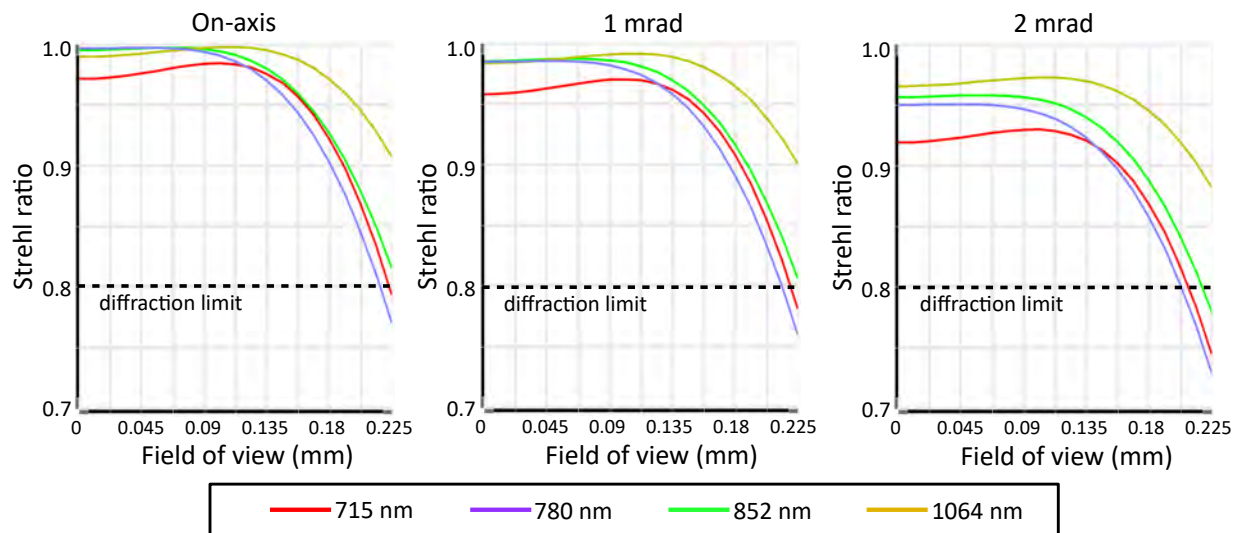


Figure 2.27: ZEMAX OpticStudio simulation of the strehl ratio of Special Optics objective vs. angular alignment to the cold window. On-axis, showing near perfect Strehl ratio of > 0.95 across different wavelength. 1 mrad alignment error, 3 times larger than what we measured from the coldbox, shows no significant degradation of Strehl ratio (> 0.95) and still remain diffraction limited over the full FoV ($\pm 225 \mu\text{m}$). At 2 mrad misalignment, the strehl ratio is still > 0.9 with a slight reduction in FoV to ($\pm 200 \mu\text{m}$).

2.4.5 Cold filter testing

There are two types of filters we install in our apparatus. One is for DC electric field control, and the other is a microwave bandpass filter. Since the DC electrodes are the closest non-grounded metal objects to the atoms, it is essential to ensure that no unintended noise can couple to them. To prevent RF and microwave noise from entering the coldbox, we designed an RC lowpass filter on an alumina PCB with a cutoff frequency of 80 kHz [Fig. 2.28(a)]. The cutoff frequency is chosen so that the voltage at the DC electrode can settle to within 0.5% of the final value in around 10 μ s. The DC electrode filters are also thermalized with the coldbox to below 45 K to block any potential BBR path. To make sure the filter characteristics remain unchanged at cryogenic temperatures, we made a test filter and dunked it in liquid nitrogen at 77 K while measuring the filter transfer function. The gain and phase of the filter are calculated by comparing the voltage V_{in} and V_{out} . We found that with COG type ceramic capacitors, the filter remains very stable even down to cryogenic temperatures [Fig. 2.28(b)].

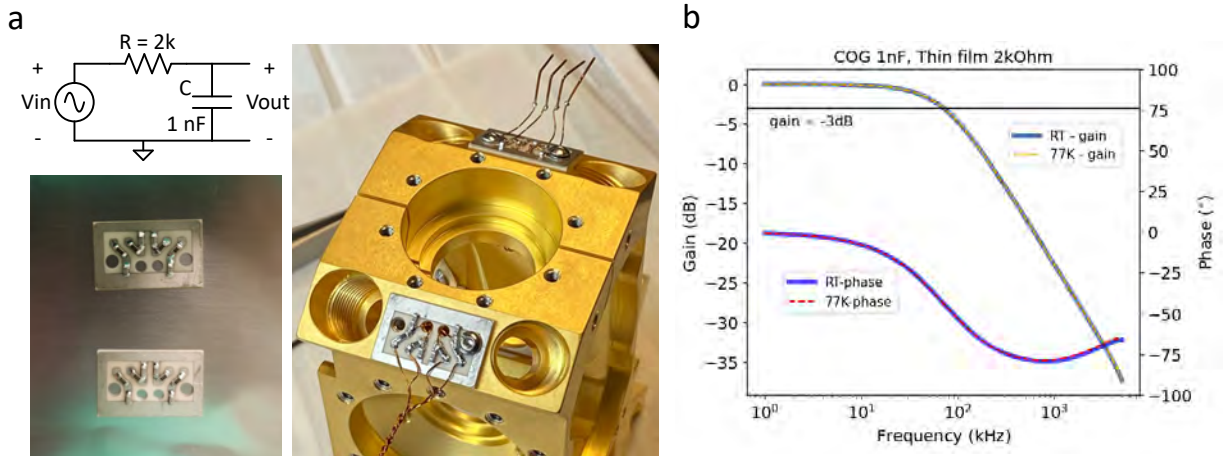


Figure 2.28: (a) schematic of the test setup and photograph of the DC electrode filter installed on the coldbox. (b) Filter transfer function at room temperature vs. submerged in liquid nitrogen at 77 K. The measurement shows essentially no change of the filter characteristics over the large temperature range due to the excellent thermal stability of COG dielectric material.

For the microwave bandpass filter, cryogenic characterization is also needed. Since the filter

has a steeper frequency response, it is expected to shift more when cooled to cryogenic temperatures. To simplify the filter construction and ensure UHV compatibility, we choose low-temperature co-fired ceramic (LTCC) filters. These filters consist of fully sintered multi-layer metal encased in a ceramic monolith, which is nonporous and has very low outgassing. This ceramic dielectric material is very similar to the C0G ceramic capacitor used in the DC electrode filters described above, providing excellent temperature stability. The actual filters are chosen based on insertion loss, passband, and stopband rejection. We tested two filters from Johanson Technology (6613BP44A1025 and 7000BP15A1600E), both providing a passband centered around 6.8 GHz and rejection over 30 dB beyond 20 GHz. Ultimately, we chose the 6613BP44A1025 due to its lower insertion loss. To test these filters, we soldered them directly to a semi-rigid coaxial cable and measured their S-parameters while immersing them in liquid nitrogen at 77 K [Fig. 2.29(a)].

The S-parameter measurements of the filter at room temperature versus 77 K show some change in the center frequency of the passband [Fig. 2.29(b)], but it is not significant for our application. The rejection and insertion loss remain unchanged between room temperature and 77 K. The sharp resonances that degrade the filter rejection between 15 and 20 GHz are measurement artifacts caused by the coaxial cable being soldered close together on the filter.

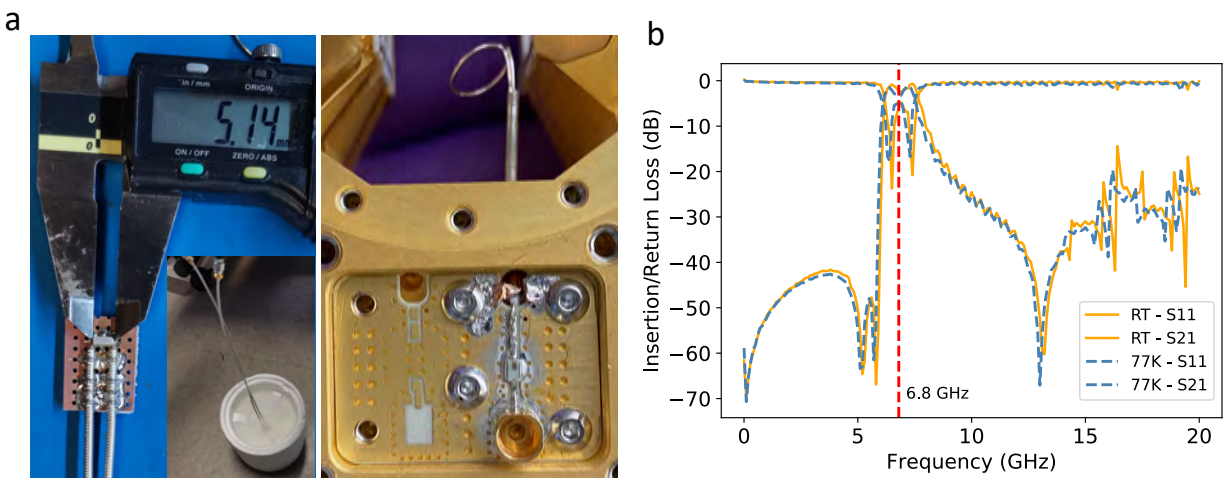


Figure 2.29: (a) photo of the microwave bandpass filter both in test setup and soldered on the PCB in the coldbox. For liquid nitrogen testing, the bandpass filter is soldered directly to semi-rigid coaxial cable and fix on a PCB for structural support. (b) the measured S-parameter of the filter at room temperature vs. 77 K. The result shows a small shift in passband frequency, but no significant difference in rejection and insertion loss.

Chapter 3

Cryogenic tweezer atom characterization

3.1 Overview

Note: For the most up-to-date analysis of cooling, imaging, and vacuum lifetime measurements, please refer to the upcoming publication "A High Optical Access Cryogenic Tweezer Array with a 3000-Second Lifetime" (in preparation).

In the previous chapter, I described the design and construction of the cryogenic tweezer apparatus. Additionally, I presented the initial test results of the mechanical stability, thermal performance, and optical performance of the apparatus. The tests showed that the optical alignment is sufficiently stable between the cold box and the objective to achieve diffraction-limited performance over the full FoV. Using a Michelson interferometer, we verified that the peak-to-peak displacement between the cold box and the optical table is around 10 nm, with an RMS of 2.1 nm. This level of vibration of the cold box is sufficient for the required trap heating and optical phase noise induced from vibration to achieve long trap lifetime and coherence. With these initial optical and mechanical measurements, we are confident that the apparatus is performing well, and we can move to the next step, which is to test the performance of the apparatus with trapped atoms.

In this chapter, I first present the loading and lifetime measurement of the MOT in a cryogenic environment. The loading rate from the background flux of rubidium from the 2D MOT is also measured, and its impact on the trapped atoms is estimated. Since the vacuum lifetime is expected to be very long, all the loss mechanisms need to be carefully characterized to infer an accurate vacuum-limited lifetime. We carefully measure the imaging and cooling losses as well as the trap

heating rate from Raman (inelastic) scattering of the tweezer light and other noise sources (RF and intensity noise). With the expected vacuum lifetime of $\tau_{\text{vac}} > 1000$ seconds, we can measure and characterize atom losses to the level of $< 10^{-3}/\text{s}^{-1}$, or with a typical tens of milliseconds imaging time, to less than 10^{-5} per image/cooling pulse. This allows us to measure an imaging loss as low as $(2.7(3) \times 10^{-4}/10 \text{ ms image time})$, with imaging infidelity of 10^{-6} , and cooling loss of $(2(1.6) \times 10^{-3}/\text{s}^{-1})$. After careful characterization, we demonstrate low loss cooling and imaging, enabling us to measure the vacuum-limited lifetime of $\tau_{\text{vac}} = 2800$ seconds with the trapped single atom array in a cryogenic environment.

In addition, the optical performance of the objective installed in the full system is measured with trapped atoms. Analysis of trap frequency and depth shows a NA of 0.48 ± 0.01 without SLM aberration correction. The FoV of the microscope is also tested, and we observe no significant degradation of optical performance over distances greater than $100 \mu\text{m}$, mostly limited by the scan angle of the AOD used in the tweezer rail. A second set of tweezers with SLM will allow us to correct for residual aberration and utilize the full FoV of the microscope.

Finally, we demonstrate that our apparatus is compatible with the LGM enhanced loading technique previously developed in our group [84]. We show an average loading efficiency of 83% across the full FoV of the microscope. We also observe good uniformity ($\pm 5\%$) of single atom loading probability and trap depth over the FoV, compared to [127]. The enhancement of loading efficiency provides a pathway to increase rearrangement efficiency and create larger tweezer arrays with a higher probability of success. This can prove to be a useful tool in scaling up the size of the quantum system.

3.2 MOT lifetime

The first step in trapping a single atom is loading the science MOT. Before trapping atoms with optical tweezers, we would like to check the vacuum condition using the MOT lifetime. The reason is a much simpler loss mechanism in the MOT compared to a single atom trapped in optical tweezers. Typically, in a room temperature vacuum chamber, MOT lifetimes of up to

a few minutes are observed [96, 102], corresponding to pressures in the range of 10^{-10} torr. In cryogenic experiments, a MOT lifetime as long as 1 hour was observed in Ref. [88]. This served as an important benchmark, allowing us to compare our system against other cryogenic apparatus, especially since the MOT lifetime reported in Ref. [58] was measured before the vacuum leak was fixed on their apparatus so the MOT lifetime reported there might not necessarily correspond to the vacuum-limited tweezer lifetime.

The loading/loss mechanism of the MOT can be described with the following equation [96, 102, 128].

$$\frac{dN}{dt} = R - \alpha N - \beta N^2 \quad (3.1)$$

The term R corresponds to background rubidium that can cause loading of the MOT. This term does not depend on the existing atom number. Due to very aggressive differential pumping between the 2D MOT chamber and the coldbox, this term is expected to be small. The coefficient $\alpha = 1/\tau_{vac}$ represents how the loss due to residual background gas can be extracted. The term β , which is proportional to N^2 , represents the two-body inelastic collision loss, e.g., light-assisted collision.

To measure the MOT lifetime, we start with a very dilute MOT containing fewer than 200 atoms. This is to suppress loss mechanisms other than the background loading and vacuum loss. With this low density, we can consider $\beta = 0$. Then, we can fit the MOT number over time with the following equation (which is a solution of Eq. 3.1 when $\beta = 0$).

$$N(t) = (N_0 - R\tau) e^{-\frac{t}{\tau}} + R\tau \quad (3.2)$$

After loading the MOT, the gate valve separating the source MOT and science chamber is partially closed to obstruct the beam path and prevent residual Rb background loading. Closing the gate valve is critical; without it, the final atom number actually increases over time, making the measurement inaccurate. Once the MOT is loaded and the gate valve is closed, the MOT is held in place, and an image is taken every 15 seconds with a 600 ms camera exposure time over the course of 6000 seconds. Then, the counts are summed and fitted with Eq. 3.2.

Typically, during normal tweezer loading operations, we load around 10^7 ^{87}Rb atoms within

a 500 ms loading time into the MOT, as shown in [Fig. 3.1(a)]. After acquiring a time trace and fitting the data (black circles) with Eq. 3.2, we extract a lifetime of $\tau_{\text{vac}} = 3800$ seconds, as depicted in [Fig. 3.1(b)]. This is the longest MOT lifetime we've ever observed in a cold atom experiment, consistent with measurements reported in Ref. [88]. Using conversions from Ref. [96], we estimate a pressure of 5×10^{-12} torr inside the cold box.

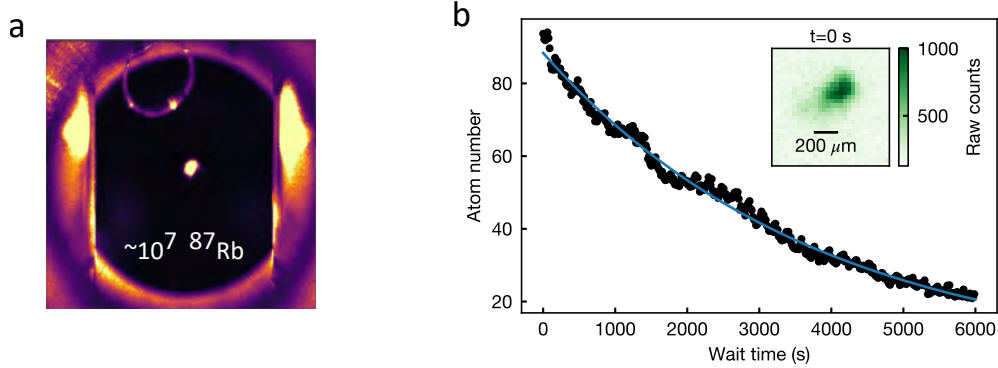


Figure 3.1: (a) Photo of the MOT of around 10^7 ^{87}Rb atoms trapped between two tweezer cold windows inside the coldbox. This is the typical MOT size during tweezer loading. The microwave loop antenna is visible on the background on the top left. (b) The MOT atom number vs time. Black solid circles is data, blue fit line on top is based on Eq. 3.2 where we extract a $\tau_{\text{vac}} = 3800$ sec. The inset is the image of the dilute MOT used for the time trace where only about 100 atoms are loaded.

3.2.1 Residual flux of 2D MOT

In Ref. [59] and [58], a significant reduction in lifetime is observed due to background Rb flux from the Zeeman slower atom source. They report a strong dependence of vacuum lifetime and the source oven temperature. With this in mind, we designed three aggressive differential pumping stages where the flux from the 2D MOT is well isolated from the cold box. To quantify the leakage of Rb atoms from the 2D MOT, we use the background loading of the MOT to estimate the total Rb flux that passes through all the differential pumping stages.

Typically, when a well-controlled atom source is used, e.g., a 2D MOT instead of a Zeeman slower, MOT loading from background rubidium cannot be observed since α is generally much

larger than R . For example, in the vacuum system described in Sec. 5.2, this background loading is never observed even with the ion pump pressure reading below 10^{-10} torr. However, due to the excellent vacuum in our apparatus, we can observe background loading in the absence of 2D MOT light. The loading is purely due to leakage from the Rb vapor that travels through the pinhole and is captured by the 3D MOT. To measure the background loading rate, we turn on the 3D MOT beam and open the gate valve. We record an image for 200 ms every 2 seconds for up to 600 seconds. We infer the atom number based on the scattering rate and solid angle of the imaging system using the following equation [106].

$$N_{count} = N_{atom} t_{img} \eta_{CCD} \frac{d\Omega}{4\pi} R_{sc} \quad , \text{ where } \quad R_{sc} = \frac{\Gamma}{2} \left(\frac{6 I/I_{sat}}{1 + 4(\Delta/\Gamma)^2 + 6 I/I_{sat}} \right) \quad (3.3)$$

Then fitting the atom number over time with the loading curve Eq. 3.4 where both vacuum loss and loading are considered we can extract the background loading rate R .

$$N(t) = R \tau (1 - e^{-\frac{t}{\tau}}) \quad (3.4)$$

Based on Eq. 3.4, we extract $R = 0.26 \pm 0.07$ atoms/s and $\tau_{vac} = (1.8 \pm 0.4) \times 10^3$ s [Fig. 3.2(a)].

To convert the captured atom flux to the total incoming flux, we need to determine the range of velocities at which the leakage atoms can be trapped by the 3D MOT. This allows us to find the ratio between all velocity classes and the trappable ones. The lower bound of the velocity is determined by the drop of the atom beam due to gravity. By plotting the atom beam trajectories vs. distance with different initial velocities, we can observe that the cutoff is around 16 m/s [shown in Fig. 3.2(b)]. Any atom launched from the 2D MOT with an initial velocity lower than this will miss the cold box completely. To calculate the maximum capture velocity of the 3D MOT, we use the following equation [129, 130].

$$v_{max} = \sqrt{a_{Rb} w_{MOT}} \approx 26 \text{ m/s} \quad \text{Where} \quad a_{Rb} = \frac{\hbar k \Gamma_{Rb}}{2 m_{Rb}} \quad , \quad w_{MOT} = 5 \text{ mm} \quad (3.5)$$

Now, by comparing the portion in the velocity range of 16-25 m/s [red shaded area in Fig. 3.2(c)] to the rest [grey shaded area in Fig. 3.2(c)], we find the ratio to be 1600, translating to 415 atoms/s

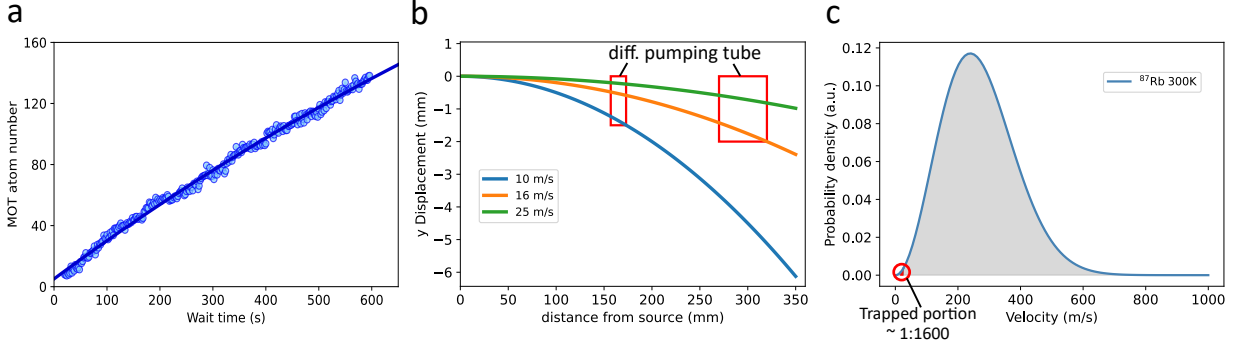


Figure 3.2: (a) Mot atom number vs. time from loading of background Rb flux from 2D MOT chamber. At $t=0$, the lasers are turned on and the gate valve between the 2D MOT and science chamber opens. (b) plotting the atom beam trajectories vs distance over different initial velocity. The red boxes represent the differential pumping tubes. Due to gravity, atom with initial velocity less than 10 m/s misses the middle differential pumping tube and initial velocity less than 16 m/s misses the coldbox. (c) Probability density over all velocity (grey shaded) assuming 300 K Rb vapor temperature. Only a portion of atom (red shaded) is slow enough to be captured by the 3D MOT.

of background rubidium from the 2D MOT.

3.2.2 Dipole-push beam

With the typical exit velocity from the 2D MOT on the order of 10-20 m/s, most of the atoms actually miss the entrance of the differential pumping on the coldbox [shown in Fig. 3.2(b)] The effect of gravity during the free flight of the atom beam is not negligible, and a simple push beam is no longer sufficient to guide the atom into the cold box due to the lack of confinement along the direction of gravity.

In order to efficiently guide the atoms, we employ a dipole trapping push beam (dipole-push) that is close detuned from the ^{87}Rb D2 line. The close detuning simultaneously provides the required trapping and scattering to push the atom along the axial direction of the dipole-push beam [131, 132].

Different from the typical push beam configuration where the atoms eventually move out of the path of the beam once they exit the 2D MOT cell, the atoms guided by the dipole-push

constantly scatter the dipole-push light, so the exit velocity is proportional to the scattering rate. Since the trap depth scales as $1/\Delta$ and scattering (thus velocity) scales as $1/\Delta^2$, where Δ is the detuning, it is possible to choose a dipole-push detuning that satisfies the following condition: the minimum required trap depth is reached before the atom is accelerated beyond the capture velocity of the 3D MOT.

We choose the dipole-push beam to be 600 MHz red detuned from the $F = 2 \leftrightarrow 3''$ cooling transition with a Gaussian waist of 0.3 mm and power approximately 10 mW. The 600 MHz detuning ensures that the dipole-push is red detuned from all the hyperfine states in the D2 excited state manifold, thus no anti-trapping occurs. We can estimate a lower bound on the trap depth and scattering rate if we consider the atom mostly cycling between $F = 2 \leftrightarrow 3''$, which gives approximately a 2 mK depth and a 0.16 MHz scattering rate. However, in reality, the atom also cycles between $F = 2 \leftrightarrow (1, 2)''$ with a smaller dipole matrix element but a closer detuning. Thus, the trap depth and scattering rate can be up to 3 times larger than the estimation above.

The intensity of the dipole push beam, therefore the atom flux and velocity, is optimized by observe the loading rate of the 3D MOT similar to the curve shown in [Fig. 2.10(c)].

The detailed calculation of the trap depth of this guiding push beam and the characterization of the velocity of the atom beam pushed out from the 2D MOT using this method will be discussed in Zhenpu Zheng's thesis.

3.3 Single atom lifetime

In the previous section, we characterized the loss and loading of the MOT in a cryogenic environment. Based on the measured MOT lifetime, we expect our single atom to have a lifetime greater than 1000 seconds. However, measuring a long vacuum-limited lifetime is not trivial. During the holding and probing of the trapped atom array, various losses are also introduced. If not treated carefully, these losses can introduce systematic errors in the inferred vacuum-limited lifetime of the single atom array.

For a single atom trapped in an optical tweezer, we consider the following loss mechanisms: heating loss out of the trap, cooling loss, and imaging loss. The time-dependent loss of each mechanism is specific to the method used to measure the single atom lifetime. In general, there are two ways for lifetime measurement: one is a single-shot image with variable hold time [Fig. 3.3(a)], and the other one is continuous measurement [Fig. 3.3(b)].

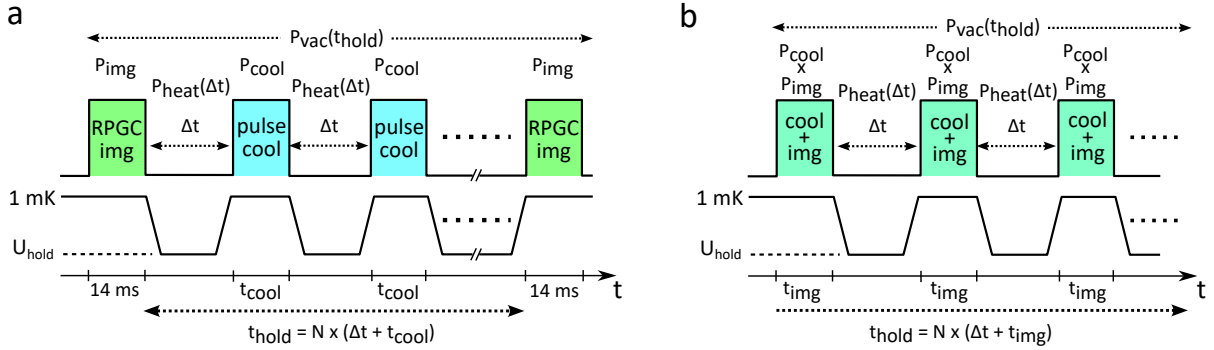


Figure 3.3: Timing sequence for single atom lifetime measurement and the associated survival probabilities of different stages during the sequence. (a) is the single shot method where the tweezer hold times varies and only two images are taken, one in the beginning and one at the end. (b) is the continuous method where the atom in the array is repeatedly imaged over time.

We can write the time dependent loss function of these two different measurement method as follows.

$$\begin{aligned}
 P_{survival}(t) &= P_{img}^2 P_{vac}(t) [P_{heat}(\Delta t) P_{cool}(t_{cool})]^N \quad \text{for single shot} \\
 P_{survival}(t) &= P_{vac}(t) [P_{img}(t_{img}) P_{heat}(\Delta t) P_{cool}(t_{img})]^N \quad \text{for continuous}
 \end{aligned} \tag{3.6}$$

Here, the first line in Eq. 3.6 is for the two-image method, where the finite imaging loss contributes to a fixed loss factor that is time-independent. The second line is for the continuous imaging case, where an image is taken at a given interval. This makes the imaging loss time-dependent. However, the exact form of the time dependence is sequence-specific, which we will discuss in Sec. 3.3.4.

3.3.1 Heating in optical tweezer

Before we can achieve a long-lived tweezer array, we need to verify whether the tweezers are introducing any unnecessary heating to the trapped atom. More heating implies more frequent cooling, which might introduce loss during the holding of the atoms. Several mechanisms can cause heating of the atom in tweezers, including intensity noise, beam pointing, and photon scattering from the tweezer light. These mechanisms all have different dependencies on trap frequency, trap depth, and power spectral density of the perturbation. Ultimately, we measured a recoil-limited heating rate, but it was not an easy task, as disentangling the various sources of heating requires careful characterization of the atom temperature under different conditions. In this section, I will briefly describe the methods we used to characterize the atom temperature and different heating mechanisms.

Recoil heating is the fundamental heating mechanism that atoms trapped in optical tweezers will experience. This is due to off-resonant photon scattering from the intense tweezer light. The heating rate is linear in time and can be defined as follows [133].

$$\alpha_{sc} = 2T_{rec} R_{sc} = 2T_{rec} \frac{\Gamma_{Rb}}{\hbar \Delta} U_{dip} \quad (3.7)$$

R_{sc} is the off-resonant scattering rate, U_{dip} is the tweezer dipole potential, T_{rec} is the recoil energy of trapping light, Δ is detuning of the trapping light with respect to ^{87}Rb D2 transition (780 nm) and $\Gamma_{Rb} = 2\pi \times 6\text{MHz}$ is the natural linewidth of ^{87}Rb . For 1 mK trap depth at 830 nm this heating rate is about $10.5 \mu\text{K/s}$.

Assuming a Boltzmann distribution of the atom energy inside the trap, with a truncation

imposed by the trap depth, the probability of an atom remaining in the trap is given by [134].

$$P_{thermal}(t, U_{esc}) = 1 - e^{-\eta(t)} \left(1 + \eta(t) + \frac{1}{2}\eta(t)^2 \right) \quad , \text{ where } \eta(t) = \frac{U_{esc}}{k_B T(t)} \quad (3.8)$$

Here $E = U_{dip}$ is the cutoff energy (trap depth) and $T(t)$ is the atom temperature as a function of time. In the absence of cooling, $T(t)$ should equal to $\alpha_{sc} t$.

As a baseline, we measure the survival of the atom without cooling. Assuming no vacuum loss, Eq. 3.8 fits the data nicely, and we extract a heating rate of $94 \mu\text{K/s}$ [Fig. 3.4] which is well above the recoil limit. This issue needs to be addressed before we can obtain an accurate measurement of the vacuum lifetime.

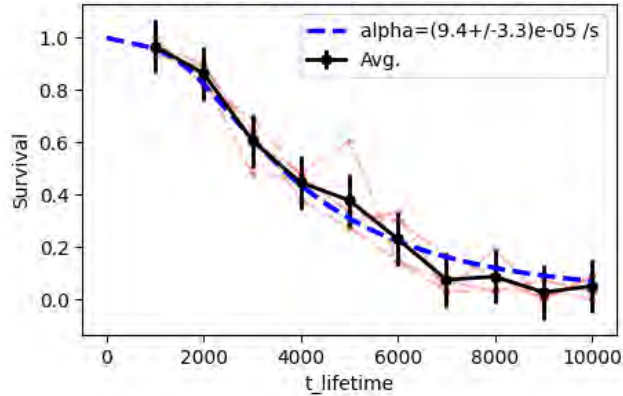


Figure 3.4: Dark tweezer lifetime without cooling. The atom survival is taken over different hold time while no cooling is applied during the wait. The trap depth is 1 mK. Fitting the data (black) to Eq. 3.8 (blue dash) we extract a $94 \mu\text{K/s}$ heating rate, which is much larger than just the recoil heating for this trap depth.

In order to measure the temperature of the atom more accurately over time, we use a release and recapture (R-R) method. Here, the trap is turned off for a variable amount of time, typically a few microseconds, then turned back on, and the atom survival is measured. The measured survival is then fitted with a curve generated by a classical trajectory Monte Carlo simulation based on the specific trapping parameters used in the experiment. This method allows us to investigate the different dependencies of the heating rate and separate different heating mechanisms.

Release and recapture Monte-Carlo simulation: Here, we describe the steps taken to

generate the R-R probability using classical trajectory Monte Carlo simulation, as described in Ref. [134, 135].

Initialization: Considering the atom inside the trap follows a Maxwell-Boltzmann distribution with temperature T , the standard deviation of position and velocity are $\Delta X = \sqrt{k_B T / m_{Rb} \omega^2}$, $\Delta v = \sqrt{k_B T / m_{Rb}}$. Then, a randomly sampled set of position and velocity $(x, y, z, v_x, v_y, v_z)_i$ can be generated.

Evolution: The trap is turned off for time t_{rr} , which gives the updated position and velocity:

$$(x + v_x t_{rr}, y + v_y t_{rr} - g t_{rr}^2 / 2, z + v_z t_{rr}, v_x, v_y, v_z)_i$$

Determine probability: After the new position is calculated, the final energy, kinetic + potential of the atom, is calculated. If the trap is perfectly harmonic, the total energy is $1/2 m v^2 + 1/2 m \omega^2 x^2$. In the case of Gaussian potential from the tweezer, assuming a harmonic trap gives an underestimation of the atom temperature because the Gaussian potential provides weaker confinement at the periphery of the trap. The difference between fitting with the Gaussian and harmonic trap is discussed in Appendix G.

If the total energy is > 0 then the atom is considered escaped. The evolution is done over a range of t_{rr} , typically with t_{rr} up to $50 \mu\text{s}$, and a survival vs t_{rr} curve can be obtained.

For most of the analysis done in this thesis, unless specified otherwise, the harmonic trap shape is used in the Monte-Carlo simulation so it can be easily compared to other literature's such as in Ref. [134, 136].

Fitting: The data can be fitted with the numerically calculated curve to minimize the least square value by varying the atom temperature T in the Monte-Carlo simulation.

The sequence for R-R consists of two atom images with the tweezer trap briefly off for t_{rr} in between, as shown in [Fig. 3.5]. Varying both t_{rr} and t_{hold} allows us to measure the heating rate of the atom inside the trap either as a function of time or sequence of interest. As an example, the temperature after our typical RPGC imaging is measured, and the best fit curve from the

Monte-Carlo simulation gives a temperature estimation of the atom around $13 \mu\text{K}$, as shown in [Fig. 3.5(b)].

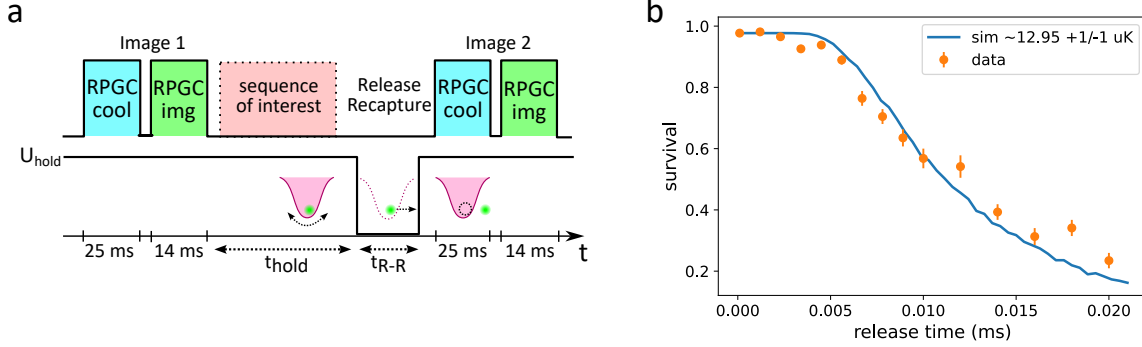


Figure 3.5: (a) Timing sequence for release and recapture measurement to measure the heating rate. The atoms are first imaged and the release and trap is briefly turned off and the atom recaptured. The second image is taken and the survival is recorded. (b) An example of the release and recapture data (circles) after the typical RPGC imaging with the best fit probability curve from the Monte-Carlo simulation (solid lines) showing an atom temperature of $13 \mu\text{K}$.

Anomalous heating due to RF Source: Initially, we observe a large heating rate that is well beyond the tweezer recoil limit. We attribute this to intensity noise caused by the intermodulation of the RF tones used to generate the tweezer array. We employed an evenly spaced 9×9 grid where the RF intermodulation perfectly overlaps with the adjacent tweezers. In this configuration, we measured a heating rate of $230 \mu\text{K/s}$ at a trap depth of 1.3 mK , whereas the recoil heating should only be $15 \mu\text{K/s}$. However, when the trap depth decreased to 0.38 mK , the heating rate dropped to $7 \mu\text{K/s}$, only twice the expected recoil heating rate of $4 \mu\text{K/s}$, even though the RF power driving the AOD did not change; only the total power from the fiber is decreased. This indicates that the process is most likely parametric heating, and as the trap depth decreases, the response of the atoms to the intensity noise at a particular frequency also shifts, resulting in a lower heating rate. To diagnose different sources of heating mechanisms, we measured the heating rate in a series of different configurations, as shown in [Fig. 3.6]. The dashed line in Fig. 3.6 represents the recoil limit, is calculated using Eq. 3.7. The tweezer recoil-limiting heating rate with a clean synthesized RF source allows us to exclude the problem originating from the laser source and focus

our efforts on the AOD and RF generator.

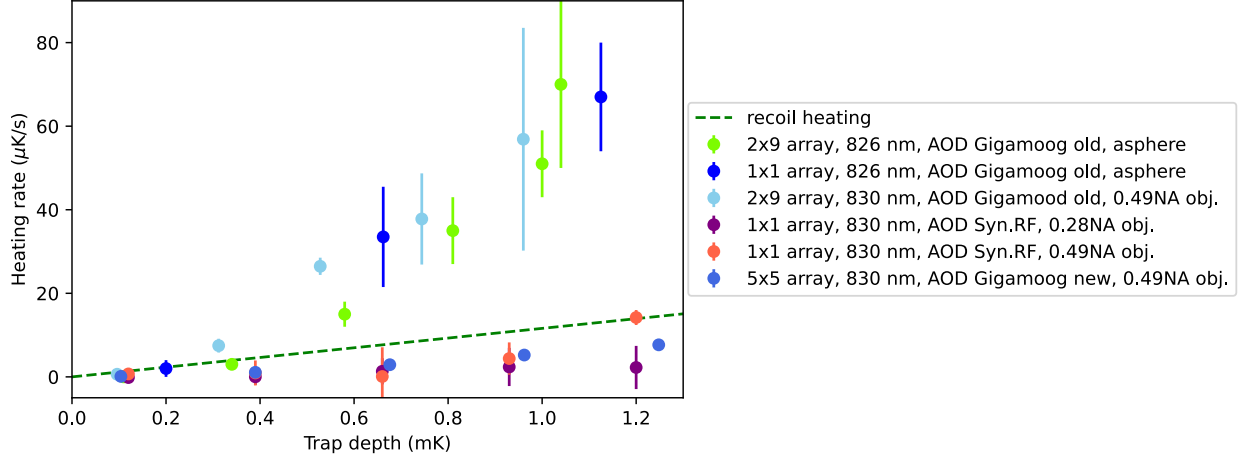


Figure 3.6: Single atom heating rate of various tweezer configuration including aspheric lens and objective, different RF source and different NA. The green dashed line is recoil limit calculated based on the tweezer configuration. The data lines below this line is recoil limited heating, means the external source is not introducing additional noise significant enough to effect the atom temperature.

To drive the tweezer AODs, we use a custom-built RF synthesizer consisting of two evaluation boards: the Xilinx KCU105 FPGA board and the Texas Instruments DAC39J84 4-channel 16-bit DAC. This system is capable of synthesizing up to 56 RF tones in real-time with the ability to change frequency, phase, and amplitude for rearrangement. The DAC is running at 614.4 MSPS, and the output frequency is in the first Nyquist zone up to 307.2 MHz. This means that the modulation bandwidth equals the baseband sample rate of 614.4 MHz, which is sufficient for the bandwidth requirement of rearrangement.

During our investigation, we found that even when the RF tones appear good on the spectrum analyzer ($> 60\text{dB}$ SFDR), there are still complicated dynamics that can arise due to nonlinearity in the AOD and the RF source. Primarily, there are time-dependent power fluctuations where the total RF power remains unchanged, but the individual tones fluctuate in a complementary manner. This is a subtle effect since our intensity servo only monitors the total power of the array and corrects for any intensity fluctuations, remaining oblivious to individual tweezer intensity fluctuations. Even worse, due to the way the RF tones interact, the total power can remain the same, but only the

ratio of power to the individual tweezers differs. To observe this effect in detail, one would need to construct a spatial filter to select the intensity of only one tweezer and measure it. This aspect is not studied in detail in this thesis.

The specific configuration that gives a very low intermodulation depends strongly on the type of RF source and the technique used to generate the signals. Eventually, an RF frequency configuration specific to our custom-built RF generator (Gigamoog) was found that can provide a low heating rate, and our AOD tweezer can operate at the recoil heating limit [(5x5 array, 830 nm, AOD Gigamoog new) in Fig. 3.6]. For a detailed discussion of the RF dynamics of the Gigamoog RF synthesizer and construction, please refer to Zhenpu Zhang's thesis.

Laser intensity noise: Another heating mechanism is parametric heating from the laser intensity fluctuation. The atom in the tweezer with sufficiently cold temperature is trapped at the bottom of the Gaussian trap which can be approximate as an a quantum harmonic oscillator. Changes in laser intensity, $\epsilon(t) = (I(t) - I_0)/I_0$, introduces small fluctuations in the spring constant of this harmonic trap. The perturbed part of this Hamiltonian can be written as follows [137].

$$H'(t) = \frac{1}{2}\epsilon(t)M_{Rb}2\pi\nu^2x^2 \quad (3.9)$$

Calculating the transition probability up the harmonic oscillator energy levels as a function on single sided power spectrum of $\epsilon(t)$ the energy increase of the atom can be derived. Follow the derivation in Ref. [137], the frequency dependent atom heating rate as a function of intensity noise power spectrum has the following relationship.

$$\langle \dot{E} \rangle = \pi^2 \nu^2 S_k(2\nu) \langle E \rangle \quad (3.10)$$

ν represents the trap frequency, and $S_k(2\nu)$ is the single-sided power spectral density of the laser intensity. From the equation, we see that the rate of energy increase is proportional to the initial temperature and the square of the trap frequency. The factor of 2 relationship between the trap frequency and PSD indicates that with the parametric heating process, fluctuations of the trap depth at frequency 2ν will heat the atom at the trap frequency of ν .

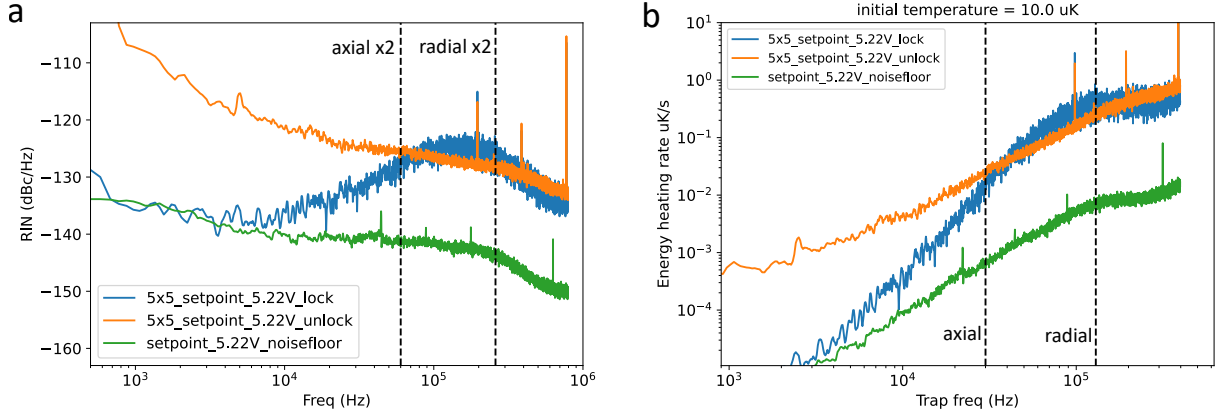


Figure 3.7: (a) Single sideband noise spectrum of tweezer RIN noise. Green is the noise floor of the measurement setup. Orange (Blue) is with (without) the intensity servo engaged. With the intensity servo engaged, the low frequency noise is suppressed and small amount of noise is added around 100 kHz. (b) Heating rate of the tweezer based on the RIN measured in (a). This is calculated using the parametric heating Eq. 3.10 and the initial atom temperature around $10 \mu\text{K}$ which is typically what we have after cooling.

To rule out the possibility of heating due to laser intensity noise, we measure the tweezer relative intensity noise spectrum (RIN) and calculate the heating rate. The tweezer RIN is measured in the final telescope just before entering the vacuum chamber, as shown in [Fig. 3.7(a)]. A significant difference is observed between the locked [blue in Fig. 3.7(a)] and unlocked [orange in Fig. 3.7(a)] intensities. We notice a slight servo bump around 200 kHz, which is near the $2 \times \nu_{\text{radial}}$ of the tweezer [black dashed lines in Fig. 3.7(a)]. The intensity servo suppresses the low-frequency noise almost to the noise floor of the measurement setup without introducing significant noise in the high-frequency part of the noise spectrum. To ensure that the heating rate is acceptable, we calculate the heating rate with an initial atom temperature of $10 \mu\text{K}$ as measured in Fig. 3.5(b), using Eq. 3.10 and [Fig. 3.7(a)]. The resulting heating rate [Fig. 3.7(b)] is much lower than $1 \mu\text{K/s}$ (and also much lower than the recoil limit), verifying that the laser intensity noise from the tweezer source is not a limiting factor in our tweezer trap.

Heating from fluctuation of trap center: Mechanical vibration of the objective will cause the shaking of the tweezer trap with respect to gravity. Imaging shaking a bowl with a ball

inside at the rate where the ball oscillate back and forth. Excessive perturbation of the trap center will cause the atom to heat up. The frequency dependence of this heating is given by [137]

$$\langle \dot{E} \rangle = 4 \pi^4 m_{Rb} \nu^4 S_k(\nu) \quad (3.11)$$

This heating rate $\langle \dot{E} \rangle$ remains constant over atom energies and lacks the factor of 2 in frequency dependence compared to parametric heating. We can observe this (or rather the lack of it) by holding the atom and measuring the temperature as a function of hold time. If the heating is parametric, the energy would increase exponentially; if it's due to shaking of the trap, it would increase linearly. We see a linear increase in energy that closely follows the recoil limit [(the purple, 1x1 0.49 NA obj. dataset) in Fig. 3.6].

To further verify that the shaking of the trap center due to mechanical vibration is not a concern, we conducted heating rate measurements with different tweezer numerical apertures by adjusting the input beam aperture [(1x1 0.28 NA obj. and 1x1 0.49 NA obj.) in Fig. 3.6]. This alters the trap frequency without changing the trap depth. The results show that in both numerical aperture settings, the heating rates are recoil-limited. Combining this with measurements of different trap depths in the given configuration, we can infer that over a broad range of trap frequencies, we do not have intensity noise or vibration of the tweezer causing heating to a level comparable to the recoil heating from the tweezer light.

3.3.2 Cooling loss

Since the recoil heating is always present as long as the optical tweezer is turned on, cooling the atom from time to time is necessary to achieve long trapping lifetime. In the absence of cooling, the recoil heating from the trap light reduces the lifetime to less than 100 seconds [58,59]. We can also infer this with Eq. 3.8 and by scaling the heating rate in (Fig. 3.4) to $9 \mu\text{K/s}$. This decay rate is significantly faster than the expected vacuum-limited lifetime, indicating that cooling during the holding of the atom is necessary. To establish an optimal cooling duty cycle, we need to understand the loss and final temperature associated with the cooling.

Firstly, we determine the saturation time for cooling to take effect by varying the cooling pulse length and measuring the survival at a fixed R-R time. It is generally preferable to choose an R-R time such that the survival rate is 0.5, maximizing sensitivity to atom temperature changes. From the measurements in [Fig. 3.5(b)], we can select an R-R time of $10 \mu\text{s}$ for a final temperature of $15 \mu\text{K}$.

Once the R-R time is established, a cooling pulse length needs to be chosen. Fixing at the 50% survival R-R time and varying the cooling pulse length, we observe saturation of cooling temperature in 10 ms, as shown in [Fig. 3.8(a)]. Therefore, choosing a standard cooling pulse length of 25 ms provides some margin, in case the saturation time varies during optimization.

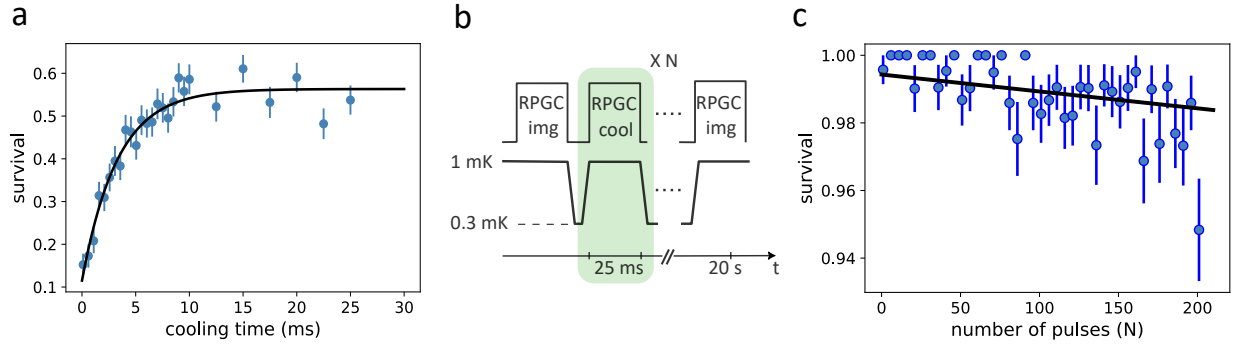


Figure 3.8: (a) Setting the R-R time to give 50% survival at nominal atom temperature we scan the cooling pulse duration. The temperature reaches equilibrium after 10 ms so we set the cooling pulse length for 25 ms to be conservative. (b) Timing sequence for the cooling loss measurement. The total sequence time is fixed, to eliminate the fluctuation in vacuum loss, and the number of cooling pulses are varied and the survival is recorded. (c) Measured atom survival vs number of 25 ms cooling pulses. Fitting a line to the survival extract a cooling loss of $5(4) \times 10^{-5}$ per 25 ms pulse or $2(1.6) \times 10^{-3} \text{ s}^{-1}$

After determining the cooling pulse length, we choose a cooling laser detuning of -60 MHz red-detuned from free space resonance (-90 MHz in a 1 mK deep trap), and the repump laser is tuned to in-trap resonance. We then optimize the cooling and repump power. The final cooling and repump intensities are $82 I_{\text{sat}}$ and $0.04 I_{\text{sat}}$ respectively, where $I_{\text{sat}} = 3.576 \text{ mW/cm}^2$.

To measure the cooling loss, we follow the procedure in [Fig. 3.8(b)], where the atom is held for a constant time of 20 seconds between two PGC images, and a variable number of cooling pulses

(shaded green box) are repeated during the 20 second hold time. The constant hold time ensures that the atom loss due to vacuum does not change from different number of cooling pulses. By fitting a line to the survival versus the number of cooling pulses [Fig. 3.8(c)] we can extract the slope, which gives a cooling loss of $5(4) \times 10^{-5}$ per 25 ms pulse or $2(1.6) \times 10^{-3} \text{ s}^{-1}$.

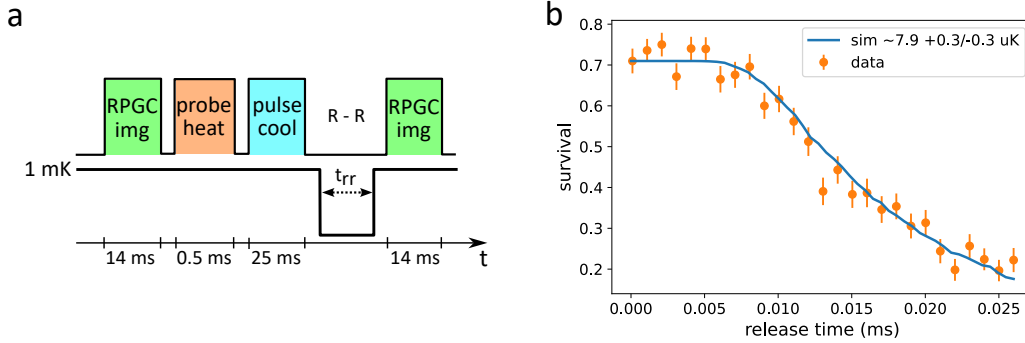


Figure 3.9: (a) Timing diagram for measuring the atom temperature after pulse cooling. The atoms are heated with a resonance beam and a cooling pulse is applied and R-R sequence is used to measure the temperature. (b) The resulting release and recapture data with Monte-Carlo temperature fit gives atom temperature of $7.9 \pm 0.3 \mu\text{K}$.

To verify that the cooling is at its optimal, we also measure the atom temperature after one cooling pulse [Fig. 3.9(b)] using the R-R technique described in Sec. 3.3.1. To prepare the atom with a higher temperature, we applied a short (0.5 ms) heating pulse after the first PGC image [Fig. 3.9(a)] to raise the atom's temperature to about $100 \mu\text{K}$. Then, a single 25 ms cooling pulse is applied, followed by an R-R sequence and a second atom image. This gives an atom temperature of $7.9 \pm 0.3 \mu\text{K}$, indicating that the pulse cooling is effective.

3.3.3 Imaging loss

In general, imaging loss is an important parameter since it directly impacts measurement fidelity, especially if one wishes to use trapped atoms as qubits. Poor imaging fidelity will also limit the success rate of forming a large atom array due to losses after rearrangement moves are performed. This is non-deterministic because every time an observation is made, an atom is possibly lost. Since the last step of rearrangement is always imaging, this loss is a fundamental limitation

for rearrangement fidelity. Furthermore, in our application where the lifetime is measured with repeated imaging, a large imaging loss can affect the apparent vacuum-limited lifetime. Therefore, careful characterization of imaging loss is necessary.

To find the imaging loss, one would need to determine an optimal imaging time so that the collected signal is large enough for good imaging fidelity. We typically use 14 ms in our red PGC imaging. This imaging time is similar to what others have used [35, 118, 138] and perhaps on the shorter side compared to the typical value ($\sim 30\text{-}50$ ms). In another case where a very low imaging loss was reported [43], 80 ms imaging time is used which is almost twice as long as typical. Now we need to determine the optimal imaging detuning and intensity where the photon count histograms are well separated from the camera noise. Taking into account the light shift from the trap ($0.8 \text{ mK} \times 28.8 \text{ MHz/mK} = 23 \text{ MHz}$), we use the Imaging 2 parameter in table 3.1. This parameter is chosen based on the balance of three factors: collected photon number, heating (loss) during imaging, and imaging fidelity.

Determining imaging fidelity: Before investigating the imaging loss, a method of determining the imaging fidelity needs to be established. It is important for the imaging infidelity to be lower than the quantity of interest to be measured. The imaging fidelity we used follows the same definition as others in optical tweezer experiments: $1 - P_{\text{false}}$, where P_{false} is the probability of false detection. False detection probability is where an atom in the tweezer is mistakenly identified as present (1-atom) while in reality it is non-present (0-atom) and vice versa.

To calculate the imaging fidelity, a number of atom array images are taken, then the images are averaged [Fig. 3.10(a)]. After averaging, each tweezer site is analyzed as follows.

- From the averaged atom image of each tweezer [Fig. 3.10(a)] three or four brightest pixels are chosen and turned into a binary mask, example shown in [Fig. 3.10(c)]. The variable number of pixels in the mask (3 or 4) is due to the possibility of the atom signal aligning between pixels on the camera. To determine whether 3 or 4 pixels are needed in each mask, the total photon count between the two cases is compared using the averaged atom image.

If the difference is larger than 5%, the configuration with more signal is used.

- The binary mask with chosen pixels is applied to each atom image (not the averaged image), and the counts on those pixels are summed. Then, these photon counts from each image are binned into a histogram [Fig. 3.10(d)].
- The 0-atom distribution and 1-atom distribution in the histogram are fitted with Gaussian functions [orange line in Fig. 3.10(d)]. We choose Gaussian instead of Poissonian because, taking into account the camera noise, the distribution is a convolution of Poissonian and Gaussian. In our case, the Gaussian standard deviation is larger than the Poissonian, thus Gaussian fits better.
- The amplitude of the fitted Gaussians is normalized, and a threshold is determined [dashed line in Fig. 3.10(d)] by minimizing the region of the two Gaussians cut off by the threshold.
- The imaging fidelity is then determined by finding the area of the Gaussian outside of the threshold and taking the ratio of this area to the total area of the Gaussian.

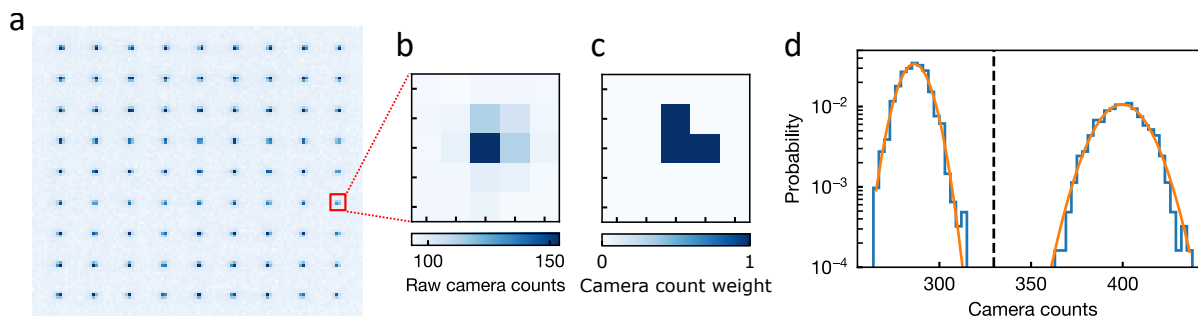


Figure 3.10: (a) CCD image of an averaged 9x9 atom array. (b) Zoom in to a single tweezer image to extract the three brightest pixels. (c) The mask applied to select the three brightest pixel in the single tweezer image and the counts on those pixels are summed together. (d) The histogram of the count vs. instances after the mask is applied and the camera photo-electron count are summed together. Gaussian functions are fitted to the histograms and a threshold is determined by minimizing the overlap of the Gaussian tail. Dashed vertical line is the threshold to determine whether or not single atom is detected. The fidelity of the imaging is determined by the area of the Gaussian below the line.

There are a few different methods other than the binary mask can be used to calculate imaging fidelity including, PSF weighted mask [95] and model-free approach [40, 43]. The PSF weighted mask uses a pixel mask where the weight of the individual pixel is calculated according to the integrated area of the tweezer PSF under each pixel, in other word, the PSF intensity is coarsely sampled by the camera pixel.

For completeness, we compare the binary pixel mask with the PFS weighted pixel mask extracted from PSF fitted to the averaged atom image. There are small differences in total photons collected, which is expected since the PFS weighted mask takes all photons into account. However, in our configuration where photons are mostly in 3 or 4 pixels, we did not observe a significant difference in infidelity between the two methods, and they are all below the imaging loss we measured.

The model-free analysis of imaging fidelity, similar to the one used in Ref. [40, 43], takes into account all the losses during imaging without any presumed distribution of photon counting statistics. This method of estimating the imaging fidelity uses 3 atom images taken in sequence without reloading of the tweezer. The measured probability of detecting an atom in each image is determined by a combination of factors: L losses during imaging, F0 fidelity for successfully detecting zero atoms, F1 fidelity for successfully detecting one atom, and iF0 and iF1, which represent their respective infidelities. Due to the causality of the sequential atom images, each image consists of a combination of these losses and fidelities. Taking many trials of the 3 image sequence, a series of probability can be measured and associated with their respected combination of losses and fidelities. By solving the set of these linear equations with the measured probabilities, L, F0 and F1 can be extracted. One draw back to this method is the extracted fidelity is only as good as the total number of trials of the 3 atom images. Therefore to measure 10^{-5} level of infidelity, one would need at least 10^5 trials or better to reach the error bar that is necessary for the measurement. In this case we do not have enough statistics to resolve losses and fidelities below 10^{-4} with sufficient error bar using the model-free method. We can only bound the loss to be as good as the value we measured.

In the end we choose to use the binary mask method for most of our analysis since it requires the least amount of data processing overhead and less atom image statistics with only small difference in fidelity estimation that is sufficient for the level of loss we measured. For detail comparison of PSF pixel mask and model-free method with the binary mask method please refer to Zhenpu Zheng's thesis.

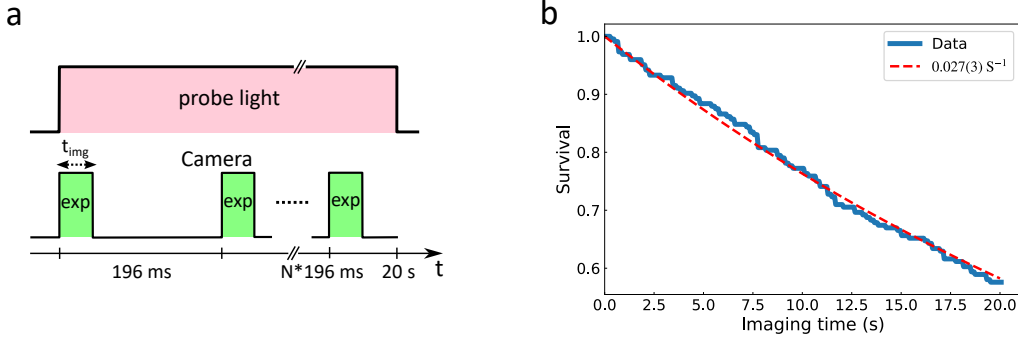


Figure 3.11: (a) Timing diagram for measuring the single atom imaging loss. The imaging light is turned on for 20 seconds and every 196 ms the camera is triggered to expose for $t_{\text{img}} = 14 \text{ ms}$ and the atom survival is recorded. (b) Atom loss vs imaging light duration. Red dash is exponential decay of $0.027(3) \text{ s}^{-1}$ or $3.8(4) \times 10^{-4}$ per image loss rate. This time constant is not obtained from the fit shown in the plot. It is from the MLE estimation using the data.

After determining good imaging parameters, the imaging loss is assessed by exposing the atom to the imaging light for a long duration (20 seconds, equivalent to 1428 images) [Fig. 3.11(a)]. The camera is triggered every 196 ms (equivalent to every 14 images) for 14 ms, and a series of 102 images is captured. The survival of the subsequent images is determined by comparing them to the very first image [Fig. 3.11(b)]. Using a maximum likelihood estimation (MLE), we extract the effective imaging loss rate of $0.027(3) \text{ s}^{-1}$ or $3.8(4) \times 10^{-4}$ per 14 ms image. This rate is among the lowest observed in optical tweezer experiments [40, 43, 138]. The red dashed line in [Fig. 3.11(b)] represents an exponential decay with the loss rate extracted by MLE method, to guide the eye.

3.3.4 Pulsed cooling

Since we know that the vacuum-limited lifetime is much longer than the recoil heating-limited lifetime, the atom must be cooled while held in the trap. In the previous sections, the cooling and imaging losses were determined to be very low. However, from Sec. 3.3.2, we know that with continuous PGC cooling, the cooling-limited lifetime is around $\tau_{\text{cool}} = 500$ s. This is significantly lower than the expected vacuum-limited lifetime. Therefore, we need to determine the optimal cooling interval for the range of vacuum lifetimes that we expect to measure. We can write the probability versus time that corresponds to our measurement sequence, [Fig. 3.12(a)], as follows.

$$P_{\text{survival}}(N * dt + t) = P_{\text{vac}}(N * dt + t) \times (P_{\text{thermal}}(dt) \times P_{\text{cool\&img}})^N \quad (3.12)$$

N is integer of total cooling and imaging pulse applied. dt is the interval between pulses and $t < dt$ is the remainder that is shorter than the pulse interval. P_{vac} is the vacuum loss that does not depend on the cooling and imaging pulses. $P_{\text{thermal}}(dt)$, defined in Eq 3.8 is the atom survival due to recoil heating of the tweezer while the cooling beam is off. $P_{\text{cool\&img}}$ is the cooling pulse where the scattering is intentionally made stronger so the atom can also be imaged during cooling. The imaging parameter is (Cooling 2 in table 3.1) and the loss is measured using method in Sec. 3.3.3.

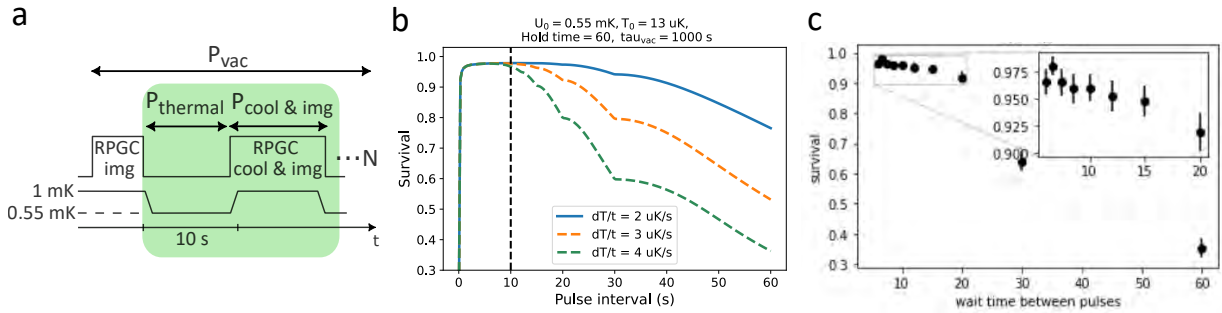


Figure 3.12: (a) Timing diagram of the pulse cooling and imaging used for atom lifetime measurement. (b) Probability vs cooling pulse interval showing an optimal range (where the survival is close to unity) of interval for each vacuum lifetime based on Eq. 3.12. (c) Measurement of survival vs pulse interval at a fix hold time of 60 seconds to determine the optimal cooling interval. Here we choose one cooling pulse every 10 seconds.

Plotting Eq. 3.12 against the pulse interval, we can see there is a range of dt where the survival is optimized [Fig. 3.12(b)]. The behavior at short dt is dominated by the losses from cooling and imaging applied too frequently, where $P_{cool\&img}$ becomes small. The loss at large dt is dominated by high atom temperature due to recoil heating, causing $P_{thermal}(Ndt)$ to be small. The optimal range for dt is where the $(P_{thermal}(Ndt) \times P_{cool\&img}) \ll P_{vac}(t)$. To find the value of dt experimentally, we take a set of data corresponds to the sequence shown in [Fig. 3.12(a)] while keeping the total hold time constant and only vary dt and N . The result, [Fig. 3.12(c)], shows similar behavior as predicted in Eq. 3.12, where at pulse cooling interval < 1 second, the survival is low, and intervals larger than 20 seconds, the survival is low as well. With wait time between 5-20 seconds, the survival remains high, [inset of Fig. 3.12(c)]. Therefore, we decide that $dt = 10$ s seems to be a nice middle ground, and that is the parameter we use for the lifetime measurement.

3.3.5 Vacuum-limited single atom lifetime

Now that we have carefully characterized all the losses that can affect the long vacuum lifetime measurement, we can measure the single atom lifetime and extract the vacuum-limited loss using the sequence shown in [Fig. 3.12(a)]. To estimate the effect of cooling and imaging on the atom lifetime, we use the loss measured in Sec. 3.3.2, where the following cooling/imaging parameter is used (Cooling 2 in table 3.1) with an interval between cooling set to 10 seconds. The effective decay time constant solely from this cooling+imaging loss is $\tau_{img} = (1/0.027) \times 10 = 37000$ s, which is much larger than the expected vacuum lifetime and shouldn't be limiting our lifetime measurement.

To better understand the relationship between the measured lifetime (τ_{eff}) with respect to the cooling pulse interval (dt) and heating rate, we calculate τ_{eff} as a function of dt and heating rate using Eq. 3.12. First, the atom survival vs time is calculated for a given heating rate and dt . Then an exponential decay function $a \times \text{Exp}(-t/\tau_{eff})$ is fitted to the calculated time trace using different parameters, and an effective lifetime τ_{eff} is extracted [Fig 3.13(a)]. All other parameters are fixed to the values we used in the lifetime measurement.

The result from [Fig 3.13(a)] shows that at $dt = 10$ s with small variation in heating rate, the

perceived τ_{eff} can change dramatically between 56% to 91% of τ_{vac} . Although the $dt = 10$ s seems to be a reasonable choice, it is possible that this cooling interval is not frequent enough depending on the heating rate. This dependence between τ_{vac} and τ_{eff} was not easily observed in the cooling duty cycle measurement in [Fig. 3.12(b and c)], which we used to determine $dt = 10$ s.

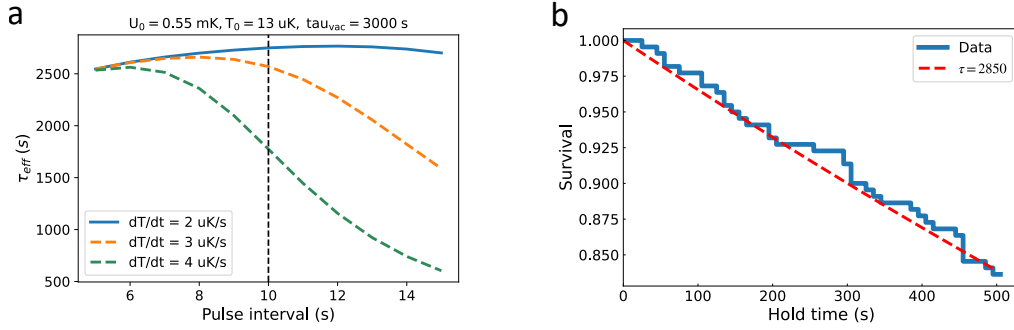


Figure 3.13: (a) Plotting the effective lifetime τ_{eff} as a function of cooling interval. under different dark tweezer heating rate. We see a strong dependence of the τ_{eff} when the heating rate is only changed slightly. (b) Single atom vacuum limited lifetime using the sequence shown in [Fig. 3.12(a)]. We measure $\tau_{\text{eff}} = 2800$ s using the MLE method to extract the time constant. The red dashed line is, again, to guide the eye.

Finally, we carry out the single atom lifetime measurement in optical tweezer in a cryogenic environment with pulse cooling+imaging every 10 seconds and a total hold time in the tweezer of up to 500 seconds [Fig. 3.12(a)]. The 500-second hold time is mainly limited by the sequence length limit of the experiment control system. Figure 3.13(b) shows the measured atom survival versus time for up to 500 seconds. The errors are correlated between each image, so the τ_{eff} of the array is determined with the MLE method, and the data is plotted without error bars. We measured a $\tau_{\text{eff}} = 2825_{-432}^{+502}$ s, and the red dashed line represents an exponential curve of $\tau_{\text{eff}} = 2850$ s to guide the eye. With the bound we get from [Fig. 3.13(a)] and $dt = 10$ seconds, we can set a lower bound on our vacuum-limited lifetime (τ_{vac}) to be at least on the order of 3000 seconds.

Type	Cooling Detuning	Cooling Intensity	Repump Detuning	Repump Intensity	Loss
Cooling 1	-90 MHz in-trap	82 I_{sat}	0 MHz in-trap	0.04 I_{sat}	$2(1.6) \times 10^{-3} \text{ s}^{-1}$ $5(4) \times 10^{-5} / \text{pulse}$
Cooling 2	-90 MHz in-trap	71 I_{sat}	0 MHz in-trap	0.3 I_{sat}	$1.2(4) \times 10^{-2} \text{ s}^{-1}$ $3.0(7) \times 10^{-4} / \text{pulse}$
Imaging 1	-88 MHz in-trap	35 I_{sat}	0 MHz in-trap	2 I_{sat}	$2.7(3) \times 10^{-2} \text{ s}^{-1}$ $3.8(4) \times 10^{-4} / \text{img}$
Imaging 2	-68 MHz in-trap	17 I_{sat}	0 MHz in-trap	1 I_{sat}	$2.0(2) \times 10^{-2} \text{ s}^{-1}$ $2.9(4) \times 10^{-4} / \text{img}$

Table 3.1: Single atom cooling and detection parameters

3.4 Tweezer FoV atom characterization

One of the most important aspect to achieve large atom array is the FoV of the objective. During the design and construction of the cryogenic tweezer array, a lot of care is taken to ensure the alignment and aberration from the coldbox is under control over the temperature range from 100 K down to 45 K. However, the ultimate test of the optical performance is done using atom trapped in the optical tweezer with the system at operating temperature. While SLM is a very useful tool to eliminate aberration from the optical systems. It is often very difficult to compensate if the aberration is not common mode across the array. For example, compensating severe coma and field curvature that only exist on the edge of the FoV is proven to be a difficult task [59,127]. Since the only reliable metric is the effective NA seen by the atom, the optimization of higher order aberration correction is increasingly difficult. These field related aberration, if left uncorrected not only impact the uniformity of the trap, but also effect the fidelity of moving and detecting of the single atoms [127]. Therefore, having a good starting point of the optical system alleviate a lot of these complicated optimization problem for the SLM.

3.4.1 NA measurement

To characterize the performance of the objective over the FOV, we generated an array of 5x5 grids spanning over the $125\ \mu\text{m} \times 125\ \mu\text{m}$ square on the tweezer plane. By measuring the trap depth and frequency of the tweezers, the effective tweezer focus waist seen by the atom, thus NA, can be extracted. To measure the trap depth U_0 , a resonance heating beam is used to drive the (^{87}Rb , D2, $F = 2 \rightarrow 3$) resonance. This resonance drive heats the atoms out of the trap, and the loss versus heating beam detuning is recorded. Figure 3.14(a) shows the measurement sequence. Due to the AC-Stark shift from the trapping light, the resonance shift U_0 is 28.8 MHz/mK. By probing the in-trap resonance and comparing it to the free-space resonances, the trap depth can be measured [Fig. 3.14(b)].

The trap frequency ν_{trap} is measured with parametric heating by applying a sinusoidal modu-

lation to the intensity of the trap that is 5 – 10% of the trap depth for about 50-100 ms [Fig. 3.14(a)]. We discussed the process of parametric heating in Sec. 3.3.1, and according to Eq. 3.10, we expect to see heating at $2\nu_{\text{trap}}$. By scanning over the modulation frequency and measuring the atom survival, we find significant atom loss at $2\nu_{\text{trap}}$ [Fig. 3.14(c)].

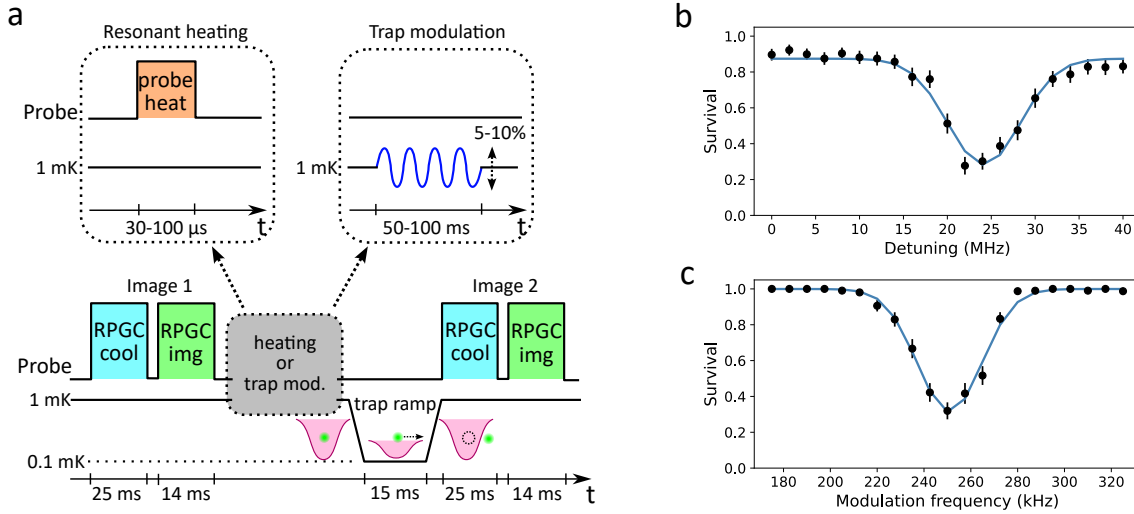


Figure 3.14: (a) Experiment timing sequence used for trap depth and trap frequency measurements. (b) Typical trap depth data measuring atom survival over heating/kick out beam resonance. The dip, shifting from zero detuning allows us to extract the trap depth with a conversion of 28.8 MHz/mK (c) Typical trap frequency measurement at 0.827 mK shows atom loss at the modulation frequency twice the trap frequency.

After measuring the trap depth and trap frequency of each individual trap across the FoV, we can determine the waist and NA using the following equation [115].

$$w_0 = \frac{1}{2\pi} \sqrt{\frac{4k_B U_0}{m_{\text{Rb}}}} \frac{1}{\nu_{\text{trap}}} \quad \text{and,} \quad \text{NA} = 0.427 \frac{\lambda_{\text{trap}}}{w_0}, \quad U_0: \text{ in Kelvin} \quad (3.13)$$

Plotting the NA of each tweezer at the corresponding location over the FoV of the objective focal plane shows the distribution of the NA [Fig. 3.15(a)]. We observe that at one corner of the FoV, the NA is slightly lower by 0.02, which is only less than 5% difference from the center, and therefore does not pose significant impact on the trapping performance. Taking the average of the data from the measurement [Fig. 3.15(b)] demonstrates, on average, diffraction-limited performance of the objective up to NA=0.48 with a standard deviation of 0.01, which aligns well with the optical

characterization conducted in Sec. 2.3.3. It's worth noting that the $125\ \mu\text{m} \times 125\ \mu\text{m}$ FoV here is limited by the AOD scan angle, and in theory, the objective can achieve a $225\ \mu\text{m} \times 225\ \mu\text{m}$ FoV with the SLM setup, over four times as large.

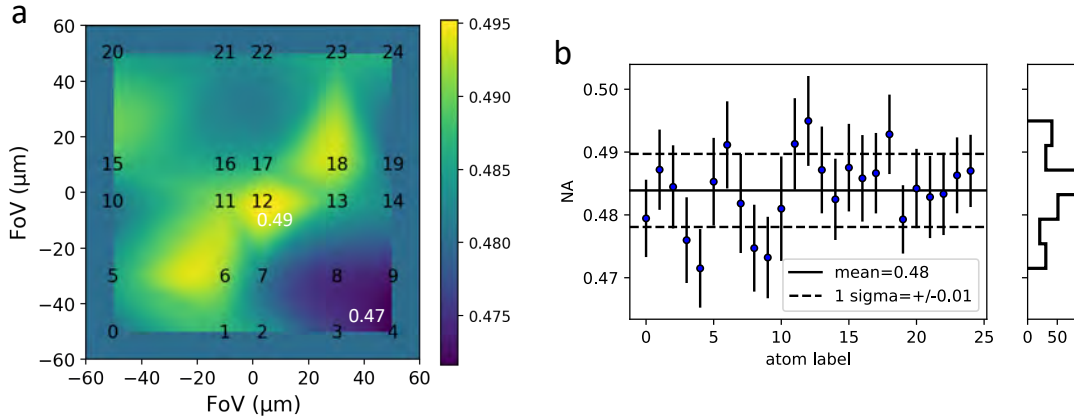


Figure 3.15: (a) Plotting NA over the $125\ \mu\text{m} \times 125\ \mu\text{m}$ FoV of the tweezer. This shows that our tweezer is relatively diffraction limited over the FoV. (b) The distribution of the NA over the field of view showing an average NA of 0.48 and standard deviation of 0.01. The number in x axis corresponds to the the tweezer location in (a).

3.4.2 LGM loading

In the typical optical tweezer array experiment, the probability of loading single atom into the optical tweezer is typically around 60%. This is due to nearly equal probability of initially loading even and odd number of atoms into the trap and after light-assisted collisions, this probability is projected into parity 0 and 1 atom remaining in the trap. The LGM loading described in Ref. [84] is a useful tool to overcome this barrier. In the application of creating a large array, higher initial loading probability can significantly reduce the rearrangement step required to assemble a defect-free array. It has been demonstrated that in single tweezer, loading rate as high as 90% can be achieved and for a larger 10×10 array loading rate can be as high as 80% [84] and 92.7% [95]. In this section we demonstrate efficient LGM enhanced loading across the $100\ \mu\text{m}^2$ FoV.

In the typical red PGC loading, when an atom is excited to a excited state of $5P_{3/2}$ from the

^{87}Rb D2 transition it can form a molecule with another $5S_{1/2}$ atom in the trap. This molecular potential is attractive and the atom moves closer to each other. When an atom emit an photon and decays, this potential no longer exist and the extra energy gain kicks both atom out of the trap, losing two atoms at a time [red solid and dash transitions in Fig. 3.16]. At the end, depends on the initial atom number in the tweezer, even or odd, 0 or 1 atoms remains. Therefore, the single atom loading probability equals to the initial probability of loading even or odd number of atoms in the trap which is around 50-60%.

In the case of LGM, the cooling light cycles through the ^{87}Rb D1 transition and is blue detuned. The resulting molecular potential between $5P_{1/2}$ and $5S_{1/2}$ is repulsive [blue solid and dashed transitions in Fig. 3.16]. Thus when the atom decays it doesn't have enough energy to kick both atom out of the trap and only one atom is lost. This results in the final atom number independent of the initial atom number in the trap. Thus achieving single atom loading probability greater than 90%

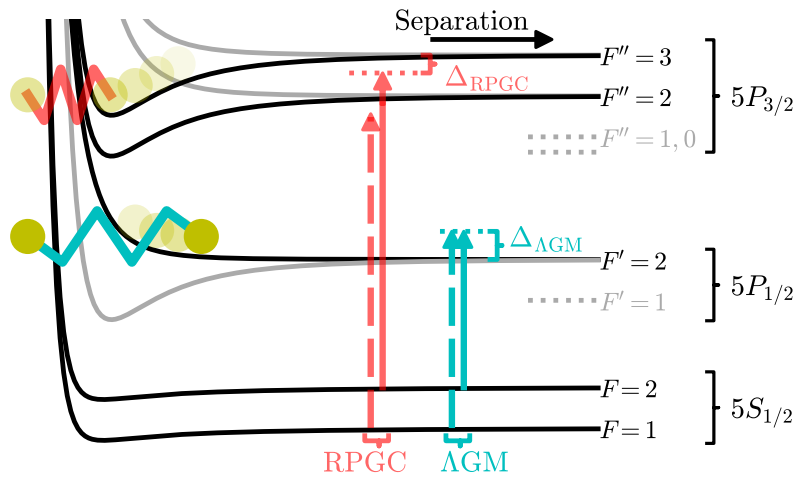


Figure 3.16: Illustration of LGM molecular potential verses typical red PGC potential. The red detuned coolign light creates bound state that ejects atoms in pairs during light assisted collisions. Causing the initial even or odd atom number in the trap to be projected into 0 or 1 remaining in the trap after cooling. The blue detuned cooling from the LGM only ejects one atom at a time thus only one atom remains after cooling independent of initial atom number. [84]

Typically LGM light assisted collision process is slower comparing to the RPGC light assisted

collision process. Therefore, to really maximize the loading rate in the order of 90%, the bias magnetic fields needs to be carefully compensated. The dynamic bias field adjustment is critical for the LGM to work over the whole cooling time. Due to the strong eddy current being generated by the copper parts at cryogenic temperature, the time constant for the eddy current to decay are in the order of 10's to 100 ms depends on the direction of the applied field. To compensate the change in bias field over time, we adjust the bias coil current every 40 ms over the 200 ms cooling time. We perform a 2D scan of the loading rate as a function of bias field over different times and find the optimal field setting for each time step [Fig. 3.17(a)]. If we plot the optimized field versus time, we can see the magnetic field decay that resemble an exponential decay due to eddy current [Fig. 3.17(b)]. A more detailed magnetic field switching behavior of the coldbox is measured in Sec. 4.3 using the magnetic field dependent microwave transition.

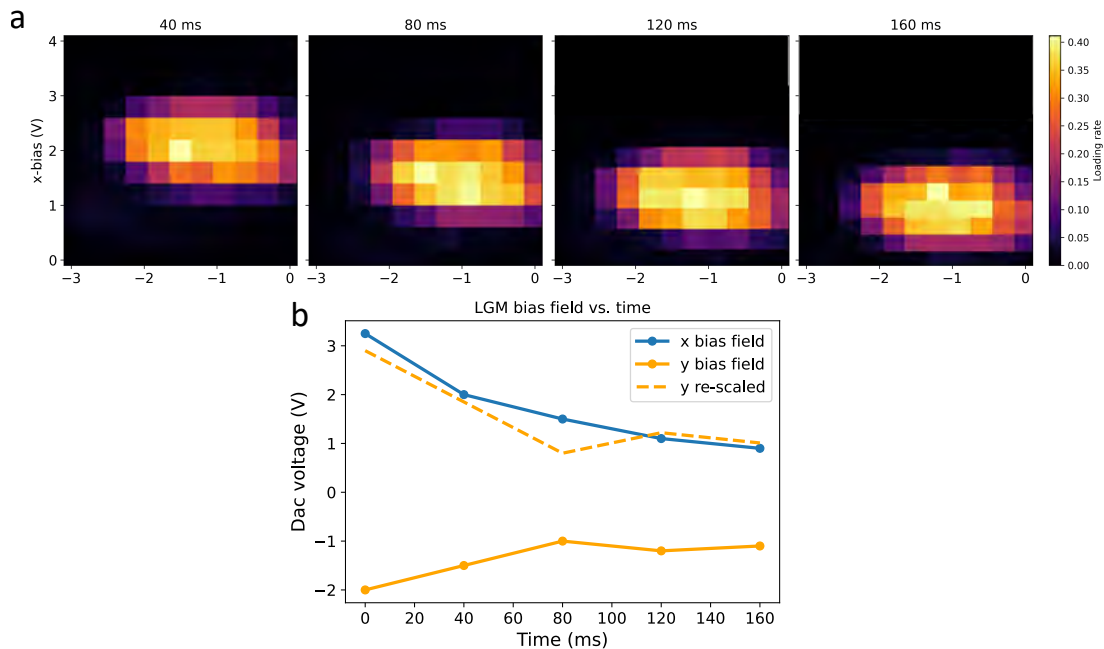


Figure 3.17: (a) LGM loading efficiency vs bias field scan at different times. We see the area of maximum loading shift as the bias magnetic fields settles due to decay in eddy current. (b) Plotting the x-bias and y-bias field as a function of time showing the decay of the eddy current. The blue trace is x-bias field, the orange trace is y-bias field and the orange dash is y-bias field but re-scaled to better compare it to the x-bias field. The more precise dynamics of the time constant for the cold box is measured in Sec. 4.3.

To verify that the tweezer is uniform enough to provide good loading across the full FoV. We perform a loading rate scan as a function of LGM 2-photon detuning (from ^{87}Rb , D1, $F = 2 \rightarrow 2'$) and the trap depth [Fig. 3.18(a)]. The region of maximum loading are nearly identical across the array, meaning good trap balancing and homogeneity across the FoV. Average the loading rate over all tweezers, we can obtain a loading rate plot where the maximum array loading can be identified [Fig. 3.18(b)]. At the end we choose to operate at the detuning and depth identified by the red star in [Fig. 3.18(b)]. Plotting the loading rate across the tweezer index [Fig. 3.18(c)] shows on average of 83% single atom loading rate with a few traps achieving $> 90\%$ loading. More careful optimization can probably push this number to $> 90\%$ but this level of enhancement is sufficient for our application now.

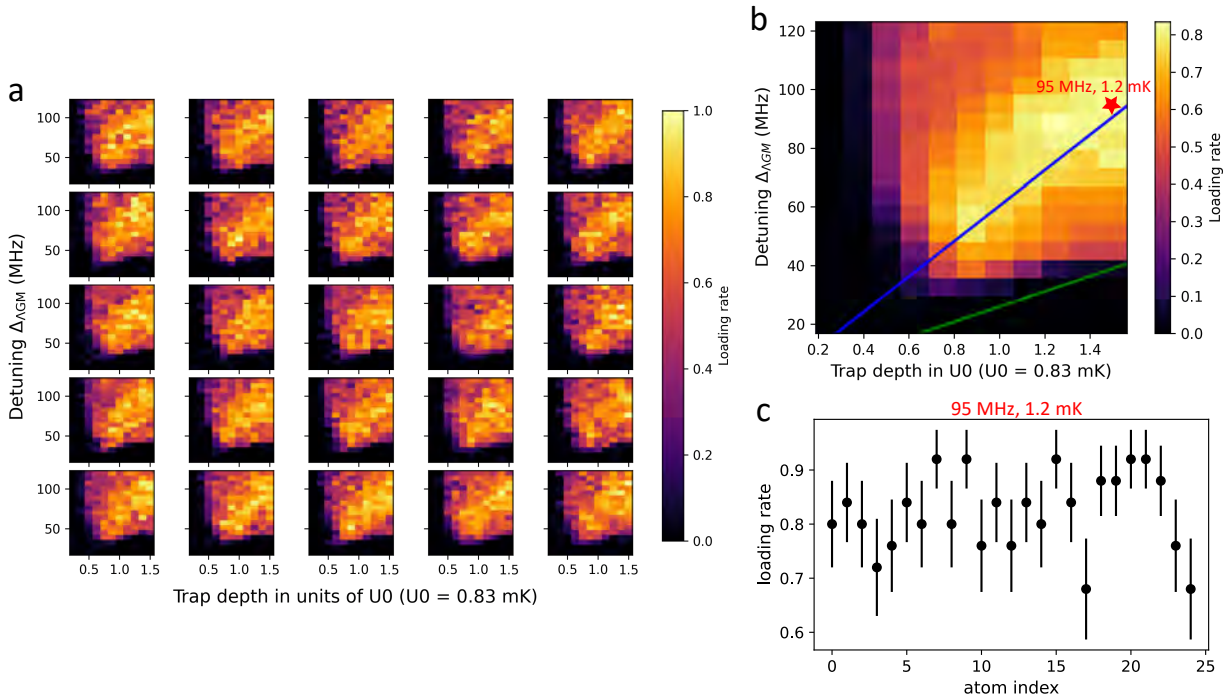


Figure 3.18: (a) The 2D scan of loading rate as a function of single photon detuning of the cooling beam and the trap depth. This allows us to see whether the traps are uniform enough to achieve good loading over the entire FoV. (b) Average loading rate over all the tweezers into one plot to find the optimal loading rate for the array over the full FoV. The star denotes the final detuning and depth we choose to operate. (c) Plotting the loading probability over all the tweezers with the loading parameters (stat point in (b)). Showing an average of 83% loading rate with site-to-site fluctuations of $\sim 5\%$. The maximum loading rate for single site can be as high as 93%.

3.5 Impact of vacuum, loading rate and imaging loss on achieving large atom array

Recent progress in quantum simulation [44, 139] and quantum computation [32, 35] has sparked a broad effort towards single-atom control of large atom arrays. There are significant incentives to scale up fully programmable single-atom array platforms up to few thousand atoms. Proposals to explore collective behavior in large ensembles [140] or to demonstrate verifiable quantum advantage [141] can greatly benefit from configurable arrays with thousands of atoms. In quantum information, even with the most resource-efficient error correction protocols, with current two-qubit gate errors in the order of 10^{-3} , encoding more than 100 error-corrected logical qubits requires several thousand physical qubits [142, 143].

In this section we are going to discuss the impact of vacuum-limited lifetime, loading rate and imaging loss to the creation of large atom arrays. These losses effect the probability of achieving a large atom array in different ways. Some are deterministic and correctable, for example vacuum loss and rearrangement loss. Some are non deterministic and not correctable, for example, cooling loss and imaging loss. First we will discuss the effect of cooling and imaging loss on achieving large array.

3.5.1 Imaging loss vs detuning and intensity

In Sec. 3.3.3 we measure the imaging loss down to $3.8(4) \times 10^{-4}$ /img using the (Imaging 1) parameters in table 3.1. However we would like to have a better understanding of what is the dependence of imaging loss with respect to different laser parameters. so expanding on the result in Sec. 3.3.3, we explore larger range of detuning and intensity of the imaging beam.

We perform a series of 2-dimensional scans with the sequence used in imaging loss measurement [Fig. 3.11(a)], varying the intensity from 40 to 230 I_{sat} and detuning from -25 to -65 MHz from free space resonance of the imaging beam. The atom survival is recorded over the imaging time under these different conditions and the loss rate per image is extracted [Fig. 3.19(a)]. The

red star in Fig. 3.19(a) marks the parameter (Imaging 1 in table 3.1). The data here is plotting with normalized intensity (scattering rate). This takes into account the detuning dependence of the imaging beam. With this, we found that with sufficiently large detuning (> 25 MHz from free space) where the PGC imaging is cooling the atom sufficiently, the imaging loss follows a linear relationship with the scattering rate in the range between 0.03 to 0.1Γ . Outside of this range, the imaging loss rate becomes exponential to the scattering rate.

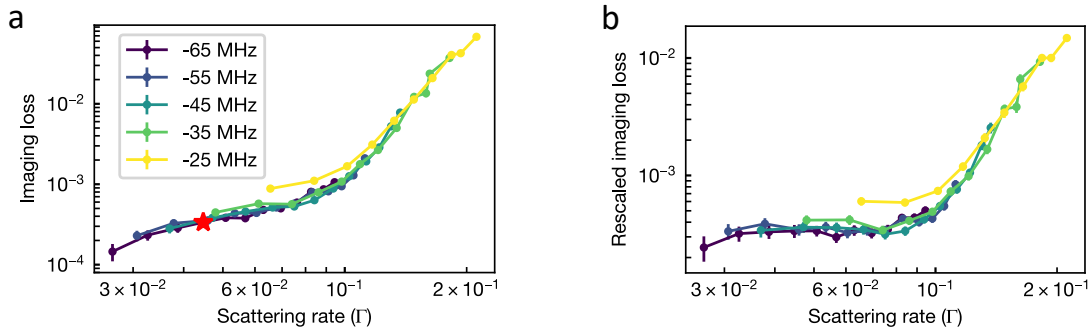


Figure 3.19: (a) Imaging loss vs. detuning and intensity. Not normalized to 42 photo-electron count on camera. (b) Imaging loss vs. detuning and intensity after normalizing to 42 photo-electron count on camera by scaling the loss as a function of time. Assuming linear photon collection rate over the single camera exposure time.

However, if we consider the goal of the imaging is to only collect enough photon for certain fidelity. Once the amount of photon and imaging fidelity is reached, we stop the imaging process. Then one can rescale the imaging loss in Fig. 3.19(a) based on the imaging time required to collect certain camera photo-electron count. Here we normalize it to the camera photo-electron count with the imaging parameter noted by the red star in Fig. 3.19(a), which is the parameter used in Fig. 3.11(b). This shows a universal scaling of imaging loss, in the range of 0.03 to 0.1Γ , only depends on the collected photon and independent of detuning, intensity and scattering rate [Fig. 3.19(b)]. One hypothesis of this fix loss rate is when atoms are in the excited state they are anti-trapped by the tweezer, thus experience loss as a function of how long they stay at the excited state. A more systematic study would be an area of interest for future high fidelity imaging and rearranging of large atom arrays, but it is beyond the scope of this thesis. The result of further

study will be documented in Zhenpu Zhang's thesis.

3.5.2 Effect of imaging loss on defect-free array

Imaging and cooling losses are important for creating large defect-free array because they are essential steps during the atom rearrangement operation. During the rearrangement, the atoms can heat up and potentially escape the trap, which requires cooling to reset the atom temperature before subsequent operation whether it's imaging or more atom move steps. In the case of imaging, the last operation following rearranging is always to take an atom array image to verify the result of the rearrangement. The cooling and imaging creates a nondeterministic loss that can not be corrected by more rearranging because these operations occur after the atom rearrangement. To visualize the impact of the cooling and imaging loss we perform a Monte-Carlo simulation of the probability of obtaining a defect free array with rearrangement and the presence of imaging and cooling loss. The simulation is set up according to the sequence in Fig. 3.20 as the following:

- The atoms are first loaded in an array with some loading fraction that is probabilistic. Typically with loading fraction of 60-80%.
- An image sequence is applied and the atoms in the array are subjected to some loss (i.e. remove from the array with some probability according to the imaging loss). This is to identify the tweezer site that has atom loaded.
- Then a rearrange step is applied and the atoms are removed randomly according to rearrangement loss similar to the step before. The rearrangement time is set according to the algorithm used and the defect-free atom number N .
- Then another image is taken and the image loss is applied to the array again. This is to verify the result of the rearrangement.
- During all the steps the vacuum loss is also applied according to the time it takes for each operation.

- Depends on the requirement of the simulation, either more rearrangement is performed, or the final result of defect-free probability and average array filled fraction is recorded.

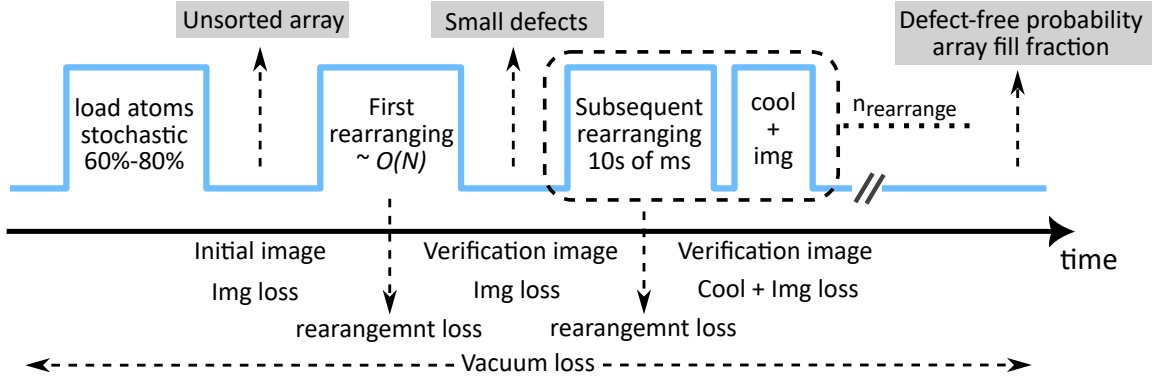


Figure 3.20: The sequence diagram used to program the rearrangement Monte-Carlo simulation. Atom are loaded stochastically into an array with 60-80% loading probability. An initial image is taken and the imaging loss is applied. Atoms are rearranged, during that time the rearrangement loss and vacuum loss is applied. A verification image is taken and the imaging loss is applied again. Depends on the simulation, extra rearrangement is performed or the final defect-free array probability and array fill factor is extracted.

We simulate two imaging loss, one is the imaging loss (0.45%) commonly observed in other tweezer experiments [144, 145]. Another one is the imaging loss we have (0.03%) we measured in Sec. 3.3.3. We see that even with rearrangement, the defect-free array probability drops dramatically from $\sim 60\%$ to less than 1% (in the case of 1000 qubits) when the imaging loss changes from 0.03% [solid lines in Fig. 3.21(a)] to 0.45% [dashed lines in Fig. 3.21(a)]. We see that at 0.45% imaging loss, the dominant source of defect is from imaging and not the vacuum lifetime that is attainable at room temperature tweezer experiments (around 300 seconds) [dashed lines comparing to green solid line Fig. 3.21(a)]. However, for imaging loss of 0.03%, a vacuum lifetime on the order of 1000 seconds becomes the limiting factor. Improvements in vacuum lifetime therefore increase the probability of a defect-free array [blue solid line and orange solid line in Fig. 3.21(a)].

If we perform additional round of rearrangement, we see that the probability of obtaining a defect-free array remains almost identical [Fig. 3.21(b)] showing that this nondeterministic loss is not correctable with more rearrangement rounds unlike vacuum or rearrangement losses. This

simulation result [Fig. 3.21(b)] matches quite close with the result from [144] where they observe the defect-free probability saturates at $\sim 33\%$ after multiple rounds of rearrangement with an array size of 225 atoms and imaging loss of 0.45%.

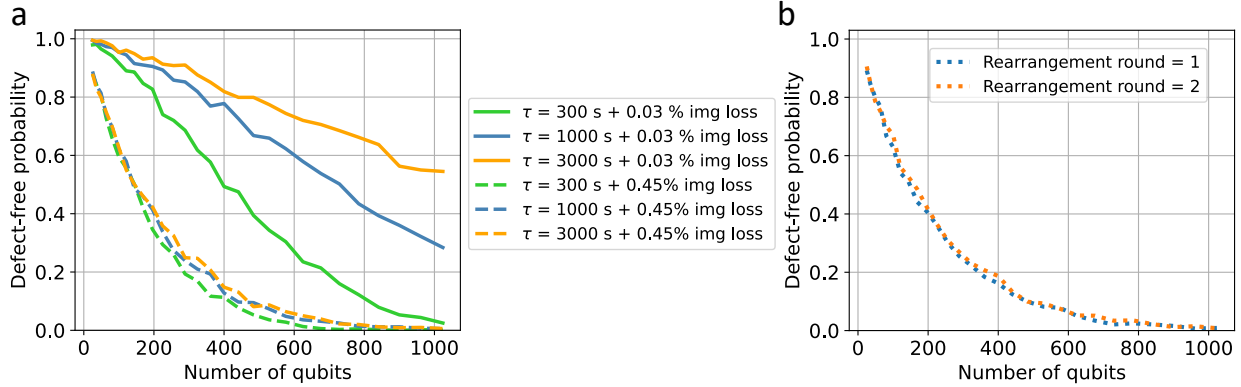


Figure 3.21: (a) Monte-Carlo simulations of single round of rearrangement show results for 0.03% imaging loss (solid lines) and 0.45% imaging loss (dashed lines) with different vacuum lifetimes (green: 300 s, blue: 1000 s, and orange: 3000 s). For 0.45% imaging loss, the vacuum lifetime is not a limiting factor for creating a defect-free array (dashed lines). However, for 0.03% imaging loss, increasing the vacuum lifetime from 300 seconds to 3000 seconds dramatically increases the probability of a defect-free array (b) Monte-Carlo simulations of multiple rounds of rearrangement with 0.45% imaging loss show that the imaging loss is not deterministic and cannot be corrected through additional rounds of rearrangement.

3.5.3 Effect of vacuum loss on defect-free array

To see the impact of the vacuum lifetime on success rate of obtaining a defect free array. We use the same code as before, but this time we turn off all the losses other than vacuum limited loss. This allows us to isolate the effect of finite vacuum lifetime. We simulate the defect-free probability with three different vacuum lifetime, 300 seconds (typical state-of-the-art room temperature tweezer experiment), 1000 seconds (best record of room temperature tweezer experiment) and 3000 seconds (our cryogenic tweezer vacuum lifetime) [Fig. 3.22(a)]. In the simulation, the rearrangement time is defined to be $50 + N * 0.85$ ms which is linearly increasing as a function of final array size (N) [27]. This time scaling was shown to be fairly efficient in the case of atom-by-atom rearrangement without parallel move of multiple atoms for rearranging a compact array [145]. From the simulation we see

a substantial improvement (around a factor of 10) of obtaining a defect free array while vacuum lifetime increases from 300 to 1000 second (only a factor of 3)[blue and orange line in Fig. 3.22(a)], meaning that a threshold for vacuum lifetime around 1000 seconds is needed to achieve usable defect-free array with the size of ~ 1000 atoms.

To further increase the defect-free probabilities, one can perform multiple round of rearranging. Since the subsequent round of rearranging requires less time, the vacuum limited lifetime has less effect on the atom loss [Fig. 3.22(b)]. However, there is always a minimal wait time required between subsequent rearrangement, therefore, the defect-free array probability will saturate by the vacuum lifetime limited loss during wait [dotted line in Fig. 3.22(b)].

Another way of increase the defect-free probability is with parallel move of the atoms. In this case, the rearrangement time can be further reduced and the threshold of ~ 1000 s can be lowered, but this is done in the expense of lower rearrangement fidelity [144].

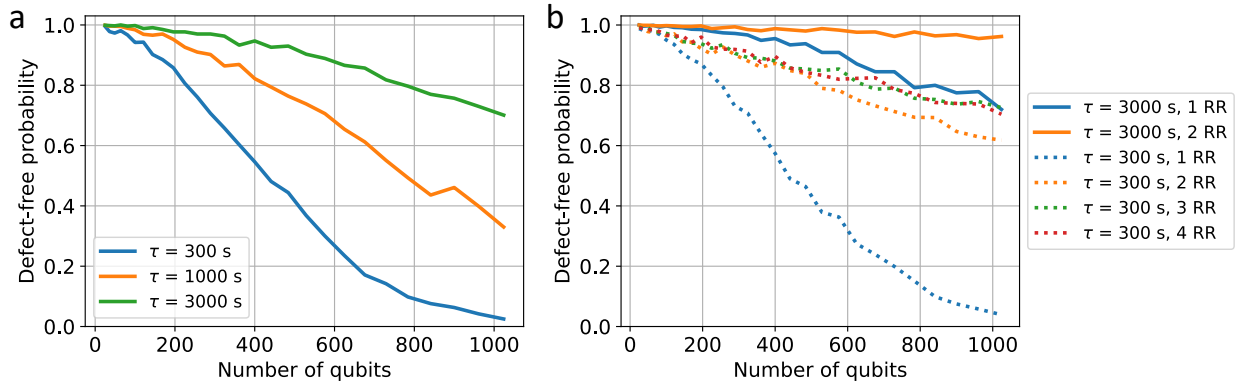


Figure 3.22: (a) Monte-Carlo simulations of single round of rearrangement with different vacuum lifetime (blue: 300 s, orange: 1000 s, and green: 3000 s) shows substantial improvement (around a factor of 10) of obtaining a defect free array at 1000 qubits while vacuum lifetime increases from 300 to 1000 second (only a factor of 3) (b) Monte-Carlo simulations of multi-round rearrangement with different vacuum lifetimes (solid: 3000 s and dotted: 300 s) shows that, with a 300-second vacuum lifetime, even with multiple rearrangement cycle, the defect-free probability saturates at a value lower than that achieved with a single round of rearrangement and a 3000-second vacuum lifetime.

Chapter 4

Cryogenic tweezer qubit manipulation

4.1 Overview

Note: For the most up-to-date analysis of ground state qubit rotation and Rydberg excitation, please refer to the upcoming publication "A High Optical Access Cryogenic Tweezer Array with a 3000-Second Lifetime" (in preparation).

One of the important aspect of our apparatus is to be able to control the atoms in the relevant state where the qubits are encoded and the entanglements are realized. Typically the qubits are encoded in the ground state of the atoms in alkali-earth atoms these are nuclear spins [95] and in alkali-metals these are hyperfine structures [29]. These states are less sensitive to environmental perturbation, so they can have coherence time in the order of seconds to 10's of seconds [32,35]. To manipulate and prepare atom to these states, optical pumping with microwave or Raman transitions are typically required. For the control interactions, these are typically done in Rydberg state where the long range dipole-dipole interactions are available to provide entanglement [23–25]. These states are sensitive to local electric field fluctuations and require a stable field either through electrodes or dissipation of accumulated charge.

In this section we show that our cryogenic apparatus is capable of such manipulations and preparation of quantum states and provides good environmental stability for the ground state single atom control. We will show the microwave rabi oscillations between ground state hyperfine levels. This will provide insight about the magnetic field stability of the apparatus and also the switching dynamics of the bias fields due to induced eddy current from metal parts in cryogenic temperatures.

This is an important first step showing single particle quantum state control that is required for quantum simulations and quantum information.

4.2 Microwave

To drive microwave transition between $|F, m_f\rangle = |1, 1\rangle \leftrightarrow |2, 2\rangle$ the atom needs to first be prepared in $|2, 2\rangle$ state with the optical pumping pulse. The optical pumping light is resonant between $F = 2 \leftrightarrow 2''$ in the ^{87}Rb D2 transition with a pure $\sigma+$ polarization. Combining with a repump resonant to $F = 1 \leftrightarrow 2''$. This creates a dark state at $|2, 2\rangle$ where the atom eventually accumulates. Figure 4.1 is the level diagram for optical pumping, repump and state selective push-out beam (same as MOT cooling beam). The push-out beam resonant to the cycling transition $F = 2 \leftrightarrow 3''$ allows us to push atoms out of $F = 2$ and detect population remaining in $F = 1$ manifold.

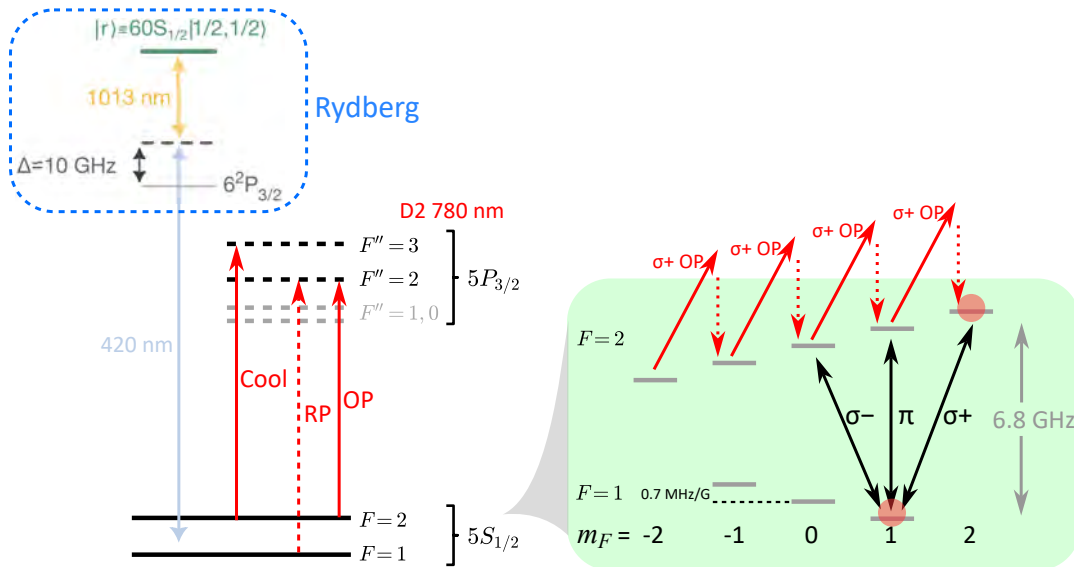


Figure 4.1: Level diagram for the ground state qubit (green box) and Rydberg transition (blue dashed box). The ground state manifold consists of $F=1$ and $F=2$ Zeeman manifold with magnetic quantum number $m_f = 0, \pm 1, \pm 2$. The energy separation between $F=1$ and $F=2$ is around 6.8 GHz. The repump and optical pumping for state preparation is within the ^{87}Rb D2 manifold. OP is on resonant with $F = 2 \leftrightarrow 3''$ and purely $\sigma+$ polarization. Repump is on resonant with $F = 1 \leftrightarrow 2''$. The Rydberg transition is a two photon transition with intermediate state detuning around 10 GHz from $6^2P_{3/2}$. The intermediate state is driven with a blue 420 nm photon and the final state is driven with a NIR 1013 nm photon.

Two components need to work in unison to achieve optimal optical pumping, the quantization

axis defined by a bias magnetic field, and polarization of the OP beam. To ensure polarization purity, a Glan-Taylor polarizer is used to generate the initial linear polarization to a contrast of $> 10000 : 1$, following a $1/2$ and $1/4$ waveplates to compensate any birefringence from the viewports and the coldbox windows. The $\sigma+$ polarization is first measured using a polarization analyzer, this gives a good starting point where the magnetic field can be aligned to the OP beam following the procedure described in Ref. [101]. Figure 4.2(a) is an example scan of atoms in $F = 1$ vs bias field. Then the $1/2$ and $1/4$ waveplates are adjusted to maximize the depumping time of the atom out of the $|2, 2\rangle$ state.

After optimization, we measure the depumping rate out of the $|2, 2\rangle$ using only the OP beam without repump. If there are any unwanted polarization the population will leak out of $|2, 2\rangle$. We measure a depumping rate of $\tau_{dp} = 0.95 \pm 0.13$ ms [Fig. 4.2(b)]. Comparing this rate with our typical OP beam pumping rate of about $\tau_{op} 10 \mu\text{s}$ we get the steady state population

$$P_{|2,2\rangle} = 1 - \exp\left(-\frac{\tau_{op}}{\tau_{dp}}\right) = 99\%$$

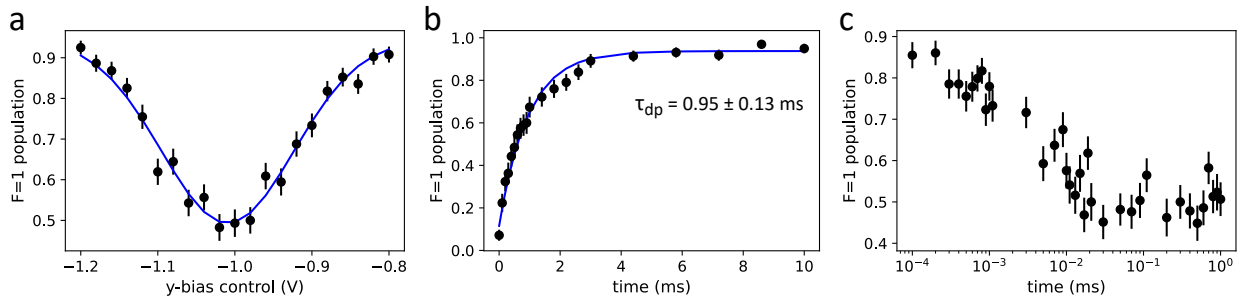


Figure 4.2: (a) Atoms in $F = 1$ vs bias field. When the bias field is optimized, the atom is mostly in $|2, 2\rangle$ therefore by minimizing the $F = 1$ population we can optimize the optical pumping bias field. (b) Atom in $F = 1$ vs OP beam on time. Since atoms that fall to $F = 1$ manifold and in $|2, 2\rangle$ will remain dark to the OP beam, we can use this to determine the impurity of polarization in OP beam by looking at the dumping rate out of $F = 2$ manifold. We find a depumping rate of $\tau_{dp} = 0.95 \pm 0.13$ ms (c) OP pumping time vs population in $F=1$ after a 0.5ms depumping time. This is to be used for optimizing the pulse duration of the OP beam to make sure it is sufficiently long to maximally pump the atoms into $|2, 2\rangle$

4.2.1 B-field calibration and noise

We use the microwave antenna with a cold bandpass filter described in Sec. 2.2.8 to couple 6.8 GHz microwave into the coldbox. This is a split loop antenna with a loop circumference half the microwave wavelength. Effectively acting like a half-wave dipole antenna folded into a circle. The antenna is around 12 mm to the atoms. Figure 4.1(a) shows the ground state zeeman manifold and microwave drive coupling the states. Depending on the m_f state the energy shift of the Zeeman levels follows the $\Delta_{\text{Zeeman}} = m_f \times B \times 0.7 \text{ MHz/Gauss}$.

To perform microwave spectroscopy on the atoms, we first prepare atoms in the $F = 2$ manifold, not necessary in the stretch state ($|2, 2\rangle$). To do this we simply turn on a repump pulse for $50\mu\text{s}$ to pump the atom out of the $F = 1$ manifold. This allows us to simultaneously make sure the push-out beam is functioning as intended. Once the atoms are in $F = 2$, the microwave is turned on and the population is scrambled across $F = 1$ and $F = 2$ manifolds when the microwave frequency is on resonance with one or more Zeeman sublevel. Finally the atoms in $F = 2$ are pushed out and population in $F = 1$ is detected, the sequence is shown in [Fig. 4.3(a)]. The long 750 ms wait is to ensure all magnetic field switching dynamics has settle to a steady state since we didn't know the decay time constant at that point. With different combination of Zeeman levels in both $F = 1$ and $F = 2$ we expect to see peaks that follows $\Delta f_{\mu w} = n \times B \times 0.7 \text{ MHz/Gauss}$, where $n=0,1,2,3$.

With a non-zero B-field we see a series of microwave resonance peaks that are evenly spaced [Fig. 4.3(c) left panel]. As the field reduces we see the different resonances merge to a single peak. The slope of frequency difference and bias coil control [dashed lines in Fig. 4.3(c middle)] can be used to calibrate the bias coil current to B-field ratio at the atom location. The calibrations for the coil gives $(x,y,z) = (5.52, 5.92, 12.52) \text{ G/A}$ which is very close to the predicted value in Sec. 2.2.7. Finally we can estimate the level of how well we can zero the field by looking at how well we can resolve the splitting in the Zeeman sublevel. The linewidth of microwave spectroscopy is roughly 20 kHz [Fig. 4.3(c) right] so $20 \text{ kHz}/(3 \times 0.7 \text{ MHz/Gauss}) \approx 10 \text{ mG}$ is the field zero error.

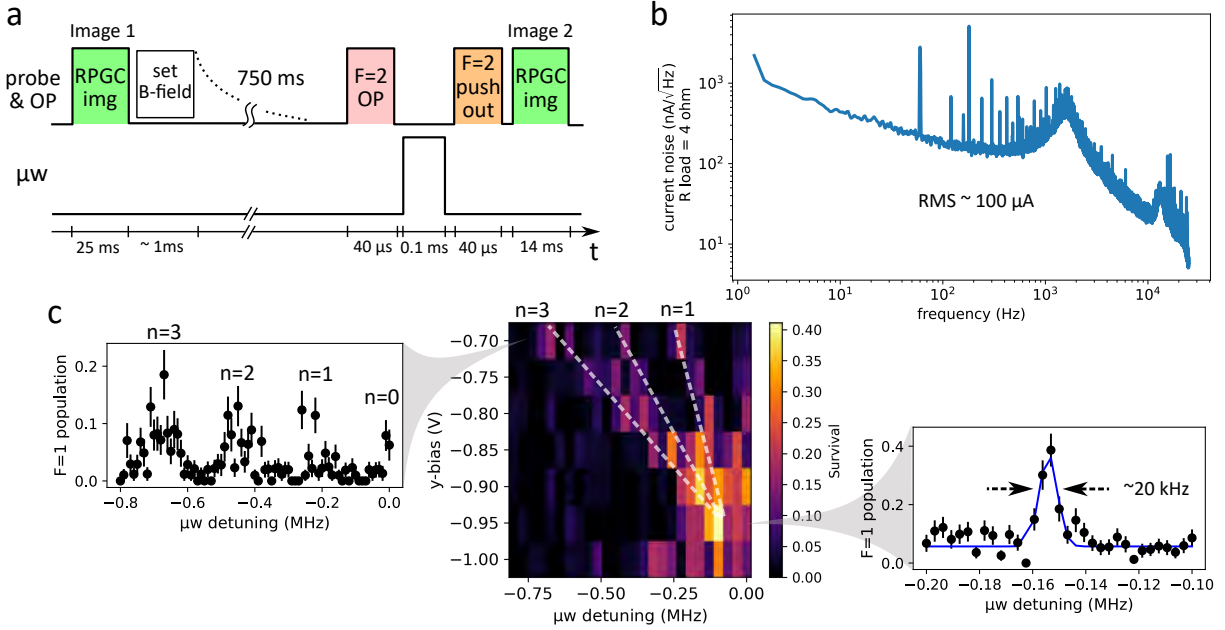


Figure 4.3: (a) Timing sequence for microwave spectroscopy. The 750 ms wait between setting the field and optical pumping is to ensure the switching dynamics has already settled. We didn't know the decay time constant at that point hence the long wait time. (b) The measured current noise spectrum in the bias field coil driver, integrate over the frequency gives $100 \mu A$ current noise. The current to field strength conversion determined in (c) gives a RMS magnetic field noise of 1.2 mG. (c) Resonance scan used to zero the field, showing the merges of the different Zeeman sub levels. Microwave resonance vs applied current on bias field current controller.

Now with the bias coil current to B-field conversion obtained from the microwave spectroscopy. We can convert the current noise measured from the coil current driver to the B-field noise. The current noise spectral density of the bias coil current driver is measured with a 4Ω sense resistor connected on the output [Fig. 4.3(b)]. The integrated RMS current noise from the spectrum is $\sim 100 \mu A$ which translate to ~ 1.2 mG RMS B-field noise.

4.2.2 Rabi

The polarization of the microwave is not controlled, but applying a bias magnetic field we can lift the degeneracy of different m_f levels within $F = 1$ and 2 manifold. Then we can selectively drive $\sigma+, \pi$ and $\sigma-$ transitions by tuning the frequency of the microwave to be resonant to a specific m_f level. We typically operate at a field of ~ 3.5 Gauss in x-direction (perpendicular to the tweezer)

which is sufficiently large to eliminate the fictitious field created by the tweezer. The fictitious field originates from tightly focusing of a linearly polarized light to a point that the Rayleigh range of the beam are in the order of a few wavelengths. Due to the sharp change in \vec{k} , the polarization creates a gradient when traveling through the focal point of the light and create a effective circular polarization transverse to the polarization plane. This in term creates an effective magnetic field pointed in the transverse direction w.r.t. tweezer propagation direction [146]. At 0.55NA and the trap depth of 1 mK this field is around 0.1 G/ μm near the tweezer focus.

To drive the rabi oscillation we first optically pumped to the stretch state $|2, 2\rangle$. Depends on the microwave transition we wish to drive, we either transfer atom to $|1, 1\rangle$ with a π -pulse or directly drive from $|2, 2\rangle$ [Fig. 4.4(a)]. By changing the microwave pulse length and measure the population remaining in $F = 1$ using the state selective push-out (push out atoms in $F = 2$) we can record the Rabi oscillation of $\sigma+$, π and $\sigma-$ transitions [Fig. 4.4(c)]. Fitting a decaying sine function to the data we extract the Rabi frequency of $(\sigma+, \pi, \sigma-) = (5.98 \pm 0.01, 22.6 \pm 0.4, 2.05 \pm 0.04)$ kHz.

From the COMSOL simulation given the drive power of 1 W into the antenna, we can plot the microwave B-field strength vs distance to the loop antenna [Fig. 4.4(b)]. At a distance of 12 mm the B-field is ~ 20 mG. Scaling this to 6 W of microwave power we should have $\sim 2\pi \times 42$ kHz, not considering the polarization of the microwave field. We can calculate the equivalent Rabi frequency from our measurement using the dipole matrix element of the microwave transition $(\sigma+, \pi, \sigma-) = (\sqrt{3}/2, \sqrt{3}/2, 1/2) \mu_B$. Normalize the rabi frequency to the $\sigma+$ transition and take the quadrature sum we have $\sqrt{5.98^2 + (22.6\sqrt{2})^2 + (2.05\sqrt{6})^2} = 33$ kHz. This is in good agreement with the 42 kHz prediction considering error in distance from microwave antenna to the atom and losses in the microwave cable and cold filter assembly.

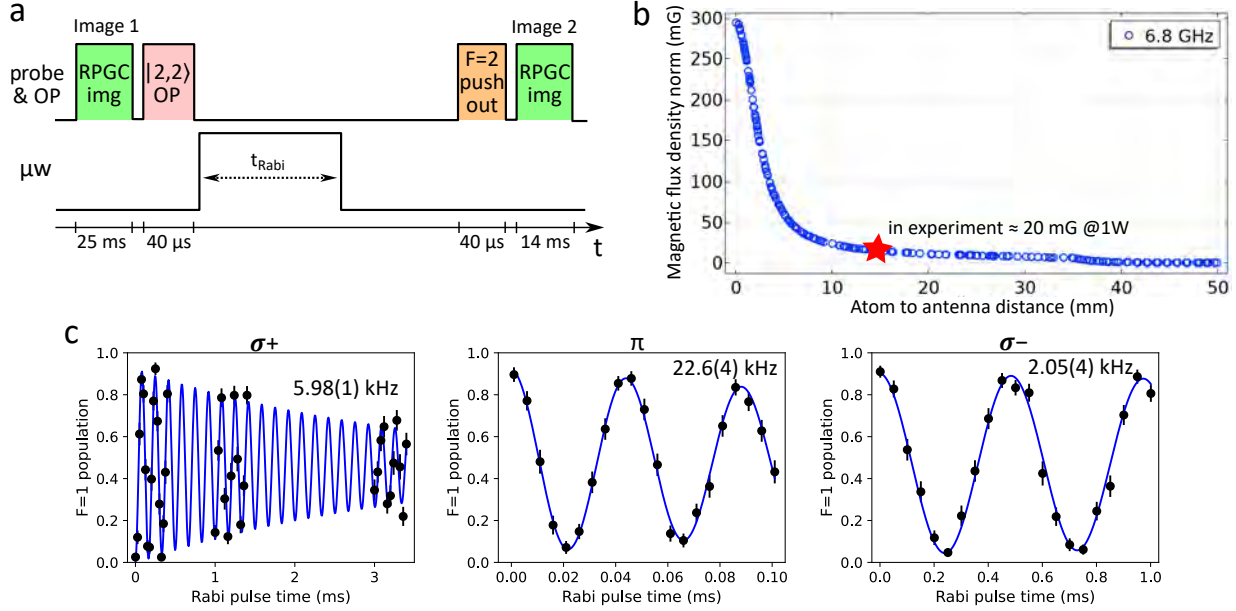


Figure 4.4: (a) Sequence for Rabi oscillation measurement. Consists of optical pumping to $|2, 2\rangle$, pulse on microwave for variable amount of time and push out atom in $F = 2$ manifold. (b) Simulation of the field strength from the half-wave loop antenna gives around 20 mG/W at the atom location in our experiment. From this we can calculate 6 W microwave input to the antenna will result in 42 kHz total Rabi frequency. (c) Rabi oscillation of $\sigma+$, π and $\sigma-$ transitions from the microwave input power of approximately 6 W into the antenna. Each transition are measured with the same microwave power and on resonance to the particular transition that is being driven.

4.2.3 Ramsey

Finally we perform Ramsey spectroscopy at the atoms between $|1, 1\rangle$ and $|2, 2\rangle$ states. Again the state is initialized to $|2, 2\rangle$ via optical pumping. Then a $\pi/2$ pulse is applied to rotate the state to the equator of the Bloch sphere. After a variable wait time T_R , a second $\pi/2$ pulse is applied and the phase of this second pulse is scanned from 0 to 2π to obtain the Ramsey fringe. The sequence is illustrated in Fig. 4.5(a). Once the second $\pi/2$ pulse is applied the population in the $F = 2$ is detected with the push-out beam and the survival (Ramsey fringe) is recorded [Fig. 4.5(b)]. We also perform a spin echo version of the same measurement by adding a π pulse in the middle of the wait time $T_R/2$ [Fig. 4.5(a)], to first order cancel out decoherence due to environmental perturbation such as magnetic field noise and we obtain a much longer coherence time. We plot the Ramsey

fringe contrast as a function of wait time, assuming the decoherence is caused by a random process we can fit a Gaussian to the decay of the contrast [Fig. 4.5(c)]. The data is plotted in log scale in the wait time due to the large difference in decoherence time between echoed and non-echoed cases. For the measurement without spin echo we measure a $T_2^* = 131(5) \mu\text{s}$ and with spin echo we measure a $T_2 = 0.95(5) \text{ ms}$ almost an order of magnitude longer.

We can convert the T_2^* measurement to the magnetic field noise using the following conversion [147].

$$\Delta B = \Delta f (2.1 \text{ MHz/G}) \quad , \text{ where } \Delta f = \frac{1}{2\pi T_2^*} \quad (4.1)$$

With the $T_2^* = 131(5) \mu\text{s}$ and the time it took to take the data we have $\Delta B \approx 0.5 \text{ mG}$ in $\sim 10 \text{ min}$ time scale. This is comparable to the magnetic field noise measured in other cryogenic experiments, for example in Ref. [47] they measured a 1.2 mG with bandwidth up to 100 Hz.

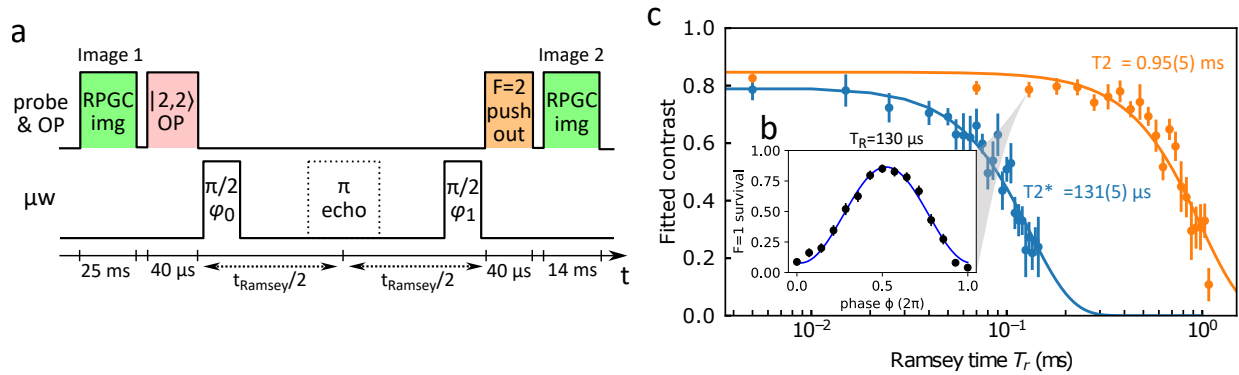


Figure 4.5: (a) The experimental sequence for the Ramsey measurement. (b) Typical Ramsey fringe, atom survival in $F=1$ vs phase of second $\pi/2$ pulse. (c) The contrast vs. wait time between two $\pi/2$ pulses. Fitting the decay to a Gaussian we can extract the coherence time with and without echo. From this we infer a RMS magnetic field fluctuation of 0.5mG over few minutes time scale.

4.3 Eddy current measurement

In the apparatus, we use a large amount of copper for its excellent thermal conductivity. For metal, if it has good thermal conductivity almost always means it also has good electrical conductivity. For standard OFHC copper used in typical cryogenic application, the residual resistance ratio is typically between 50-100. This means they are highly conductive with very low residual resistance. This creates a problem when the external magnetic field is subject to change, for example, during the switching of the quantization axis. Due to its proximity to the atoms, the local magnetic field seen by the atom is perturbed by the induced eddy current in the nearby copper. The induced eddy current is almost unavoidable as long as the OFHC is used and the system is under cryogenic temperature. In Ref. [58], they did not observe significant adverse effect in loading and cooling of single atoms from the long decay time constant of eddy current in the OFHC used in the cryostat. As a precaution, we put slits on our coldbox and with a combination of higher resistance copper alloys, the resistance of the current loop is increased hoping to reduce the effect of eddy current. Initially we had the same observation as Ref. [58] where the loading of MOT and cooling of single atoms are okay, but as we start to setup optical pumping and microwave spectroscopy, we observe instability in setting of the magnetic field. These operation requires a more dynamic switching of the magnetic field up to a few Gauss to create a quantization axis. In addition, we also see a substantially different magnetic field settings for cooling and tweezer loading between when the apparatus is at 300 K vs at 45 K. The difference can be as large as several Gauss. This lead us to believe that a substantial amount of eddy current is present in our system.

Therefore, we decided to to perform a careful study of the magnetic field switching characteristics with microwave spectroscopy we described in Sec. 4.2.1. After the first atom image, the field is zeroed and wait for 750 ms for the field to settle. Then the atoms are prepared in $F = 2$ via optical pumping following with a magnetic field jump. After the field jump a microwave pulse of 0.1 ms is turned on with variable delay (T_{wait}) and detuning, [Fig. 4.6(a)] is the experiment sequence for the measurement. This gives a microwave spectrum [similar to the one in Fig. 4.2.1(c)] as a

function delay time.

We clearly observe a double exponential decay where a fast decay in the order of (1-2 ms) corresponds to coil current switching and a slower time constant (5-100 ms), depends on the axis, corresponds to the induced eddy current decay. Fitting to the time trace, we obtain the slow switching time constant $(\tau_x, \tau_y, \tau_z) = (100 \text{ ms}, 60 \text{ ms}, 5 \text{ ms})$ for three axis of the coldbox. These time constant qualitatively match the coldbox geometry. The z axis which has the fastest decay is where we put the slit. The x axis that has the longest time constant has the thickest copper cross section.

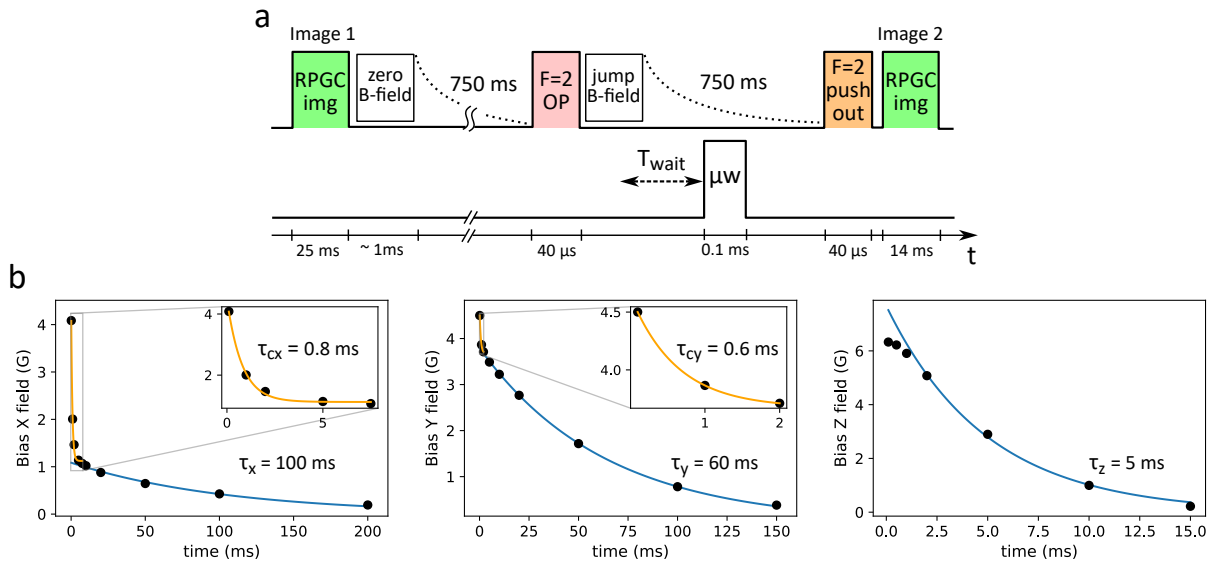


Figure 4.6: (a) The experimental sequence for characterizing the eddy current of the coldbox in x,y and z axis. (b) The magnetic field at the atom location as a function of time after the bias field is jumped. The time trace shows a double exponential decay where a fast decay ($\sim 1 \text{ ms}$) is from magnetic field coil switching and the slower (5-160 ms) decay is from the eddy current induced in the coldbox. We measured the slow decay time constants $(\tau_x, \tau_y, \tau_z) = (100 \text{ ms}, 60 \text{ ms}, 5 \text{ ms})$

4.4 Outlook

This thesis describe several efforts of creating a new type of experimental platform where cryogenic environment is leveraged to provide better isolation of the atom arrays from the environment. We focus on two aspect of isolation, one is minimizing the collision between the atom with residual background gas. Another one is isolating the Rydberg atom from the microwave BBR background. The effort of reducing the effect of residual background gas collision through trapping atoms in a cryogenic environment, combining with atom rearrangement provide a way of creating long lived atom arrays for quantum simulation and computation. In the meantime, recent advances in technique of driving Rydberg transition [148] in conjunction with the microwave BBR shielding provided by the cryogenic environment further improves coherence comparing to at room temperature. The benefit of cryogenic tweezer array will allow us to access experimental parameter space previously limited by the vacuum lifetime and coherence.

Combining cryogenic environment with high NA optical access comes with it's own set of challenges. Aside from the thermal considerations typically associated with cryogenic setup, maintaining stringent optical alignment over a large temperature range is required to maintain the optical performance of the microscope objective. We have demonstrated a series of technique that we developed to achieve stable optical alignment from 400 K to 40 K. These techniques are essential for future application of cryogenic environment to optical tweezer and quantum gas microscope experiments.

Beyond the experimental advances, we are able to study imaging and cooling losses to a very low level (10^{-5}) owing to the excellent vacuum lifetime the cryogenic tweezer is able to provide. These losses are previously not accessible since the typical vacuum lifetime being in the order of 300 seconds and only until recently 1000 seconds [43]. Achieving low imaging and cooling losses are essential for advances in high fidelity quantum gate operation, for example, in transport based protocol where atoms are extensively manipulated by the tweezers. In the context of large array, low imaging and cooling losses are important since these losses are nondeterministic and can not

be corrected with more rearrangement rounds as discussed in Sec. 3.5.2.

Furthermore, we carefully characterize the cryogenic environment with atoms including measuring the magnetic field stability and eddy current decay from the coldbox. The next step would be setting up the Rydberg lasers and measuring the coherence and electric field stability inside the coldbox with the Rydberg transition.

4.4.1 Atom Array, SLM and optical lattice

Currently there is only one set of trapping potential from AOD tweezers. AOD tweezer, although very configurable dynamically, suffers from RF intermodulation and is not suitable for holding the atoms long term. In addition, the arrangement of the AOD tweezer trap is restricted on a grid and can not be arbitrary. In the immediate future, we will add a secondary potential generated by an SLM projected through the microscope objective (Fig. 2.18). We can estimate the achievable tweezer number with the current objective FoV of larger than $\pm 200 \mu\text{m}$ and the atom spacing of $3 \mu\text{m}$, to be 10000 tweezers. Combining with rearrangement technique similar to the one used in [149], enhanced loading from Sec. 3.4.2 and Ref. [84,95] and the long vacuum lifetime of our cryogenic platform, defect free array of greater than 8000 atoms is possible. At this point we will be limited by the laser power and heat dissipation of the absorbed trapping light from the objective.

As part of the design consideration of the coldbox, ultimately we plan to include bi-chromatic optical lattice to trap Rydberg atoms and ground state atoms simultaneously. This provide a power efficient way of generating large number of traps. Currently, one of the limitation is anti-trapping of the Rydberg state during gate operation [57]. The trapping of Rydberg state eliminates atom loss during Rydberg excitation, therefore increase the coherence of the Rydberg drive and reduce the error during sequential gate operations. This can also reduce the amount of hardware overhead required for error correction [31] and mid-circuit measurements.

Following the additional trapping potential, we will also install the second microscope objective. This allows us to send one of the Rydberg light tightly focused through the objective and

achieve site selective Rydberg state manipulation [32].

4.4.2 Cryogenic enhancement: cryopumping

In the current coldbox design, we utilize a low outgassing environment created by the 45 K cryogenic shield (discussed in Appendix D) that enclose the atom array from the room temperature vacuum chamber almost entirely. While this shield is very low outgassing, its cryopumping ability for common residual gas in UHV chamber, e.g., H_2 , CO or CH_4 , are relatively weak (Fig. D.2). Therefore, we place a 4 K cold finger with slits cut out to increase the surface area inside the coldbox with high conductance to the atom. However, this cryopumping surface did not have direct line of sight to the atoms and the surface area is not enough to sustain efficient cryosorption for a long time (see Appendix D for details about cryosorption). We typically see the lifetime degrades after a few days from 3000 seconds to around 1500 seconds and remain at that value until we regenerate the cold finger by heating it up to 20 K for a few hours. During normal operation, we regenerate the 4 K cold finger daily.

Given that our design minimize the 4 K cryopumping surface protruding into the coldbox, significant improvements can be made from improving the geometry of the 4 K cryopumping cold finger. To further increase the saturation time of the cryopumping cold finger and to achieve more efficient pumping. Two modifications can be done to the 4 K cold fingers. For longer saturation time, we can increase the surface area of the 4 K cold finger with large volume to surface ratio media, e.g., porous or mesh. Typically, activated charcoal or molecular sieves are used. However, thermalizing these materials to 4 K and attaching them to the cold finger requires the use of epoxy which is not preferred in our chamber. Alternatively, metal or ceramic of various porosity and meshes can be used. An extensive study was done in Ref. [150] where the cryosorption ability of various materials are investigated. Here are some of the potential candidates for sintered metal and porous ceramic cryosorption materials (McMaster-Carr part number: 9224T83, 9446T32 and 8978T793). These are example part numbers for sintered stainless porous discs, porous alumina and copper mesh, specific mesh size or pore size depends on the application and needs to be chosen

accordingly.

Additionally, the 4 K cold finger can be extended further into the cold box, increasing line of sight exposure to the atom trapping location (Fig. 2.2.10). This allows the residual gas that enters the coldbox through the small openings having higher probability to collide with the cryopumping surface before interacting with the trapped atoms.

4.4.3 ITO coating

The coldbox presented in this thesis only has normal AR coatings on the glass windows. From other experimental observation [47] microwave BBR leaking through the window opening can significantly effect the coherence of the Rydberg state. From our estimation, we can expect up to a factor of 50% increase in Rydberg lifetime in our current coldbox design from the microwave BBR leaking through the glass windows on the coldbox. In the future, if we wish to take the full advantage of the 45 K environment, ITO conductive coating can be added to the glass windows on the coldbox. This forms a Faraday cage where the microwave up to 100 GHz can be effectively shielded. The ITO coatings capable of shielding microwave signals typically has a very low sheet resistance in the order of $10 \Omega/\text{sq}$. One drawback for these type of ITO coating is the optical loss becomes fairly large ($\sim 10\%$) because the coating needs to be thick (around 150 - 200 nm) [151], so careful planning is needed in terms of increasing heatload and coating damage from high power lasers. One potential solution to reduce the laser absorption on the ITO coating is to use the thinner ITO coating with larger sheet resistance on the window where high power laser shines through, for example, the tweezer ports, and thicker coating with higher optical loss on the low power windows (MOT and probe). We expect the tweezer windows might not need as much microwave shielding because the opening is on the order of microwave wavelength in tens of GHz range, thus the microwave might not couple through the tweezer window holes efficiently.

Chapter 5

Metasurface lens experiment

5.1 Overview

In neutral atom tweezer array high-NA optics are key for creating trapping potentials, the optical addressing of individual atoms in quantum gate protocols, and imaging the fluorescence of single atoms [3, 16]. Often multielement objective lenses are required to achieve the requisite performance [3, 16, 152], although single aspheric lenses have also been instrumental in state-of-the-art experiments studying interacting Rydberg atoms [153]. They suffer from relatively small FoV and chromatic focal shift.

Optical tweezers require both low aberrations to achieve tight confinement and high focusing efficiency to achieve sufficient trap depth for a given trapping power and to efficiently image single atoms. Achromatic properties are needed for simultaneously collecting atom fluorescence, conservative trapping in a far off-resonance trap, and often also the delivery of excitation light that controls the atomic state in individual tweezers [154]. Broadband operation is especially important for multispecies or molecular optical tweezer experiments [155–157]. Further, arbitrary and clean polarization control is increasingly desired to provide additional degrees of freedom in controlling the internal state of the atoms.

A long working distance (WD) is required to allow access for laser cooling beams, to maintain sufficient distance between the lens substrate and atoms in high-energy Rydberg states that are sensitive to surface electric dipoles, and to focus light into a complex vacuum chamber or cryogenic environments [58]. In addition, stability of the optics is crucial, for example, in registration of

optical tweezers and lattices or for in-vacuum applications. Further, perturbations to the trap focus due to multi-beam interference or scattered light need to be minimized, especially if they are not static, as these fluctuations can drive atom motion.

In this section I describe a proof-of-principle experiment where, for the first time, a high-NA focusing metasurface lens is used to create array of optical tweezer to trap and detect single atoms. The optical tweezer trap is then tested with atoms for their diffraction limited performance. The result is compared to the optical measurement using subwavelength pinhole with good agreement. Finally, I will discuss future metasurface lens design with characteristics that are desirable for single atom trapping. Our successful demonstration of trapping single atoms with metasurface lens shows indicates that potential deleterious effects, for example, scattered light, the presence of undeflected zero-order light, or deformations due to absorption and heating of the lens makes negligible contributions to the trapping performance.

5.2 UHV system

The goal of this apparatus is to create a platform that can accommodate wide range of different metasurface samples and rapid testing of these metasurface with atoms. Specific requirements when designing the metalens UHV systems includes

- Simple design, easily adapt to different science cells
- Reusable science glass cell for multiple samples
- Compact design for vacuum processing (assembly, baking and metalens sample swap)
- Maximize optical access for tweezer experiment
- Vacuum level in the 10^{-10} torr range.

This results in a simple UHV chamber consists of a source glass cell, a science glass cell and a pump, CAD model of the UHV system shown in (Fig. 5.1). The source glass cell is purchased commercially from ColdQuanta and is connected to the rest of the system through a differential pumping pinhole.

The science glass cell is connected adjacent to the source cell and to an ion pump with pumping speed of 25 l/s. The estimated differential pumping ratio is given by the conductance to the pump and the source cell pinhole which is calculated to be around 10 l/s and 0.05 l/s respectively. This gives a differential pumping ratio of 200, allow the science cell to maintain pressure in the 10^{-10} torr range while the source can operate at around 10^{-8} torr for efficient capture of ^{87}Rb background vapor by the 2D+ MOT.

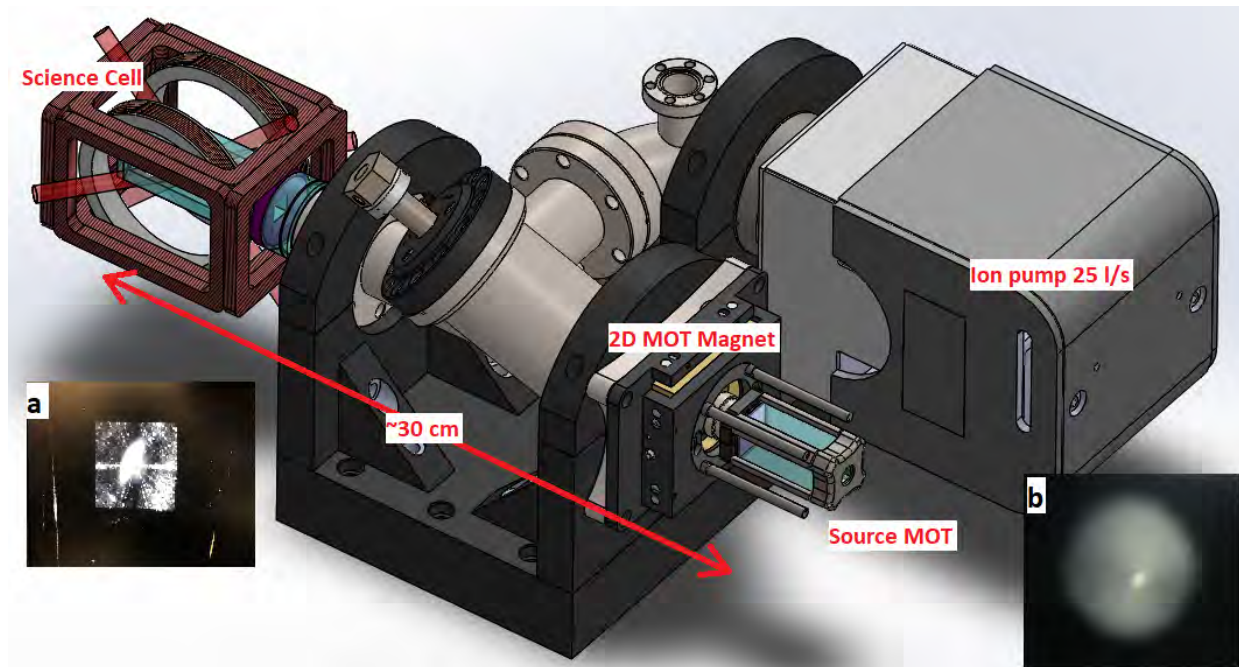


Figure 5.1: Main: CAD model of the metalens UHV chamber. Source cell (right) and science cell (left) are connected through a modified 3-way in-line all-metal valve to an 25 l/s ion pump. The separation between source MOT and science MOT is about 30 cm and the 2D MOT magnet is on a translation stage to align the center of the magnetic field gradient to the differential pumping pinhole. (a) Image of science MOT (white patch at the center) in front of the metalens sample (square background). (b) Image of the source MOT (white dot at the center) view from the end of the source cell.

The 3-way connection between the source cell, science cell and ion pump is done through a modified all-metal inline valve (MDC vacuum, P/N 316000) where a third port is added on the tube part after the valve body. This reduces the required vacuum hardware and keep the distance between source MOT [Fig. 5.1(b)] and science MOT [Fig. 5.1(a)] short at around 30 cm. Keeping

the distance short allows a denser atomic beam from the 2D MOT to reach the science cell for more efficient atom transfer to the 3D MOT. The all-metal inline valve serve to isolate the source cell from the rest of the system during sample swap. When swapping the metalens sample, the valve is closed and the ion pump and the science cell are vented to air.

5.2.1 ColdQuanta source cell

The source cell is purchased from ColdQuanta. It consists of a special glass cell with a 0.75 mm diameter pinhole to achieve the desired differential pumping and four electrical connection for two Rb dispenser from SAES Getters (model Rb/NF/3.4/12). The pinhole on the glass cell has a conductance of 0.05 l/s ¹ to isolate the higher vapour pressure inside the source cell from the rest of the UHV system during operation. The dispensers are activated during bake-out of the vacuum chamber (see appendix B for additional detail). The source cell mounts on a stainless steel adapter plate to allow the mounting of the the 2D+ MOT magnet translation stage, [Fig. 5.2(a)].

The required magnetic field gradient for the 2D+ MOT is created through a set of four permanent bar magnets on a translation stage, [Fig. 5.2(b)]. This provides a 37 gauss/cm 2D quadruple magnetic field gradient along the transverse direction (cooling laser direction) [Fig. 5.2(c)] and the atom are captured at the center of the gradient (zero B-field). The relative position of the magnet assembly can be changed w.r.t. the glass cell to align the field gradient center to the pinhole.

To operate the 2D MOT, we use two pairs of retro-reflected beams in transverse direction with elliptical beam diameters of 12 x 25 mm in $\sigma+$ and $\sigma-$ configuration. The transverse cooling beams are red detuned 2.5Γ from ^{87}Rb D2 $F = 2 \rightarrow 3''$ transition with 27 mW in each beam. Typical dispenser current ranges between 2-3A. Using a push beam with 1 mW power, same detuning as the 2D+ MOT beam and a diameter of 2 mm, the atoms are pushed into the science glass cell. In this configuration the source MOT delivers an atom flux in the order of $10^7 - 10^8$ atoms/s in the

¹ The conductance is taken from the datasheet of ColdQuanta (Infleqtion) cold atom source cell (CASC) it's a 0.7 mm diameter pinhole on 1 mm thick silicon substrate.

² Image from ColdQuanta (Infleqtion) CASC datasheet

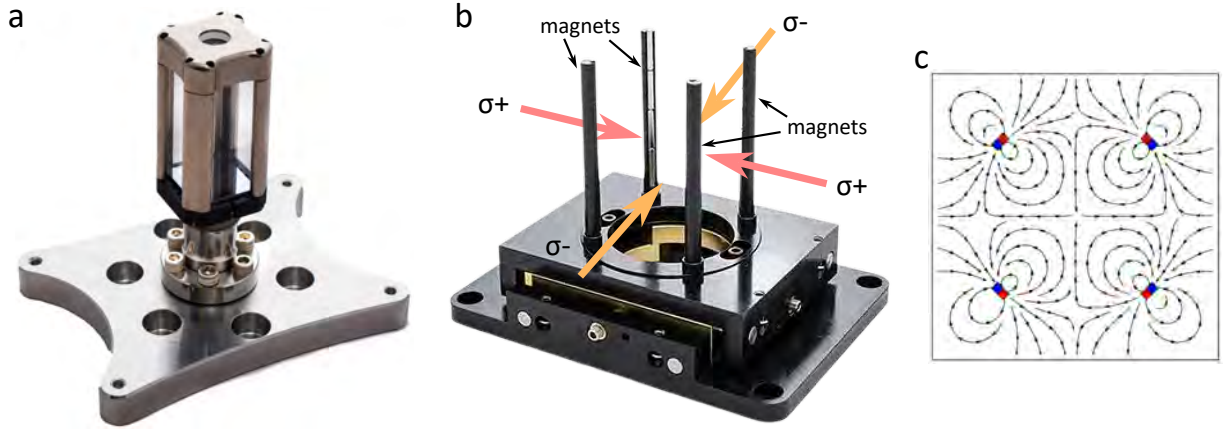


Figure 5.2: (a) The source glass cell on the stainless steel adapter plate ². The pinhole on the silicon end plate is visible in the middle. The 0.7mm diameter pinhole creates a differential pumping of 0.05 l/s to isolate the high vapour pressure of Rb when the dispenser is operating. (b) The 2D+ MOT magnet assembly ². The black aluminum base is the translation stage that attaches to the stainless steel adapter plate (in (a)) for aligning the 2D quadruple zero B-field location, which determines the 2D+ MOT location, w.r.t. the pinhole. (c) The field line of the B-field gradient created by the permanent bar magnet viewing from the rear of the assembly (axial direction of the 2D MOT) ².

science cell. To measure the exit velocity of the atom beam as well as the transverse temperature, a retro-reflected probe beam is set up to measure the size and vertical drop of the atom beam near the end of science cell. The probe beam, launched vertically along the gravity, is retro-reflected to reduce momentum kick on the atoms. It is on resonance and has an intensity around $10 I_{sat}$ with 5% repump co-propagating. The measured vertical drop is 3 mm and transverse FWHM is 4.2 mm. Using the simple free fall equation $\Delta y = \frac{1}{2}gt^2$ we can calculate the time it takes for the atom beam to travel the distance between the 2D+ MOT and the end of the science cell, which is around 30 cm. Thus we infer the atom beam exits the 2D MOT cell with a velocity of 12 m/s, and with eq. 5.1 we calculate the transverse temperature of the pre-cooled atom beam to be $\sim 80 \mu\text{K}$.

$$\sigma_f = \sqrt{\sigma_i + \frac{k_B T}{m_{Rb}} t^2} \quad (5.1)$$

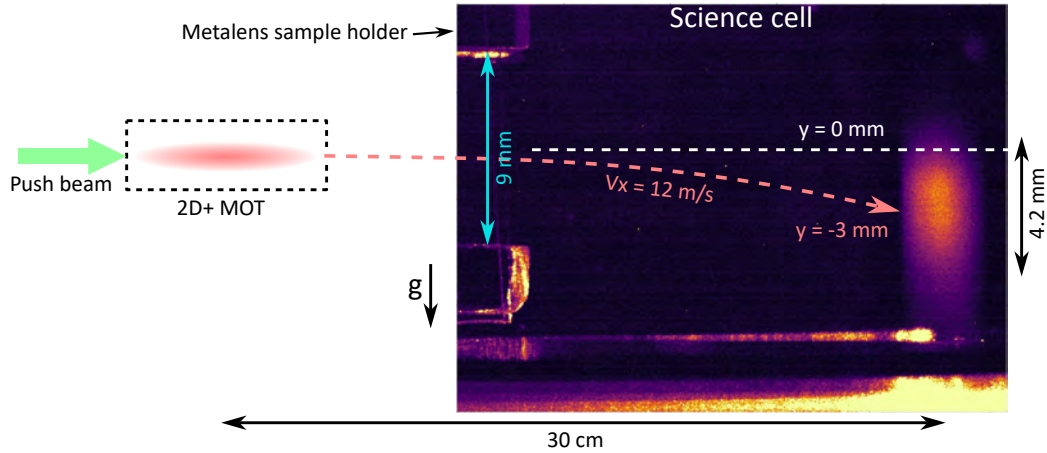


Figure 5.3: A schematic showing the source MOT w.r.t. the science cell and probing of the Source MOT atom beam that is cooled in transverse direction. The probe beam is launched vertically (along the gravity direction) and retro-reflected to minimize momentum kick of the probe photon. Probing at the end of the science cell (30 cm from the 2D+ MOT) shows the atom beam had an FWHM of 4.2 mm and a vertical drop of 3 mm. This allows us to calculate the atom velocity to be 12 m/s using free fall equation and infer the transverse temperature of the atom beam to be $\sim 80 \mu\text{K}$ from divergence of the beam. From the loading rate of our 3D MOT we estimate the atom flux in the science cell is in the order of $10^7 \sim 10^8$ atoms/s.

5.2.2 Science glass cell AR coating

Uncoated glass surface on the science cell will create unwanted interference if input laser light is collimated and nearly normal incident. This will create intensity fluctuation in the order of 10% which will be detrimental for the optical tweezer. To circumvent this, we coat the outer surface of the science cell with AR coating. There are two types of AR coating, the coating on the top and bottom is designed for 35° AOI for the science MOT beams shining at that angle. For the front and back, the coating is designed for 0° AOI for the tweezer light incident almost perpendicular to the cell wall. The coating is designed using Thin Film Cloud software from LightMachinery¹. Then a test coating is made on a glass sample and the reflection is measured using a spectrophotometer. Due to the high temperature required for anodic bonding. The reflectivity of the coating on the sample is measured again after subject to various thermal cycling with temperature ranging from

¹ The Thin Film Cloud is a web based design software where the optimization is run on LightMachinery's server. It can be access through <https://lightmachinery.com/optical-design-center/thin-film-cloud/>.

200 °C to 300 °C. After thermal cycle, the coating shows minimal shift in reflectivity and bandwidth [Fig. 5.4(b)].

The AR coating consists of alternating layers of high and low index of refraction dielectric thin films. The thin films are deposited through ion beam sputtering in an argon atmosphere. The AR coating layer stack up are described below, the high index material is TiO_2 and low index material is SiO_2 and numbers are in nm.

- 0° AOI AR coating: Pyrex, H 39, L 50.6, H 79.2, L 163.6, Air
- 35° AOI AR coating: Pyrex, H 9, L 154.7, H 2.6, L 208.6, H 39, L 24.5, H 121.4, L 151.6, Air

To coat the cuvette that will become the science cell, a special holder is made to only expose one side of the science cell to the sputtering target at a time [Fig. 5.4(a)]. The two different coating display a different hue when viewing under room light [Fig. 5.4(a) bottom]. After coating the transmission is verified using Agilent Cary 5000 spectrophotometer. The maximum transmission of 96% is due to the inside of the glass cell not AR coated [Fig. 5.4(c)]. Taking that into account, the performance is similar to the typical AR coatings that are commercially available.

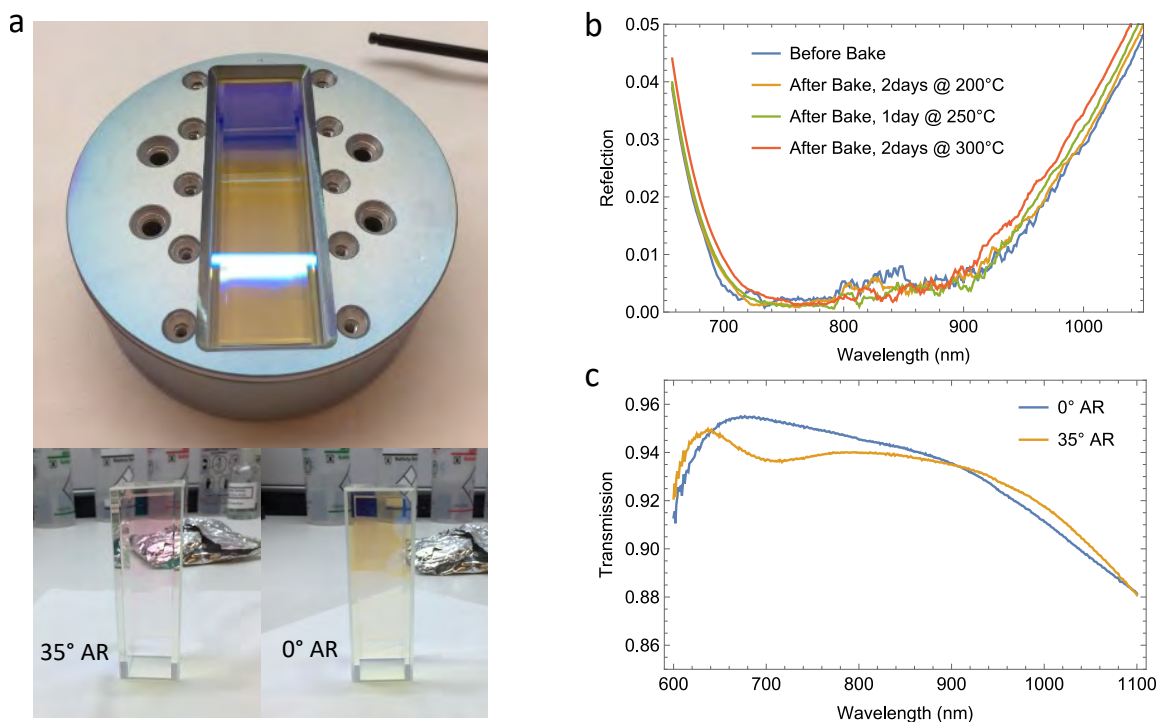


Figure 5.4: (a) Aluminum holder for holding the Pyrex cuvette in the ion beam sputtering chamber. The holder only expose one side of the cell at a time by masking other three side of the cuvette. Teflon gasket is used to press against the cell to prevent metal directly contacting the glass. (bottom left) The side with AR coating optimized for 35° AOI showing a pinkish hue. (bottom right) The side with AR coating optimized for 0° AOI showing a brown hue. (b) AR coating reflectivity after thermal cycling to temperature up to 300°C . The coating changes slightly after thermal cycling, but not significant enough to effect the functionality. (c) Transmission curve measured with the Agilent Cary 5000 spectrophotometer. Measurement include losses from the uncoated side of the cuvette. Blue trace is the transmission of AR coating optimized for 0° AOI. Brown trace is the transmission of AR coating optimized for 35° AOI. The performance of the coating is very similar to the coating that are commercially available.

5.2.3 Science glass cell

The science glass cell consists of three parts, the AR coated Pyrex cuvette, silicon adapter and the glass to metal transition. The cuvette was purchased custom made from FireflySci Inc. with wall thickness of 3.5 mm and outer dimension of 26 mm x 26 mm x 70 mm [Fig. ??(a)]. The silicon adapter has an outer diameter of 38 mm with a square hole of 19 mm x 19 mm in the middle and is machined from a 3 mm thick double side polished silicon wafer also shown in [Fig. 5.5(a)].

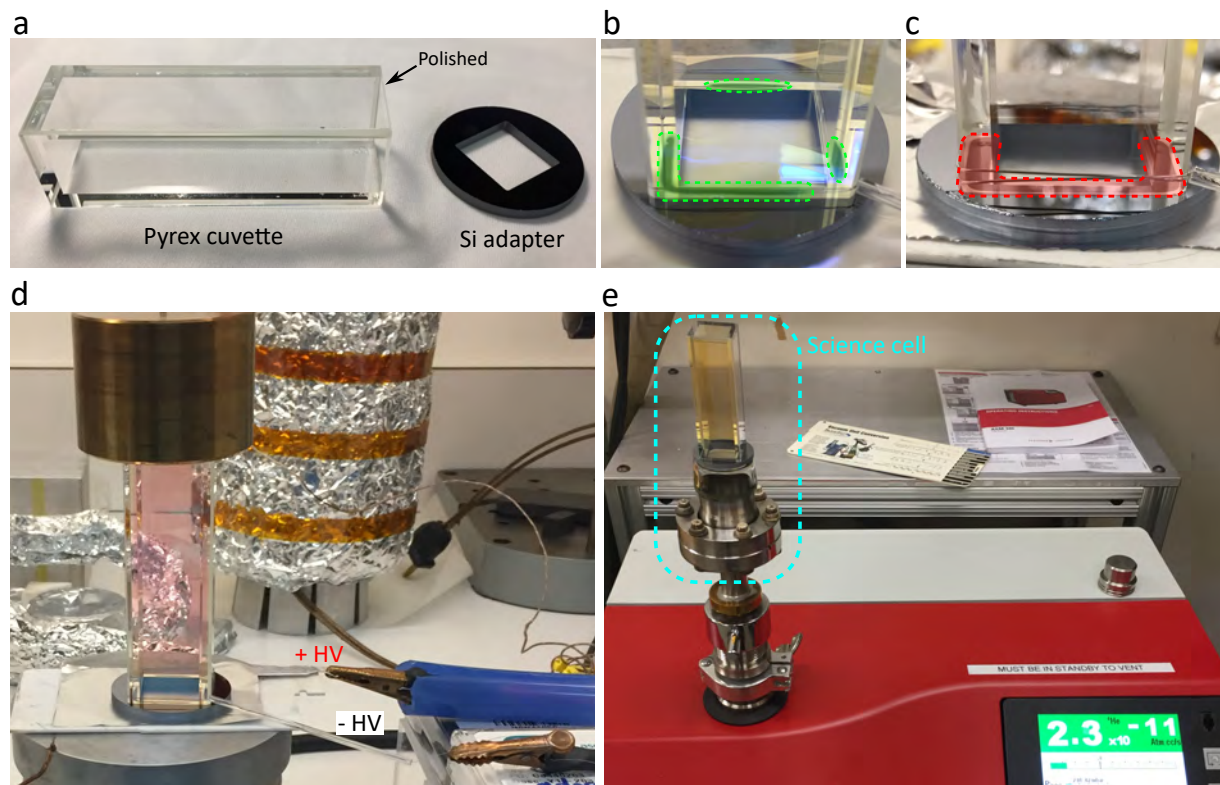


Figure 5.5: (a) The pyrex cuvette (left) is polished at the end for anodic bonding. The silicon adapter (right) is double side polished, 4 mm thick, 38 mm in diameter with a 19 mm square opening at the center. (b) Partially optically contacted (green shaded area) between pyrex cuvette and silicon adapter before anodic bonding. (c) Fully anodically bonded pyrex cuvette and the silicon adapter. The dark (red shaded part) area is the bonded region now fully extended around the polished edge of the cuvette forming a UHV seal. (d) The setup for anodic bonding the science cell cuvette and the silicon adapter. The hotplate at the bottom is set to 350°C with temperature ramp rate of roughly 3-4°C/min. The electrical connection to the pyrex (negative) and silicon (positive) is visible on the right. A brass weight is placed on the top to maintain pressure for good thermal connection to the hotplate and prevent the stack from shifting. (e) The completed cell connected to the helium leak checker. The leak rate is tested to be $< 5 \times 10^{-11}$ Atm · cc/s

The end of the glass cell and glass to metal transition are polished to an optical polish with flatness better than 1λ per cm. If the components are sufficiently polished and clean placing them together will show regions that are optically contacted [green shaded in Fig. 5.5(b)]. To anodically bond the parts, electrodes are attached to the Pyrex (negative) and the silicon (positive) parts and the assembly is heated to 350°C at a rate of 3-4°C/min. A metal weight is placed on the assembly to keep gentle pressure on the parts [Fig. 5.5(d)]. After the temperature stabilized at the bond

area, high voltage is applied and the bond is formed between Pyrex and silicon [red shaded region in Fig. 5.5(c)] become a UHV seal. Two anodic bond are performed to bond the Pyrex cell to the silicon adapter and then to the glass to ConFlat 2.75" adapter. For a more detailed procedure and description of anodic bonding see appendix C. After bonding the components together, the completed science glass cell is helium leak checked with a Pfeiffer Vacuum ASM 340 leak detector to a level $< 5 \times 10^{-11}$ Atm · cc/sec [Fig. 5.5(e)].

5.2.4 Metalens sample mounting

In high NA application, any stress on the substrate will cause wavefront distortion on the metasurface. In order to maintain the flatness of the metasurface, the substrate is mounted to the sample holder through optical contact bonding. Optical contact bonding is an adhesive free bonding method that rely purely on the Van der Waals force between the two surfaces. Due to this nature, the flatness is preserved and the bond can withstand high temperature (typically up to 250 °C) during UHV baking from the lack of adhesive. One of the requirement to achieve optical contact bonding is the surfaces needs to be optically flat. Typical surface flatness to achieve bonding is around $\lambda/4$ per cm or better depends on the thickness of the substrate. In the metalens experiment the sample holder is machined from a fused silica wedge window (Thorlabs P/N WW41050) with a 0.5° wedge, this eliminates any residual interference between the metalens substrate and the uncoated inner surface of science cell. The sample holder is glued to the inside of science glass cell with Epo-Tek 353nd high temperature low outgassing UHV compatible epoxy. Then the metalens substrate is optically contact bonded to the C-shaped sample holder [Fig. 5.6(a)]. Afterwards, the cell is baked and UHV of $10^{-10} - 10^{-11}$ torr is reached [Fig. 5.6(b)] is metalens sample in experiment after UHV baking.

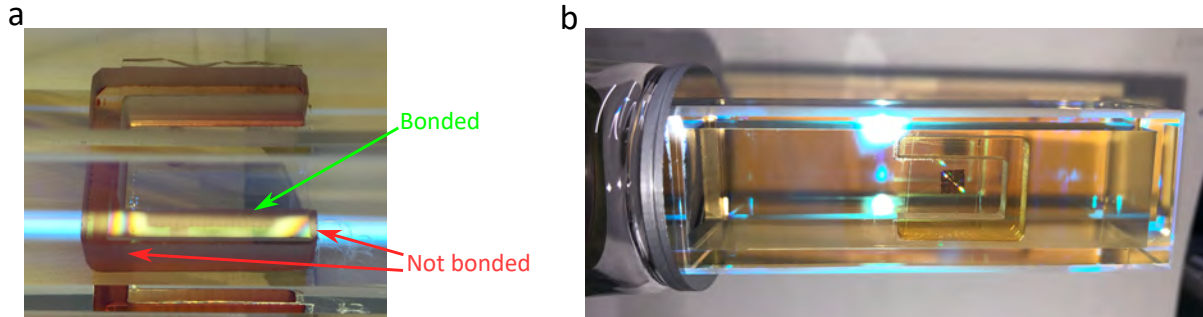


Figure 5.6: (a) Sample mounted with optical contact bonding on the C-shaped sample holder epoxied onto the inside of the glass cell with Epo-Tek 353nd. The sample holder, machined from a Thorlabs fused silica window, has a 0.5° wedge to prevent interference. Most of the substrate near the center are bonded (dark region) and the outer part of the substrate are not bonded (interference fringes are visible). Even though the edges are not fully bonded, it provides enough adhesion to secure the sample. (b) Sample mounted in the science cell connected to the rest of the vacuum system and after the vacuum bake. The pressure after the bake is typically between $10^{-10} - 10^{-11}$ torr.

5.3 Metasurface Overview

Metamaterials are artificially engineered materials that exhibit properties that ordinarily do not exist in the constituent materials. Electromagnetic metamaterials typically consist of sub-wavelength geometric structures that can significantly modify the resulting materials' response to electromagnetic waves depending on the geometry of these structures. Metamaterials were first explored in the 1950's in the form of artificial dielectric in the microwave spectrum [158–160] in applications such as beam forming and antennas. During the study of artificial dielectric, it was found that the response of these subwavelength structures to electromagnetic radiation, either as lumped element resonators or particles, behave as dielectric medium with an effective permittivity and permeability. The values of the permittivity and permeability can be designed to be arbitrarily large or small even negative, which does not exist in nature. The electromagnetic properties of these particle ensembles solely depend on the shapes, sizes and arrangements and not the intrinsic properties of the material. For example, these artificial dielectrics can be made into lenses [Fig. 5.7(a)] by changing the geometry of the resonator structure and achieving dielectric constant as high as 225

(index of refraction of 15) [159,161] which allows the lens to be made very thin comparing to the freespace wavelength of the operating microwave frequency. The dielectric constant of the aforementioned lens is not possible with ordinary materials. More recently, with advances in fabrication and computational numerical simulation of electromagnetic waves in late 1990's, the first microwave metamaterial exhibit negative refractive index is developed in 2001 [162]. This composite material consists of coupled sub-wavelength split-ring resonators and is the first metamaterial that exhibit physical properties that is not available in nature [Fig. 5.7(b)]. This is the first metamaterials that uses the concept of meta-atoms similar to the one uses in modern metasurface which we will introduce next.

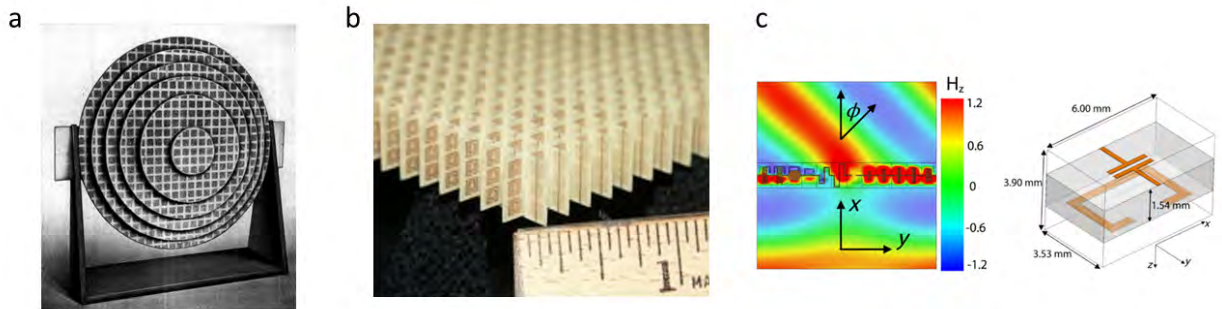


Figure 5.7: (a) Artificial dielectric microwave lens formed with subwavelength metallic structure (dark square) arranged on support structure (large white disks) to create effective dielectric constant as large as 225. Image from ref [161] (b) Photo of composite microwave metamaterial that exhibit negative refractive index. Image from ref [163] (c) Microwave Huygens metasurface designed to deflect 40° . Image from ref [164]

5.3.1 Optical metasurface

optical metasurfaces are planar metamaterials that operates in optical spectrum. They are planar photonic elements typically composed of periodic array of of subwavelength dielectric or metallic nanostructures with their thickness normally ranging from 0.1λ to 1λ [165–167]. These nanostructures couple to the incoming electromagnetic radiation either resonantly or off-resonantly, and re-radiate with a transformed phase, polarization, and amplitude determined by the nanostruc-

ture's shape, size, and material composition. Due to fabrication challenges, optical metasurfaces are not feasible until the last two decades where nanofabrication technologies are more accessible in academic settings [165, 168, 169].

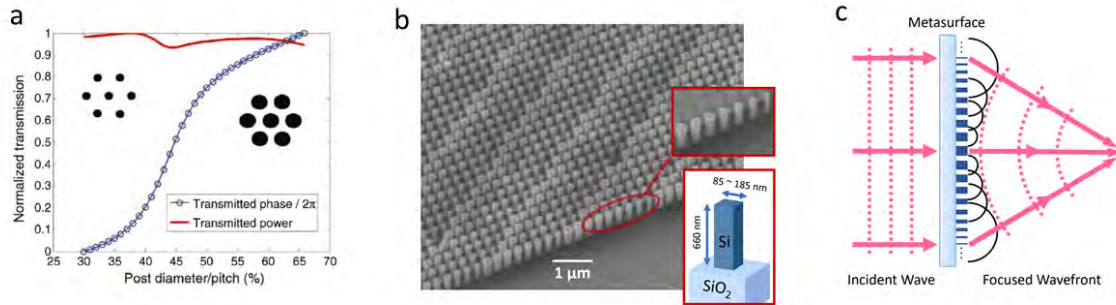


Figure 5.8: (a) Plot showing transmission and phase of light after transmitting through the nanopillar of diameter and pitch ratio. The optical transmission remains near unity while the phase varies from 0 to 2π . This is the basic requirement for metasurface that will be used as a phase shifting element [77]. (b) Scanning electron microscope image of the nanostructure that creates a spatially varying phase profile with sub-wavelength resolution. The pillars are silicon of 660 nm height with variable square cross section on fused silica substrate [115]. (c) Notional illustration of metasurface lens where the incident plane wavefronts (pink dashed lines) interact with the metasurface and creating secondary wavelets (black semicircles) with various phase profile which interferes at the far field to create the desire wavefront [115].

Conventional optics relies on refraction and reflection where the wavefront shaping (optical phase) arises from the propagation of light with varying optical path length, either through media with different index of refraction or different path length. In the contrary, metasurface introduce the optical phase shift via the interaction of the nanostructure (nanoscatterer) with the incoming electromagnetic wave (this is also the distinction between metasurface and conventional diffractive optical elements). These interactions, which is deterministic, can create abrupt changes in optical properties of the transmitted/reflected light in a distance that is a fraction of the operating wavelength of the metasurface. One criteria for the nanoscatterer is to achieve a full 2π phase shift while maintaining high optical transmission, one method to achieve this is changing the pitch to diameter ratio of the pillars [Fig. 5.8(a)]. By changing the configuration of the nanoscatterer (for

example, size shape, spacing and orientation), the array of nanoscatterers create a spatially varying optical response with subwavelength spatial resolution [77, 170], [Fig. 5.8(b)] shows an SEM image of a metasurface with nanoscatterer arranged in subwavelength spacing for wavefront manipulation. The re-scattered light is then interfered at the far field to create the desire optical wavefront [Fig. 5.8(c)]. Thus metasurface are conceptually similar to reflectarrays and transmitarrays in microwave and millimeter-wave community [171, 172].

5.3.2 Anisotropic plasmonic nano-antennas

When the optical metasurface was first demonstrated in the mid-IR [165] and NIR [168], it was based on nanoscopic metallic metal antennas. In order to fully control the optical wavefront, these subwavelength antenna needs to be able to scatter with phase shift relative to the incident light up to 2π and the ability to change the polarization of the incident light. Ref. [173] shows that a plasmonic element supporting two independently tunable resonance mode that are orthogonal can provide enough degree of freedom to completely control the amplitude, phase and polarization of scattered light, therefore, suitable for application in metasurface. The V-shaped design of the plasmonic nano-antenna used in Ref. [165] is one example that support individually tunable resonance mode [Fig. 5.9(a)]. The symmetric mode, excited by one linear polarization, creates current symmetric to the bend. The antisymmetric mode, excited by the orthogonal linear polarization, has the current flowing across the bend over the whole antenna. By tuning the angle Δ and the arm length h of the antenna and the relative angle of the antenna with respect to the incoming linear polarization (along y-axis) a complete control of phase of scattered light in the opposite polarization can be achieved. The grey-scale shading on the antenna in [Fig. 5.9(a)] is the current density of the resonator mode [173]. The simulation of an array of nano-antenna to find the angle needed to achieve a specific phase delay. These antennas, when excited by a y-polarized incident light, each scatters in x-polarization and creates $\lambda/8$ ($\lambda = 8 \mu\text{m}$) more phase delay than the previous element [165, 173] [Fig. 5.9(b)].

An array of nanoantenna arranged to create a periodic $0-2\pi$ linear phase gradient over the

period of $11\mu\text{m}$ [highlighted yellow in Fig. 5.9(c)] allows efficient negative reflection and refraction (negative index of refraction) with up to 30% efficiency [165]. The same plasmonic nano-antenna can also be arranged to create light with angular momentum [165]. A vortex waveplate of $L=1$ is created for $\lambda=8\mu\text{m}$. To create such waveplate, different zones consists of each types of the antenna from [Fig. 5.9(a)] are arranged to generate a phase shift that varies from $0-2\pi$ azimuthally [Fig. 5.9(d)]. The resulting vortex beam is analyzed by interfering with a Gaussian beam through a beamsplitter creating a interferogram with a distinct y-shaped fringe at the center [Fig. 5.9(e)].

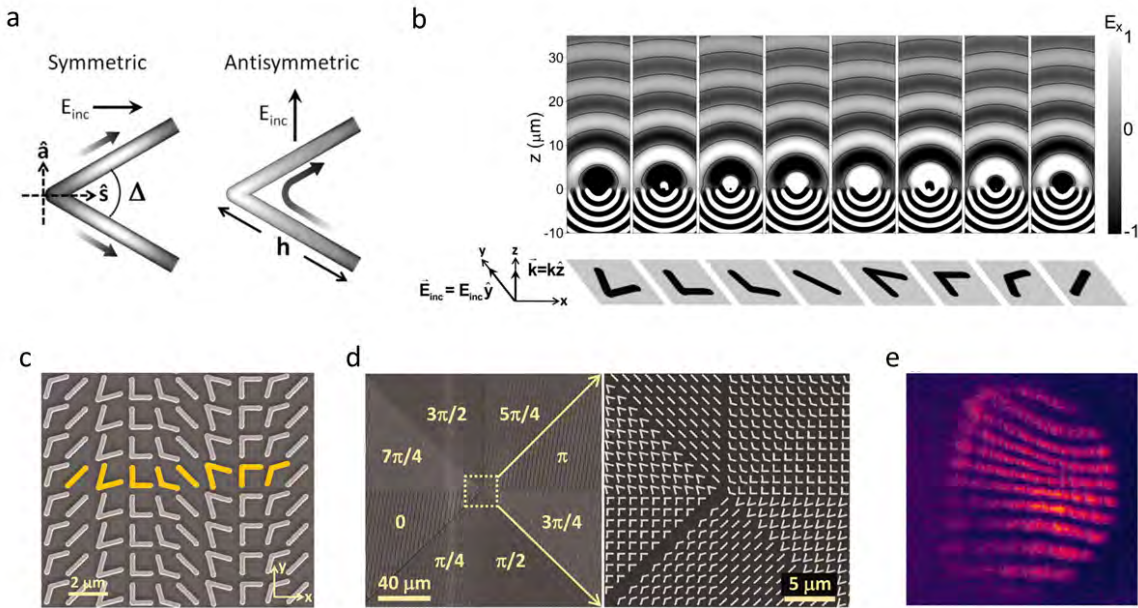


Figure 5.9: (a) Scanning electron micrograph of gold nano-antenna of 50 nm thick. The highlighted portion corresponds to nano-antenna that creates a phase shift spanning $0-2\pi$ [165]. (b) Scanning electron micrograph of nano-antenna arranged in a vortex waveplate configuration. The eight sections creates a linear phase from $0-2\pi$ azimuthally [165]. (c) Interference between the vortex beam and a tilted Gaussian beam through a beam splitter creating a distinctive interference pattern with a Y shape fringe at the center [165].

5.3.3 Dielectric metasurface

The plasmonic metasurface successfully demonstrate the fundamental principle of metasurfaces. However due to their plasmonic nature, they need to be fabricated with deep sub-wavelength

thickness. This causes large ohmic losses and combining with the reflectivity of the metal limits their use in practical applications especially in transmission mode [77, 174].

This leads to significant effort in developing dielectric resonators due to wide selection of dielectric materials that are intrinsically low loss in optical wavelengths. The first dielectric counter part of plasmonic antenna are silicon dielectric antennas where they can be designed to exhibit strong birefringence. The anisotropic response of the silicon nanobeam antenna and the Pancharatnam-Berry phase optical elements enable highly efficient transmissive metasurface devices [175]. Similar to the plasmonic nano-antennas, Pancharatnam-Berry phase is a geometric phase added to the light, on top of the polarization conversion, when transmitted through a waveplate. The Si nanobeam antennas are designed to be half-waveplates that convert the helicity of circularly polarized light while adding the Pancharatnam-Berry phase according to the following relation [175].

$$\phi_{pb}(x, y) = \pm 2\theta(x, y)$$

Here $\phi_{pb}(x, y)$ is the added phase between input and scattered light as a function of spacial coordinate (x, y) across the metasurface. $\theta(x, y)$ is the angle between the fast axis of the nanobeam antenna and the incoming polarization.

Similar to the plasmonic nano-antenna, the two orthogonal mode (TE and TM) of the silicon nanobeam antenna with a 2π phase delay, give rise to the birefringence [Fig. 5.10(a)]. Depends on the angle of input polarization θ a linear combination of the two mode are excited, with the 2π phase shift between the TE and TM mode any arbitrary phase delay between $0 - 2\pi$ can be realized. To test the efficiency of the Si nanobeam antenna a grating is constructed by arrange the Si nanobeam in close spacing with a periodic phase profile and the measured diffraction when light of different polarization incidents the metasurface [Fig. 5.10(b)]. The efficiency is high for this grating [Fig. 5.10(b)] but the response of the metasurface is strongly dependent on the input polarization and only work with circularly polarized light.

In order to create metasurfaces without polarization dependence, another type of dielectric

resonators were created. This type of resonators has isotropic response to the incoming light, thus no birefringence. Instead, the phase control between the input and output are tuned through the pitch/diameter ratio of the silicon nanodisks [176]. However, due to the varying diameter of the nanodisk they inadvertently have resonances that will cause discontinuity in phase and low transmission. To eliminate the resonance reflection in the nanodisk dielectric resonator to maintain high transmission throughout the full $0-2\pi$ phase delay, both electric and magnetic dipole modes are utilized. The TE and TM excitation [Fig. 5.10(c)] have similar resonance frequencies but opposite phase destructively interfere, which creates near unity transmission around the resonances [176,177]. This type of metasurface is called Huygens' metasurface due to lack of the use of Pancharatnam-Berry phase.

A Huygens metasurface grating is constructed with periodically varying diameter (in this case 50 nm spacing between the disk while the disk radius ranges from 115 to 155 nm) of densely packed nanodisk resonators, visible within a unit cell in [Fig. 5.10(c)]. The measure deflection showing high efficiency into the first order and it is polarization insensitive [Fig. 5.10(c) bottom].

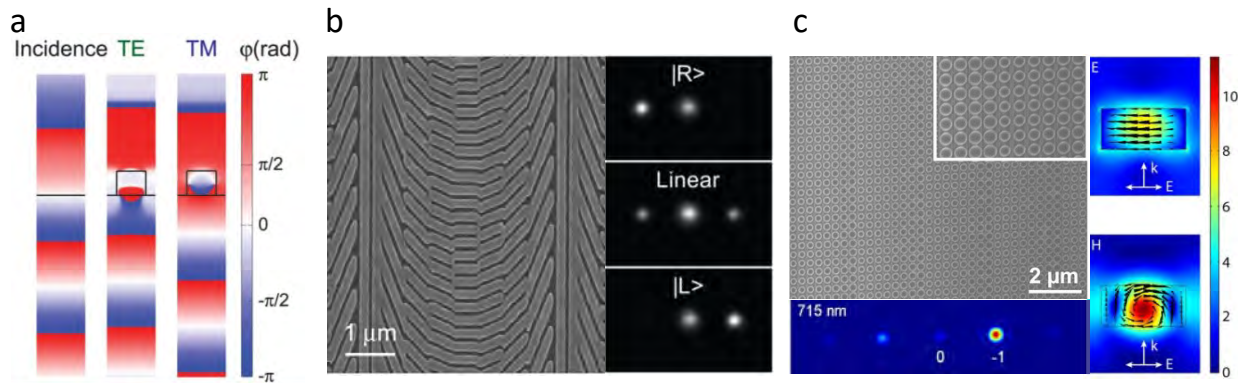


Figure 5.10: (a) The electric field simulation of dielectric nanobeam antenna where the two polarization excite the orthogonal TE and TM resonance mode that has 2π phase shift [175]. By rotate the angle of the input polarization, different linear combination of the TE and TM mode can be excited thus create arbitrary $0-2\pi$ phase delay. (b) A grating created with the nanobeam antenna from [175]. Showing efficient diffraction, but the phase chirp direction is polarization dependent. (c) A polarization independent Huygens metasurface utilizing silicon discs that are tightly spaced together. This type of metasurface does not require polarization to achieve $0-2\pi$ phase shift, but they suffer from inter resonator coupling due to close spacing [176].

Even though both Pancharatnam-Berry phase and dielectric Huygens' metasurface overcome the low transmission of metal metasurface there are still some challenges limit its practicality. First, due to the constraint from the electric and magnetic dipole mode sometimes the height of the nanodisk resonator needs to change to achieve full $0-2\pi$ phase coverage [77]. This make the structure difficult to fabricate with standard nanofabrication technologies. Second, due to the resonance mode requirement of these resonators, they require subwavelength thickness which make the resonance modes have a lot of evanescent components. Combining with the dense spacing required in these metasurfacesm coupling to the adjacent nanoscatterer in both Pancharatnam-Berry phase and Huygens' metasurface are considerable [77, 175–177], which make the design of metasurface challenging without full simulation and the performance is also sensitive to fabrication imperfections. The strong adjacent resonator coupling also makes achieving large deflection angle (thus phase gradient) while maintaining high transmission is difficult [77], which is required in high NA application.

As a result, more groups shift their attention to metasurfaces using high-contrast transmit/reflect array (HCA). These types of metasurfaces uses thicker high-index dielectric where the height of the nanoscatterers are typically around 0.5λ to λ [77] surrounded by low-index medium such as air. The first of high-contrast array structure are blazed binary optical elements described in Ref. [178]. In the early HCAs the waveguides in the arrays are uncoupled so the spacing only allow one transverse mode to propagate and the collective propagation is equal to effective index of refraction of the individual waveguide [77], this is also called effective field theory (EMT) regime [178]. Later it is demonstrated that using higher-index refraction material can result in devices with higher efficiency for large deflection angles, despite having pillar spacing larger than the structural cut-off but small enough that other transverse mode are suppressed. Structural cut-off is the largest waveguide/resonator spacing where only one transverse mode is supported [178].

The frist high-NA demonstration of HCA metasurface uses Si-nanopillar where the TE and TM modes are well confined within the structure [167]. Even with different diameters the mode tructure all mostly concentrated within the dielectric resulting in a very little cross coupling between

the adjacent resonators [Fig. 5.11(a)]. This high efficiency, high-NA HCA metasurface lens designed for $\lambda = 1550$ nm [Fig. 5.11(b)] demonstrated focusing efficiency of 82% at the NA of 0.5 and 42% at NA of 0.97 while maintaining a diffraction limited spot [Fig. 5.11(c)]. The parameter d in [Fig. 5.11(c)] is the designed focal length of different metasurface lens all with lens diameter of 400 μm , which translate to NA ranging from 0.5 to 0.97.

With the use of high-index materials, HCAs allows the nanoscatterers to be designed individually due to stronger mode confinement and they can be designed with constant thickness over the full $0-2\pi$ phase while maintaining high transmission because multiple resonator mode contribute to a given phase delay [77,179]. This makes them the primary design approach in modern state of the art metasurfaces.

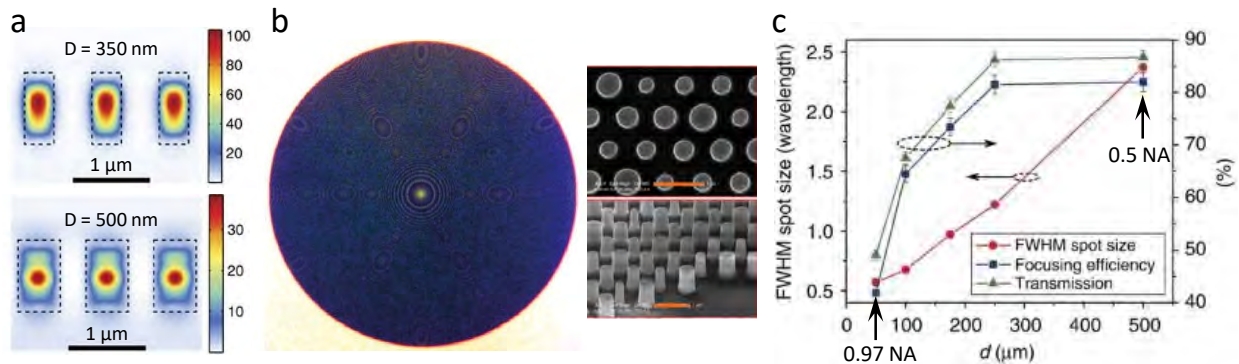


Figure 5.11: (a) Numerical mode simulation of HCA metasurface design. Shows the mode mostly confined inside the dielectric results in small resonator cross coupling [167]. (b) A high NA metalens constructed with HCA array showing a looser resonator spacing than shown in Fig. 5.10 [167]. (c) The efficiency and PSF measurement over samples with different NA shows high focusing efficiency at $\text{NA} > 0.7$ with diffraction limited performance [167].

5.4 Design principle of metasurface and metalens

Our nano-fabrication collaborators that is in charge of designing and fabricating the nano-pillar structures follows the general three step design flow [Fig. 5.12]. The design starts from acquiring the desire optical phase profile $\phi_i(x, y)$ for a specific wavelength λ_i . Here (x, y) represent the spatial coordinates on the metasurface device. The goal is to introduce a spatially varying phase profile when the light propagate through the metasurface, so when the transmitted wavefront interfere at the far-field it creates the desire effect. The phase profile can be obtained through several different methods depends on the application. For holograms, Fourier optics methods can be used to generate the phase profile. For gratings and beam deflectors, grating equations can be used to calculate the phase profile. For simple metalens, the following analytical form is used [78, 180].

$$\phi_i(r) = \frac{-2\pi}{\lambda_i} \left(\sqrt{r^2 + f^2} - f \right) \quad (5.2)$$

This is the hyperbolic phase profile that give no aberration for on-axis incident ray to focus to a diffraction limited spot. r in Eq. 5.2 is the radial distance from center which equals to $\sqrt{x^2 + y^2}$, f is the desire focal length of the designed metalens and λ_i is the design wavelength.

Early metalens demonstrated in Ref. [167, 181] uses this type of phase profile. The metalens demonstrated in this thesis also use the hyperbolic phase profile. Even though the on-axis performance of these type of lens is very good, the field-of-view is very limited and any off-axis incident angle quickly result in coma and astigmatism optical aberrations similar to a singlet plano-convex aspheric lens.

More advance simulation with ray-tracing software is required to generate metalens design that contains multiple surfaces or non-rotational symmetric, for example, metalens doublet or metalens achromatic lens. The tool we used in this thesis for ray-tracing simulation is OpticStudio from Zemax. For rotational symmetric phase profile, it is often approximate with the sum of polynomials described in the following form.

$$\phi(r) = \sum_n^N a_n \left(\frac{r}{R}\right)^{2n} \quad (5.3)$$

For free-form optical elements such as cylindrical lens or phase plate, a generalized polynomial expression is used.

$$\phi(x, y) = \sum_{m,n}^{M,N} a_{mn} x^m y^n \quad (5.4)$$

M, N are maximum polynomial order user define for approximation, typically order less than 16 is used. a_n and a_{mn} are coefficients of different polynomial orders. R is lens diameter normalization factor. With these expressions and parameters, a figure of merit can be defined and the coefficient can be found through ray-tracing optimization by minimizing the optical path difference(OPD).

The second step is to construct a library of nanostructure with full-wave electromagnetic simulation solver such as Lumerical or RSoft. This provide a connection between a given structure and the transmission and phase it can provide. Fig. 5.12(step 2) shows a simulated transmission and phase when light pass through a 660 nm tall silicon nanopillar of different diameter on fused silica substrate. This is the same library used in the metalens sample in Ref. [115].

The last step is the mapping of the nanopillar to the metasurface device. The phase of the pillar is digitized into few steps based on the steepest phase gradient in the phase profile $\phi_i(x, y) \pmod{2\pi}$. The resulting phase vs. position along the metasurface needs to satisfy the Nyquist criterion meaning the density of the pillar needs to be half the period created by the steepest phase gradient in the range of $0-2\pi$ [78]. Once the sampling coordinate (x_i, y_i) of the phase profile is determined, the pillar type can be match to the phase value and a layout file can be generated for lithography. Fig. 5.12(step 3) shows an example of a metalens layout file for lithography. Scale bar at the bottom shows the typical sampling density for nanopillars in high-NA metalens application. The quasi-periodic phase profile in the radial direction near the peripheral of the metalens is due to the phase wrapping every 2π of the steeper phase gradient of hyperbolic phase Eq. 5.2 at large radius.

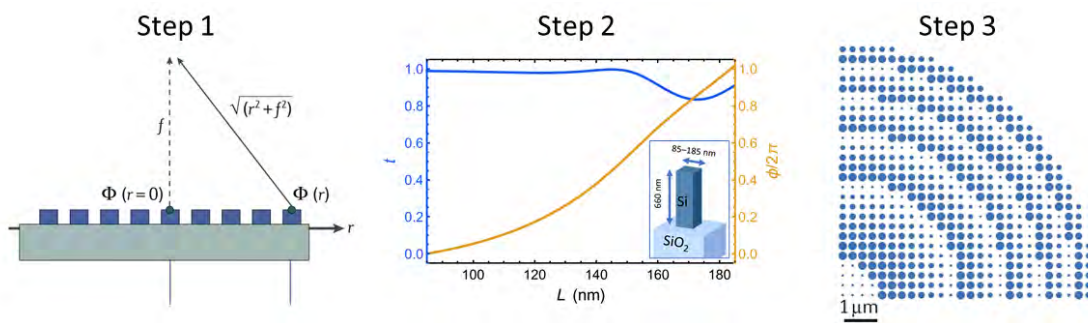


Figure 5.12: Steps for designing a metasurface. Step 1: obtain the desired phase profile, either with analytical form, computer simulation with Fourier optics method or commercial ray tracing software such as ZEMAX. Step 2: generate the desired nanopillar design through FDTD software such as Lumerical. Most common approach is parameter sweep of the pillar dimensions (diameter, height, pitch etc...). Step 3: Take the phase profile from step 1 and create a list of coordinates and phase where the nanopillars will be placed. The sampling depends on the conversion efficiency of the metasurface required and the steepest phase gradient. The sampling needs to satisfy the Nyquist criterion to sufficiently sample the phase profile [78].

5.5 Metalens sample

In this section we present the metalens samples used in this thesis and the optical characterization of the samples before they are put into the vacuum chamber for atom trapping. The samples are made in collaboration with Amit Agrawal and Wenqi Zhu from NIST Gaithersburg. The nanopillar designs, numerical simulations and sample fabrications are done by the collaborators. The optical design of the future metalens samples, for example the doublet and hybrid lens optical design are done in our group. There are several different combination of samples that was used in the metalens experiment. Including NA of 0.5 and 0.8, polarization multiplexed and non-polarization sensitive lenses and working distance (EFL) of 1 mm and 4 mm. We have attempted atom trapping with several samples but only was able to successfully detect atom signal with the 0.5NA, 4mm WD, non-polarization sensitive lens due to some fabrication challenges which cause the focusing efficiency to be low.

5.5.1 Non-polarization multiplexed lens

In this section we describe the metalens used in Ref. [115] for single atom trapping. Including the phase profile, materials used, fabrication steps and the optical testing of the metalens. Before designing the lens we need to identify the required NA, working distance, focal length and operating wavelength of the metalens. Due to restriction in optical access that is required for creating a MOT around the focus of the metalens we choose a less aggressive NA of 0.55 and a working distance of 3-5 mm. After taking into the consideration of electron-beam lithography time, which is directly proportional to the area of the metalens and thus proportional to the focal length square of the metalens, a shorter focal length of 3 mm is preferred. once the parameter is chosen, the size of the metalens is set to be 4 mm in diameter to achieve the required NA.

For trapping and imaging of single Rb atom, a 852 nm optical tweezer trapping light is used and detection of Rb D2 fluorescence at 780 nm is required. This set the two primary constraint on wavelength for nanopillar material selection. Since the tight optical confinement is more important

in this application, we choose to design the metalens primary at the trapping wavelength $\lambda_T = 850$ nm and with reduced performance at the detection wavelength of $\lambda_d = 780$ nm.

The metalens described in this section uses amorphous silicon (a-Si) nanopillars with square cross section. The square cross section allows for polarization independent phase delay. The substrate is chosen to be fused-silica due to optical transmission, flatness and ease of processing for sample mounting in the vacuum chamber for atom testing. Each nanopillar unit has side width L and height $H = 660$ nm, acts as a phase-delay waveguides that are weakly coupled to each other. Fig. 5.13(a) shows the SEM image of the fabricated metalens where the quasi periodic phase wrap over 2π can be seen as the width L changes. The zoomed in part of [Fig. 5.13(a)] shows the square cross section of the pillar and spatially varying width to create the spatial varying optical phase delay. The nanopillars are arranged in a square lattice with spacing of $a = 280$ nm, this ensure the pillars are sufficiently far apart to minimize cross coupling, but also dense enough to sample the fast varying phase gradient near the edge of the high NA phase profile.

To connect the nanopillar geometry to their corresponding phase delay, FDTD simulation with Lumerical is used to determine the side width L of the pillars. By vary L between 85 nm to 185 nm we create a library of unit-cell design that offers transmittance close to unity with relative phase shift ϕ covering the full 0 to 2π range. Fig. 5.13(b) shows the simulated transmission (blue line, left y-axis) close to unity and phase delay between incident and transmitted light from 0 to 2π (yellow line, right y-axis).

This design library is then used to implement the hyperbolic phase profile given by Eq. 5.2 [78, 180, 182]. where λ is the design wavelength (here, $\lambda = 852$ nm), f is the focal length (here, $f = 3$ mm), and r is the rotationally symmetric coordinates of sampled phase position relative to the lens center.

However, field-of-view simulations that we will introduce later requires the use of Zemax OpticStudio. Instead of using the analytical form of hyperbolic phase, OpticStudio uses the polynomial phase up to order N to approximate a given phase profile. Thus with good approximation we represent the hyperbolic phase profile with 5.4 up to 8 polynomial terms ($N=8$) and normal-

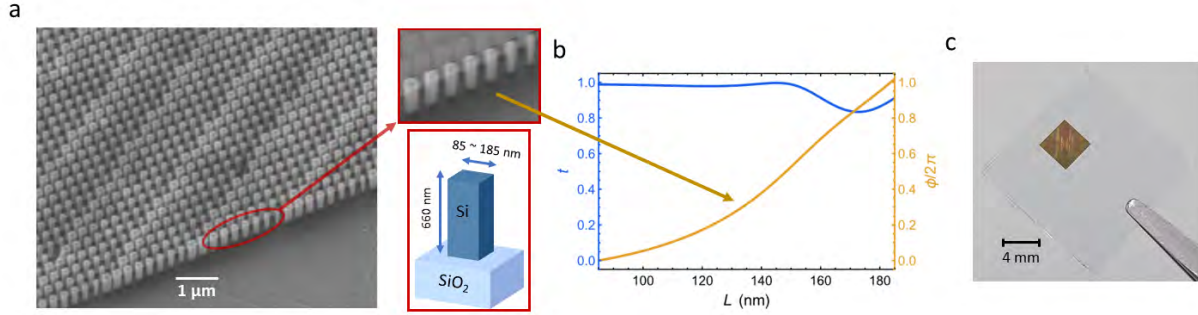


Figure 5.13: (a) Scanning electron micrograph of the fabricated metasurface lens containing a periodic array (lattice constant = 280 nm) of amorphous-Si nanopillars (height 660 nm) of width ranging from 85 nm to 185 nm (dark blue) on top of a 500 μm thick fused-silica substrate (light blue). Red box shows the varying nanopillar width to achieve the desired phase shift. (b) Transmittance t and phase shift ϕ as a function of nanopillar side length L . (c) photo of the sample used in single atom trapping experiment.

ization radius R of 2.3 mm. Then the coefficients a_n can be extracted for n up to 8. Fig. 5.14(a) shows the hyperbolic phase over the whole metalens before modulo- 2π . Fig. 5.14(b) are the zoom in part with modulo- 2π of different region in [Fig. 5.14(a)]. Near the center we see the phase wrap over 2π with increasing spatial frequency [Fig. 5.14(b) top] meaning the phase getting steeper as a function of radius. At the edge of the lens the phase are effectively a sawtooth profile [Fig. 5.14(b) bottom] of nearly the same spatial frequency over some large radius range (10-100 μm). For high-NA metalens, the phase gradient difference can be as large as a factor of 20, ranging from 0.03 $(2\pi)/\mu\text{m}$ near the center of the lens to 0.6 $(2\pi)/\mu\text{m}$ near the edge of the lens.

5.5.2 Metasurface fabrication

The metasurface optic is fabricated by depositing a layer of 660 nm thick amorphous silicon film (a-Si) on a 500 μm thick fused silica (SiO₂) wafer using plasma enhanced chemical vapor deposition (PECVD) [Fig. 5.15(a)]. The film thickness and index of refraction is checked with ellipsometry. Next, a 300 nm thick layer of electron beam resist (ZEP 520A) followed by a 20 nm thick layer of anti-charging conductive polymer (ESpacer 300Z) are spin-coated onto the a-Si film [Fig. 5.15(b)]. To write the nanopillar pattern a 100 keV electron beam lithography system is used

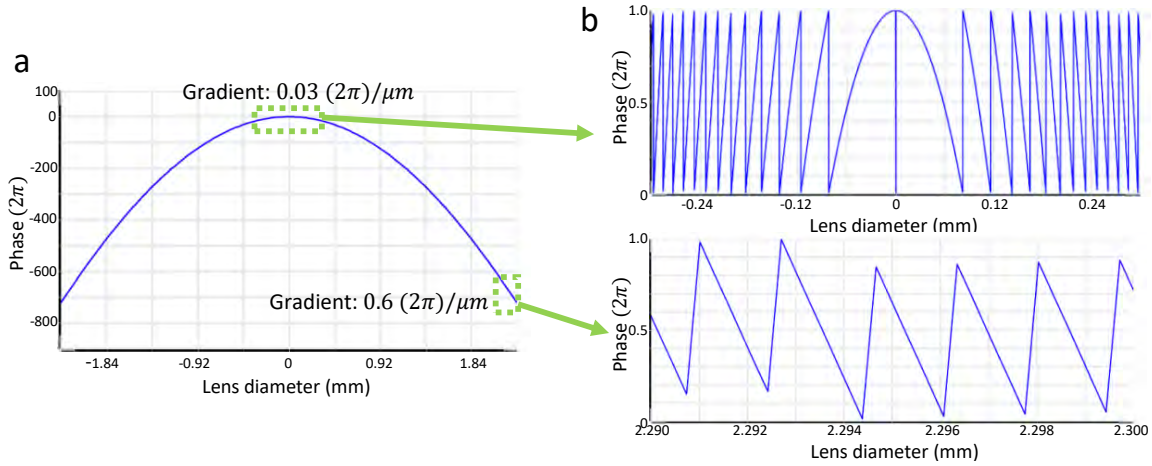


Figure 5.14: (a) The phase profile of a 0.55 NA ideal lens with focal length of 3 mm and diameter of 4 mm. (b) The phase profile after modulus 2π . This is the actual phase used for fabricating the metalens for single atom trapping. Top is the phase near the center, Bottom is the phase near the edge of the lens. We can see after 0.5 mm from the center, the phase can be approximate as sawtooth with gradually varying slope as a function of lens radius.

to expose the pattern onto the resist [Fig. 5.15(c)]. The ES Spacer 300Z is removed with deionized water at room temperature, and resist development with hexyl acetate at 4 °C. A 70 nm thick Al_2O_3 is electron-beam-evaporated on to the developed resist layer [Fig. 5.15(d)] and the pattern is transferred to Al_2O_3 after the ZEP resist is lift-off [Fig. 5.15(e)]. By using the patterned Al_2O_3 layer as an etch mask, the underlying a-Si film is etch off with inductively-coupled-plasma reactive ion etching (ICP-RIE) [Fig. 5.15(f)]. The following ICP-RIE parameters are used (gas mixture: SF_6 and C_4F_8 ; ICP power: 1750 W; radio frequency (RF) power: 15 W) at etch temperature of 15 °C to create the high-aspect-ratio a-Si nanopillars. The metasurface optics fabrication is finalized by soaking the wafer in a mixture of hydroperoxide and ammonia hydroxide solutions at 80 °C for 30 minutes to remove the Al_2O_3 etch mask and any etch residue [Fig. 5.15(g)].

5.5.3 Optical testing

In the next few sections we present the methods and result of testing the fabricated metalens through optical means. Before the lens can be put into the vacuum chamber it needs to be verified

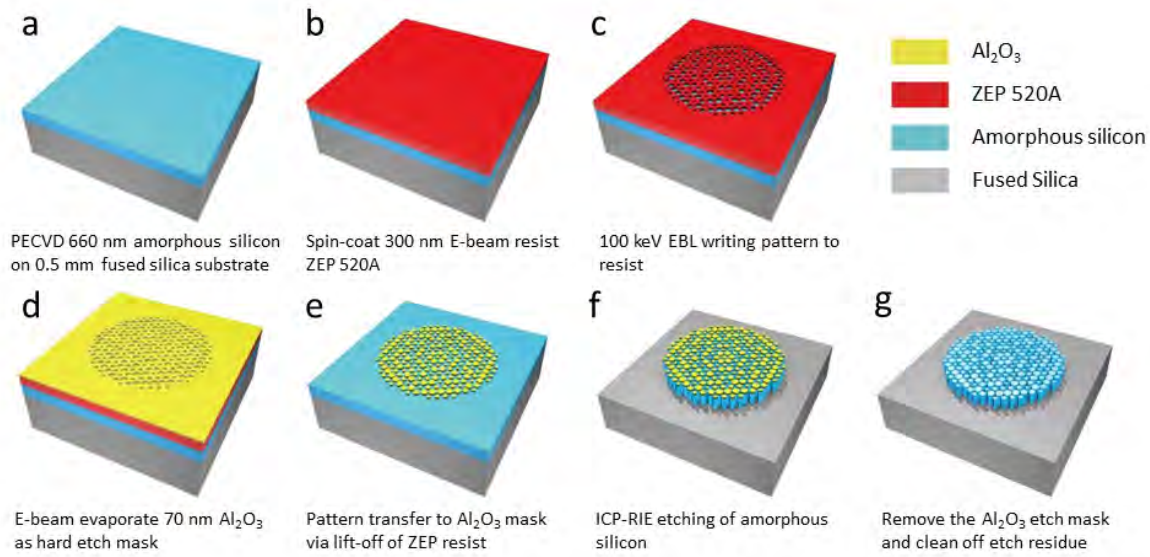


Figure 5.15: Metalens fabrication steps for the lens used in single atom trapping demonstrated in this thesis, figure adapted from Ref. [183].

that the optical performance is as designed. Some of the most important metrics to determine whether the metalens is good enough to be put into the vacuum chamber are

- (1) Focusing efficiency = power at focus / total input power to substrate
- (2) Diffraction limited performance
- (3) Chromatic performance including chromatic focal shift and spot size vs wavelength

Testing of the focusing efficiency is rather tricky due to the high-NA design of the metasurface lens. It is often difficult to separate light that is focused from forward scattered, non-diffracted, and absorbed by the nanopillars. Initially a subtraction method is used where the power of transmitted light at the far field (non-diffracted) is measured. However, it was later realized due to fabrication variability, assuming negligible losses in the material is not valid. There are significant amounts of forward scattering (not diffracted) component that is diverging, thus not being captured by the far-field power measurement and counted as part of focusing efficiency by error.

To mitigate these errors and obtain a much more accurate focusing efficiency a spatial filtering

technique is used, where only the light around the focus is sampled with a pinhole. The size of the pinhole is chosen so that it is much larger than the focused spot, however still small enough that it samples negligible portion of the scattered light and non-diffracted light.

A spatial filter is constructed with a collimated lens. This ensures the light that hits the power meter has consistent input angle to eliminate any angle dependent power measurement error. Fig. 5.16(a) shows the setup, the additional camera is used to check the spatial filter pinhole alignment by imaging the collimated beam after the asphere. Fig. 5.16(b) is another spatial filter constructed without the asphere. In this case the transmission efficiency of the asphere is eliminated, but the angular response of the power meter is added. We see the efficiency measurement difference in the order of a few percent between these two measurement methods [Fig. 5.16(a, b)]. Fig. 5.16(c) is the setup to measure the total transmitted power through the metalens. In this measurement the power meter with large aperture is placed sufficiently close so all the light through the metalens is captured.

The table below are the result of various metalens samples including some of the low NA lenses (sample number 1 and 2 in Table 5.1) for generating optical lattice and dipole trap. These sample exhibit higher transmission and focusing efficiency, but still not as high as what was reported in literature such as Ref. [167]. Sample # 4 is the only sample that ended up being tested with single atom trapping. This sample has acceptable focusing efficiency of 54 % at the detection wavelength of 780 nm. We will discuss some of the reason for low focusing efficiency in Sec. 5.6.6.

5.5.4 Metalens PSF with subwavelength pinhole

In this section we describe the method we use to test whether the metalens is diffraction limited. The purpose of this test is two fold. One is to verify that the metalens is diffraction limited at the design wavelength of 850 nm for tight single atom trapping. Second, is to test if the image system is good enough to allow single atom detection.

Testing a high-NA lens is always difficult due to increase sensitivity in alignment and lack of reference target that has sufficiently high resolution. There are several different approach for

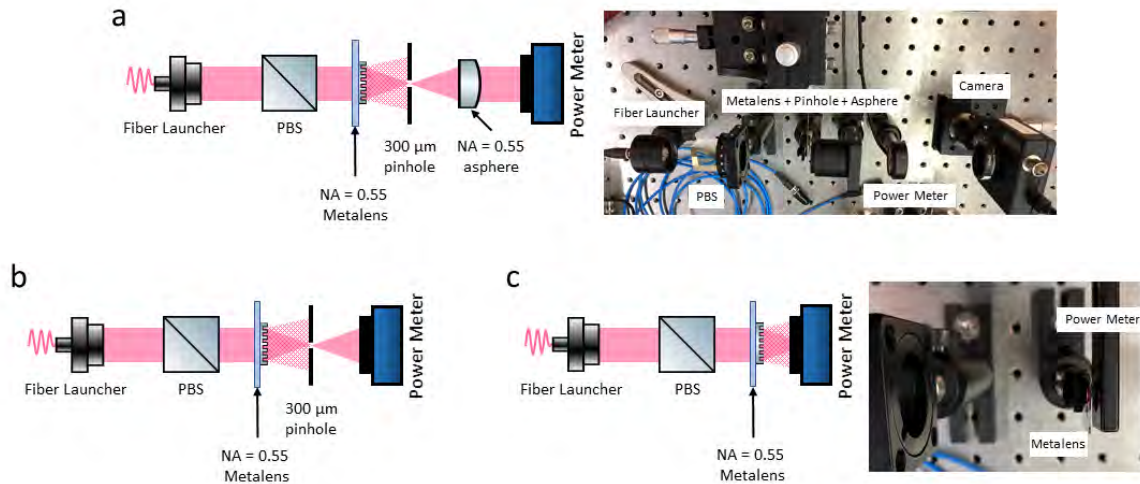


Figure 5.16: Two different types of spatial filter technique used to measure the focusing efficiency of the metalens. (a) uses an conventional lens to form a telescope with the metalens and the spatial filter pinhole is placed in between the telescope. This allows the power meter to be placed further away from the metalens. (b) directly filter out the unwanted light at the focus with the spatial filter and place a large power meter in a short distacne directly after. This might introduce angle dependent error from the power meter and is not suitable for high NA lens. (c) Setup to capture total power transmitted through the lens. A large area photodiode is placed as close to the metalens as possible.

measuring the performance of an imaging system. Including, measuring the MTF of the system, direct image of the PSF and using high resolution target. Out of all the options, the most common way is using an objective that has higher-NA to image the PSF of the device under test however this method has several drawback including.

- (1) Optical performance of the imaging objective is not guaranteed to be diffraction limited
- (2) Alignment can be difficult due to most commercial objective having no well defined optical reference surface for alignment (i.e. flat front or back optical surface).
- (3) Using aberration as a metric for alignment can be risky, due to possibility of some aberration being corrected by misalignment, for example, coma, astigmatism can be canceled by angular misalignment and spherical aberration can be partially compensated by defocus.

Due to high-NA for some of our metalens sample and potential drawback listed above, we

Sample #	EFL / NA / Wavelength	Total Transmission	Far-field Efficiency	Spatial Filter Efficiency	0-th order Leakage	Other Losses
1	EFL=150 mm, NA=0.001, 850 nm	72 %	48 %	43 %	24 %	5 %
2	EFL=150 mm, NA=0.001, 850 nm	70 %	44 %	38 %	26 %	6 %
3	EFL=1.5 mm, NA=0.8, 780 nm	54 %	41 %	13 %	12 %	29 %
4	EFL=3 mm, NA=0.55, 780 nm	67 %	not measured	56 %	not measured	11 %
	Same lens but at 850 nm	63 %	not measured	58 %	not measured	5 %

Table 5.1: Metalens Focusing Efficiency

decide to measure the PSF of the metalens by imaging a flat high resolution target. The target that we used is the same as in Ref. [101,122]. This target consists of 200 nm of silicon-nitride membrane on top of a 300 μm thick silicon substrate and 600 nm of gold coated on top of the membrane. A window through the silicon substrate is etched to create a suspended area of silicon-nitride and gold membrane. Two sub-wavelength pinhole with diameter of 300 nm are created with electron beam milling. The pinholes are 6.86 μm apart. Knowing the separation of the pinhole allow us to calibrate the magnification of the test image independent of the expected magnification of the optical system. Fig. 5.17(a) shows the test setup schematic for acquiring the image of the pinhole with the metalens. The two fiber launcher are for alignment of the metalens and illuminate the pinhole.

Once we have the pinhole image the following steps are taken to determine the performance of the metalens

- (1) The image is converted to real size on camera sensor with the pixel size of the camera (i.e.

pixel to length conversion). In this case each pixel is $4.4 \mu\text{m} \times 4.4 \mu\text{m}$

- (2) The magnification is calibrated by fitting the center of the two spots, calculate the distance and divided by the known separation ($6.86 \mu\text{m}$) of the pinhole. Once the magnification is known, the image is re-scaled to it's real size based on this ratio.
- (3) The gaussian waist ω_0 is extracted by fitting a gaussian function to the imaged point-spread function. The function is defined as

$$I(r) = I_0 \exp\left(\frac{-2r^2}{\omega_0^2}\right) \quad (5.5)$$

- (4) According to diffraction theory the image of a point source through a finite NA optical system results in a point-spread function (PSF) that can be described by the Airy function which is defined as below [101,153]

$$I(r) = I_0 \left(\frac{2J_1(\zeta)}{\zeta}\right)^2 \quad \text{where} \quad \zeta = \frac{2\pi r NA}{\lambda} \quad (5.6)$$

By fitting the imaged PSF to this function the effective NA of the optical system can be extracted.

Fig. 5.17(b) is the image of the pinholes through the metalens. Fitting the center of the two PSF, we determine the magnification to be $44.5(1)$, which is within 10% of the designed value of 49. On the right is the cross-sectional cut of one of the pinhole after re-scaling with the measured magnification. The red line is the fitted Airy function (Eq 5.6). A gaussian function (Eq 5.5) is also fitted to the same data. We extract a $1/e^2$ Gaussian waist of $0.72 \pm 0.02 \mu\text{m}$ and an effective NA of 0.53 ± 0.01 . This is sufficiently close to the designed NA of 0.55. So we deem that the metalens is diffraction limited at the tweezer wavelength of 850 nm.

5.5.5 Atom image system test

Another test we perform with the pinhole is the performance of imaging optics to compensate for the chromatic focal shift of the metalens between the trapping (850 nm) and Rb fluorescence

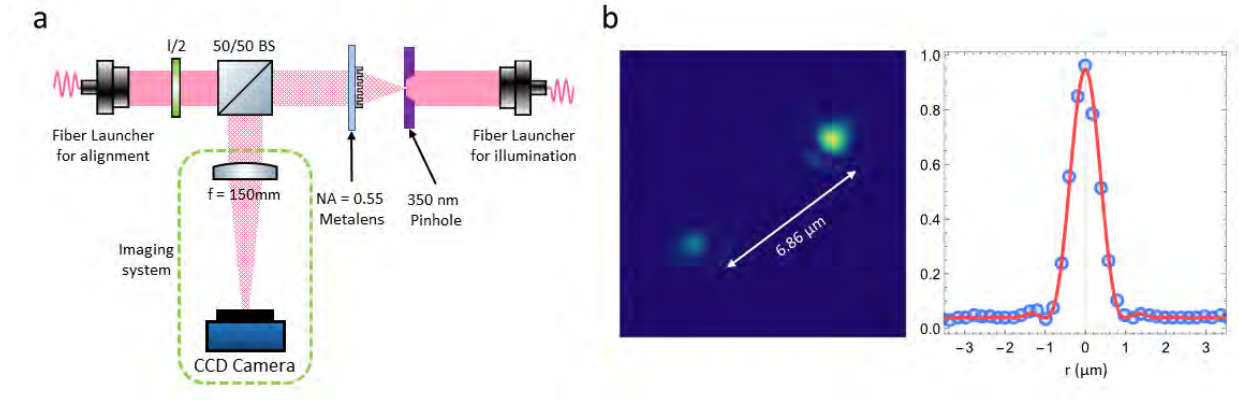


Figure 5.17: (a) Schematic illustration of the pinhole test to test the optical performance of the metalens. (b) The image of the pinhole from the metalens. The distance between the two pinholes are well calibrated. This allows us to calibrate the magnification of the imaging system. After calibration we can measure the Gaussian waist of $0.72 \pm 0.02 \mu\text{m}$

wavelength (780 nm). Opposite from conventional lenses, the focal length of the metalens increases as the wavelength increase. Fig. 5.18(a) shows the measured focal length of the sample 4 in Table 5.1. The focal length changes from 3.25 mm at 780 nm to 3.04 mm at 850 nm. This means the atom trapped at the 850 nm focus and emit 780 nm fluorescence will be at the location shorter than the 780 nm focus of the metalens. Thus the light will exit the metalens diverging. This diverging light once focused by a single imaging lens onto the camera will not be diffraction limited, further more, the diverging beam will be too large before reaching the imaging lens. In order to correct for this, a relay optical system is designed with two achromatic doublets (Thorlabs AC254-150-B) [L1 and L2 in Fig. 5.18(c)]. The first lens L1 is placed 111 mm away from the metalens. This creates a collimated light between L1 and L2 making the space between L1 and L2 infinite conjugate. The light is then focused by L2 onto the camera. In order to eliminate the extra degree of freedom introduced by adding the optical relay, the distance between L2 and the camera is pre-aligned by focusing a collimated beam on the camera. The only remaining adjustment to focus the whole image system is the distance between the metalens and L1.

[Fig. 5.18(c) right] are the Zemax OpticStudio simulation result of the imaging system showing diffraction limited performance of the optical relay lenses both on axis and off axis.

To test the imaging system, the green dashed portion in Fig. 5.17(a) is replaced by the imaging system from Fig. 5.18(c) without changing the distance between the metalens and the subwavelength pinhole. Once everything is aligned, the illumination light is changed to 780 nm and the image on the camera is focused by moving L1 w.r.t. the metalens.

Fig. 5.18(b) is the image of the pinholes at 780 nm. Following the procedure identical to 850 nm pinhole test, we measure the magnification to be 11.42. The measured PSF has $1/e^2$ Gaussian waist of $1.1 \pm 0.05 \mu\text{m}$ (correspond to NA of 0.32 ± 0.01) which is not diffraction limited (due to metalens has spherical aberration at 780 nm) but sufficient for single atom detection, and the effective solid angle for light collection is equivalent to 0.55 NA. The precise determination of the magnification is important because the magnification is not as easy to calculate in this more complex imaging system.

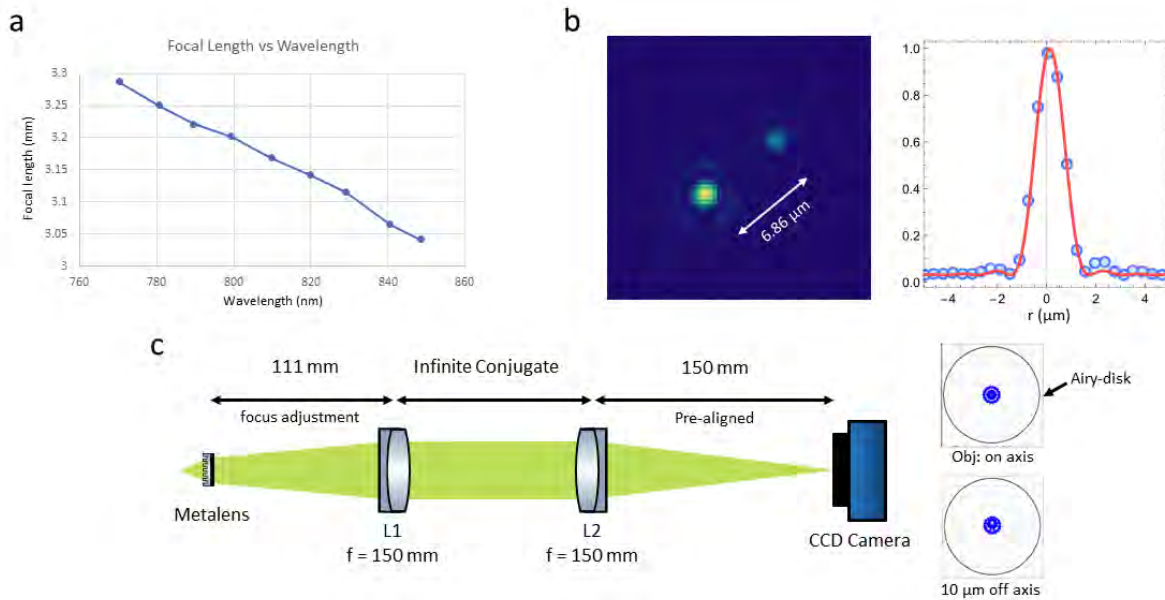


Figure 5.18: Metalens pinhole test, $\text{NA} = 0.323$ $\text{mag} = 11.42$ (d) Schematic illustration of optical tweezer imaging path with lenses that compensate for out-of-focus imaging due to chromatic focal shift introduced by the metalens. Insets are the ray-tracing simulation of the imaging system (object on-axis and $10 \mu\text{m}$ off axis) assuming metalens only has chromatic focal shift and no other aberration. The result shows L1 and L2 does not introduce additional aberrations. Black circle is the diffraction limited Airy-disk.

5.6 Testing with atom

In this section we present the result of single-atom trapping in a metalens generated optical tweezer array. After testing the 0.55NA metalens with the sub-wavelength pinhole and determine the optical performance of the lens. The metalens is put into the science glass cell by optical contacting the substrate onto the sample holder. The chamber is then baked at 200 °C for 5 days resulting in a vacuum environment of $< 10^{-10}$ torr measured at the ion pump.

5.6.1 Single atom loading and detection

Atoms are captured into the optical tweezers by overlapping the focus of the metalens with a magneto-optical trap (MOT) and applying polarization-gradient cooling (PGC) while the optical tweezer traps are on. The single atom loading starts with the three-dimensional (3D) science MOT. The atoms from the dispenser in the source cell are cooled in the transverse direction with MOT laser red detuned from ^{87}Rb $D2$ $F = 2$ to $F' = 3$ transition (free-space atomic resonance) by 14 MHz and transported to the science cell via a push laser beam. The collimated atom beam has a flux up to 10^8 s^{-1} . Fig. 5.19(a) is the image of the 2D source MOT viewed from the end. The science MOT loading lasts 500 ms with a typical MOT size of (3×10^7) atoms and a density of 10^9 cm^{-3} . Fig. 5.19(b,c) are image of the science MOT viewed from the front of the metalens and from the top perpendicular to the metalens substrate. This is also used to determine whether or not the MOT is aligned to the metalens focus.

After loading the science MOT, the source MOT lasers are shut off and the magnetic field gradient is turned off and the MOT lasers are changed to 144 MHz red detuned from free-space atomic resonance to perform PGC with $\sigma_+ - \sigma_-$ configuration for 15 ms. During the PGC the optical tweezer is turned on to load atoms into the tweezer. The typical free-space PGC temperature is between 30 μK to 50 μK , and the tweezer trap depth is typically at 1.3 mK during loading. During the PGC loading the laser is red detuned from the atomic resonance resulting in light assisted collision that assures only a single atom is trapped [3].



Figure 5.19: (a) Image of the source MOT (bright spot in the middle) viewing from the push beam direction. The diameter of the 2D MOT is ~ 1 mm. (b) Image of the science MOT in from of the metalens. Metalens (4 mm x 4 mm square) can be seen in the background. (c) Science MOT looking from the top, verifying that the location overlaps well with the metalens focus.

To image a single atom in the tweezer, we utilize PGC imaging. The PGC configuration with less detuning cools the atom while scattering photons. The trapped atom is illuminated with a $500 \mu\text{m}$ $1/e^2$ Gaussian waist and $150 \mu\text{W}$ PGC/probe beam propagating parallel to the substrate to avoid scattering off the metasurface (beam geometry shown in Fig. 5.20(c), $\approx 10I_{\text{sat}}$, 47 MHz red detuned from free-space atomic resonance) for 25 ms and the fluorescence is collected by the metalens (I_{sat} is the saturation intensity of ^{87}Rb $D2$ $F = 2$ to $F' = 3$ transition). After passing through the metalens, the slightly diverging fluorescence is reflected by a dichroic mirror and passed through the compensation and imaging lens (L1 and L2 in Fig. 5.18(c)) and focused onto a Princeton Instruments PIXIS 1024B CCD camera. While a full analysis of fluorescence collection efficiency requires calibration of the probe light intensity, trap depth and imaging path efficiency we can roughly estimate the expected CCD count. The total fluorescence collected in the experiment is around 2.5% which is consistent with the expected efficiency of 4.5% given some of the imaging elements not being calibrated. The data presented are in CCD counts and are not converted to photon count.

We first analyze in detail one trap that is at the center of the metalens FoV. We plot a histogram of the fluorescence counts collected through the metalens and registered on the camera (CCD counts) versus occurrence from a single pixel at the atom location (Fig. 5.20(a) and 5.20(b)).

The lower count histogram peak corresponds to background signal with no atom and the second higher CCD count peak corresponds to the fluorescence of the single atom. Collisional blockade prevents loading of more than one atom into the tweezer, as reflected in the absence of a two-atom peak [3]. We find a loading probability of $(47\pm 5)\%$. However, due to the probe beam being perpendicular to the tweezer direction (Fig. 5.20(c)), there is no axial cooling during imaging. Since the axial direction has weaker confinement from the trap we see $(10\pm 2)\%$ atom loss during imaging which is higher than typical. Taking this into account, a loading probability of $(52\pm 5)\%$ is comparable to typical loading efficiency from other optical tweezer experiments [184].

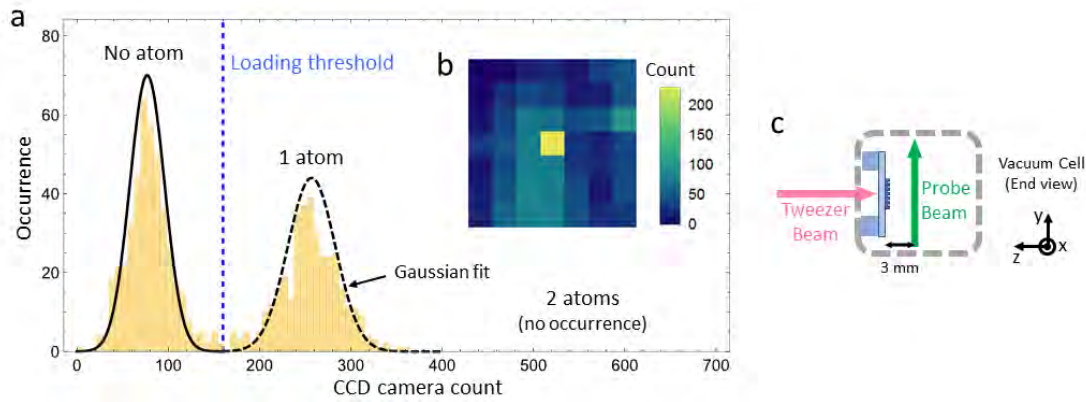


Figure 5.20: (a) Camera count histogram indicating presence of either 0 or 1 atoms in a tweezer trap. A threshold is chosen to determine if an atom is trapped and to calculate the loading efficiency. (b) Typical single shot fluorescence image of a single atom imaged through the metalens with PGC imaging. (c) End view of the vacuum cell, showing the probe beam (also resonant heating beam) orientation in relation to metalens sample and tweezer beam. Probe beam has $500 \mu\text{m}$ $1/e^2$ Gaussian waist, shines vertically up and is 3 mm away from the metalens overlapping with the optical tweezer focus.

We also determined the length of time a single atom remains trapped in the optical tweezer focus (vacuum lifetime), with no cooling light present, by holding the atom with variable time between two consecutive images. The measurement gives a lower bound of exponential decay lifetime of 10 sec; atom lifetime assessment in a metalens trap beyond this scale will require additional investigation of background gas collision rates due to finite vacuum level and potential atom heating and loss due to inelastic light scattering from residual trapping light.

5.6.2 Trap depth

To measure the tweezer trap depth a resonant heating beam is used to measure the induced AC-Stark shift from the tweezer trap. This beam is identical to the tweezer probe beam other than the detuning. The beam has $500 \mu\text{m}$ $1/e^2$ Gaussian waist and the geometry is shown in Fig. 5.20(c). The experiment sequence for this measurement is in Fig. 5.21(a). The first PGC image is taken to verify the loading of single atom in a experiment run. Then the resonance heating beam is turned on for $60 \mu\text{s}$ with intensity of $100 \mu\text{W}$ ($\approx 6I_{\text{sat}}$). This pulse time and intensity are carefully chosen so that the atom is not being overly driven by the heating beam (i.e. survival not zero). After the heating pulse, the trap intensity is lowered to 0.25 mK for 15 ms . This allows the hot atom to escape. Then a second PGC image is taken and the survival between the two images vs. heating beam detuning is recorded. Fig. 5.21(b) shows the typical resonance scan. A gaussian fit (solid red line) is used to extract the center of the shifted resonance and the width is used to check whether or not the atomic transition is over driven. The AC-Strak shift created by the 850 nm trapping light on the ^{87}Rb $D2$ $F = 2$ to $F' = 3$ transition is 28.8 MHz/mK . Comparing to the free-space resonance (dotted gray line) allows the trap depth to be calculated.

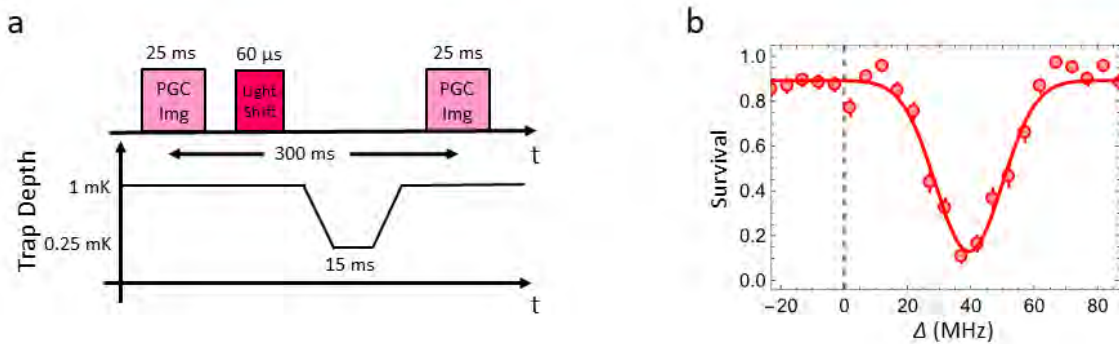


Figure 5.21: (a) Experiment sequence of the light shift measurement. Heating beam is turned on for for $60 \mu\text{s}$ with intensity of $100 \mu\text{W}$ between two PGC image separated by 300 ms . (b) Typical light-shift measurement with a Gaussian fit (red line) to the shifted atomic resonance. Dashed line corresponds to free-space ^{87}Rb $D2$ $F = 2$ to $F' = 3$ transition

5.6.3 Trap frequency

To characterize the effective tweezer waist seen by the atom we need to measure the trap frequency (harmonic oscillator strength of atom moving in the optical tweezer light). There are several methods that can be used to measure the trap frequency, all of them require measuring the atom's frequency response to an excitation. Two methods are the most popular, the one used in Ref. [153], excite the atom by temporarily switch off the tweezer trap and measure the oscillation frequency of the atom afterwards. Another method, which is used in this thesis is the parametric excitation method. Here the trap is modulated between 5% and 10% of its depth around the nominal value at variable frequency for 50 ms. After modulation, the trap is lowered to 250 μK for 15 ms which is much longer than the period of the atom oscillating in the trap. This allows the hot atoms to escape the trap. Fig. 5.22(a) shows the experiment sequence of the trap frequency measurement where the parametric excitation happens between two PGC images. On the right is the illustration of how the modulation (blue dashed line) changes the trapping potential (black solid line) and the atom wave function (red and purple).

After the modulation and trap lowering, the atom survival vs. modulation frequency is recorded. Fig. 5.22(b) shows the typical trap frequency measurement where the atom is heated at twice the trap frequency (ν_{trap}) and subsequently loss from trap lowering.

The trap waist can be deduced from the slope of a graph that plots the trap frequency versus depth as per the equation below

$$\nu_{\text{trap}}(U, w_0) = \frac{1}{2\pi} \sqrt{\frac{4U}{w_0 m_{\text{Rb}}}} \quad (5.7)$$

U is the tweezer trap depth, m_{Rb} is the mass of Rb_{87} , w_0 is the tweezer Gaussian waist and ν_{trap} is the trap frequency.

Taking trap depth and trap frequency measurements at different tweezer intensity and fitting to the data we extract a $1/e^2$ Gaussian waist of $w_0 = (0.80 \pm 0.04) \mu\text{m}$ at 852 nm (Fig. 5.22(C)), which is consistent with the value determined from the sub-wavelength pinhole characterization (Fig. 5.17(b)). With the clipped Gaussian beam illumination used for the optical tweezer trapping

(versus uniform illumination during characterization) we expect the tweezer to have a waist of $0.78 \mu\text{m}$, consistent with the measured value.

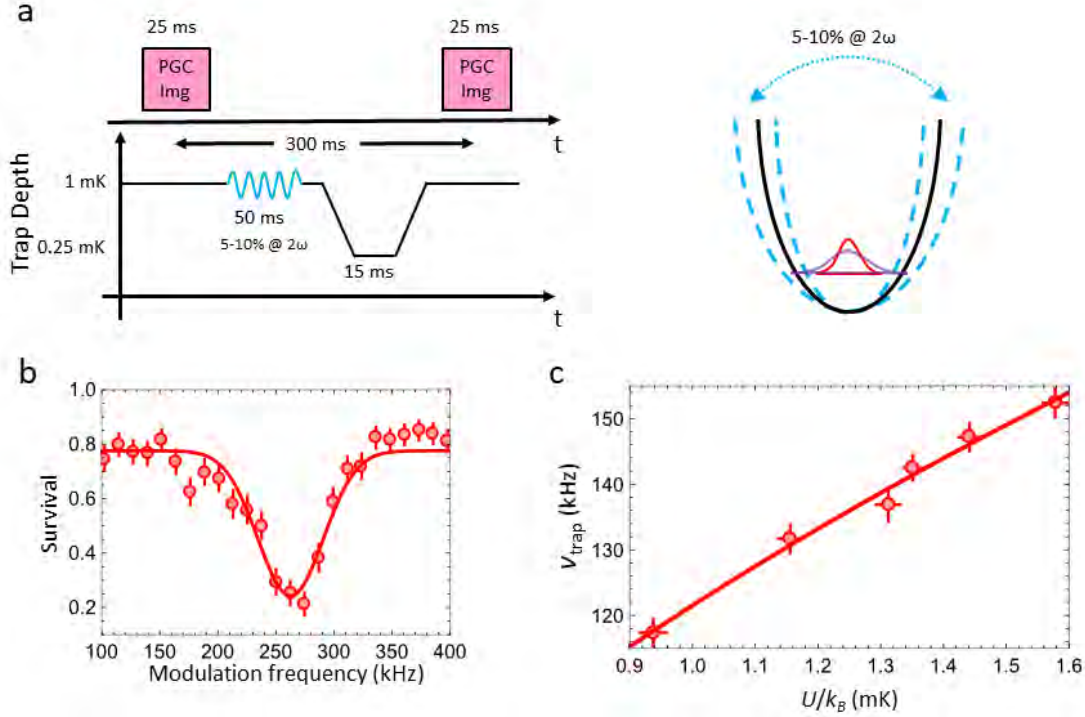


Figure 5.22: (a) Experiment sequence of the trap frequency measurement. Between the two PGC image separated by 300 ms, the tweezer trap is modulated for 50 ms and the trap is lowered to $250 \mu\text{K}$ to eject the hot atoms. (b) Typical parametric heating measurement with a Gaussian fit (red line) to extract the trap frequency (ν_{trap}) from the modulation resonance ($2\nu_{\text{trap}}$). Each point is an average of 100 trap loading sequences. (c) Measured trap frequency versus trap depth (light shift) obtained from multiple measurements similar to (c) and (d). The solid red line is a model fit (see main text) to extract the effective Gaussian tweezer waist seen by the trapped atom.

5.6.4 Tweezer array setup and FoV

An important metric for creating and imaging large atom arrays is the lens FoV. To study the FoV of the metalens, we create an array of tweezers with an acousto-optic deflector (AOD). AOD uses RF to diffract an input laser beam at an angle that is proportional to the RF frequency. By injecting several different frequencies into the AOD input, one can create a series of diffracted beams at different angles. After focused by the tweezer lens, it became an array of optical tweezers

for single atom trapping.

Fig. 5.23(a) is the schematic illustration of the tweezer setup. The tweezer light collimated with $1/e^2$ waist = 2 mm at 852 nm (pink shaded beams) is launched into the AOD (AA Opto-electronics Model: DTSXY-400-850.930-002). This produces a series of deflected beams with variable angle controlled by the AOD input RF frequencies. This array of angled collimated light is then imaged with a 1:1 relay lens with focal length of 150 mm (Thorlabs AC254-150-B) onto the back aperture of the metalens substrate. The relay lens ensures all the deflected beams coincide on the metalens to minimize asymmetric beam clipping. Fig. 5.23(b) is an average image of 3x3 array after 100 loading cycles.

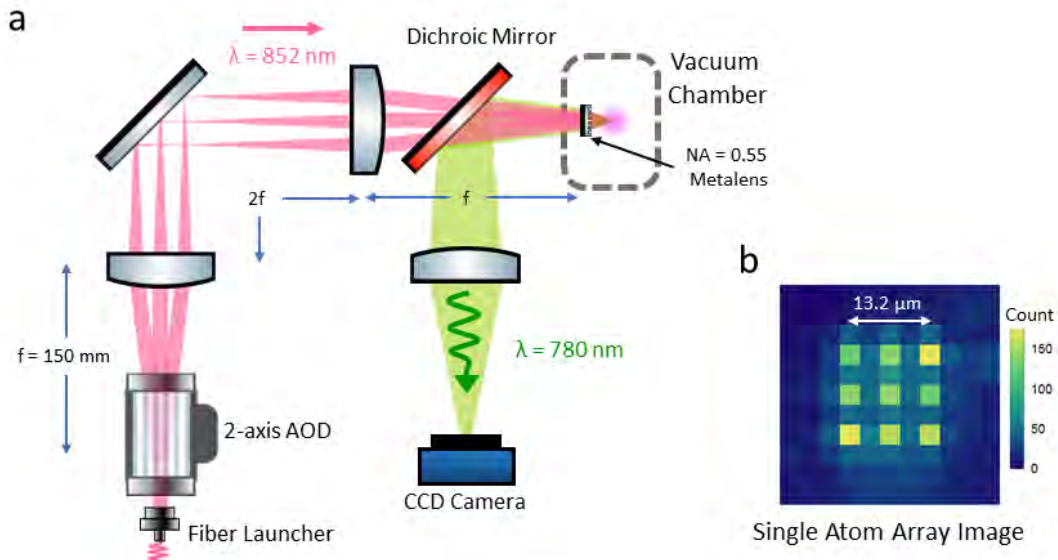


Figure 5.23: (a) Optical setup for trapping (pink) and fluorescence imaging (green) of single atoms in an array created with multiple input beams generated using a 2-axis acousto-optic deflectors. (b) Image of a trapped ^{87}Rb array created by averaging over multiple experiment iterations (100 in this case) with $\sim 52\%$ probability of a single atom in each trap per image. The variation in the averaged intensity is caused by trap depth and shape variations that affect relative loading probability and imaging signal in the array.

For this, we create four traps with the lower left tweezer at the center of the FOV (optical axis), and characterize the traps (with various spacing) the same way as in Sec. 5.6.2 and Sec. 5.6.3. Fig. 5.24(a) is the tweezer image showing how the array is arranged in this measurement. In the

presence of aberrations the traps become asymmetric, resulting in non-degenerate frequencies in the radial dimensions of the trap. This will manifest as a double-dip structure in the trap frequency measurement (Fig. 5.24(b)). We characterize the FoV by plotting the waist determined from the trap frequency and depth measurements as a function of the distance from the optical axis (Fig. 5.24(c)) and find the aberrations are consistent with FDTD calculations (see Sec. 5.6.5 for details of FDTD simulation) of tweezer intensity from our metalens optical field distribution (blue dash lines in Fig. 5.24(c)). Here FoV is defined as the distance to a point where the average waist is 10% larger (Strehl ratio > 0.8) than at the center, and we find a FoV of $\pm 11 \mu\text{m}$ ($\pm 0.2^\circ$).

5.6.5 Focusing efficiency and FoV simulation

We use the grating averaging technique [185] to estimate the focusing efficiency, the fraction of incident light remaining as undeflected zeroth-order light, and the total reflectance of the mm-scale diameter metalens. Following this technique, we approximate the metalens as a combination of aperiodic beam deflectors. For an aperiodic beam deflector with a deflection angle θ_D ($\theta_D = \sin^{-1}(\lambda/Na)$, where N was chosen to calculate θ_D between 0° to 50°), the deflection efficiency η_1 , the fraction of light in the 0th-order η_0 , and the reflectance η_{refl} , for unpolarized input light, are calculated (circles in Fig. 5.25(a)) using rigorous coupled wave analysis (RCWA), and fitted with parabolic functions (solid lines in Fig. 5.25(a)). Finally, the focusing efficiency of the metalens T_1 , the total fraction in the undeflected 0th-order T_0 , and the total reflectance T_{refl} , are estimated as the area average of η_1 , η_0 , and η_{refl} , respectively, using:

$$T_i = 1/(\pi R^2) \iint_S \eta_i ds = 2/R^2 \int_0^R \eta_i(r)r dr, \quad (5.8)$$

where $i= 1, 0$, or refl ; $r = f \tan \theta_D$; and R is the radius of the metalens.

To simulate the FoV the beam waist at the focal spot as a function of the distance from the metalens optical axis or, equivalently, the incident angle of the input beam, is calculated using FDTD technique, with a minimum mesh size of 4 nm. Due to the millimeter scale size of the metalens, a cylindrical metalens is simulated instead, implemented by using one unit-cell along

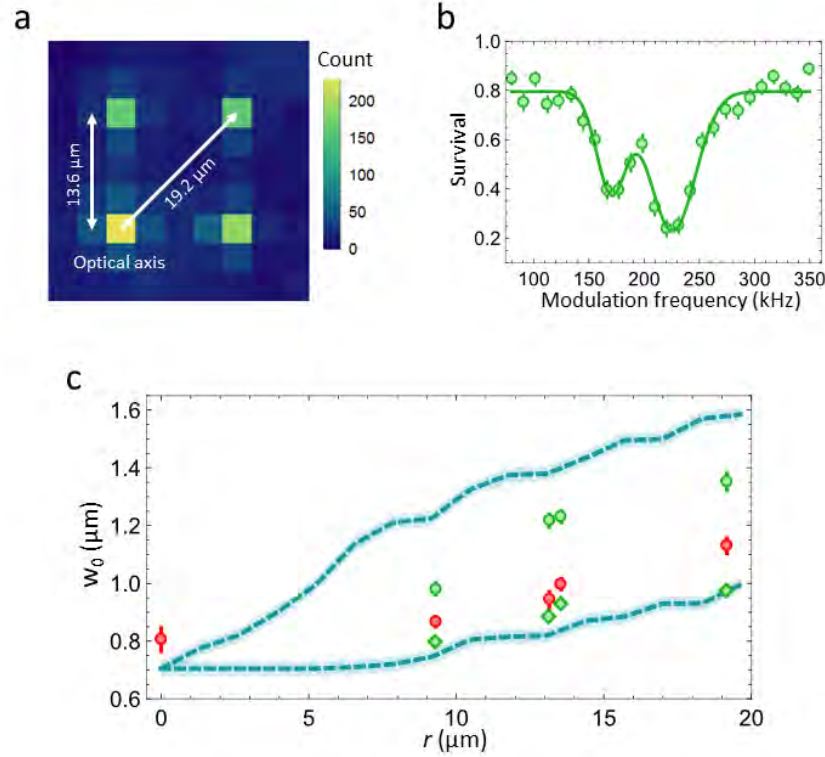


Figure 5.24: (a) PGC fluorescence image of atom array trapped with metasurface optical tweezers. Image is averaged over 100 experimental cycles. Bottom left tweezer is on optical axis of the metalens. The off-axis tweezer site typically have a lower loading probability and non-optimal PGC imaging detuning resulting in a dimmer single atom signal. (b) Example of typical trap frequency measurement data at $\approx 13.6 \mu\text{m}$ from FoV center where asymmetric aberrations in the trap are present, along with a double Gaussian (green line) fit. (c) Extracted Gaussian waist as determined from the atom trapping as a function of distance (r) to the metalens optical axis (center of FoV). The average waist extracted from a single Gaussian fit to the trap frequency data (red), and the major waist (green circle) and minor waist (green diamond) extracted from data similar to (b) when the two trap frequencies are distinguishable. We compare to theory of the major and minor Gaussian waist fitted from FDTD simulation (see Sec. 5.6.5).

the y -axis with periodic boundary condition. All the unit cells along the x -axis are included in the simulation, and the oblique incidence angle is only applied along the x -direction. For a given incident angle, a near-field monitor records the electric and magnetic fields of the output beam at a distance of 50 nm from exit surface of the metasurface. A near-field to far-field projection is then used to calculate the focal spot intensity profile at the focal plane (Fig. 5.25(b)). The major and

minor waists of the focal spot are obtained as the distance from the intensity peak to the $1/e^2$ of peak intensity along the x -axis (blue dash lines in Fig. 5.24(c)).

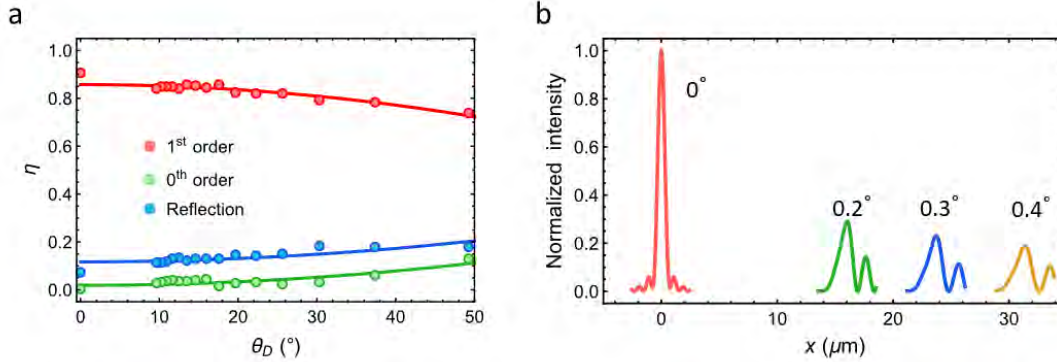


Figure 5.25: (a) Calculated deflection efficiency η_1 , the fraction of light in the undeflected 0th-order η_0 , and the reflectance η_{refl} of aperiodic metasurface beam deflectors as a function of deflection angle θ_D . Circles are data from RCWA simulations and solid lines are parabolic fit. (b) FDTD simulated beam profiles of the focal spots as a function of the angle of incident light.

5.6.6 Discussion and challenges

From the focus efficiency measurement done in Ref. 5.5.3 (sample 4 in Table 5.1) the metalens used for single atom trapping has focus efficiency of 58% at 852 nm and 56% for 780 nm. This is about 20% lower than the theoretical estimate done in Sec. 5.6.5 and Fig. 5.25(a). We found that the transmitted power through the substrate is significantly lower than the simulated value by the amount close the loss in focus efficiency. Possible reasons for the reduction of the transmission efficiency and increase of zeroth-order light in comparison to theory are likely due to fabrication imperfections resulting in nonideal nanopillar cross sections and sidewall tapering which is evident in some of the SEM images taken from low efficiency samples. The nonideal nanopillar cross section due to lithography calibration or anisotropic etching was observed in sample 1&2 in Table 5.1 where we see strong polarization dependent focus efficiency change of up to 30% from one polarization to another. The material loss was ruled out by testing the a-Si film loss tangent before patterning the nanopillars and using different silicon film deposition method including epitaxial, yields similar

focus efficiency.

As one comparison, we discuss the performance of a typical commercial asphere that has been used in optical tweezer experiments. Reference [153] uses an aspheric lens with $NA = 0.5$, a working distance of 5.7 mm, a focal shift of $-40 \mu\text{m}$ from 852 nm to 780 nm, and a focal length of 8 mm. This aspheric lens has a transverse field of view of $\pm 25 \mu\text{m}$ ($\pm 0.18^\circ$), an inferred beam waist of $1 \mu\text{m}$ for the trapping wavelength, and a $0.9 \mu\text{m}$ waist for the imaging wavelength. The metasurface studied here has a worse focal shift than a standard asphere, but as discussed in 5.7 this was not of primary concern in our experiments given the prospects for future control, for example, using wavelength polarization multiplexing. The singlet metasurface here achieves the Gaussian $1/e^2$ radius (waist) of the focused tweezer spot to be $w_0 = (0.80 \pm 0.04) \mu\text{m}$ which is better than the asphere in Ref. [153] and FoV (average waist 10% larger or Strehl ratio > 0.8) of $\pm 11 \mu\text{m}$ ($\pm 0.2^\circ$) which is consistent with a full theoretical model of the metalens (Fig. 5.24(c) and Fig. 5.25(b)) and comparable to Ref. [153] in terms of focal length to FoV ratio, i. e. angle.

5.7 Future sample

A complex high-NA objective lenses used for atom trapping and imaging can have FOV of a few 100 μm ($\approx \pm 0.5^\circ$) combined with achromatic operation over a wide range of wavelengths [16, 186]. While the singlet metalens described in this thesis does not yet achieve these metrics, we now discuss the horizon of prospects for design features of future metasurfaces. In the following sections we will present some future metalens design ideas for a few different metrics desirable for single atom trapping such as FoV and Chromatic performance.

As discussed previously, with a metasurface it is possible to achieve a focusing response that is either polarization selective [187] or one that transforms the polarization [188], which are functions not offered by traditional optical lenses. For example, polarization multiplexing provides a method to trap and collect fluorescence at the diffraction limit for two different wavelengths using a singlet metasurface lens, and may find utility in combining additional multifunctional beams in complex trapping experiments.

To illustrate this prospect, we have designed and optically tested a sample with rectangular shape cross-section nanopillars that achieves equal focal lengths for 780 nm and 852 nm light of orthogonal polarization with diffraction limited performance at NA of 0.8. This concept can be used to trap at 852 nm, and collect fluorescence at 780 nm, with a 50% efficiency due to the random polarization of the scattered light from atoms. The design and optical testing of this metalens will be described in the next section (Sec. 5.7.1).

More functionality can be achieved with expanding the number of surfaces offered in the design. To focus on FoV as one metric, an enhanced FoV up to $\pm 25^\circ$ has been achieved by patterning both sides of the substrate to create a double-layer metasurface [81]. We estimate that by using design components similar to the singlet lens presented here, expanding to a doublet can improve the field angle to beyond $\pm 5^\circ$ at 0.7 NA. To demonstrate this capability, we present a phase map design of such doublet in Sec. 5.7.2 demonstrating mm scale FoV with working distance similar to objective used in Ref. [16, 186].

Further design improvements can be achieved through the use of an expanded unit-cell library to include cross, donut and other exotic nanopillar shapes [189] or via inverse design [190]. Choosing optimal materials and designs that are robust to nanofabrication variation is expected to offer higher efficiencies that exceed that achieved in the experiments presented here [78]. Further, a hybrid lens design consisting of a curved refractive surface and a metasurface patterned on the same substrate will offer additional prospects for enhanced design space [182, 191]. In Sec. 5.7.3 we present an example design of this type of hybrid lens with less chromatic aberration.

5.7.1 Polarization multiplexed lens

The metalens sample used in this thesis and Ref. [115] utilize nanopillar with square cross section (Fig. 5.13(a)), therefore the focusing response has no polarization dependence. One popular method for creating polarization dependent response is using asymmetrical cross-section nanopillars such as in [79, 188].

When light incident to the nanopillars, a portion is confined in the nanostructure while the rest leaks to the surrounding air. This is very similar to an optical waveguide, so we can consider the nanopillars as truncated waveguides. By changing the size of the nanopillar, the ratio of the mode inside the waveguide and in the air changes, thus the effective index of refraction seen by the incident light also changes. Due to the symmetry of the structure, two orthogonal linear polarization excites two orthogonal TE mode in the waveguide. If the cross-section is anisotropic, the incident linear polarized light will experience a different effective index, n_l and n_s , when passes through the long and short axis of the nanopillar [78]. Fig. 5.26(a) is the effective index calculated with Lumerical for TiO_2 nanopillar arranged in square lattice of 400 nm spacing and cross-section of 250 nm by 80 nm. When the incident light is polarized along the long axis, it experiences a larger effective index of refraction (red curve). This is because most of the electric-field is localized inside the nanopillar. Conversely, when the polarization is along the short axis, the mode is mostly in the air, resulting a low effective index (blue curve). Two subplot in Fig. 5.26(b) shows the structure of the electric-field of each mode, top panel is polarization along the long axis and bottom panel is

polarization along the short axis.

The complex transmission from the anisotropy can be written as [78]:

$$t = |t| \exp\left(\frac{2\pi i}{\lambda}(n_{eff} - 1)h\right) \quad (5.9)$$

Where the n_{eff} is the effective index calculated in Fig. 5.26(a) (i.e. n_l and n_s) and h is the height of the nanopillar. Fig. 5.26(c) is the calculated phase shift of $h=600$ nm TiO₂ nanopillar on the long and short axis. The solid lines are from effective index in panel(a), square are FDTD simulation. Deviation of phase at low wavelength might due to resonances and excitation of higher-order modes.

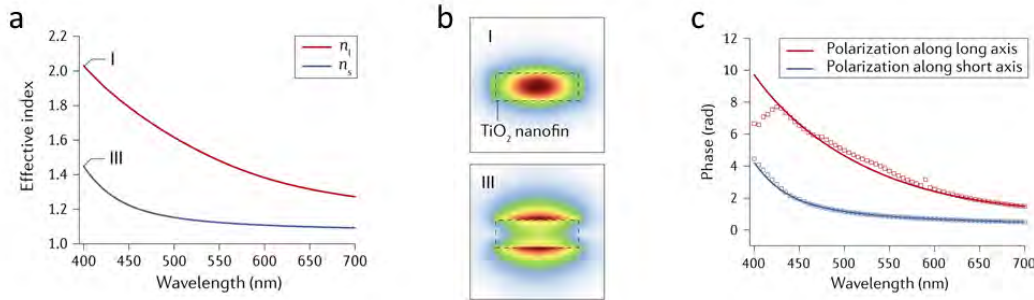


Figure 5.26: (a) Effective index of the nanopillar with different width along the long (250 nm) and short (80 nm) axis. If the polarization of the input light lines up with the long axis will experience a large effective refractive index comparing to the polarization aligned to the short axis. [78] (b) Simulated E-field distribution of the two different polarization alignment with respect to the long (i) and short (iii) axis of the nano-pillars. In case (i) the mode structure is mostly inside the dielectric so it experience larger effective index (red curve in (a)). For (iii) the mode is mostly in air so it sees a lower effective index (blue curve in (a)). [78] (c) Phase shift of different linear polarization alignment to the pillar. The solid line is calculated from the effective index in (a) the squares are FDTD simulation. Deviation at shorter wavelength might due to higher order mode in the pillars. [78]

Following this general principle we designed a metalens to implement an ideal-lens phase function for x -polarized light at $\lambda = 780$ nm and for y -polarized light at $\lambda = 850$ nm, simultaneously, targeting a focal length of 0.5 mm and NA of 0.8, for both wavelengths (Fig. 5.27(c)). This is achieved by assembling the metalens with a library of a-Si birefringent nanopillar unit-cells, each having an rectangular cross-section that can simultaneously impose the desired local phase shift ϕ_x for x -polarized light at $\lambda = 780$ nm and ϕ_y for y -polarized light at $\lambda = 850$ nm based on

Eq. 5.2 (Fig. 5.27(b)). Fig. 5.27(a) shows the phase as a function of lens radius with respect to wavelength of 780 nm in x-pol and 850 nm in y-pol. Fig. 5.27(b) shows input polarization w.r.t. the nanopillar orientation. Fig. 5.27(c) shows the two wavelength with orthogonal polarization, after passing through the polarization multiplexed metalens, creates identical focusing wavefront.

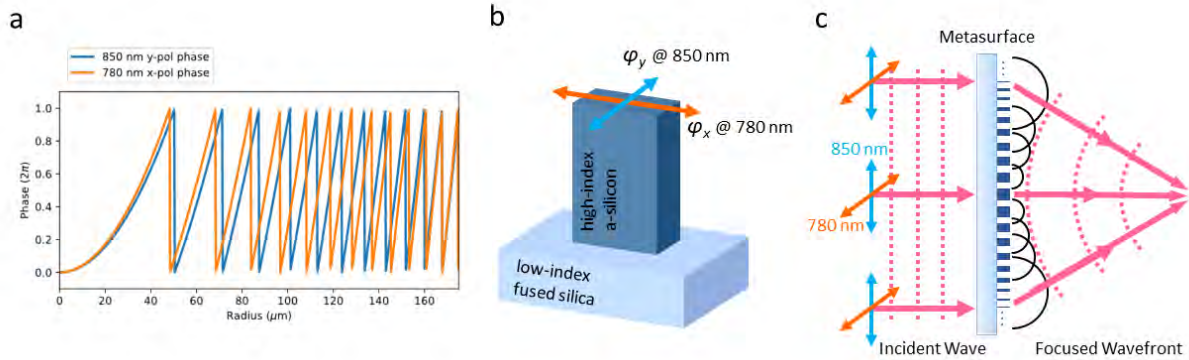


Figure 5.27: (a) Phase map of polarization multiplexed lens (b) amorphous-Si nanopillar (dark blue) with rectangular cross section on fused silica substrate (light blue) creates phase delay for two orthogonal polarization independently (polarization multiplexing). (c) Illustration of polarization multiplexed metasurface lens operation. Input wavefront (pink dash) with orthogonal polarization for 780 nm (green) and 852 nm (blue) propagates and interact with metasurface. Secondary wavelets (black semicircles) re-emitted by the nanopillars interfere and creates identical focusing wavefront for both 780 nm and 852 nm.

A sample is fabricated, based on the phase profile in Fig. 5.27(a), we subject it to the same focusing efficiency measurement and PSF imaging described in Sec. 5.5.3 and Sec. 5.5.4. We found that the focusing efficiency is only less than 20% which is significantly lower than typical expected value of 60-80%. This is most likely due to the same fabrication challenges we discussed in Sec. 5.6.6. The polarization dependent PSF measurement is done by filtering out the unwanted polarization with a PBS before the light entering the imaging lens and focused onto the CCD camera (by replacing the 50/50 BS with a PBS in Fig. 5.17(a)). The PSF are imaged without changing the focal distance between the metalens and subwavelength pinhole to test if the polarization multiplexing is working properly. The measured intensity distributions at the targeted focal plane reveal diffraction-limited focal spots for both wavelengths (Fig. 5.28(a) and Fig. 5.28(b)). Measured

NA for 780 nm x -polarized light is 0.8 ± 0.01 and 850 nm y -polarized light is 0.82 ± 0.01 .

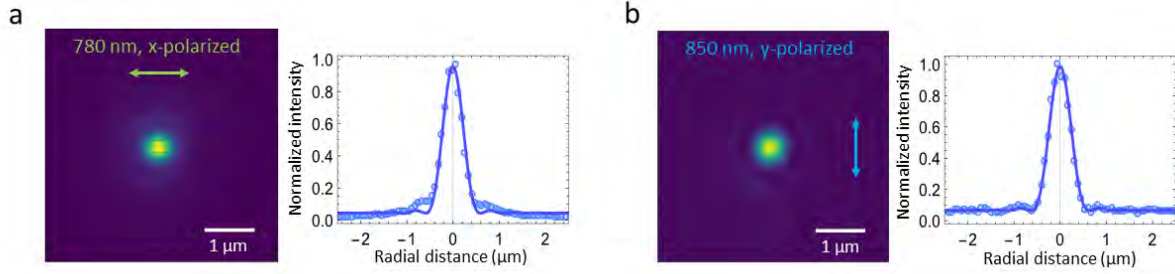


Figure 5.28: (a,b) Experimental PSF by imaging the subwavelength pinhole with the metalens for 780 nm x -polarized and 852 nm y -polarized light. The image of two wavelength configuration are obtained without changing the focus distance between the polarization-multiplexed metalens and the subwavelength pinhole. 2D cuts of the PSF shows the fitted Airy function from which the NA is extracted.

5.7.2 Doublet design

In this section we present a metalens-doublet design that takes a similar approach to Ref. [81]. The doublet in Ref. [81] has 0.44 NA, focal length $\approx 350 \mu\text{m}$ and a FoV of $\pm 25^\circ$ ($\pm 150 \mu\text{m}$). This doublet consists of an aperture metalens that has very little focusing power and a focusing metalens that has most of the focusing power. The aperture metalens, when placed at an optimal distance, corrects for the aberration that can be introduced under large FoV angle. The function of the aperture metalens behave exactly like a Schmidt corrector plate which controls coma and astigmatism aberration. Normally this corrector plate is placed at the distance equals to the radius of curvature of the lens on the opposite side of the focus which equals to $f(n-1)$ where n is the index of refraction of the lens. Fig. 5.29 shows the general shape of the Schmidt corrector plate and how the rays are bend (left panel), combining with a spherical lens (middle) resulting in a diffraction limited doublet (right) and when the aperture of the system is place at the correct position (typically at the Schmidt plate) the corrector plate also compensate for coma and astigmatism.

Here we choose a working distance that is similar to the one in Ref. [153] and NA of 0.7. We setup the location of the Schmidt corrector plate and the focusing metalens. Once those

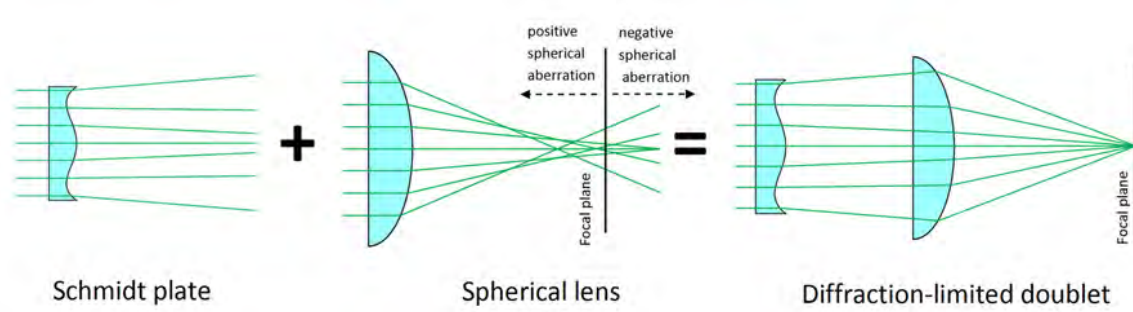


Figure 5.29: Schematic illustration of the doublet design that consists of a Schmidt corrector plate and a focusing metalens. The Schmidt corrector plate corrects for the field related aberration when placed at the back of the focusing lens $f(n_l - 1)$ away from the lens. figure from Ref. [81]

parameters are determined, we set up the optimizer using Eq. 5.3 with maximum term ($N = 9$). We let the optimizer in Zemax OpticStudio run for maximum FoV possible and we found that this configuration gives a diffraction limited FoV of ± 1.1 mm ($\pm 7^\circ$). Fig. 5.30(a) shows the configuration of the surfaces for this doublet design, the substrate material is a 12.7 mm thick fused silica. The aperture metalens is 12.7 mm in diameter and the focusing metalens is 15 mm in diameter. Inset of Fig. 5.30(a) shows the ray converges to a diffraction limited point under different FoV settings. Fig. 5.30(b) shows the simulated PSF at different FoV and their cross-sections. We can see the Strehl ratio remains high (>0.8) for up to FoV of 1.1 mm.

Table 5.2 is the coefficients used to generate the metalens doublet design. The resulting phase profile is shown in Fig. 5.31(a,b) for the aperture and focus metalens. This phase profile has the general shape described in Fig. 5.29 and Ref. [81].

Normalized radius (R): 5 mm, Substrate thickness: 12.7 mm, Substrate: Fused silica									
Surface	r^2	r^4	r^6	r^8	r^{10}	r^{12}	r^{14}	r^{16}	r^{18}
1	-2111.72	699.9	58.5	155.72	-196.82	188.4	-101.78	30.314	-3.718
2	-1.056E4	-3.699	16.524	-19.3	11.578	-3.974	0.793	-0.083	3.4E-3

Table 5.2: Metalens Doublet Coefficients, NA 0.7, FoV= ± 1.1 mm, WD= 7 mm

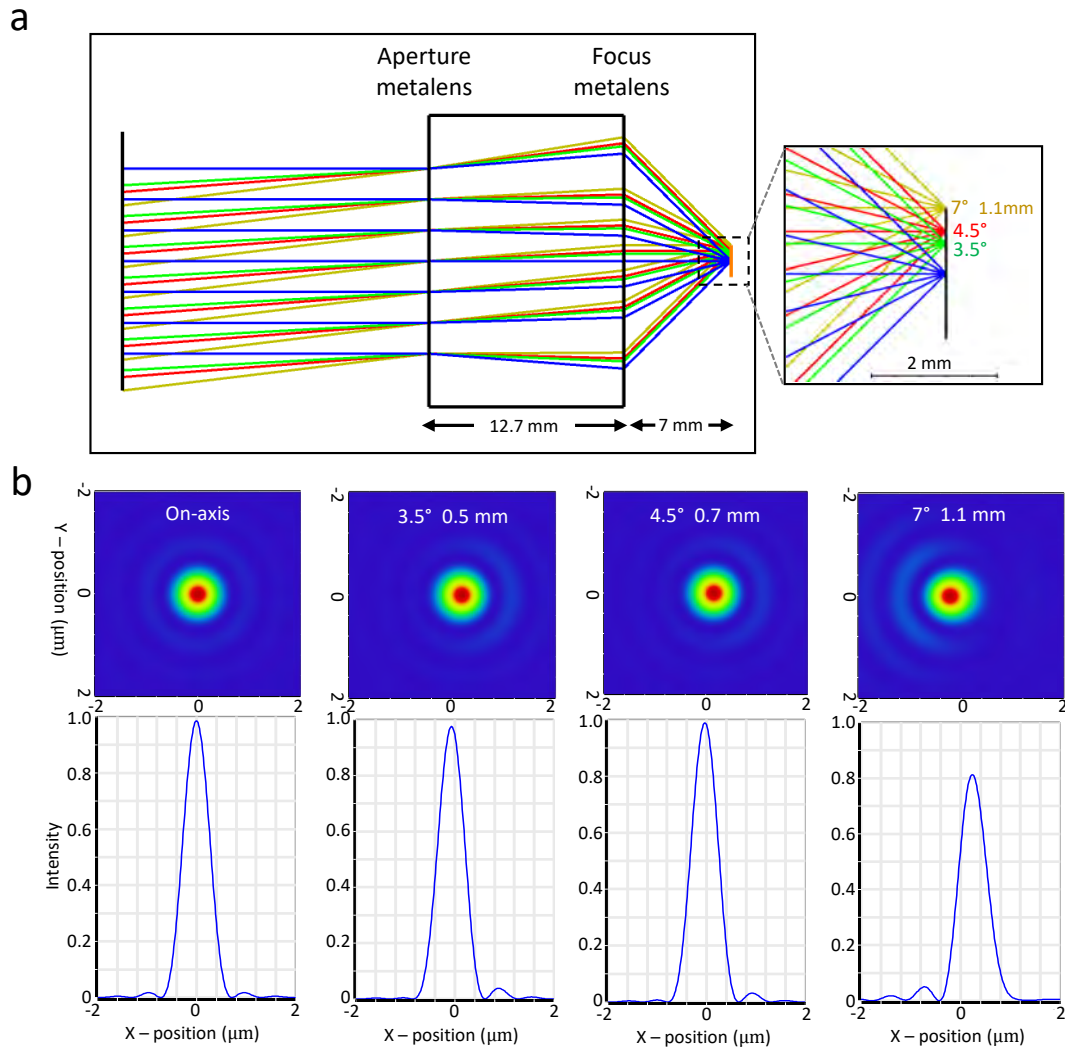


Figure 5.30: (a) The lens setup to design the metalens doublet with FoV up to 2.2 mm and NA of 0.7. The stop aperture is set on the aperture metalens and the substrate is 12.7 mm thick. The zoom in part shows the ray converges to a diffraction limited point at the focus. (b) The simulated PSF over the FoV of the lens up to 1.1 mm half FoV. The angular FoV is 7° . The position is determined by when the Strehl ratio drops to 0.8.

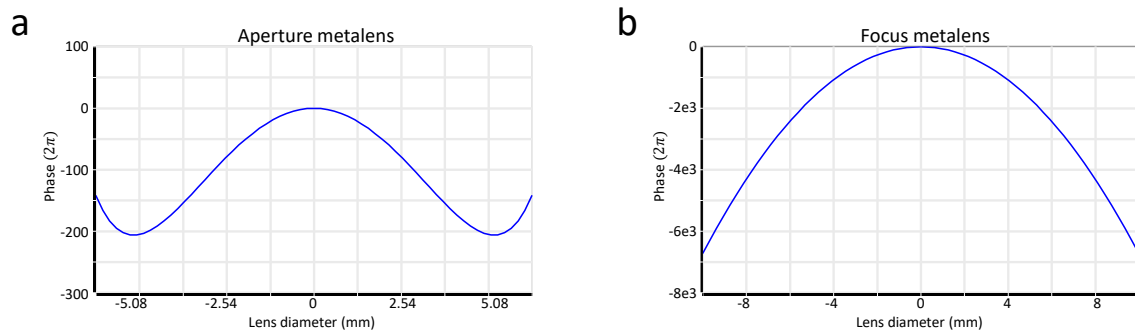


Figure 5.31: Metalens doublet surface phase based on tabel 5.2. We see the shape of the phase on the corrector metasurface looks like the curvature of the Schmidt corrector plate. The phase of the focusing lens looks parabolic with very high gradient for strong focusing.

5.7.3 dual wavelength lens

A conventional refractive focusing lens exhibit larger index of refraction for shorter wavelength due to material dispersion. This results in chromatic aberration where shorter wavelength light focus closer to the lens (Fig. 5.32(a)top). Contrary to refractive optical element, a diffractive lens exhibit longer focal length for larger wavelength, due to the angle of diffraction is proportional to the wavelength (Fig. 5.32(a)middle). This give rise to the possibility where chromatic aberration of a refractive and diffractive optical elements can be balanced (Fig. 5.32(a)bottom).

We use the binary 2 surface from ZEMAX to design a hybrid lens with a conventional lens and a metasurface. The binary 2 surface models a diffractive surface that is infinitely thin with a continuous phase change across the surface. It also take into account the wavelength dependent diffraction angle. By balancing the optical (focusing) power of the two surfaces one can create a hybrid lens where the chromatic focal shift cancel out each other over a large spectral range. The resulting chromatic behavior will be better than achromatic lens and closer to an super-apochromatic lens. We present a preliminary design of an hybrid lens utilizing a commercially available asphere from Thorlabs (AL1210) and metalens on a N-BK7 substrate. The choice of N-BK7 for metalens substrate is to match the CTE of the metalens to the CTE of the asphere, in most cases are S-LAH64 from Ohara. CTE of N-BK7 is roughly 7.1 ppm/K and S-LAH64 is about 6.1 ppm/K so they are sufficiently close. The lens layout is illustrate in (Fig. 5.32(b)), the letalens is on a 0.5 mm thick substrate in close contact to the asphere.

After optimizing the phase profile of the metalens using the same polynomial phase from before Eq. 5.3, we obtain a phase profile shown in (Fig. 5.32(d)) that resembles a weak focusing lens. The resulting optical performance is shown in (Fig. 5.32(c) where the Strehl ratio is plotted over a wide wavelength range with several FoV configuration up to 20 *mum*. We can see the hybrid lens is diffraction limited (Strehl ratio >0.8) from 760 nm to 870 nm continuously with a FoV of $\pm 18 \mu\text{m}$ (similar to the original asphere). This design has a much wider spectral range than the typical achromatic lens where only two wavelength will be on focus.

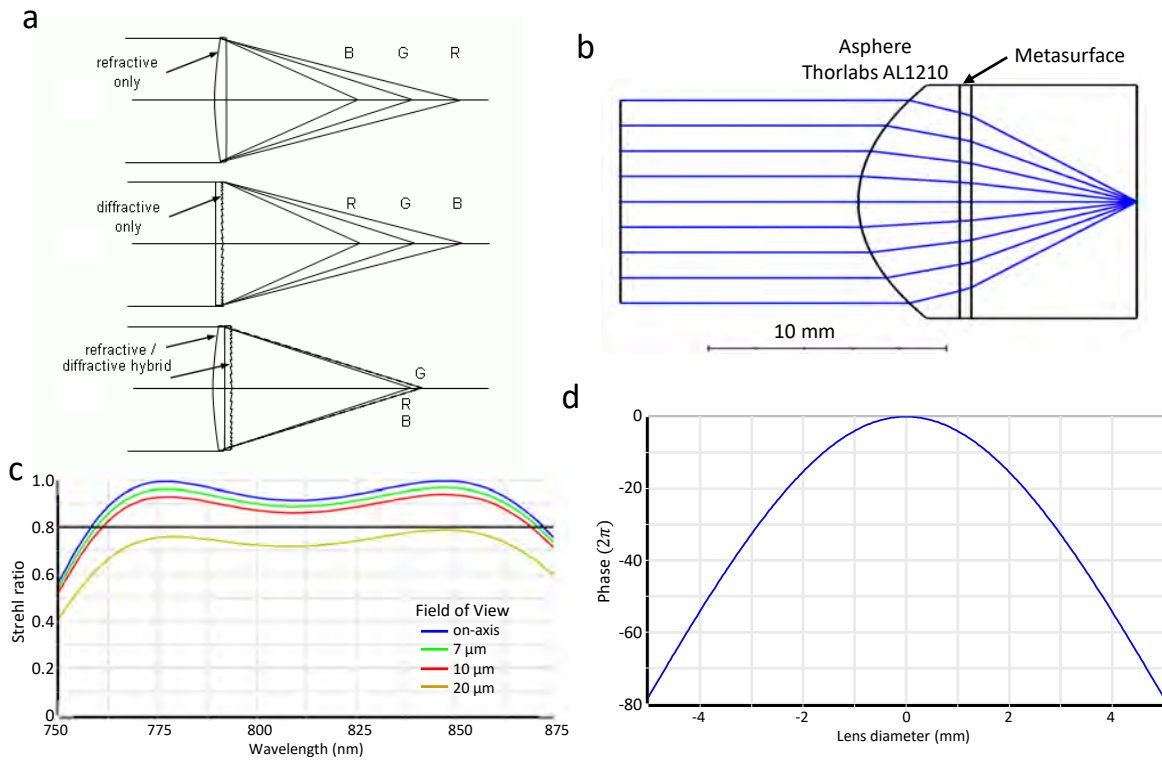


Figure 5.32: (a) Hybrid metalens concept. The dispersion of a refractive and a diffractive element have opposite sign. Therefore, by combining the two the dispersion can cancel and one can get an achromatic focusing lens. (b) The ZEMAX setup showing Combining a metasurface with a Thorlabs AL1210 asphere to correct for chromatic aberration over a large range. (c) Simulated Strehl ratio of the hybrid design over wavelength and different FoV up to 20 μm . (d) Surface profile of the metalens, showing a relatively weak focusing lens which should give a high focusing efficiency make this lens suitable for atom trapping.

5.8 Outlook

In this chapter, we demonstrate that metasurface lenses hold promise for future atom trapping experiments that requires a robust multifunctional surface. We successfully trapped single atoms using a metasurface lens generated high NA optical tweezer up to 0.5 NA. Additionally, we showed that the metasurface is capable of efficiently imaging single atoms with low background. Finally, we studied the field of view (FoV) behavior of the metalens with an atom array generated by combining the high NA metalens with an AOD. We found that the FoV of the singlet metasurface lens is $\pm 11 \mu\text{m}$, similar to a singlet aspheric lens of the same focal length.

An immediate improvement could be achieved by increasing the efficiency of the current sample through better fabrication techniques. In this work, our metalens achieved only 56% focusing efficiency, whereas efficiencies between 80-90% have been routinely demonstrated in the literature [185, 190, 192]. This can be accomplished through improvements in the fabrication process, including better deposition of dielectric materials, improved etching homogeneity, and tighter control over nanopillar dimensions.

Further improvements through design of the nano-pillars can be achieved through the use of an expanded unit-cell library to include cross, donut and other exotic nanopillar shapes [189] or via inverse design [190]. Choosing optimal materials and designs that are robust to nanofabrication variation is expected to offer higher efficiencies that exceed that achieved in the experiments presented here [78]. Further, a hybrid lens design consisting of a curved refractive surface and a metasurface patterned on the same substrate (design shown in Sec.5.7.3) will offer additional prospects for enhanced design space [182, 191].

5.8.1 Polarization multiplex

Looking forward, a few direction can immediately benefit the single atom trapping community. As discussed previously, with a metasurface it is possible to achieve a focusing response that is either polarization selective [187] or one that transforms the polarization [188], which are functions

not offered by traditional optical lenses. For example, polarization multiplexing provides a method to trap and collect fluorescence at the diffraction limit for two different wavelengths using a singlet metasurface lens, and may find utility in combining additional multifunctional beams in complex trapping experiments. To illustrate this prospect, we have designed and optically tested a sample with in-plane rectangular shape pillars that achieves equal focal lengths for 780 nm and 852 nm light of orthogonal polarization (see Sec. 5.7.1). This concept can be used to trap at 852 nm, and collect fluorescence at 780 nm, with a 50% efficiency due to the random polarization of the scattered light from atoms.

Another application of the multifunctional polarization-dependent response of the metasurface is to generate a fast-switchable trapping potential that depends on the input polarization to the metalens (Fig. 5.33). Unlike AOD or SLM devices, where switching occurs on the order of hundreds of kHz for AODs and approximately 100 Hz for SLMs, using EOMs can achieve nanosecond-level polarization changes, enabling very rapid switching between different trap configurations. Some of these fast-switchable trapping potentials are being explored in Ref. [193], where metasurfaces are used as switchable holograms to project different trapping potentials with the use of a high NA objective.

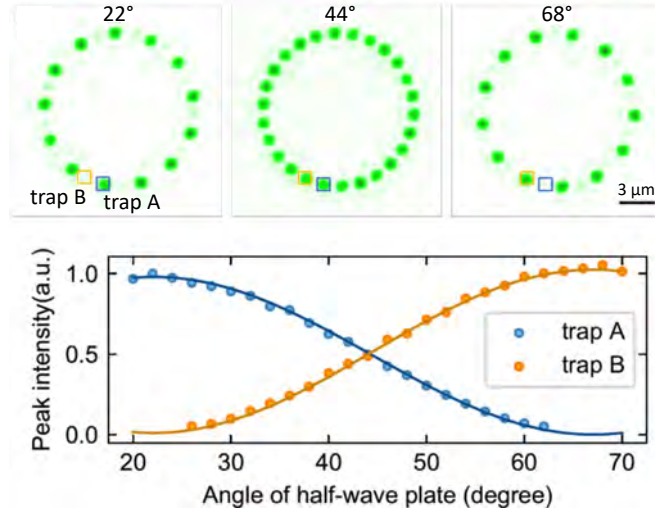


Figure 5.33: A series of traps generated by light diffracted through a polarization dependent metasurface hologram and focused through a high NA objective. The resulting trapping potential is a function of input polarization (top three panels). A continuous switching between two configuration is done through the rotation of linear polarization of the input light. Monitoring the intensity of two trap location (trap A and B) one can obtain the extinction ratio between the two configurations (bottom panel). This figure is reproduced from Ref. [193].

5.8.2 Large FoV doublet metalens

More functionality can be achieved with expanding the number of surfaces offered in the design. To focus on FoV as one metric, an enhanced FoV up to $\pm 25^\circ$ has been achieved by patterning both sides of the substrate to create a double-layer metasurface [81]. This enhancement is of great interest in quantum gas microscope experiments [17, 194, 195], where high-resolution imaging over a large FoV is necessary to observe atoms trapped in optical lattices. In quantum simulation and computation applications, where atoms are trapped in large arrays of tweezers [44, 45] or shuttled between different interaction zones separated by large distances [31, 35], increasing the FoV can also provide significant benefits.

For comparison, state-of-the-art microscope objectives can achieve FoV around $\pm 500 \mu\text{m}$ with an NA of 0.6 [Fig. 5.34(a)] [43]. In contrast, our metalens doublet design (see Sec. 5.7.2) is capable of $\pm 1.2 \text{ mm}$, which is over four times larger [red dashed circle in Fig. 5.34(b)]. Additionally, the mechanical robustness of the metalens is advantageous, while the laser power required to generate

thousands of tweezers can reach tens of watts [43], traditional large objectives may suffer from optical performance degradation due to thermal dissipation issues. Since the metalens is flat, thermal deformation is not a concern, and heat dissipation is more efficient due to its simpler mechanical structure and lower optical losses. Alternatively, using a sapphire substrate instead of fused silica can further enhance thermal conductivity. These favorable qualities of metasurface lenses can offer significant benefits for trapping and imaging large arrays of atoms, holding great promise for future atom trapping experiments.

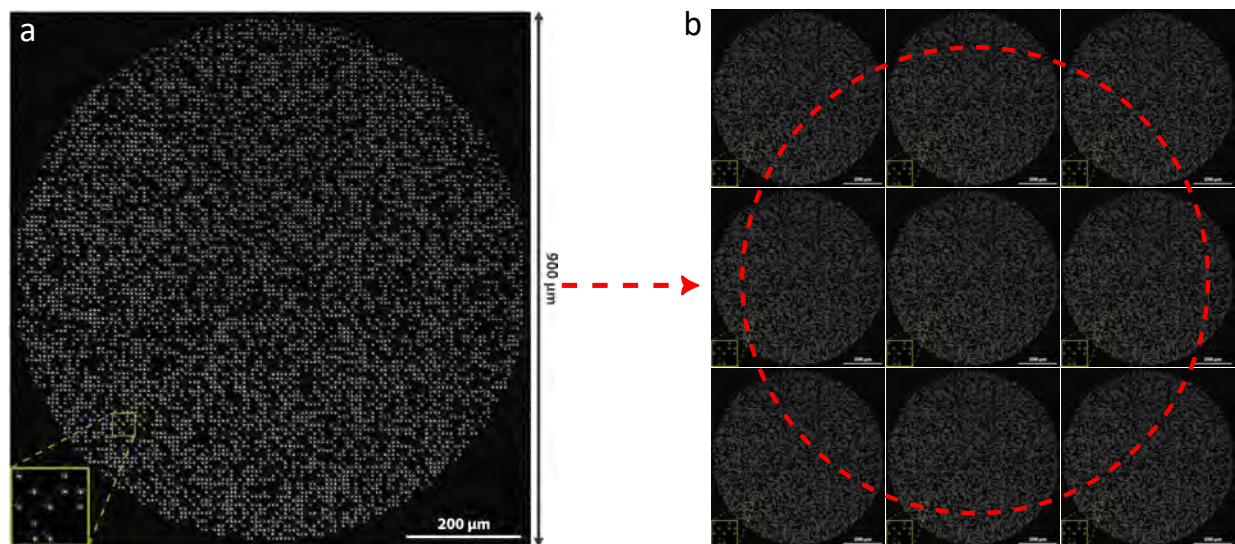


Figure 5.34: (a) Image of over 6000 atoms loaded in optical tweezer projected from the state-of-the-art objective with the FoV around $\pm 450 \mu\text{m}$ [43]. (b) The capability of the doublet design from Sec. 5.7.2 with FoV over $\pm 1.2 \text{ mm}$ (ref dashed circle) comparing to the state-of-the-art objective with multiple optical elements and 50 times the volume and weight. Figure reproduced from Ref. [43].

Bibliography

- [1] M. H. Anderson, J. R. Ensher, M. R. Matthews, C. E. Wieman, and E. A. Cornell. Observation of Bose-Einstein condensation in a dilute atomic vapor. Science, 269(5221):198, 1995.
- [2] K. B. Davis, M. O. Mewes, M. R. Andrews, N. J. Van Druten, D. S. Durfee, D. M. Kurn, and W. Ketterle. Bose-Einstein Condensation in a Gas of Sodium Atoms. Phys. Rev. Lett., 75:3969, 1995.
- [3] N. Schlosser, G. Reymond, I. Protsenko, and P. Grangier. Sub-poissonian loading of single atoms in a microscopic dipole trap. Nature, 411:1024, 2001.
- [4] Michel Brune, F Schmidt-Kaler, Abdelhamid Maali, J Dreyer, E Hagley, JM Raimond, and S Haroche. Quantum rabi oscillation: A direct test of field quantization in a cavity. Physical review letters, 76(11):1800, 1996.
- [5] E Hagley, X Maitre, G Nogues, C Wunderlich, M Brune, Jean-Michel Raimond, and Serge Haroche. Generation of einstein-podolsky-rosen pairs of atoms. Physical Review Letters, 79(1):1, 1997.
- [6] C. Monroe, D. M. Meekhof, B. E. King, W. M. Itano, and D. J. Wineland. Demonstration of a Fundamental Quantum Logic Gate. Phys. Rev. Lett., 75:4714, 1995.
- [7] QA Turchette, CS Wood, BE King, CJ Myatt, D Leibfried, WM Itano, C Monroe, and DJ Wineland. Deterministic entanglement of two trapped ions. Physical Review Letters, 81(17):3631, 1998.
- [8] Santosh Kumar, Haoquan Fan, Harald Kübler, Jiteng Sheng, and James P Shaffer. Atom-based sensing of weak radio frequency electric fields using homodyne readout. Scientific reports, 7(1):42981, 2017.
- [9] Tobias Bothwell, Dhruv Kedar, Eric Oelker, John M Robinson, Sarah L Bromley, Weston L Tew, Jun Ye, and Colin J Kennedy. Jila sri optical lattice clock with uncertainty of. Metrologia, 56(6):065004, 2019.
- [10] Daniel González-Cuadra, Dolev Bluvstein, Marcin Kalinowski, Raphael Kaubruegger, Nishad Maskara, Piero Naldesi, Torsten V Zache, Adam M Kaufman, Mikhail D Lukin, Hannes Pichler, et al. Fermionic quantum processing with programmable neutral atom arrays. Proceedings of the National Academy of Sciences, 120(35):e2304294120, 2023.

- [11] Loïc Henriët, Lucas Beguin, Adrien Signoles, Thierry Lahaye, Antoine Browaeys, Georges-Olivier Reymond, and Christophe Jurczak. Quantum computing with neutral atoms. Quantum, 4:327, 2020.
- [12] Peter W Shor. Algorithms for quantum computation: discrete logarithms and factoring. In Proceedings 35th annual symposium on foundations of computer science, pages 124–134. Ieee, 1994.
- [13] Aram W Harrow, Avinatan Hassidim, and Seth Lloyd. Quantum algorithm for linear systems of equations. Physical review letters, 103(15):150502, 2009.
- [14] Lov K Grover. A fast quantum mechanical algorithm for database search. In Proceedings of the twenty-eighth annual ACM symposium on Theory of computing, pages 212–219, 1996.
- [15] Richard P Feynman. Simulating physics with computers. International journal of theoretical physics, 21(6/7):467–488, 1982.
- [16] W. S. Bakr, J. I. Gillen, A. Peng, S. Fölling, and M. Greiner. A quantum gas microscope for detecting single atoms in a hubbard-regime optical lattice. Nature, 462:74, 2009.
- [17] W. S. Bakr, A. Peng, M. E. Tai, R. Ma, J. Simon, J. I. Gillen, S. Fölling, L. Pollet, and M. Greiner. Probing the Superfluid-to-Mott Insulator Transition at the Single-Atom Level. Science, 329:547, July 2010.
- [18] Takeshi Fukuhara, Peter Schausz, Manuel Endres, Sebastian Hild, Marc Cheneau, Immanuel Bloch, and Christian Gross. Microscopic observation of magnon bound states and their dynamics. Nature, 502(7469):76–79, 2013.
- [19] Takeshi Fukuhara, Adrian Kantian, Manuel Endres, Marc Cheneau, Peter Schausz, Sebastian Hild, David Bellem, Ulrich Schollwöck, Thierry Giamarchi, Christian Gross, Immanuel Bloch, and Stefan Kuhr. Quantum dynamics of a mobile spin impurity. Nat Phys, 9(4):235–241, 2013.
- [20] Jonathan Simon, Waseem S. Bakr, Ruichao Ma, M. Eric Tai, Philipp M. Preiss, and Markus Greiner. Quantum Simulation of an Antiferromagnetic Spin Chains in an Optical Lattice. Nature (London), 472:307, April 2011.
- [21] R. A. Hart, P. M. Duarte, T.-L. Yand, X. Liu, T. Paiva, E. Khatami, R. T. Scalettar, N. Trivedi, D. A. Huse, and R. G. Hulet. Observation of antiferromagnetic correlations in the Hubbard model with ultracold atoms. Nature (London), 519:1, 2015.
- [22] Seth Lloyd. Universal quantum simulators. Science, 273(5278):1073–1078, 1996.
- [23] D Jaksch, JI Cirac, P Zoller, SL Rolston, R Côté, and MD Lukin. Fast quantum gates for neutral atoms. Phys. Rev. Lett., 85(10):2208, 2000.
- [24] Mikhail D Lukin, Michael Fleischhauer, Robin Cote, LuMing Duan, Dieter Jaksch, J Ignacio Cirac, and Peter Zoller. Dipole blockade and quantum information processing in mesoscopic atomic ensembles. Physical review letters, 87(3):037901, 2001.
- [25] MD Lukin and PR Hemmer. Quantum entanglement via optical control of atom-atom interactions. Physical review letters, 84(13):2818, 2000.

- [26] Sylvain de Léséleuc, Daniel Barredo, Vincent Lienhard, Antoine Browaeys, and Thierry Lahaye. Optical control of the resonant dipole-dipole interaction between rydberg atoms. *Physical review letters*, 119(5):053202, 2017.
- [27] D. Barredo, S. de Léséleuc, V. Lienhard, T. Lahaye, and A. Browaeys. An atom-by-atom assembler of defect-free arbitrary two-dimensional atomic arrays. *Science*, 354(6315):1021–1023, November 2016.
- [28] M. Endres, H. Bernien, A. Keesling, H. Levine, E. R. Anschuetz, A. Krajenbrink, C. Senko, V. Vuletic, M. Greiner, and M. D. Lukin. Atom-by-atom assembly of defect-free one-dimensional cold atom arrays. *Science*, 354(6315):1024–1027, November 2016.
- [29] L. Isenhower, E. Urban, X. L. Zhang, A. T. Gill, T. Henage, T. A. Johnson, T. G. Walker, and M. Saffman. Demonstration of a neutral atom controlled-not quantum gate. *Phys. Rev. Lett.*, 104:010503, January 2010.
- [30] T. Wilk, A. Gaëtan, C. Evellin, J. Wolters, Y. Miroshnychenko, P. Grangier, and A. Browaeys. Entanglement of two individual neutral atoms using rydberg blockade. *Phys. Rev. Lett.*, 104:010502, 2010.
- [31] Dolev Bluvstein, Simon J Evered, Alexandra A Geim, Sophie H Li, Hengyun Zhou, Tom Manovitz, Sepehr Ebadi, Madelyn Cain, Marcin Kalinowski, Dominik Hangleiter, et al. Logical quantum processor based on reconfigurable atom arrays. *Nature*, 626(7997):58–65, 2024.
- [32] TM Graham, Y Song, J Scott, C Poole, L Phuttitarn, K Jooya, P Eichler, X Jiang, A Marra, B Grinkemeyer, et al. Multi-qubit entanglement and algorithms on a neutral-atom quantum computer. *Nature*, 604(7906):457–462, 2022.
- [33] Simon J Evered, Dolev Bluvstein, Marcin Kalinowski, Sepehr Ebadi, Tom Manovitz, Hengyun Zhou, Sophie H Li, Alexandra A Geim, Tout T Wang, Nishad Maskara, et al. High-fidelity parallel entangling gates on a neutral-atom quantum computer. *Nature*, 622(7982):268–272, 2023.
- [34] Craig Gidney and Martin Ekerå. How to factor 2048 bit rsa integers in 8 hours using 20 million noisy qubits. *Quantum*, 5:433, 2021.
- [35] Dolev Bluvstein, Harry Levine, Giulia Semeghini, Tout T Wang, Sepehr Ebadi, Marcin Kalinowski, Alexander Keesling, Nishad Maskara, Hannes Pichler, Markus Greiner, et al. A quantum processor based on coherent transport of entangled atom arrays. *Nature*, 604(7906):451–456, 2022.
- [36] Kevin Singh, Conor E Bradley, Shraddha Anand, Vikram Ramesh, Ryan White, and Hannes Bernien. Mid-circuit correction of correlated phase errors using an array of spectator qubits. *Science*, 380(6651):1265–1269, 2023.
- [37] Kevin Singh, Shraddha Anand, Andrew Pocklington, Jordan T Kemp, and Hannes Bernien. Dual-element, two-dimensional atom array with continuous-mode operation. *Physical Review X*, 12(1):011040, 2022.
- [38] Jacob P Covey, Harald Weinfurter, and Hannes Bernien. Quantum networks with neutral atom processing nodes. *npj Quantum Information*, 9(1):90, 2023.

- [39] Ying Li and Simon C Benjamin. Hierarchical surface code for network quantum computing with modules of arbitrary size. Physical Review A, 94(4):042303, 2016.
- [40] Jacob P Covey, Ivaylo S Madjarov, Alexandre Cooper, and Manuel Endres. 2000-times repeated imaging of strontium atoms in clock-magic tweezer arrays. Phys. Rev. Lett., 122(17):173201, 2019.
- [41] Aaron W Young, William J Eckner, William R Milner, Dhruv Kedar, Matthew A Norcia, Eric Oelker, Nathan Schine, Jun Ye, and Adam M Kaufman. Half-minute-scale atomic coherence and high relative stability in a tweezer clock. Nature, 588(7838):408–413, 2020.
- [42] Damien Bloch, Britton Hofer, Sam R Cohen, Antoine Browaeys, and Igor Ferrier-Barbut. Trapping and imaging single dysprosium atoms in optical tweezer arrays. Physical Review Letters, 131(20):203401, 2023.
- [43] Hannah J Manetsch, Gyohei Nomura, Elie Bataille, Kon H Leung, Xudong Lv, and Manuel Endres. A tweezer array with 6100 highly coherent atomic qubits. arXiv preprint arXiv:2403.12021, 2024.
- [44] Sepehr Ebadi, Tout T Wang, Harry Levine, Alexander Keesling, Giulia Semeghini, Ahmed Omran, Dolev Bluvstein, Rhine Samajdar, Hannes Pichler, Wen Wei Ho, et al. Quantum phases of matter on a 256-atom programmable quantum simulator. Nature, 595(7866):227–232, 2021.
- [45] Giulia Semeghini, Harry Levine, Alexander Keesling, Sepehr Ebadi, Tout T Wang, Dolev Bluvstein, Ruben Verresen, Hannes Pichler, Marcin Kalinowski, Rhine Samajdar, et al. Probing topological spin liquids on a programmable quantum simulator. arXiv preprint arXiv:2104.04119, 2021.
- [46] T. L. Nguyen, J. M. Raimond, C. Sayrin, R. Cortinas, T. Cantat-Moltrecht, F. Assemat, I. Dotsenko, S. Gleyzes, S. Haroche, G. Roux, Th. Jolicoeur, and M. Brune. Towards quantum simulation with circular rydberg atoms. Phys. Rev. X, 8:011032, Feb 2018.
- [47] Tigrane Cantat-Moltrecht, Rodrigo Cortiñas, Brice Ravon, Paul Méhaignerie, Serge Haroche, Jean-Michel Raimond, Maxime Favier, Michel Brune, and Clément Sayrin. Long-lived circular rydberg states of laser-cooled rubidium atoms in a cryostat. Physical Review Research, 2(2):022032, 2020.
- [48] Sam R Cohen and Jeff D Thompson. Quantum computing with circular rydberg atoms. PRX Quantum, 2(3):030322, 2021.
- [49] Randall G Hulet and Daniel Kleppner. Rydberg atoms in” circular” states. Physical review letters, 51(16):1430, 1983.
- [50] RG Cortiñas, M Favier, B Ravon, P Méhaignerie, Y Machu, JM Raimond, C Sayrin, and M Brune. Laser trapping of circular rydberg atoms. Physical Review Letters, 124(12):123201, 2020.
- [51] I. I. Beterov, I. I. Ryabtsev, D. B. Tretyakov, and V. M. Entin. Quasiclassical calculations of blackbody-radiation-induced depopulation rates and effective lifetimes of rydberg ns, np, and nd alkali-metal atoms with $n_j \geq 80$. Phys. Rev. A, 79:052504, May 2009.

- [52] M Saffman. Quantum computing with atomic qubits and rydberg interactions: Progress and challenges. J. Phys. B, 49(20):202001, 2016.
- [53] Johannes Zeiher, Rick Van Bijnen, Peter Schauß, Sebastian Hild, Jae-yoon Choi, Thomas Pohl, Immanuel Bloch, and Christian Gross. Many-body interferometry of a rydberg-dressed spin lattice. Nature Physics, 12(12):1095–1099, 2016.
- [54] Johannes Zeiher, Jae-yoon Choi, Antonio Rubio-Abadal, Thomas Pohl, Rick Van Bijnen, Immanuel Bloch, and Christian Gross. Coherent many-body spin dynamics in a long-range interacting ising chain. Physical review X, 7(4):041063, 2017.
- [55] Thomas Boulier, Eric Magnan, Carlos Bracamontes, James Maslek, EA Goldschmidt, JT Young, Alexey V Gorshkov, SL Rolston, and James V Porto. Spontaneous avalanche dephasing in large rydberg ensembles. Physical Review A, 96(5):053409, 2017.
- [56] WE Cooke and TF Gallagher. Effects of blackbody radiation on highly excited atoms. Physical Review A, 21(2):588, 1980.
- [57] Iris Cong, Harry Levine, Alexander Keesling, Dolev Bluvstein, Sheng-Tao Wang, and Mikhail D Lukin. Hardware-efficient, fault-tolerant quantum computation with rydberg atoms. Physical Review X, 12(2):021049, 2022.
- [58] Kai-Niklas Schymik, Sara Pancaldi, Florence Nogrette, Daniel Barredo, Julien Paris, Antoine Browaeys, and Thierry Lahaye. Single atoms with 6000-second trapping lifetimes in optical-tweezer arrays at cryogenic temperatures. Phys. Rev. Applied, 16:034013, 2021.
- [59] Kai-Niklas Schymik. Scaling-up the Tweezer Platform-Trapping Arrays of Single Atoms in a Cryogenic Environment. PhD thesis, Université Paris-Saclay, 2022.
- [60] Morten Kjaergaard, Mollie E Schwartz, Jochen Braumüller, Philip Krantz, Joel I-J Wang, Simon Gustavsson, and William D Oliver. Superconducting qubits: Current state of play. Annual Review of Condensed Matter Physics, 11:369–395, 2020.
- [61] Aaron Somoroff, Quentin Ficheux, Raymond A Mencia, Haonan Xiong, Roman Kuzmin, and Vladimir E Manucharyan. Millisecond coherence in a superconducting qubit. Physical Review Letters, 130(26):267001, 2023.
- [62] Petar Jurcevic, Ali Javadi-Abhari, Lev S Bishop, Isaac Lauer, Daniela F Bogorin, Markus Brink, Lauren Capelluto, Oktay Günlük, Toshinari Itoko, Naoki Kanazawa, et al. Demonstration of quantum volume 64 on a superconducting quantum computing system. Quantum Science and Technology, 6(2):025020, 2021.
- [63] M Brownnutt, M Kumph, P Rabl, and R Blatt. Ion-trap measurements of electric-field noise near surfaces. Reviews of modern Physics, 87(4):1419, 2015.
- [64] Jaroslaw Labaziewicz, Yufei Ge, Paul Antohi, David Leibbrandt, Kenneth R Brown, and Isaac L Chuang. Suppression of heating rates in cryogenic surface-electrode ion traps. Physical review letters, 100(1):013001, 2008.
- [65] Louis Deslauriers, S Olmschenk, D Stick, WK Hensinger, J Sterk, and C Monroe. Scaling and suppression of anomalous heating in ion traps. Physical Review Letters, 97(10):103007, 2006.

- [66] Craig R Clark, Holly N Tinkey, Brian C Sawyer, Adam M Meier, Karl A Burkhardt, Christopher M Seck, Christopher M Shappert, Nicholas D Guise, Curtis E Volin, Spencer D Fallek, et al. High-fidelity bell-state preparation with ca+ 40 optical qubits. Physical Review Letters, 127(13):130505, 2021.
- [67] AD Leu, MF Gely, MA Weber, MC Smith, DP Nadlinger, and DM Lucas. Fast, high-fidelity addressed single-qubit gates using efficient composite pulse sequences. Physical Review Letters, 131(12):120601, 2023.
- [68] G. Pagano, P.W. Hess, H. B. Kaplan, W. L. Tan, P. Richerme, P. Becker, A. Kyprianidis, J. Zhang, E. Birkelbaw, M. R. Hernandez, Y. Wu, and C. Monroe. Cryogenic trapped-ion system for large scale quantum simulation. arXiv:1802.03118, 2018.
- [69] Ichiro Ushijima, Masao Takamoto, Manoj Das, Takuya Ohkubo, and Hidetoshi Katori. Cryogenic optical lattice clocks. Nature Photonics, 9(3):185–189, 2015.
- [70] Kang-Kuen Ni, Till Rosenband, and David D Grimes. Dipolar exchange quantum logic gate with polar molecules. Chemical science, 9(33):6830–6838, 2018.
- [71] M Morgado and S Whitlock. Quantum simulation and computing with rydberg-interacting qubits. AVS Quantum Science, 3(2), 2021.
- [72] Erik W Streed, Benjamin G Norton, Andreas Jechow, Till J Weinhold, and David Kielpinski. Imaging of trapped ions with a microfabricated optic for quantum information processing. Physical review letters, 106(1):010502, 2011.
- [73] Kenneth R Brown, Jungsang Kim, and Christopher Monroe. Co-designing a scalable quantum computer with trapped atomic ions. npj Quantum Information, 2(1):1–10, 2016.
- [74] Karan K Mehta, Chi Zhang, Maciej Malinowski, Thanh-Long Nguyen, Martin Stadler, and Jonathan P Home. Integrated optical multi-ion quantum logic. Nature, 586(7830):533–537, 2020.
- [75] Donggyu Kim, Alexander Keesling, Ahmed Omran, Harry Levine, Hannes Bernien, Markus Greiner, Mikhail D Lukin, and Dirk R Englund. Large-scale uniform optical focus array generation with a phase spatial light modulator. Optics letters, 44(12):3178–3181, 2019.
- [76] Daniel Barredo, Vincent Lienhard, Sylvain De Leseleuc, Thierry Lahaye, and Antoine Browaeys. Synthetic three-dimensional atomic structures assembled atom by atom. Nature, 561(7721):79–82, 2018.
- [77] Seyedeh Mahsa Kamali, Ehsan Arbabi, Amir Arbabi, and Andrei Faraon. A review of dielectric optical metasurfaces for wavefront control. Nanophotonics, 7(6):1041–1068, 2018.
- [78] Wei Ting Chen, Alexander Y. Zhu, and Federico Capasso. Flat optics with dispersion-engineered metasurfaces. Nature Reviews Materials, 5(8):604–620, August 2020.
- [79] Mingze Liu, Wenqi Zhu, Pengcheng Huo, Lei Feng, Maowen Song, Cheng Zhang, Lu Chen, Henri J. Lezec, Yanqing Lu, Amit Agrawal, and Ting Xu. Multifunctional metasurfaces enabled by simultaneous and independent control of phase and amplitude for orthogonal polarization states. Light Sci Appl, 10(1):107, May 2021.

- [80] Ehsan Arbabi, Jiaqi Li, Romanus J. Hutchins, Seyedeh Mahsa Kamali, Amir Arbabi, Yu Horie, Pol Van Dorpe, Viviana Gradinaru, Daniel A. Wagenaar, and Andrei Faraon. Two-Photon Microscopy with a Double-Wavelength Metasurface Objective Lens. *Nano Letters*, 18(8):4943–4948, August 2018.
- [81] Benedikt Groever, Wei Ting Chen, and Federico Capasso. Meta-lens doublet in the visible region. *Nano Letters*, 17(8):4902–4907, August 2017.
- [82] Lingxiao Zhu, Xuan Liu, Basudeb Sain, Mengyao Wang, Christian Schlickriede, Yutao Tang, Junhong Deng, Kingfai Li, Jun Yang, Michael Holynski, et al. A dielectric metasurface optical chip for the generation of cold atoms. *Science Advances*, 6(31):eabb6667, 2020.
- [83] William R McGehee, Wenqi Zhu, Daniel S Barker, Daron Westly, Alexander Yulaev, Nikolai Klimov, Amit Agrawal, Stephen Eckel, Vladimir Aksyuk, and Jabez J McClelland. Magneto-optical trapping using planar optics. *New Journal of Physics*, 23(1):013021, 2021.
- [84] M. O. Brown, T. Thiele, C. Kiehl, T.-W. Hsu, and C. A. Regal. Gray-molasses optical-tweezer loading: Controlling collisions for scaling atom-array assembly. *Phys. Rev. X*, 9:011057, 2019.
- [85] Gerald Gabrielse, X Fei, LA Orozco, RL Tjoelker, J Haas, H Kalinowsky, TA Trainor, and W Kells. Thousandfold improvement in the measured antiproton mass. *Physical review letters*, 65(11):1317, 1990.
- [86] M Diederich, H Häffner, N Hermanspahn, M Immel, HJ Kluge, R Ley, R Mann, W Quint, S Stahl, and G Werth. Observing a single hydrogen-like ion in a penning trap at $t = 4$ k. *Hyperfine interactions*, 115:185–192, 1998.
- [87] Tom Manovitz, Sophie H Li, Sepehr Ebadi, Rhine Samajdar, Alexandra A Geim, Simon J Evered, Dolev Bluvstein, Hengyun Zhou, Nazli Uğur Köyliüoğlu, Johannes Feldmeier, et al. Quantum coarsening and collective dynamics on a programmable quantum simulator. *arXiv preprint arXiv:2407.03249*, 2024.
- [88] PA Willems and KG Libbrecht. Creating long-lived neutral-atom traps in a cryogenic environment. *Physical Review A*, 51(2):1403, 1995.
- [89] Sebastien Gleyzes, Stefan Kuhr, Christine Guerlin, Julien Bernu, Samuel Deleglise, Ulrich Busk Hoff, Michel Brune, Jean-Michel Raimond, and Serge Haroche. Quantum jumps of light recording the birth and death of a photon in a cavity. *Nature*, 446(7133):297–300, 2007.
- [90] Simon Bernon, Helge Hattermann, Daniel Bothner, Martin Knufinke, Patrizia Weiss, Florian Jessen, Daniel Cano, Matthias Kemmler, Reinhold Kleiner, Dieter Koelle, et al. Manipulation and coherence of ultra-cold atoms on a superconducting atom chip. *Nature communications*, 4(1):2380, 2013.
- [91] A. Gaëtan, Y. Miroshnychenko, T. Wilk, A. Chotia, M. Viteau, D. Comparat, P. Pillet, A. Browaeys, and P. Grangier. Observation of collective excitation of two individual atoms in the Rydberg blockade regime. *Nat. Phys.*, 5:115, 2009.
- [92] Lucas Beguin. *Measurement of the van der Waals interaction between two Rydberg atoms*. Theses, Institut d’Optique Graduate School, December 2013.

- [93] L. Béguin, A. Vernier, R. Chicireanu, T. Lahaye, and A. Browaeys. Direct Measurement of the van der Waals Interaction between Two Rydberg Atoms. Phys. Rev. Lett., 110(26):263201, June 2013.
- [94] Heiner Saßmannshausen, Frédéric Merkt, and Johannes Deiglmayr. High-resolution spectroscopy of rydberg states in an ultracold cesium gas. Physical Review A, 87(3):032519, 2013.
- [95] Alec Jenkins, Joanna W Lis, Aruku Senoo, William F McGrew, and Adam M Kaufman. Ytterbium nuclear-spin qubits in an optical tweezer array. Physical Review X, 12(2):021027, 2022.
- [96] T Arpornthip, CA Sackett, and KJ Hughes. Vacuum-pressure measurement using a magneto-optical trap. Physical Review A, 85(3):033420, 2012.
- [97] Andras Dallos and Fortunat Steinrissler. Pumping speed of getter-ion pumps at low pressures. Coordinated Science Laboratory Report no. R-302, 1966.
- [98] Milton Ohring. Chapter 2 - vacuum science and technology. In Milton Ohring, editor, Materials Science of Thin Films (Second Edition), pages 57–93. Academic Press, San Diego, second edition edition, 2002.
- [99] Niels Marquardt. Introduction to the principles of vacuum physics. 1999.
- [100] Hannes Bernien, Sylvain Schwartz, Alexander Keesling, Harry Levine, Ahmed Omran, Hannes Pichler, Soonwon Choi, Alexander S Zibrov, Manuel Endres, Markus Greiner, M. Lukin, and V. Vuletic. Probing many-body dynamics on a 51-atom quantum simulator. Nature, 551(7682):579, 2017.
- [101] Adam Kaufman. Laser cooling atoms to indistinguishability: Atomic Hong-Ou-Mandel interference and entanglement through spin exchange. PhD thesis, Boulder, CO, 11-2015 2015.
- [102] Stephen Eckel, Daniel S Barker, James A Fedchak, Nikolai N Klimov, Eric Norrgard, Julia Scherschligt, Constantinos Makrides, and Eite Tiesinga. Challenges to miniaturizing cold atom technology for deployable vacuum metrology. Metrologia, 55(5):S182, 2018.
- [103] Daniel S Barker, Bishnu P Acharya, James A Fedchak, Nikolai N Klimov, Eric B Norrgard, Julia Scherschligt, Eite Tiesinga, and Stephen P Eckel. Precise quantum measurement of vacuum with cold atoms. Review of Scientific Instruments, 93(12), 2022.
- [104] Roberto Kersevan. Analytical and numerical tools for vacuum systems. 2007.
- [105] Nagamitsu Yoshimura. Foundations of Molecular-Flow Networks for Vacuum System Analysis. Academic Press, 2019.
- [106] Daniel A. Steck. Rubidium 87 D Line Data. Published: available online at <http://steck.us/alkalidata> (revision 2.1.4, 23 December 2010).
- [107] Katharina Battes, Christian Day, and Volker Hauer. Outgassing behavior of different high-temperature resistant polymers. Journal of Vacuum Science & Technology A, 36(2), 2018.

- [108] Sergio Giacomo Sammartano. Outgassing rates of peek, kapton® and vespel® polymers, 2020.
- [109] Sergio Giacomo Sammartano, Giuseppe Bregliozzi, Paolo Chiggiato, and Ivo Wevers. Outgassing rates of peek, kapton® and vespel® foils. Technical report, CERN, 2020.
- [110] Vincent Baglin. Cryopumping and vacuum systems. [arXiv preprint arXiv:2006.01574](#), 2020.
- [111] Chris Day. Basics and applications of cryopumps. 2007.
- [112] Chr Day, D Murdoch, and R Pearce. The vacuum systems of iter. *Vacuum*, 83(4):773–778, 2008.
- [113] Cristoforo Benvenuti. Molecular surface pumping: cryopumping. Technical report, CERN, 1999.
- [114] P Micke, J Stark, SA King, T Leopold, T Pfeifer, Lisa Schmoeger, M Schwarz, LJ Spieß, PO Schmidt, and JR Crespo López-Urrutia. Closed-cycle, low-vibration 4 k cryostat for ion traps and other applications. *Review of Scientific Instruments*, 90(6), 2019.
- [115] T-W Hsu, Wenqi Zhu, Tobias Thiele, Mark O Brown, Scott B Papp, Amit Agrawal, and Cindy A Regal. Single-atom trapping in a metasurface-lens optical tweezer. *PRX Quantum*, 3(3):030316, 2022.
- [116] Jaime Ramirez-Serrano, Nan Yu, James M Kohel, James R Kellogg, and Lute Maleki. Multistage two-dimensional magneto-optical trap as a compact cold atom beam source. *Optics letters*, 31(6):682–684, 2006.
- [117] Natascia Castagna, Jocelyne Guéna, MD Plimmer, and Pierre Thomann. A novel simplified two-dimensional magneto-optical trap as an intense source of slow cesium atoms. *The European Physical Journal Applied Physics*, 34(1):21–30, 2006.
- [118] TM Graham, L Phuttitarn, R Chinnarasu, Y Song, C Poole, K Jooya, J Scott, A Scott, P Eichler, and M Saffman. Midcircuit measurements on a single-species neutral alkali atom quantum processor. *Physical Review X*, 13(4):041051, 2023.
- [119] II Beterov, DB Tretyakov, II Ryabtsev, A Ekers, and NN Bezuglov. Ionization of sodium and rubidium n s, n p, and n d rydberg atoms by blackbody radiation. *Physical Review A*, 75(5):052720, 2007.
- [120] ED Marquardt, JP Le, and Ray Radebaugh. Cryogenic material properties database. *Cryocoolers 11*, pages 681–687, 2002.
- [121] A. Fuhrmanek, R. Bourgain, Y. R. P. Sortais, and A. Browaeys. Light-assisted collisions between a few cold atoms in a microscopic dipole trap. *Phys. Rev. A*, 85:062708, 2012.
- [122] B. Lester. [Atom-by-atom control and readout for studying spin-motional dynamics and entanglement in neutral atom arrays](#). PhD thesis, Boulder, CO, 2016-11 2016.
- [123] Xin Zhang, Wei Ma, Songjin Zhang, Hongliang Huang, Liu Ouyang, Wei Peng, Jiayi Ye, and Cheng Chen. A comparative study of adhesion evaluation methods on ophthalmic ar coating lens. *Coatings*, 10(10):979, 2020.

- [124] Roland Matt. Parallel control of a dual-isotope trapped ion register. PhD thesis, ETH Zurich, 2023.
- [125] Robin Oswald. Characterization and control of a cryogenic ion trap apparatus and laser systems for quantum computing. PhD thesis, ETH Zurich, 2022.
- [126] K Barr, Tamsin Cookson, and KG Lagoudakis. Operation of a continuous flow liquid helium magnetic microscopy cryostat as a closed cycle system. Review of Scientific Instruments, 92(12), 2021.
- [127] Kai-Niklas Schymik, Bruno Ximenez, Etienne Bloch, Davide Dreon, Adrien Signoles, Florence Nogrette, Daniel Barredo, Antoine Browaeys, and Thierry Lahaye. In situ equalization of single-atom loading in large-scale optical tweezer arrays. Physical Review A, 106(2):022611, 2022.
- [128] D Sesko, T Walker, C Monroe, A Gallagher, and C Wieman. Collisional losses from a light-force atom trap. Phys. Rev. Lett., 63(9):961, 1989.
- [129] TG Tiecke, SD Gensemer, A Ludewig, and JTM Walraven. High-flux two-dimensional magneto-optical-trap source for cold lithium atoms. Physical Review A, 80(1):013409, 2009.
- [130] Matteo Barbiero, Marco G Tarallo, Davide Calonico, Filippo Levi, Giacomo Lamporesi, and Gabriele Ferrari. Sideband-enhanced cold atomic source for optical clocks. Physical Review Applied, 13(1):014013, 2020.
- [131] SP Ram, SR Mishra, SK Tiwari, and SC Mehendale. Note: Investigation of atom transfer using a red-detuned push beam in a double magneto-optical trap setup. Review of Scientific Instruments, 82(12), 2011.
- [132] Yoann Bruneau, Guyve Khalili, Pierre Pillet, and Daniel Comparat. Guided and focused slow atomic beam from a 2 dimensional magneto optical trap. The European Physical Journal D, 68:1–6, 2014.
- [133] Rudolf Grimm, Matthias Weidemüller, and Yurii B Ovchinnikov. Optical dipole traps for neutral atoms. In Advances in atomic, molecular, and optical physics, volume 42, pages 95–170. Elsevier, 2000.
- [134] C. Tuchendler, A. M. Lance, A. Browaeys, Y. R. P. Sortais, and P. Grangier. Energy Distribution and Cooling of a Single Atom in an Optical Tweezer. Phys. Rev. A, 78:033425, 2008.
- [135] Georges Reymond, Nicolas Schlosser, Igor Protsenko, and Philippe Grangier. Single-atom manipulations in a microscopic dipole trap. Philosophical Transactions of the Royal Society of London. Series A: Mathematical, Physical and Engineering Sciences, 361(1808):1527–1536, 2003.
- [136] Harry Jay Levine. Quantum information processing and quantum simulation with programmable Rydberg atom arrays. PhD thesis, Harvard University, 2021.
- [137] M E Gehm, K M O’Hara, T A Savard, and J E Thomas. Dynamics of noise-induced heating in atom traps. Phys. Rev. A, 58(5):3914, 1998.

- [138] Karl N Blodgett, David Peana, Saumitra S Phatak, Lane M Terry, Maria Paula Montes, and Jonathan D Hood. Imaging a li 6 atom in an optical tweezer 2000 times with λ -enhanced gray molasses. Physical Review Letters, 131(8):083001, 2023.
- [139] Pascal Scholl, Michael Schuler, Hannah J Williams, Alexander A Eberharter, Daniel Barredo, Kai-Niklas Schymik, Vincent Lienhard, Louis-Paul Henry, Thomas C Lang, Thierry Lahaye, et al. Quantum simulation of 2d antiferromagnets with hundreds of rydberg atoms. Nature, 595(7866):233–238, 2021.
- [140] Matthew J O’Rourke and Garnet Kin-Lic Chan. Entanglement in the quantum phases of an unfrustrated rydberg atom array. Nature Communications, 14(1):5397, 2023.
- [141] Jonas Haferkamp, Dominik Hangleiter, Adam Bouland, Bill Fefferman, Jens Eisert, and Juani Bermejo-Vega. Closing gaps of a quantum advantage with short-time hamiltonian dynamics. Physical Review Letters, 125(25):250501, 2020.
- [142] Qian Xu, J Pablo Bonilla Ataides, Christopher A Pattison, Nithin Raveendran, Dolev Bluvstein, Jonathan Wurtz, Bane Vasić, Mikhail D Lukin, Liang Jiang, and Hengyun Zhou. Constant-overhead fault-tolerant quantum computation with reconfigurable atom arrays. Nature Physics, pages 1–7, 2024.
- [143] Sergey Bravyi, Andrew W Cross, Jay M Gambetta, Dmitri Maslov, Patrick Rall, and Theodore J Yoder. High-threshold and low-overhead fault-tolerant quantum memory. Nature, 627(8005):778–782, 2024.
- [144] Weikun Tian, Wen Jun Wee, An Qu, Billy Jun Ming Lim, Prithvi Raj Datla, Vanessa Pei Wen Koh, and Huanqian Loh. Parallel assembly of arbitrary defect-free atom arrays with a multitweezer algorithm. Physical Review Applied, 19(3):034048, 2023.
- [145] Kai-Niklas Schymik, Vincent Lienhard, Daniel Barredo, Pascal Scholl, Hannah Williams, Antoine Browaeys, and Thierry Lahaye. Enhanced atom-by-atom assembly of arbitrary tweezer arrays. Physical Review A, 102(6):063107, 2020.
- [146] Bernhard Albrecht, Yijian Meng, Christoph Clausen, Alexandre Dareaux, Philipp Schneeweiss, and Arno Rauschenbeutel. Fictitious magnetic-field gradients in optical microtraps as an experimental tool for interrogating and manipulating cold atoms. Physical Review A, 94(6):061401, 2016.
- [147] F Schmidt-Kaler, S Gulde, M Riebe, T Deuschle, A Kreuter, G Lancaster, C Becher, J Eschner, H Häffner, and R Blatt. The coherence of qubits based on single ca+ ions. Journal of Physics B: Atomic, Molecular and Optical Physics, 36(3):623, 2003.
- [148] Harry Levine, Alexander Keesling, Ahmed Omran, Hannes Bernien, Sylvain Schwartz, Alexander S. Zibrov, Manuel Endres, Markus Greiner, Vladan Vuletić, and Mikhail D. Lukin. High-fidelity control and entanglement of rydberg-atom qubits. Phys. Rev. Lett., 121:123603, Sep 2018.
- [149] Aaron W Young, Shawn Geller, William J Eckner, Nathan Schine, Scott Glancy, Emanuel Knill, and Adam M Kaufman. An atomic boson sampler. Nature, 629(8011):311–316, 2024.
- [150] Chr Day and D Murdoch. The iter vacuum systems. In Journal of Physics: Conference Series, volume 114, page 012013. IOP Publishing, 2008.

- [151] Florian Meinert, Christian Hölzl, Mehmet Ali Nebioglu, Alessandro D’Arnese, Philipp Karl, Martin Dressel, and Marc Scheffler. Indium tin oxide films meet circular rydberg atoms: prospects for novel quantum simulation schemes. Physical Review Research, 2(2):023192, 2020.
- [152] A. M. Kaufman, B. J. Lester, and C. A. Regal. Cooling a single atom in an optical tweezer to its quantum ground state. Phys. Rev. X, 2(4):041014, November 2012.
- [153] Y. R. P. Sortais, H. Marion, C. Tuchendler, A. M. Lance, M. Lamare, P. Fournet, C. Armellin, R. Mercier, G. Messin, A. Browaeys, and P. Grangier. Diffraction-limited optics for single-atom manipulation. Phys. Rev. A, 75:013406, 2007.
- [154] X. L. Zhang, L. Isenhower, A. T. Gill, T. G. Walker, and M. Saffman. Deterministic entanglement of two neutral atoms via rydberg blockade. Phys. Rev. A, 82:030306(R), 2010.
- [155] Lee R Liu, Jonathan D Hood, Yichao Yu, Jessie T Zhang, Kenneth Wang, Y-W Lin, Till Rosenband, and K-K Ni. Molecular assembly of ground-state cooled single atoms. Physical Review X, 9(2):021039, 2019.
- [156] Kevin Singh, Shraddha Anand, Andrew Pocklington, Jordan T Kemp, and Hannes Bernien. A dual-element, two-dimensional atom array with continuous-mode operation. arXiv preprint arXiv:2110.05515, 2021.
- [157] Loïc Anderegg, Lawrence W Cheuk, Yicheng Bao, Sean Burchesky, Wolfgang Ketterle, Kang-Kuen Ni, and John M Doyle. An optical tweezer array of ultracold molecules. Science, 365(6458):1156–1158, 2019.
- [158] Artificial dielectrics having refractive indices less than unity. Proceedings of the IEE-Part IV: Institution Monographs, 100(5):51–62, 1953.
- [159] SSD Jones and J Brown. Metallic delay lenses. Nature, 163(4139):324–325, 1949.
- [160] SB Cohn. Analysis of the metal-strip delay structure for microwave lenses. Journal of Applied Physics, 20(3):257–262, 1949.
- [161] Winston E Kock. Metallic delay lenses. Bell System Technical Journal, 27(1):58–82, 1948.
- [162] David R Smith, Willie J Padilla, DC Vier, Syrus C Nemat-Nasser, and Seldon Schultz. Composite medium with simultaneously negative permeability and permittivity. Physical review letters, 84(18):4184, 2000.
- [163] Jeffrey D Wilson and Zachary D Schwartz. Multifocal flat lens with left-handed metamaterial. Applied Physics Letters, 86(2), 2005.
- [164] Carl Pfeiffer and Anthony Grbic. Metamaterial huygens’ surfaces: tailoring wave fronts with reflectionless sheets. Physical review letters, 110(19):197401, 2013.
- [165] Nanfang Yu, Patrice Genevet, Mikhail A Kats, Francesco Aieta, Jean-Philippe Tetienne, Federico Capasso, and Zeno Gaburro. Light propagation with phase discontinuities: generalized laws of reflection and refraction. science, 334(6054):333–337, 2011.

- [166] Amir Arbabi, Yu Horie, Mahmood Bagheri, and Andrei Faraon. Dielectric metasurfaces for complete control of phase and polarization with subwavelength spatial resolution and high transmission. Nature nanotechnology, 10(11):937–943, 2015.
- [167] Amir Arbabi, Yu Horie, Alexander J Ball, Mahmood Bagheri, and Andrei Faraon. Subwavelength-thick lenses with high numerical apertures and large efficiency based on high-contrast transmitarrays. Nature Communications, 6(1):1–6, 2015.
- [168] Xingjie Ni, Naresh K Emani, Alexander V Kildishev, Alexandra Boltasseva, and Vladimir M Shalaev. Broadband light bending with plasmonic nanoantennas. Science, 335(6067):427–427, 2012.
- [169] Jingyi Yang, Sudip Gurung, Subhajit Bej, Peinan Ni, and Ho Wai Howard Lee. Active optical metasurfaces: comprehensive review on physics, mechanisms, and prospective applications. Reports on Progress in Physics, 85(3):036101, 2022.
- [170] Nanfang Yu and Federico Capasso. Flat optics with designer metasurfaces. Nature materials, 13(2):139–150, 2014.
- [171] David M Pozar, Stephen D Targonski, and HD Syrigos. Design of millimeter wave microstrip reflectarrays. IEEE transactions on antennas and propagation, 45(2):287–296, 1997.
- [172] John Huang and Jose Antonio Encinar. Reflectarray antennas. John Wiley & Sons, 2007.
- [173] Nanfang Yu, Patrice Genevet, Francesco Aieta, Mikhail A Kats, Romain Blanchard, Guillaume Aoust, Jean-Philippe Tetienne, Zeno Gaburro, and Federico Capasso. Flat optics: controlling wavefronts with optical antenna metasurfaces. IEEE Journal of Selected Topics in Quantum Electronics, 19(3):4700423–4700423, 2013.
- [174] Jingyi Yang, Sudip Gurung, Subhajit Bej, Peinan Ni, and Ho Wai Howard Lee. Active optical metasurfaces: comprehensive review on physics, mechanisms, and prospective applications. Reports on Progress in Physics, 85(3):036101, March 2022.
- [175] Dianmin Lin, Pengyu Fan, Erez Hasman, and Mark L Brongersma. Dielectric gradient metasurface optical elements. science, 345(6194):298–302, 2014.
- [176] Ye Feng Yu, Alexander Y Zhu, Ramón Paniagua-Domínguez, Yuan Hsing Fu, Boris Luk'yanchuk, and Arseniy I Kuznetsov. High-transmission dielectric metasurface with 2π phase control at visible wavelengths. Laser & Photonics Reviews, 9(4):412–418, 2015.
- [177] Manuel Decker, Isabelle Staude, Matthias Falkner, Jason Dominguez, Dragomir N Neshev, Igal Brener, Thomas Pertsch, and Yuri S Kivshar. High-efficiency dielectric huygens' surfaces. Advanced Optical Materials, 3(6):813–820, 2015.
- [178] Philippe Lalanne, Simion Astilean, Pierre Chavel, Edmond Cambril, and Huguette Launois. Blazed binary subwavelength gratings with efficiencies larger than those of conventional échelette gratings. Optics letters, 23(14):1081–1083, 1998.
- [179] Seyedeh Mahsa Kamali, Amir Arbabi, Ehsan Arbabi, Yu Horie, and Andrei Faraon. Decoupling optical function and geometrical form using conformal flexible dielectric metasurfaces. Nature communications, 7(1):11618, 2016.

- [180] Yongli He, Boxiang Song, and Jiang Tang. Optical metalenses: fundamentals, dispersion manipulation, and applications. Frontiers of Optoelectronics, 15(1):24, 2022.
- [181] Sonny Vo, David Fattal, Wayne V Sorin, Zhen Peng, Tho Tran, Marco Fiorentino, and Raymond G Beausoleil. Sub-wavelength grating lenses with a twist. IEEE Photonics Technology Letters, 26(13):1375–1378, 2014.
- [182] Wei Ting Chen, Alexander Y. Zhu, Jared Sisler, Yao-Wei Huang, Kerolos M. A. Yousef, Eric Lee, Cheng-Wei Qiu, and Federico Capasso. Broadband achromatic metasurface-refractive optics. Nano Letters, 18(12):7801–7808, December 2018.
- [183] Zhi-Bin Fan, Zeng-Kai Shao, Ming-Yuan Xie, Xiao-Ning Pang, Wen-Sheng Ruan, Fu-Li Zhao, Yu-Jie Chen, Si-Yuan Yu, and Jian-Wen Dong. Silicon nitride metalenses for unpolarized high-*na* visible imaging. In CLEO: Science and Innovations, pages STh3I–8. Optica Publishing Group, 2018.
- [184] B. J. Lester, N. Luick, A. M. Kaufman, C. M. Reynolds, and Cindy A. Regal. Rapid production of uniformly filled arrays of neutral atoms. Phys. Rev. Lett., 115(7):073003, 2015.
- [185] Amir Arbabi, Ehsan Arbabi, Mahdad Mansouree, Seunghoon Han, Seyedeh Mahsa Kamali, Yu Horie, and Andrei Faraon. Increasing efficiency of high numerical aperture metasurfaces using the grating averaging technique. Scientific Reports, 10(1):1–10, 2020.
- [186] Matthew A Norcia, Aaron W Young, William J Eckner, Eric Oelker, Jun Ye, and Adam M Kaufman. Seconds-scale coherence on an optical clock transition in a tweezer array. Science, 366(6461):93–97, 2019.
- [187] Yueqiang Hu, Xudong Wang, Xuhao Luo, Xiangnian Ou, Ling Li, Yiqin Chen, Ping Yang, Shuai Wang, and Huigao Duan. All-dielectric metasurfaces for polarization manipulation: principles and emerging applications. Nanophotonics, 9(12):3755–3780, September 2020. Publisher: De Gruyter.
- [188] Chen Chen, Shenglun Gao, Xingjian Xiao, Xin Ye, Shengjie Wu, Wange Song, Hanmeng Li, Shining Zhu, and Tao Li. Highly efficient metasurface quarter-wave plate with wave front engineering. Advanced Photonics Research, 2(3):2000154, 2021.
- [189] Sajjan Shrestha, Adam C. Overvig, Ming Lu, Aaron Stein, and Nanfang Yu. Broadband achromatic dielectric metalenses. Light: Science & Applications, 7(1):85, December 2018.
- [190] Thaibao Phan, David Sell, Evan W. Wang, Sage Doshay, Kofi Edee, Jianji Yang, and Jonathan A. Fan. High-efficiency, large-area, topology-optimized metasurfaces. Light: Science & Applications, 8(1):48, May 2019.
- [191] Daniel K. Nikolov, Aaron Bauer, Fei Cheng, Hitoshi Kato, A. Nick Vamivakas, and Jannick P. Rolland. Metaform optics: Bridging nanophotonics and freeform optics. Science Advances, 7(18):eabe5112, April 2021.
- [192] Wei Ting Chen, Alexander Y Zhu, Vyshakh Sanjeev, Mohammadreza Khorasaninejad, Zhu-jun Shi, Eric Lee, and Federico Capasso. A broadband achromatic metalens for focusing and imaging in the visible. Nature Nanotechnology, 13(3):220–226, 2018.

- [193] Xiaoyan Huang, Weijun Yuan, Aaron Holman, Minho Kwon, Stuart J Masson, Ricardo Gutierrez-Jauregui, Ana Asenjo-Garcia, Sebastian Will, and Nanfang Yu. Metasurface holographic optical traps for ultracold atoms. Progress in Quantum Electronics, page 100470, 2023.
- [194] M. F. Parsons, F. Huber, A. Mazurenko, C. S. Chiu, W. Setiawan, K. Wooley-Brown, S. Blatt, and M. Greiner. Site-Resolved Imaging of Fermionic ${}^6\text{S}\text{Li}$ in an Optical Lattice. Phys. Rev. Lett., 114:213002, 2015.
- [195] M. F. Parsons, A. Mazurenko, C. S. Chiu, G. Ji, D. Greif, and M. Greiner. Site-resolved observations of antiferromagnetic correlations in the Hubbard model. arXiv:1605.02704, 2016.
- [196] David R Scherer, David B Fenner, and Joel M Hensley. Characterization of alkali metal dispensers and non-evaporable getter pumps in ultrahigh vacuum systems for cold atomic sensors. Journal of Vacuum Science & Technology A, 30(6), 2012.
- [197] M Succi, R Canino, and B Ferrario. Atomic absorption evaporation flow rate measurements of alkali metal dispensers. Vacuum, 35(12):579–582, 1985.
- [198] Thomas MH Lee, Debbie HY Lee, Connie YN Liaw, Alex IK Lao, and I-Ming Hsing. Detailed characterization of anodic bonding process between glass and thin-film coated silicon substrates. Sensors and Actuators A: Physical, 86(1-2):103–107, 2000.
- [199] George Wallis and Daniel I Pomerantz. Field assisted glass-metal sealing. Journal of applied physics, 40(10):3946–3949, 1969.
- [200] Ludwig W Bruch, Milton W Cole, and Eugene Zaremba. Physical adsorption: forces and phenomena. Courier Dover Publications, 2007.
- [201] Paul Aveling Redhead, J Peter Hobson, and Ernest Victor Kornelsen. The physical basis of ultrahigh vacuum. Springer, 1968.
- [202] Oswald Gröbner. Vacuum and cryopumping. 2004.
- [203] Christian Day. Cryotechnology and cryopumps. Handbook of Vacuum Technology, pages 511–564, 2016.
- [204] V Baglin. Mesure de la rugosité de surfaces techniques à l’aide de la méthode bet. Technical report, 1997.
- [205] KA Jadeja and SB Bhatt. Study of hydrogen pumping through condensed argon in cryogenic pump. In Journal of Physics: Conference Series, volume 390, page 012028. IOP Publishing, 2012.
- [206] JH Kamperschroer, MB Cropper, HF Dylla, V Garzotto, LE Dudek, LR Grisham, GD Martin, TE O’Connor, TN Stevenson, A Von Halle, et al. Cryosorption of helium on argon frost in tokamak fusion test reactor neutral beam lines. Journal of Vacuum Science & Technology A: Vacuum, Surfaces, and Films, 8(3):3079–3083, 1990.
- [207] JL De Segovia. Physics of outgassing. Technical report, Cern, 1999.
- [208] Ana Sotirova. A michelson interferometer for vibration measurements, fibre noise cancellation setup, study of ion trap loading mechanisms, 2018.

- [209] Andreas Fuhrmanek, Andrew Matheson Lance, Charles Tuchendler, Philippe Grangier, Yvan RP Sortais, and Antoine Browaeys. Imaging a single atom in a time-of-flight experiment. New Journal of Physics, 12(5):053028, 2010.

Appendix A

Montana cold window test

Overview: In this appendix we discuss the test of cold windows done in Montana Instrument CryoStation optical cryostat. Before designing the coldbox window structure, we need to verify the thermal performance of the double window and the dimensional stability that the indium foil gasket can provide under cryogenic environments. The dimensional stability of the indium seal is measured with the relative angular change between two windows in the window stack. The angle between windows are measured optically with a resolution of better than 0.02 mrad. The temperatures of the cold windows are measured with cryogenic sensors attached to the center of the window and the gradient is measured between the holder and the window.

A.1 Double window thermal test

To conduct this test, we created a simple structure resembling the thickness and separation of the coldbox windows [design shown in Fig. 2.14(b)]. The assembly was then attached to a test cryostat from Montana Instruments and cooled to 60 K, which is the radiation shield temperature of the test cryostat. The distance of the window to the room temperature shield was kept similar to the coldbox configuration to ensure the thermal radiation coupling was as similar as possible.

Figure A.1(a) shows the schematic of the test setup, showing the room temperature enclosure and windows, test window assemblies, and temperature sensor locations. Sensors T1 and T4 are attached to the metal parts of the test window assemblies, while sensors T2 and T3 are attached to the center of the glass window with Stycast 2850 epoxy to ensure accurate temperature measure-

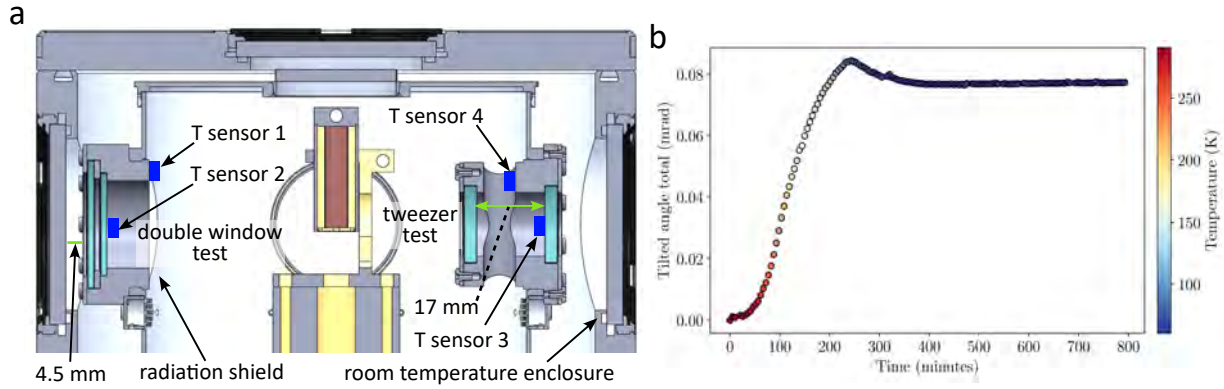


Figure A.1: (a) Schematic of double window and tweezer window test. Both the thermal and optical alignment stability are tested. Various temperature sensors measure the temperature difference between the glass and the aluminum heatsink. Showing good agreement between the simulated and measured value. (b) Relative alignment of windows on tweezer windows test assembly vs temperature recorded during the Montana Instrument cryostat test.

ments. After the system reaches thermal equilibrium at 60 K, the temperature differences between T1/T2 and T3/T4 are measured. The results show a temperature difference of less than 3 K for the double-pane window (T2-T1), which is similar to the simulated value in Sec. 2.2.9. However, this measurement represents an upper bound since the glass used here is much thinner (1.5 mm vs. 2 and 3 mm) compared to the ones used in the coldbox design. For T3-T4, we measure a temperature difference of less than 6 K, which is also similar to the COMSOL simulation. This demonstrates that the indium gasket provides sufficient thermal contact to thermalize the glass window to the metal structure.

A.2 Indium seal dimensional stability

To test the dimensional stability of the indium gasket for maintaining good angular alignment between the two tweezer windows, we utilize light reflected from the surfaces of the windows. Since the Montana Instrument cryostat provides optical access, this setup is relatively simple. The setup [similar to Fig. 2.26(a)] uses a collimated incoherent light source with a 10 nm bandwidth to eliminate interference from different sides of the windows. The 10 nm bandwidth is sufficiently small

to minimize chromatic focal shift of the focusing lens. The reflected light from the windows are focused with a lens of EFL=300 mm onto a CCD camera, converting angular changes of the beam into positions on the CCD camera.

The focused spots have 60 μm Gaussian waist and the pixel size of the CCD camera is 4.4 μm . The typical fit uncertainties to the centroid of the Gaussian is less than 15 μm (less than 4 pixels). This translate to the angular uncertainties of $< 50 \mu\text{rad}$. Figure A.1(b) shows the angular change of the test windows, indicating a deviation of less than 0.1 mrad between the two windows from 300 K to 60 K. This demonstrates that the indium foil gasket can provide the required dimensional stability sufficient for the objective to remain diffraction-limited.

Appendix B

SAES Rb Dispenser Activation

Overview: In this appendix we discuss the operating principle of the Rb alkali metal dispenser from SAES getter. We also document the activation steps of these type of dispenser and the typical behavior during activation.

B.1 The Alkali Metal Dispenser

The main component of the SAES alkali metal dispensers (AMDs) are alkali metal salt and reducing agents. In this case the chromate is Rb_2CrO_4 which is stable under atmosphere. The reducing agent used in SAES AMDs is a type of non-evaporable getter material consists of Zr 84% and Al 16% (st101) [196, 197]. To release the alkali metal the dispenser needs to be heated to a suitable temperature, typically between 550-850°C [197]. This starts the reducing reaction between the chromate and the St101 alloy and cause the alkali metal to evaporate. Besides the reducing reaction, the ST101 getter also absorbs most of the reactive gasses produced during the reaction which allows a clean source of alkali metal vapor to be produced [197]. However, some amount of H_2 and CO_2 are released during normal operation of the dispenser [196, 197]. Even though the rubidium chromate is stable at room temperature, the reducing agent oxidizes when exposed to air. Therefore the dispenser needs to be activated under vacuum before first use. The st101 alloy needs to be activate at a temperature beyond 600°C which requires a current of larger than 5A through the dispenser. The activation also serve to degas the dispenser.

B.2 Dispenser Activation

The activation of the dispenser depends on the operating current and vapor flux required during normal operation. Typically for AMO experiment, the flux required are much lower than the intended purpose of the AMDs which is coating of alkali metal film. So the AMDs are typically run at $<3.5\text{A}$ instead of $4.5\text{-}7\text{ A}$ stated in the SAES AMD manual. This results in a much lower and shorter activation cycle (typically $5.5\text{A @ }1\text{ min}$ repeated 3 times). The Rb dispenser in the source cell was activated during vacuum system bakeout. The activation was done according to the following steps.

- (1) When the source cell reaches baking temperature (typically around $200\text{ }^{\circ}\text{C}$) record the pressure. Turn the dispenser current to 3 A slowly and monitor the chamber pressure. Leave current at 3 A until the pressure stabilized (typically in 15 min) and record the initial, peak and end pressure as well as the voltage across the dispenser.
- (2) Turn the dispenser current to 5.5 A for 1 min and record initial, peak and end pressure as well as the voltage across the dispenser. Then set the current back to 3 A and wait for the pressure to stabilize.
- (3) Repeat step 2 three times.
- (4) Turn the dispenser current off, wait for the pressure to stabilize then record the final pressure.
- (5) Typical dispenser resistance should be around $1\ \Omega$ or less when measured at the high temperature lead.

The table below is the typical activation record for SAES AMDs for reference. The operating current for this dispenser is 3 A .

Before activation, Bake temperature: 170 °C, P_{init} : 1.8×10^{-7} torr					
Current (A)	Initial Pressure (torr)	Initial Voltage (V)	Max Pressure (torr)	Final Pressure (torr)	Final Voltage (V)
Pre-activate @ 3A	1.8×10^{-7}	0.9 V	2.8×10^{-6}	4.3×10^{-7}	0.9 V
4.5A @ 1 min	2.2×10^{-7}	1.3 V	1.2×10^{-6}	9.7×10^{-7}	1.3 V
5.5A @ 1 min	2.2×10^{-7}	1.6 V	1.3×10^{-6}	8.0×10^{-7}	1.6 V
4.5A @ 1 min	2.2×10^{-7}	1.3 V	2.5×10^{-7}	2.5×10^{-7}	1.3 V
Dwell dispenser current at 3 A, P_{end} : 1.8×10^{-7} torr					

Table B.1: Typical activation behavior of SAES alkali metal dispenser

Appendix C

Anodic Bonding

Overview: In this appendix we discuss the basic principle of anodic bonding and the steps we took to bond the metalens science glass cell.

C.1 Anodic Bonding

Anodic bonding is a technique to produce hermetic seals between glass and metal. The most common types of seal is between silicon and alkali-glass, e.g. Pyrex, Schott Borofloat 33, Corning 7740, and is most widely used in MEMS industry for sensor packaging [198]. It is an electrochemical process requiring heat and electric field to form a new oxide layer between silicon and glass. The systematic investigation of the anodic bonding process was first published in 1969 with bonding between glass to metals or silicon [199]. It has several benefits that makes it excellent for forming vacuum tight seal for UHV application. These benefits including

- both silicon and borosilicate glass are UHV compatible materials
- Borosilicate glass is commonly used as optical windows
- the bonding process is relatively low temperature with no melting
- no adhesive is needed to form the bond
- relatively relaxed surface flatness ($1-2\lambda$ per cm) comparing to other direct bonding process, e.g. optical contacting ($\lambda/10$ per cm or better)

However there are several limitations for material selection. Due to the heating required during the bonding process, the substrate materials requires similar CTE. Also, the glass needs to have high alkali content such as Na_2O or K_2O to achieve the required electrical resistivity. The most common combination is silicon and borosilicate glass, both have CTE of 3 ppm/K. For successful bonding, a RMS roughness of less than 10 nm on the substrate is preferred [198]. Although the anodic bonding process is fairly tolerant to surface contaminant, a mechanical scrubbing or chemical cleaning can increase the bond quality [198, 199].

C.2 Bonding Principle

The principle of anodic bonding is using heat to disassociate and mobilize ionic compounds added in the glass [Fig. C.1(a)]. In borosilicate glass these compounds are usually Na_2O or K_2O . Once the ions are mobilized, the electric field is applied and draws the oxygen ion towards the bond interface. During this process, a depletion layer is formed where there are no sodium ions in the glass [Fig. C.1(b)]. This cause an excess of oxygen near the bond interface and a new oxide layer starts to grow and forming a permanent connection between the two bonded materials [Fig. C.1(c)].

The anodic bonding process roughly separates into three parts:

- **Heating:** The bond interface is heated to temperature between 250-450 °C. The rate of temperature rise depends on the uniformity of the applied heat and geometry of the bonded parts, typically around 2-10 °C/min.
- **Apply electric field:** The electric field required to form the bond is applied through electrodes contacting the two bonded materials. The glass is negatively charged and silicon is positively charged. The electric field needs to be intense and uniform so typically several 100's to 2 KV is applied through electrodes touching the substrates depends on the geometry. During this process, the current flowing through the bond exponentially decreases and a bond front starts to propagate from the region nearest to the electrodes outwards. Typically it takes a few minutes to form a complete bond, which depends on

bond geometry.

- **Cool down:** After the completion of the bond, the electric field and the heat are removed and the parts cool down. The cooling rate needs to be slow since the CTE of the two bonded material are not identical and stress can accumulate if the part is cooled too rapidly. Typical cooling rate is around 2-10 °C/min depending on the geometry.

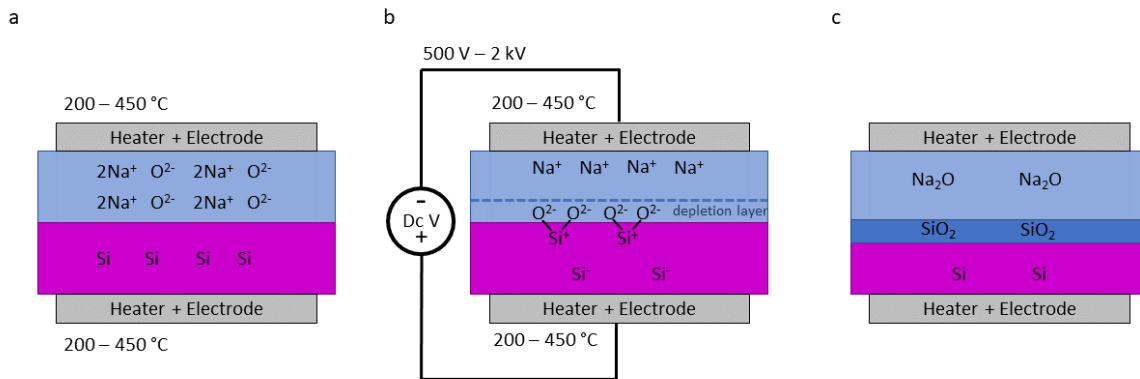


Figure C.1: (a) The borosilicate glass substrate (top light blue) and silicon substrate (bottom magenta) are optically polished and put in physical contact with each other. Then the substrates are heat up to 200-450 °C. This cause the sodium oxide in the borosilicate glass to disassociate and become mobile. (b) A high voltage between 500 V - 2 kV is applied, with negative side connects to the borosilicate glass and positive side connects to silicon. This cause the sodium ion to drift away from the substrate interface creating a depletion layer. Excess oxygen then forms silicate bond with silicon across the substrate interface. (c) After the new layer of silicon dioxide is formed across the interface, the high voltage and heat are removed. The bond between the two substrate become permanent.

C.3 Metalens Cell Bonding Parameter

Here are the parameters and steps used for the anodic bonding of the metalens science glass cell.

- **Heating:** An oven is constructed to heat the parts to 350 °C at the rate of 1 °C/min for coated glass cells and 5 °C/min for uncoated glass cell.

- **Applied Voltage:** Electrodes made of thin stainless steel wire is wrapped around the parts to ensure uniform electric field distribution. A voltage of 1000 V is applied in 100 V increment to keep the bond current within manageable level. The peak current is recorded and when the current drops to 25% of the peak current the power supply is turned off.
- **Cool down:** The heater is turned off and the part is cooled at the rate of 5 °C/min.

Appendix D

Basic Principle of cryopumping

Overview: In this section we introduce the basic concept of cryopumping and how the temperature effects the outgassing property of a surface. We describe the roles of the 45 K and 4 K surface in our coldbox and the behavior of their ability to adsorb gas on the surface. We first describe the basic principle of cryopumping and give a list of pressures of different gas species under different temperature. Finally, we discuss the design of coldbox and cold fingers from the cryopumping point of view.

D.1 Cryopumping Principle

A cryopump is one of the most prominent types of entrapment pumps, similar to sputter ion pumps and getter pumps, that captures and immobilizes gases without requiring an outlet. Cryopumping leverages the most rudimentary aspect of reducing pressure by reducing the temperature of the gas that is being pumped. The kinetic energy of the gas is reduced following \sqrt{T} and thus the pressure in the system is reduced. When the temperature of the gases are low enough, they can be freeze onto the cold surface provided by the cryopump. Typically, the intermolecular forces involved in these low-temperature processes are relatively weak (Van der Waals type), and no chemical reactions or chemical bonds are present, unlike in getter pumps. Consequently, cryopumping can pump all gasses including noble gasses, for sufficiently low temperatures on the pumping surface. This property is the main distinction between a cryopump and other capture pumps.

There are many factors that can affect the amount of gas molecules adsorbed and the equilibrium pressure attainable by a cryogenic surface including surface temperature, physicochemical properties of gas, surface energy distribution and mechanical properties of the surface (roughness, porosity etc...). There are three main types of physisorption mechanism to achieve cryopumping (Fig. D.1), which we will describe below.

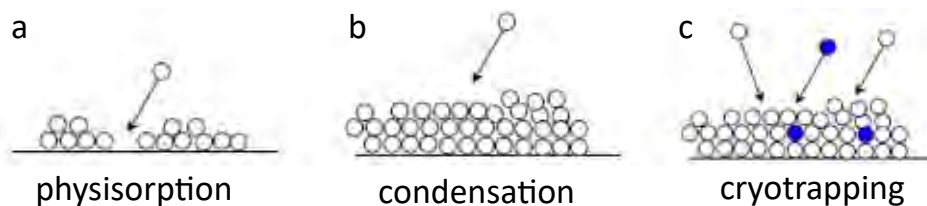


Figure D.1: Three different cryopumping regime: (a) physisorption (b) condensation and (c) cryotrapping depends on the amount of gases, temperature and gas type. (Image from [110])

D.1.1 Cryocondensation

In the case of cryocondensation [Fig. D.1(b)], the temperature of the surface is kept cold enough that the gasses condenses. Typically the pressure where cryopump operates is below the triple point pressure of all gasses, so the gas undergoes sublimation transition from gas to solid and vice versa. In order for the cryocondensation to occur, the cold surface must be saturated by the gas being pumped. The pressure achievable in this case depends only on the gas species and temperature of the surface, following the sublimation equilibrium pressure curve (Fig. D.2). This pressure curve (Fig. D.2) is obtained when the rate of condensation and sublimation equals (zero net pumping speed) under a given temperature. In theory, all gases can be condensed to very low pressure, but in practice the pressure is limited by the lowest attainable temperature by the cryogenic refrigerator typically around 4 K. From (Fig. D.2) we can see that temperature around 100 K is sufficient to condense water and all hydrocarbon to pressure below 10^{-12} torr. Below 20 K, all air components can be condensed out including most noble gasses other than neon. At 4 K all gases other than hydrogen and helium can be condensed out.

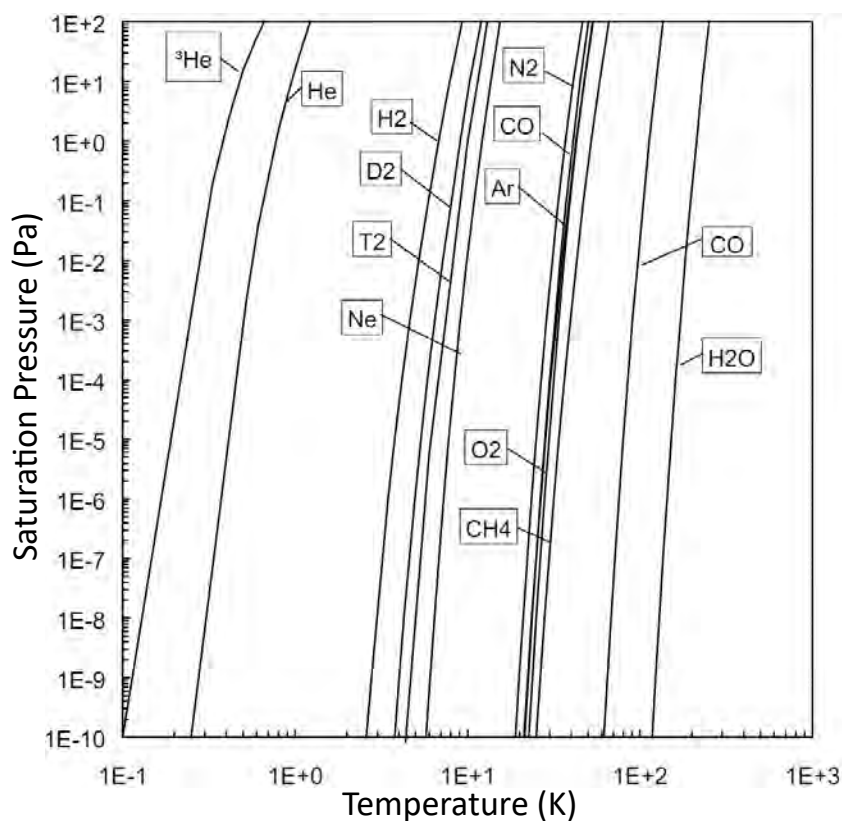


Figure D.2: Saturation curve (sublimation equilibrium pressure) of common gasses versus temperature. The saturation pressure is obtained when the rate of condensation equals to the rate of sublimation at a given temperature. (Image from [111])

D.1.2 Cryosorption

When the amount of gas of the particular species being pumped is not sufficient to cover the cryopumping surface up to a monolayer, the cryopumping follows another mechanism call cryosorption [Fig. D.1(a)]. Cryosorption is when gas particles come into contact with surfaces at sufficiently low temperature, they can loose so much kinetic energy that they stay attached to the surface by weak intermolecular forces [112,200]. The equilibrium pressure of adsorbed gas is much lower than that of condensed gas due to the higher binding energy between gas molecules and the solid surface compared to the binding energy between gas molecules in the case of cryocondensation. The difference in activation energy of gas molecules and solid surface is typically 2-3 times higher comparing to activation energy between gas molecules. The difference is even more significant for

light gases, ~ 10 for H_2 and ~ 30 for He. See Refs. [110, 113, 201] for list of activation energy between common gases and between gases on cold surfaces. Therefore, once the gas molecules are cryoadsorbed onto the surface, the likely hood of them escaping is much lower, thus achieving lower pressure. This mechanism is essential for pumping helium and hydrogen at 5 K, much higher than their condensation temperature.

However, the cryosorption process is quite complex and strongly dependent on surface condition (chemical, physical and geometry) and the gas coverage on the surface [110, 111, 202, 203]. Typically large surface area materials, such as activated charcoal or molecular sieves, are used to provide large surface to volume ratio ($\sim 1000 \text{ m}^2/\text{g}$) to prevent saturation of the surface. Sometimes in particle accelerator applications, technical surfaces such as metal, glass, or NEG surfaces are also used for cryosorption (Fig. D.3). These surfaces has much lower porosity but provides pumping along the whole beam line [204]. This is sometimes favorable since thermal regeneration of activated charcoal can be difficult and most of the cryopump outgasses significantly at room temperature and can not withstand high temperature UHV bakeout.

Typically monolayer gas coverage is around $10^{15} \text{ H}_2/\text{cm}^2$ [110]. However, even with low monolayer coverage, the probability of gas molecules immediately binding to the surface is still low. Therefore, the gas molecules typically takes a few bounces on the cold surfaces before being captured. This means the pumping efficiency of cryosorption is lower comparing to cryocondensation, but with lower ultimate pressure [111]. Beyond a few monolayer surface coverage, the surface effect becomes negligible and the pumping characteristics follows the cryocondensation behavior. To leverage the increased pumping speed of cryosorption at higher temperatures (especially for H_2 and He), one must provide a large pumping surface area to prevent saturation under the given gas load.

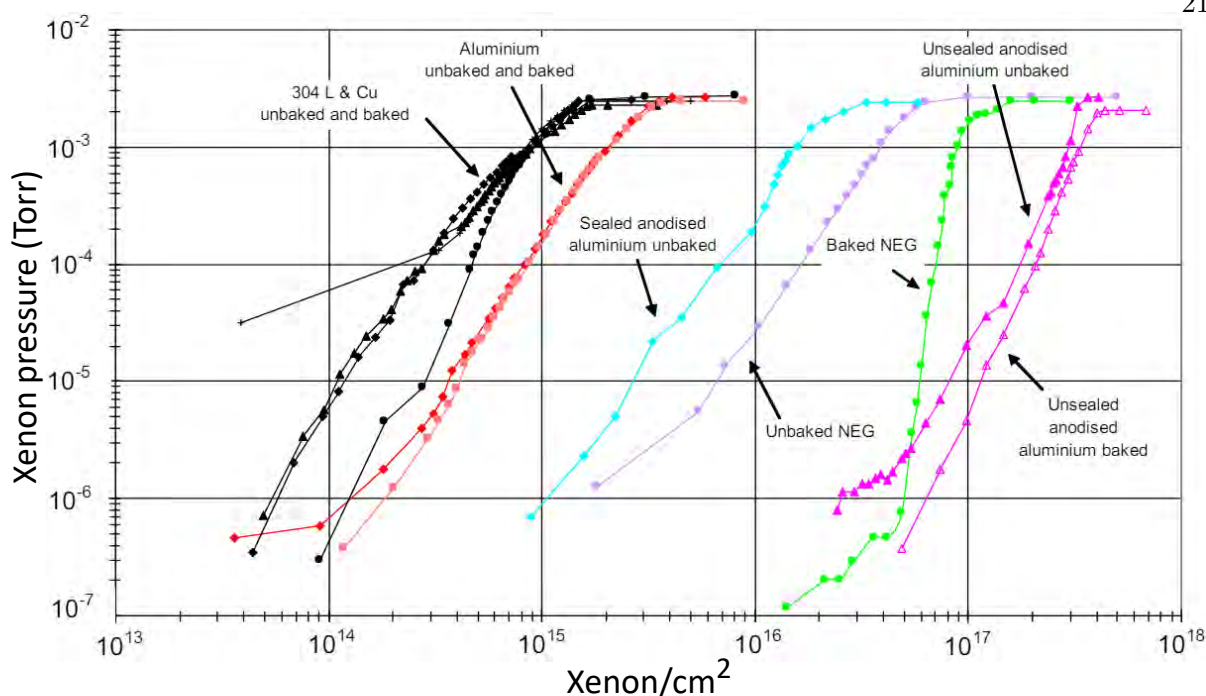


Figure D.3: Xenon adsorption isotherm curve at 77 K of selected technical surfaces including stainless, copper, aluminum (bare and anodized) and NEG. (Image from Ref. [204]) Note: It is appropriate to use xenon at 77 K because its saturated vapor pressure at this temperature is similar to that of hydrogen at 4 K and follows a roughly equivalent curve. Thus, any enhancement in equilibrium pressure due to surface effects and cryosorption will be similar once the temperature is scaled.

D.1.3 Cryotrapping

In the case of cryotrapping [Fig. D.1(c)], two (or more) species or gas are co-pumped. The cryotrapping process involves using a dominant gas species that is condensable at a much higher temperature to form a porous cryodeposit layer. Non-condensable gases, such as H_2 and He, are entrapped during this process. A fresh layer of condensable gas continuously freezes onto the cold surface, trapping the cryosorbed gas underneath and achieving a lower equilibrium pressure than cryosorption alone [111,202]. Typically, Ar is used as the entrapment gas due to its higher freezing point and being chemical inert [205,206]. One main drawback of cryotrapping is a continuous supply of condensable gas is needed and during regeneration of a cryopump, significant amount of gas load is generated and needs to be pump away with mechanical pumps [111].

D.2 Outgassing at low temperature

From the discussion in the cryosorption section above, we know that as the temperature of a surface becomes colder, the probabilities of gases trapped by the weak intermolecular potential becomes greater. If we consider outgassing from the surface as the release of trapped gas after some sojourn time, it does not matter whether the gas source is diffusion through the wall or capture from the environment. An infinite sojourn time on the surface implies that the gas is pumped out. Then, at sufficiently low temperature, we can write the sojourn time τ_s as a function of temperature according to the Frenkel equation as follows [113, 202, 207].

$$\tau_s = \frac{1}{\nu_0} e^{E/kT} \quad (\text{D.1})$$

$\nu_0 \sim 10^{12} \text{ s}^{-1}$ is the vibration frequency of the molecules in the intermolecular potential well near the cold surface. E is the binding energy of the surface potential in kJ/mole. k and T are ideal gas constant and temperature in Kelvin. To illustrate the effect of temperature on the sojourn time, for a binding energy of 0.4 kJ/mole which is typical for physisorbed molecules on the surface [202] the average sojourn time is around 10^{-8} s at room temperature. However, at 77 K this time would increase to around 1 year. Meaning the outgassing rate from a given surface and diffusion rate of gas from the bulk are significantly reduced. This strong temperature dependence of outgassing rate is what we rely on when we design the coldbox.

Appendix E

Stinger Cryostat

Overview: In this appendix we discuss the basic principle of stinger cryostat and its operation. We first discuss the construction and operation of the Stinger cryocooler. Then we will discuss the clogging issues of the cryocooler and some of the additional filters we put in to prolong the operation of the Stinger cold hold time. Finally, we will present solutions that can potentially solve the contamination problem that causes the cryocooler to be clogged.

E.1 Stinger cryocooler operating principle

The cryostat of our choice is the Stinger system from Coldedge Technologies. The stinger cryocooler is a fully closed-cycle flow cryostat with a flexible interface to decouple the vibration generated from the Gifford-McMahon (GM) cryocooler. The flexible coupling also allows a more relaxed space constraint near the main experiment chamber. The Stinger cryocooler consists of three parts, two separate helium loops and the UHV cryostat. The first loop is a standard Sumitomo Gifford-McMahon cryocooler (Model RDK-408D2 with 1 W cooling power at 4.2 K and is driven by a Sumitomo F-70 compressor). This is where the main cooling power is generated (orange dashed box in Fig. E.1). The second helium loop (outline with blue dash in Fig. E.1) is driven by a recirculating compressor (Sumitomo HC-4E1) and connects to a manifold before entering the Stinger cryocooler.

The manifold contains valves to isolate the Stinger from the recirculating compressor and pressure regulator to control the flow and a vacuum port for pumping out the loop inside the

Stinger cryocooler. The manifold can also be used to maintain the Stinger helium loop, including refilling helium, and pumping and flushing out residual air in the system.

This secondary loop couples to the GM cooler via heat exchangers (HX1, HX2 and HX3) located inside the Stinger cryocooler body. The cooled helium exit through a 1.5 m long flexible helium transfer line (attached to the Stinger body) with temperature ~ 6 K, pressure ~ 110 psi and flow rate around 20 liter/min. The Stinger cryocooler body and the transfer line are vacuum insulated and this insulating vacuum is completely separated from the UHV part of the experiment. At the end of the transfer line there is a capillary restriction that further reduces the helium temperature to below 4K through Joule-Thomson effect. This provides ~ 700 mW of cooling power at 4.2 K at the 4 K stage and 5 W of cooling power at 50 K at the radiation shield attachment point. This transfer line is removable from the UHV cryostat without effecting the UHV portion of the experiment. The transfer line tip is identical to the one used in most liquid helium flow cryostat. This allows modular design of the UHV cryostat without changing the Stinger cryocooler. Due to the complicated dynamics in the Joule-Thomson expansion orifice and the long helium flex line used for vibration decoupling, the passive temperature stability of this system is worse than that of the GM alone. Therefore, it might not be suitable for applications where precise temperature control is required.

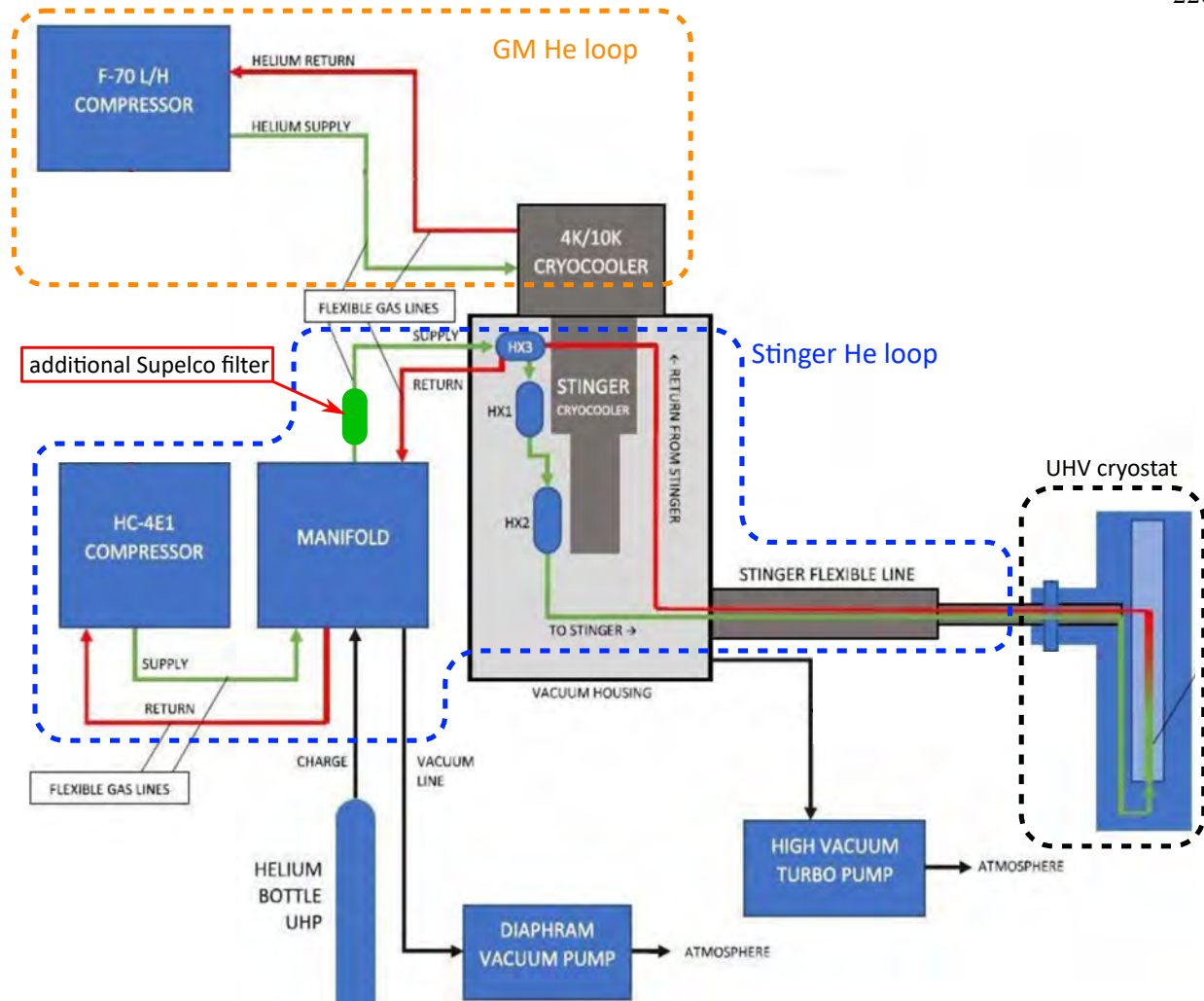


Figure E.1: Stinger block diagram adapted from the Stinger user manual. The stinger includes a primary GM helium loop to drive the cryocooler that cools the helium through heat exchangers. The secondary helium loop circulates the cooled helium to the UHV cryostat. And the UHV cryostat separates the helium path and the UHV chamber while providing cooling attachment points. (Image adapted from ColdEdge Stinger manual)

E.2 The UHV cryostat

The UHV cryostat attached to the main experiment functions as a heat exchanger, so its construction is relatively simple, with no moving parts. It is designed to be UHV-compatible and capable of withstanding UHV bakeout. The flexible helium transfer line eliminates the need for a copper thermal braid for vibration decoupling, which can be a potential source of outgassing in

the absence of UHV bakeout due to its large surface area. Since the flexible helium transfer line provides most of the vibration decoupling, we put bags of lead shot on top of the transfer line to dampen the residual vibration transmitted through the line [Fig. E.2(a)]. The copper braid mentioned in Sec. 2.2.9 is for small alignment adjustments rather than vibration decoupling.

The UHV cryostat mounts on a standard 4.5" CF UHV flange. The cryogenic temperature sensor wires are routed through the UHV feed through on the 4.5" CF flange. It contains a 4 K stage and a radiation shield attachment point. The helium exit the Joule-Thomson capillary flows through the 4 K stage heat exchanger in a spiral path. Then the returning helium flows through the radiation shield heat exchanger before exiting the UHV cryostat back to the transfer line [Fig. E.2(b)]. The 4 K stage heat exchanger and radiation shield heat exchanger are connected to each other and to the flange through thin stainless steel tube for thermal decoupling and structural rigidity.

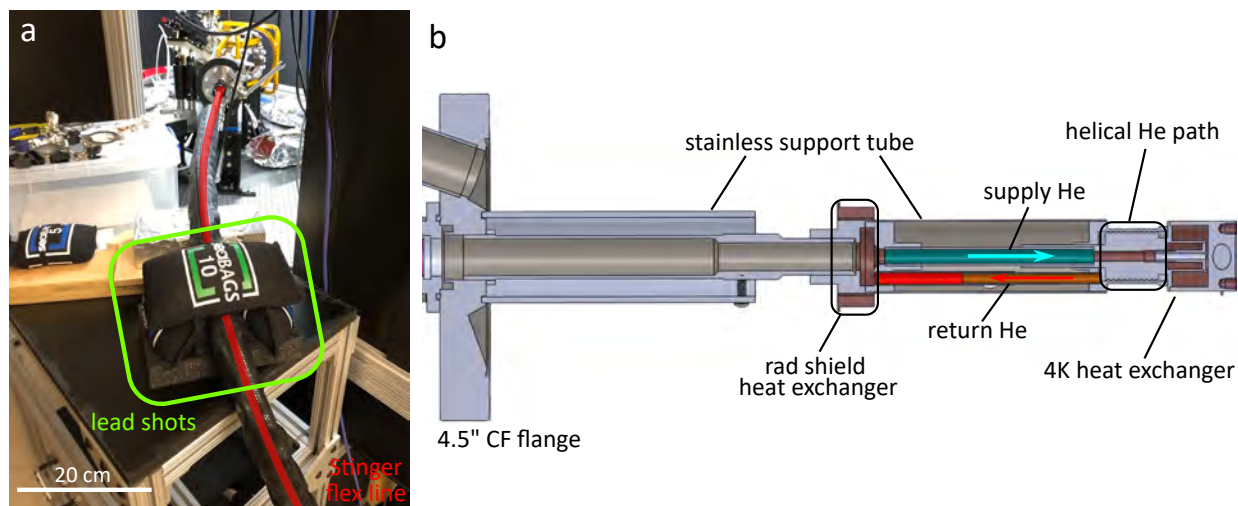


Figure E.2: (a) The photo showing how the lead shots are placed on top of the Stinger flex helium line to dampen the residual vibration from the GM cryocooler transmitted through the line. (b) The cut out of the CAD model of the UHV cryostat showing the 4 K stage attachment point and radiation shield attachment point as well as the helium flow path.

E.3 Compressor helium contamination issue

During the operation of the cryostat, we see gradual clogging of the helium transfer line. This gradual clogging limits the cold hold time to around two weeks before the cryostat spontaneously warms up. The sudden warm up of the cryostat is hard to predict even with a flow meter monitoring the helium flow. The point where the clog will be triggered varies from run to run. The symptoms typically consists of a slow drop of the helium flow (~ 5 liter/min) over a period of time (a few days) [Fig. E.3(a)]. Then a sudden clog will be triggered either with the perturbation of the line or pressure change, and the flow completely stops within one hour [zoomed in part of Fig. E.3(a)]. Our hypothesis is that the contaminating gas in the helium loop freezes, causing ice to build up over time inside the Stinger cryostat heat exchanger and the transfer line. Eventually, the ice breaks loose due to helium flow or perturbations in the line, blocking the orifice of the Joule-Thomson capillary.

Here are a few hypothesis we have from our observations when running the system.

- We see that every time we replace the helium in the loop with UHP (99.997%) pure helium the Stinger will clog during the first few cooldown. This means that the UHP helium is not sufficiently pure and the pump, flush and refill process might introduce contamination from the outside.
- Although the system initially stays cold for a long time, we observe a gradual degradation in cold hold time. Warming up and pumping out the contaminant, then cooling down without adding extra helium, appears to have no effect on resolving the clogging. This indicates that the source of contamination is internal to the helium circulating loop and not external.
- With freshly charged helium, after running the system for a while, we notice that the vented helium has an odor similar to that of some organic solvents. This odor persists regardless of how many times the helium is replaced, indicating that the contaminant may be coming

from the compressor oil breaking down or from gas dissolved in the oil.

With these observations and hypothesis we have come up with some solutions. One solution we employ is to use a freshly serviced compressor and high purity helium filter (Supelco helium purifier, part number: 27601-U) in the helium line between the manifold and the Stinger cryocooler (Fig. E.1). The Supelco filter can purify UHP grade (99.997%) helium to a cumulative level of 100 ppb (hydrocarbons + moisture + oxygen + carbon monoxide + carbon dioxide). By combining this with regular warm-ups of the 4 K stage to 20 K, which helps to loosen the ice, we observe cold hold times of up to several months. Eventually the flow drops significantly (~ 5 liter/min) then we perform a full warm up to room temperature and use the manifold to pump out all the contaminating gas in the Stinger cryocooler helium loop and the flow can be restored [Fig. E.3(b)]. However, the condition of the serviced compressor from Sumitomo is not consistent from one to another. Although they are all within specification according to Sumitomo, not all of them are clean enough to sustain long cold hold time in our system.

A more permanent solution is to use a dry compressor, where a diaphragm compressor is employed instead of an oil compressor. Due to the high pressure (7 bar or 100 psi) and high flow rate (30 liters/min) there are only a few compressor choices. At the end we settled on KNF N630.15 combine with the Supelco helium filter. This can potentially prolong the cold hold time to as long as the diaphragm service interval of the compressor (normally 3-5000 hrs of continuous operation). Another advantage of the KNF compressor is that, unlike the HC-4E1, the diaphragm maintenance can be done on our own without sending the pump back to the manufacturer, thus reduce the down time of the cryostat. Initial tests with these pumps done by ColdEdge and NIST ion storage group shows no degradation of cooling power and clogging over extended periods of time from the Stinger cryostat. Therefore, we will soon replace our Sumitomo HC-4E1 with the dry compressor solution.

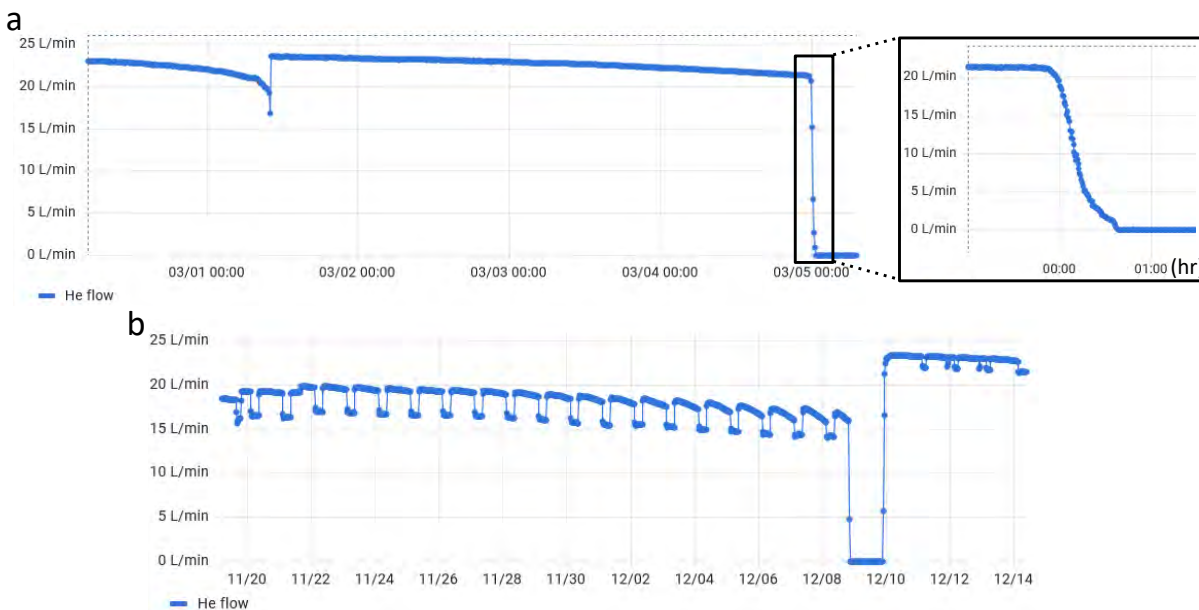


Figure E.3: (a) The helium flow versus time during a typical clogging and warm up. We see drops in helium flow over the course of days, and a sudden initiation of the clog and the flow completely stops within 1 hour (zoomed in portion on the right). A partial clog that revived itself was observed between 3/1 and 3/2. Illustrates the unpredictable nature of the Stinger cryostat clogging behavior. (b) The helium flow during the long months scale operation of the cryostat showing a slow degradation over a long time and partial revival of the flow after each regeneration of the 4 K cold tip at 20 K. A full warm up to room temperature was carried out between 12/9 and 12/10 and the helium flow was restored to the original value. No helium replacement is done during full warm up.

Appendix F

Laser phase noise from cryostat vibration

Overview: In this appendix we discuss the potential decoherence effect of mechanical vibration between the coldbox and the optical breadboards where the Rydberg excitation light is launched. The displacement caused by the cryostat is important as it can potentially introduce optical phase error in the Rydberg excitation light or Raman light. Depending on the duration of the optical pulse, the phase noise in different spectrum either introduce shot-to-shot fluctuation or noise within the optical drive pulse.

F.1 Converting a vibration spectrum to phase noise

To calculate the phase noise introduced by the cryostat vibration, we can use the interferometric spectrum [Fig. 2.22(c)] measured in Sec. 2.4.2. The conversion is the following.

$$PSD_{phase\ noise} = (PSD_{vibration} \lambda)^2 \quad (\text{F.1})$$

λ is the laser wavelength, for Rydberg it's 420 nm and 1013 nm, and for Raman it's 795 nm. The unit for $PSD_{phase\ noise}$ is (rad²/Hz) and $PSD_{vibration}$ is (nm/ $\sqrt{\text{Hz}}$). With this relation we can compare the phase noise from the cryostat vibration against the phase noise of the laser itself [Fig. F.1(a)]. We see that the cryostat vibration induced phase noise is much lower than the laser phase noise by 2 orders of magnitude for both 420 nm and 1013 nm. Therefore, this residual phase noise from the cryostat vibration will not be the limiting factor for the Rydberg and Raman coherence up to 100s of milliseconds. As a comparison, we take the vibration time trace from one

of the low vibration cryogenic ion trap from Jonathan Home's group at ETH [124, 125, 208]. This measurement was done by forming an interferometer between the 4 K stage and the breadboard outside the cryostat. In their case, the RMS vibration is around 40 nm and pk-pk around 200 nm [Fig. F.1(b)], which results in a coherence time in the order of 10 ms [124] when addressing the individual ions with free space beam launched from the breadboards. For us, the RMS vibration is less than 3 nm [Fig. F.1(c)] and pk-pk is around 20 nm even with the interferometer drift. This yields an expected coherence time (considering only vibration-induced phase noise) on the order of 100 milliseconds, which is much longer than the time scales for Rydberg and Raman transitions (less than 1 millisecond) and other dephasing mechanisms such as magnetic field noise.

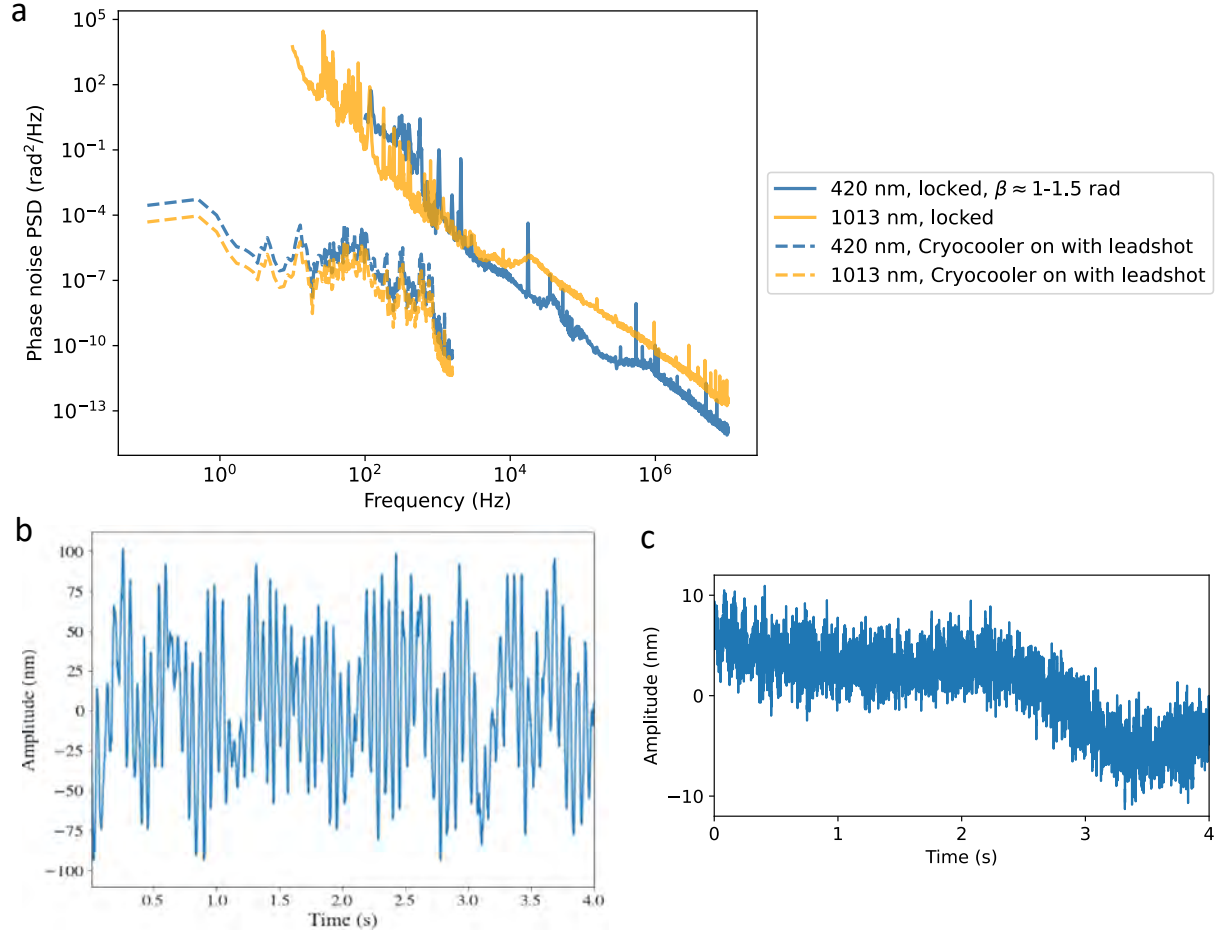


Figure F.1: (a) Vibration induced laser phase noise spectrum calculated from [Fig. 2.22(c)] in Sec. 2.4.2. Solid lines are laser phase noise measured after locking to the stable cavity (blue data is 420 nm laser phase noise, orange data is 1013 nm laser phase noise). The dashed lines are phase noise calculated from the cryostat vibration spectrum (Blue is with respect to 420 nm and orange is with respect to 1013 nm). (b) Cryostat vibration time trace reproduced from Ref. [124, 125, 208] corresponds to 40 nm RMS vibration amplitude this yields around 10 ms coherence time on the qubit drive. (c) Coldbox vibration time trace of our experimental setup. This corresponds to less than 3 nm RMS vibration amplitude, more than 10 times less comparing to Ref. [124].

Appendix G

Release-recapture Gaussian vs harmonic trap

Overview: In this appendix we discuss the difference between fitting the release and recapture data with Gaussian trap and Harmonic trap. We observe that fitting the same release-recapture data with a harmonic potential results in a lower atom temperature comparing to fitting to a Gaussian trap. We discuss qualitatively the difference between two methods and discrepancies that we see between fitting to the two different trap shapes.

G.1 Harmonic trap

Historically the release-recapture Monte-Carlo simulation is done assuming a harmonic trap over the full tweezer trap depth [134, 136, 152]. If assuming a harmonic potential over the full trap depth, the total energy of an atom in the trap is expressed as $1/2mv_i^2 + 1/2m\omega^2x_f^2$, where v_i is the initial atom velocity, x_f is the final atom position after the release-recapture time and ω is the trap frequency. If the initial atom temperature is low enough, typically less than 1/10 of the trap depth, then the atom samples the bottom of the Gaussian function which can be approximate as harmonic trap with good accuracy. In fact this is typically done when dealing with analysis of atoms in tweezers. However, this is not accurate since in release and recapture the atom samples significant portion of the periphery of the trap regardless of initial atom temperature. If we plot the trap shape of the harmonic potential vs. Gaussian and Airy, we can see that the confinement is much less near the brim of the trap for Gaussian and Airy shape (Fig. G.1).

G.2 Gaussian and Airy

To fit with the Airy or Gaussian trap shape, we first assume the atom initial temperature is low so that the initial position and velocity can be sampled identically as in Sec. G.1. The difference now is that after flashing off the trap, the final energy of the atom is the initial kinetic energy plus the potential energy at the atom location after the trap is turned back on. The potential energy is numerically determined based on the trapping parameters.

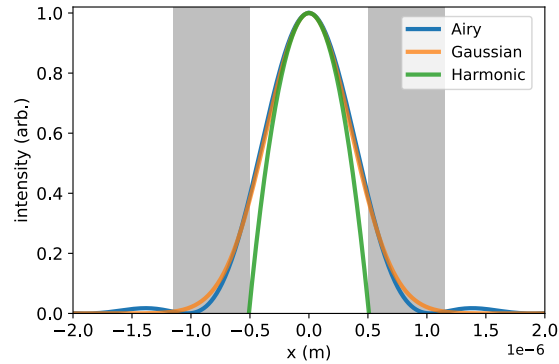


Figure G.1: The trap profile difference between Airy (blue), Gaussian (orange), and harmonic (green). The three trap shapes are normalized to the same trap frequency at the bottom of the trap (intensity maximum). The grey shaded parts are where the atom is recaptured by the Gaussian and Airy trap profile, but will escape if assuming a harmonic trapping potential.

G.3 Comparison

For harmonic trap shape, we see good agreement of temperature measurements between the R-R and Raman-sideband spectroscopy and free space time-of-flight imaging [152, 209]. If we compare the harmonic trap shape to the Gaussian and Airy, we see that the harmonic shape has a smaller recapture volume, which is shown in grey shaded regions in Fig. G.1. When fitted to the same data, the temperature and heating rate with harmonic trap shape is consistently lower by about a factor of 3 comparing to the Gaussian and Airy case. When we compare this to the calculated recoil heating limit, we see harmonic trap goes below the calculated recoil limit ($5 \pm 2 \mu\text{K/s}$ vs. $10 \mu\text{K/s}$), but the Gaussian ($12 \pm 4 \mu\text{K/s}$) and Airy ($12 \pm 5 \mu\text{K/s}$) agrees well

with the calculated recoil limit, [Fig. G.2(a)].

Examining the actual fit of the data with different trap shapes, we see that the harmonic trap curve lies above the data points to the left of the red dashed line and below the data points to the right of the dashed line. In contrast, the Gaussian and Airy fits describe the data better [Fig. G.2(b)]. This systematic skew when fitting the data with the harmonic trap shape is also observed in other studies (for example Ref. [59]) using release and recapture for atom temperature measurement.

This comparison is to describe the discrepancies we observe while using release and recapture as a method of measuring temperature and not an extensive study of the cause of this discrepancy. For ease of comparison to other literature, we use harmonic fit in this thesis unless otherwise specified. A more thorough investigation of the origin of this discrepancy will subject to future study.

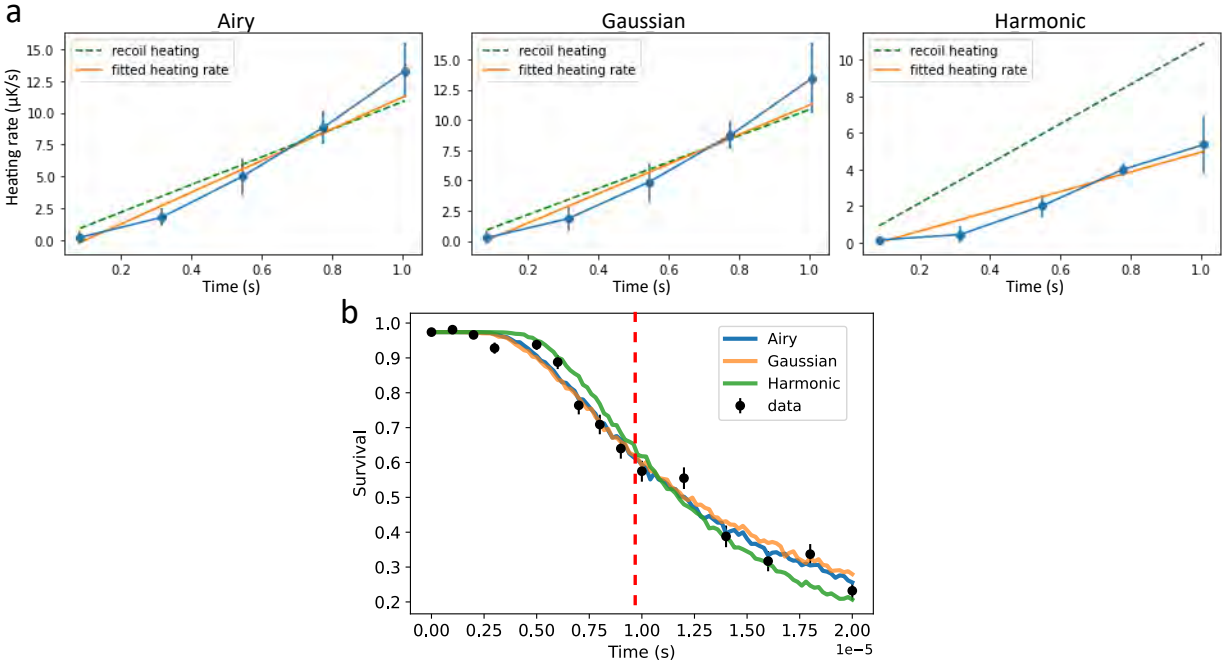


Figure G.2: (a) Fitted recoil limited heating rate between between Airy, Gaussian, and harmonic. The Gaussian and Airy gives similar heating rate of $12 \pm 4 \mu\text{K/s}$ and $12 \pm 5 \mu\text{K/s}$ respectively, while the harmonic gives $5 \pm 2 \mu\text{K/s}$ about twice as low as the prediction from recoil limit. (b) Release and recapture data fitted with Monte-Carlo using Airy, Gaussian and harmonic trap shape. The Airy and Gaussian gives similar temperature result of $38 \pm 4 \mu\text{K}$ and $41 \pm 5 \mu\text{K}$ while the harmonic gives $13 \pm 3 \mu\text{K}$. The small difference between the Airy and Gaussian trap shape near the brim of the trap have negligible effect on the resulting temperature. However, fitted with harmonic trap consistently gives a lower temperature by a about a factor of 3. Visually we see that harmonic over fit in the region to the left of the red dashed line and under fit in the region on the right, and the Gaussian/Airy fits better to the data.

ProQuest Number: 31488215

INFORMATION TO ALL USERS

The quality and completeness of this reproduction is dependent on the quality and completeness of the copy made available to ProQuest.



Distributed by
ProQuest LLC a part of Clarivate (2024).
Copyright of the Dissertation is held by the Author unless otherwise noted.

This work is protected against unauthorized copying under Title 17,
United States Code and other applicable copyright laws.

This work may be used in accordance with the terms of the Creative Commons license or other rights statement, as indicated in the copyright statement or in the metadata associated with this work. Unless otherwise specified in the copyright statement or the metadata, all rights are reserved by the copyright holder.

ProQuest LLC
789 East Eisenhower Parkway
Ann Arbor, MI 48108 USA